Ollscoil na hÉireann, Corcaigh

National University of Ireland, Cork

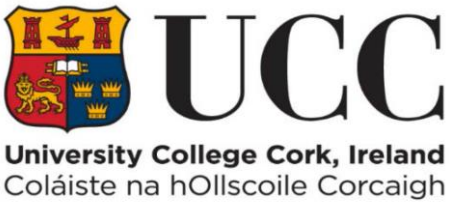

Fabrication and characterization of UV-LEDs

Thesis presented by

Pietro Pampili, M.Sc.

for the degree of

Doctor of Philosophy

University College Cork

School of Engineering

Head of School: Prof. William P. Marnane

Research conducted at Tyndall National Institute

Supervisor: Prof. Peter J. Parbrook

2019

Table of contents

Declaration

I hereby state that all of the work undertaken in this thesis is original in content and was carried out by the author. Work carried out by others has been duly acknowledged in the thesis. The work presented has not been accepted in any previous application for a degree.

Signed: ……

Date: ……

Abstract

This thesis investigates the emerging technology of ultraviolet light-emitting diodes (UV LEDs) based on III-nitride materials. Despite the incredible improvement of these devices over the past decade, if compared with visible LEDs based on the same semiconductor system, UV LEDs still suffer from a much reduced efficiency that severely limits their potential. The technological issues responsible for this problem have been analysed and possible solutions and mitigation strategies have been proposed, both at growth and fabrication level.

In particular, the *n*-type doping of the AlGaN materials used in the cladding layers of these devices has been optimized, for AlN concentrations in the range of 50–85%. The transport mechanism in these materials has also been studied, and the presence of a significant impurity conduction at room temperature has been detected; the consequences of this fact on the doping optimization have been highlighted.

A deep-UV LED for space application emitting below 250 nm, and a near-UV LED emitting at 340 nm—in whose active region an InAlN alloy has been used in place of the more common AlGaN—have both been successfully demonstrated.

The use of micron-sized emitters has been investigated with the aim of improving switching characteristics and light-extraction efficiency of these devices. An optical bandwidth of over 20 MHz has been demonstrated for the deep-UV LED, as required by the funding agency. Thanks to the optimization work performed on the reflective sidewalls of the micro-emitters, an increase of light-extraction efficiency up to four times was shown.

Acknowledgments

First and foremost, I would like to express my deepest gratitude to my supervisor Prof. Peter Parbrook for giving me the opportunity to carry out my PhD in his group at Tyndall National Institute. I'm especially grateful to Peter for being an endless source of ideas and insightful comments while, at the same time, encouraging me to take control of my research and pursue my own ideas.

I also wish to thank Mr. Brian Corbett and all the members of his group, for their constant support during my research and for giving me the opportunity to collaborate with them.

In particular, I would like to thank Dr. Mahbub Akhter for introducing me to the art of III-nitride device fabrication, and for being always available when I needed help in the clean room. And also a very special thanks to Mr. Pleun Maaskant for his infinite kindness and thoughtfulness, and for his dedication to creating a welcoming and collaborative work environment for our joint group.

I would like to acknowledge all the present and past members of Peter's group: Dr. Vitaly Zubialevich, Dr. Duc van Dinh, Dr. Haoning Li, Dr. Michele Conroy, Dr. Matthew Smith, Dr. Zhiheng Quan, and Dr. Shahab Norouzian, who in a way or another have helped me along the way. In particular, I am especially grateful to Vitaly, Haoning and Duc for their support with the MOVPE growth. Vitaly also deserves a special thanks for our fruitful collaboration in many projects, our stimulating discussions (spanning from optical properties of semiconductors to linguistics), and above all for his friendship. *Grazie!*

I am indebted to Dr. Farzan Gity for his kind help in many instances, and also for training me on the use of the Hall-effect equipment, which opened up a whole chapter of this thesis. But in addition to that, I would like to thank Farzan especially for the enjoyable time spent together, particularly on the squash pitch, for the nice discussions, and for being such a good friend!

Finally, I wish to thank my whole family, without whom I would have not been able to complete this thesis. My thoughts go to my parents, who unfortunately did not live to see the result of my work, and to my parents-in-law for their unconditional love, encouragement and much needed support. And, above all, I wish to thank my wife

Daniela for being beside me throughout this journey, for her patience, understanding, and encouragement in every possible way.

List of publications

Related to this work:

P. Pampili, D. V. Dinh, V. Z. Zubialevich, and P. J. Parbrook, "Significant contribution from impurity-band transport to the room temperature conductivity of silicon-doped AlGaN," Journal of Physics D: Applied Physics, vol. 51, 06LT01, 2018.

P. Pampili and P. J. Parbrook, "Doping of III-nitride materials," Materials Science in Semiconductor Processing, vol. 62, pp. 180-191, 2017.

D. V. Dinh, **P. Pampili**, and P. J. Parbrook, "Silicon doping of semipolar (11-22) $Al_xGa_{1-x}N$ ($0.50 \leq x \leq 0.55$)," Journal of Crystal Growth, vol. 451, pp. 181-187, 2016.

P. Pampili, M. Akhter, C. Eason, V. Z. Zubialevich, P. P. Maaskant, Z. Quan, et al., "250-nm emitting LED optimized for optical fibre coupling," in IEEE Summer Topicals Meeting Series (SUM 2015), Nassau, Bahamas, 2015, pp. 177-178.

M. Akhter, **P. Pampili**, V. Z. Zubialevich, C. Eason, Z. H. Quan, P. P. Maaskant, et al., "Over 20 MHz modulation bandwidth on 250 nm emission of AlGaN micro-LEDs," Electronics Letters, vol. 51, pp. 354-355, 2015.

V. Z. Zubialevich, T. C. Sadler, D. V. Dinh, S. N. Alam, H. Li, **P. Pampili**, et al., "Enhanced UV luminescence from InAlN quantum well structures using two temperature growth," Journal of Luminescence, vol. 155, pp. 108-111, 2014.

Other publications:

V. Z. Zubialevich, **P. Pampili**, and P. J. Parbrook, "Fast Growth of Smooth AlN in a 3 × 2″ Showerhead-Type Vertical Flow MOVPE Reactor," Physica Status Solidi (B) Basic Research, vol. 255, 1700472, 2018.

G. Sabui, V. Z. Zubialevich, M. White, **P. Pampili**, P. J. Parbrook, M. McLaren, et al., "GaN Nanowire Schottky Barrier Diodes," IEEE Transactions on Electron Devices, vol. 64, pp. 2283-2290, 7883894, 2017.

Abbreviations

AC	Alternating current
AFM	Atomic force microscopy
AES	Auger electron spectroscopy
BOE	Buffered oxide etch
cTLM	Circular transmission line measurement
CV	Capacitance–voltage characteristics
DC	Direct current
DUT	Device under test
EE	Electrical efficiency
EL	Electroluminescence
EBL	Electron blocking layer
EQE	External quantum efficiency
ECR	Electron cyclotron resonance
EDS	Energy dispersive X-ray spectroscopy
FWHM	Full width at half maximum
IQE	Internal quantum efficiency
ICP	Induction-coupled plasma
IV	Current–voltage characteristics
LEE	Light extraction efficiency
LI	Radiant-power–current characteristics
MOVPE	Metal-organic vapour phase epitaxy
MBE	Molecular beam epitaxy

MIGS	Metal-induced gap states
NNH	Nearest-neighbour hopping
NBE	Near band-edge
PL	Photoluminescence
PMT	Photomultiplier tube
QCSE	Quantum confined stark effect
RF	Radio-frequency
RTA	Rapid thermal annealing
sccm	Standard cubic-centimetre per minute
SEM	Scanning electron microscopy
TE	Transverse electric
TM	Transverse magnetic
TMGa	Trimethylgallium
TMAl	Trimethylaluminium
TMIn	Trimethylindium
TLM	Transmission line measurement
TEM	Transmission electron microscopy
UV	Ultraviolet
LED	Light-emitting diode
WPE	Wall-plug efficiency
XRD	X-ray diffraction
XPS	X ray photoelectron spectroscopy

1 Ultraviolet LEDs: state of the art, and applications

Ultraviolet Light Emitting Diodes (UV LEDs) are an emerging technology whose market is already worth more than 200 million US dollars [1]. According to analysts' forecast, its growth is also due to continue exponentially for the next few years, as shown in Figure 1.1, taken from a Yole Développement report [1]. Although the market is still dominated by traditional UV sources—such as mercury, metal-halide, xenon and deuterium lamps—the gap between UV LEDs and these is shrinking each year. In fact, while the UV LED market share was only 8% in 2008, it is now more than 30%, and it is believed it can exceed 40% by 2019. Not only will UV LEDs eventually replace gas-based lamps in current applications, but they are also expected to create new applications that are inaccessible to the current technology.

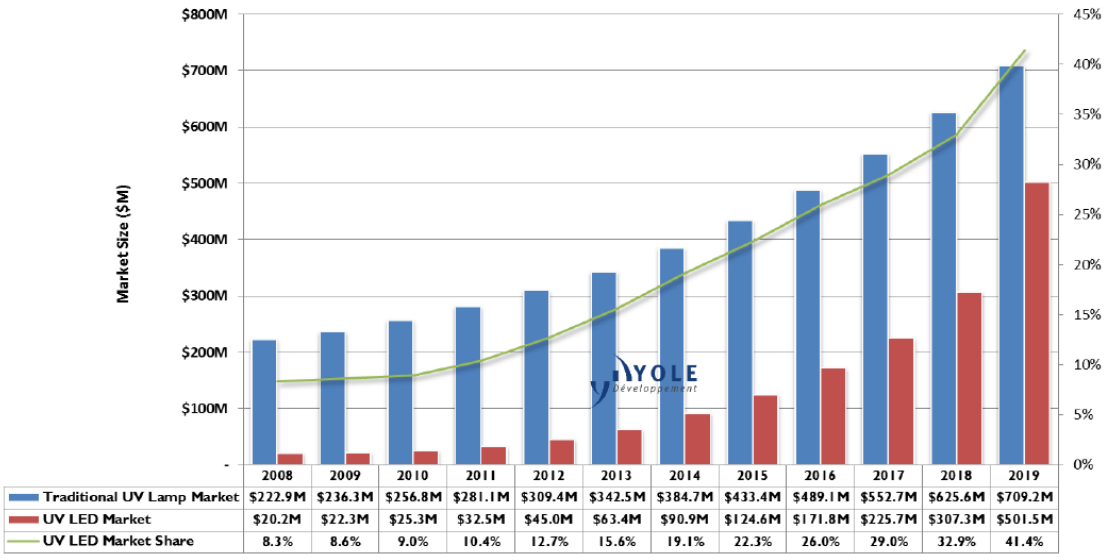

	2008	2009	2010	2011	2012	2013	2014	2015	2016	2017	2018	2019
Traditional UV Lamp Market	$222.9M	$236.3M	$256.8M	$281.1M	$309.4M	$342.5M	$384.7M	$433.4M	$489.1M	$552.7M	$625.6M	$709.2M
UV LED Market	$20.2M	$22.3M	$25.3M	$32.5M	$45.0M	$63.4M	$90.9M	$124.6M	$171.8M	$225.7M	$307.3M	$501.5M
UV LED Market Share	8.3%	8.6%	9.0%	10.4%	12.7%	15.6%	19.1%	22.3%	26.0%	29.0%	32.9%	41.4%

Figure 1.1: UV LED market shares

Comparison of traditional vs UV LED market sizes for the following applications: water and air disinfection / purification, analytical instruments, medical phototherapy, photocatalytic purification, counterfeit detection, UV curing, and R&D. Taken from [1], also downloadable from the LED Taiwan conference website at <http://bit.ly/2zPkw1A> (full URL in bibliography).

Compared to UV lamps—which are usually very bulky and fragile, contain toxic materials, and require complex high-voltage electronic drives—UV LEDs are compact,

shock resistant and environmentally friendly devices, whose emission wavelengths can be arbitrarily varied by changing the material bandgap of their active regions. They do not require any warm-up times and can exhibit optical modulation bandwidths in excess of 20 MHz [2].

Notwithstanding these interesting characteristics, a significant amount of work is still needed in order to reduce their price, increase optical power and efficiency, and extend their working lifetime. For this reason, although UV LEDs are already competitive in many high-end applications, their potential is not fully developed and an increasing number of applications are expected in future switch to UV LEDs, assuming the current trend of technology development continues.

1.1 Applications of UV LEDs

There are many different applications that require UV radiation and that can potentially make use of UV LEDs as light sources; as shown in Figure 1.2, their requirements vary both in terms of power and emission wavelength.

Traditionally, the ultraviolet light is divided in three regions[1], namely: UVA (400–320 nm), UVB (320–280 nm), and UVC (280–200 nm). In the UVA, the LEDs can be used as sources for curing of inks, paints, coatings, resins, polymers, and adhesives as well as 3D-printing for rapid prototyping and lightweight construction [3]. They can also be used in the area of sensing as many biomolecules such as NADH (also absorbing in the UVC), collagens, elastin, and lipopigments have strong absorption bands in this range that can induce fluorescence [4]. Other applications, also based on fluorescence, include counterfeit detection of ID cards and banknotes, or white light production using broad spectrum phosphors. Direct-write photolithography based on UVA μ-LED has also been recently demonstrated [5]

In the UVB, LEDs have potential for the treatment of skin conditions, such as psoriasis and vitiligo [6, 7], as their narrow emission spectrum can provide effective treatment of the condition without damage from exposure to shorter wavelengths. Other applications include plant growth lighting to stimulate the production of phytochemicals responsible for quality traits such as taste, scent, colour, and nutritional value, or to induce natural plant responses [8, 9].

[1] This subdivision is not fully standardized, and different researchers might use slightly different ranges.

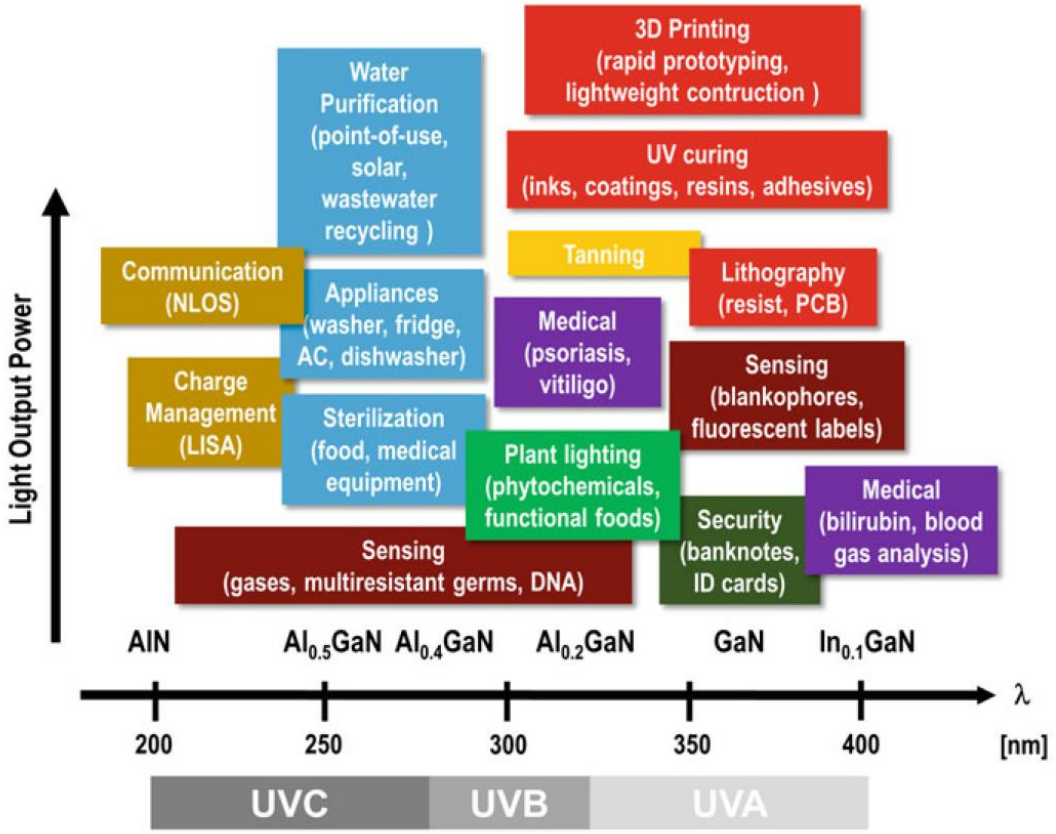

Figure 1.2: UV LED applications

The main applications of UV LEDs are shown for different wavelengths and output power required. Taken from [3].

In the UVC, the ability of the high-energy photons to disrupt DNA or RNA of microorganisms rendering them unable to reproduce, allows germicidal and water purification applications [10]. Fluorescence effects can also be used in this range for sensing applications of biomolecules such as tryptophan, NADH, tyrosine, DNA, and RNA [11].

Gas detection by absorption spectroscopy is a well-developed technique whose detection range is usually limited to the infrared, the region in which molecular vibrations can be excited. However, the availability of reliable UV sources might extend its domain of interest to both UVB and UVC regions, where molecules such as NH_3, NO, O_3, SO_2, NO_2, and some hydrocarbons show a strong electron absorption [12].

Other less common applications in the UVC range include non-line-of-sight communication [13], and charge management of proof-masses in space applications by use of the photoelectric effect [14, 15].

1.2 III-nitride semiconductor system

In order to emit light in the UV range, LEDs and laser diodes require the use of direct semiconductor materials with bandgaps higher than 3.1 eV. The III-nitride semiconductor system—i.e. gallium nitride (GaN), indium nitride (InN) and aluminium nitride (AlN), along with their ternary and quaternary alloys—can provide such materials. After almost thirty years from the first fundamental breakthroughs made by Akasaki, Amano and Nakamura [16-19], this semiconductor system is now especially known for being at the base of the very successful technology of the blue laser and the blue and white LEDs. Devices based on III-nitride materials have become part of our everyday life and can be found, for example, in background illumination of mobile phones and televisions, in energy-saving light-bulbs, or in high-definition Blu-ray players [20-22]. The importance of this technology has also been recognized by the Royal Swedish Academy of Sciences who awarded the three aforementioned Japanese researchers with the Nobel Prize for Physics in 2014 [23].

Theoretically, as can be seen from Figure 1.3, the light emission from the III-nitride system can span not only the whole visible spectrum, but also part of the infrared down to 1.7 μm (0.7 eV for InN [24]), and much for the whole ultraviolet down to ~210 nm (6.0 eV for AlN [25]). In the same way as introducing some InN in the GaN lattice reduces the alloy bandgap and shifts the emission towards the blue and the green, adding increasing amounts of AlN has the opposite effect of shortening the emission wavelength, so that all the UVA, UVB and UVC spectral ranges can in theory be covered.

Unfortunately, this is not a straightforward process. As more and more aluminium is introduced into the crystal, many technological issues begin to appear which limit the characteristics of the devices: the quality of material degrades, ohmic contacts become more difficult to achieve, larger amounts of UV light get trapped inside the semiconductor. This explains why—notwithstanding visible LEDs are very efficient devices, with lifetimes up to 50 000 h [26] and package prices as low as 1 $/klm [27]—their UV counterparts have efficiencies one or two orders of magnitude lower, often much shorter lifetimes and dramatically higher costs [3]. Even compared to the costly standard UV lamps, the average selling prices of UVB and UVC LEDs are still orders of magnitudes higher, although this might be partially compensated by higher lifetimes, and lower maintenance and power supply costs [28].

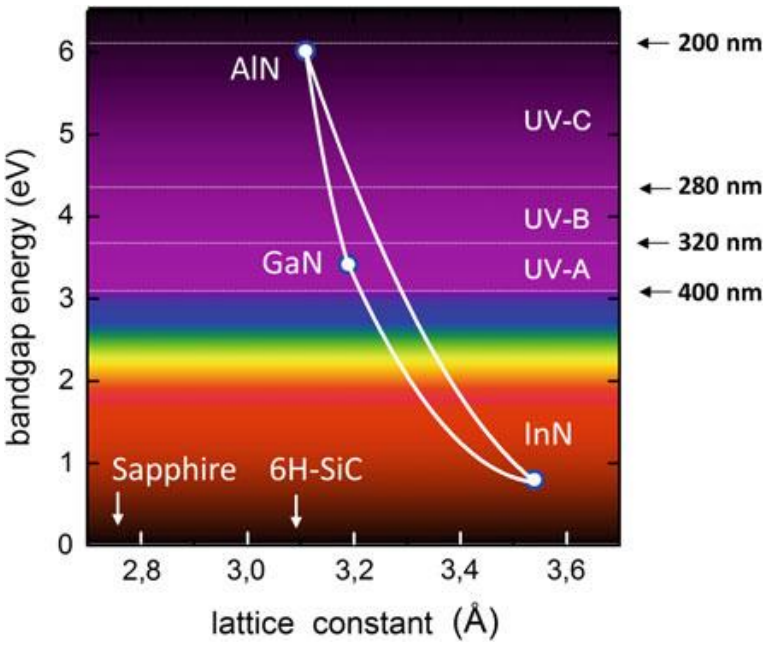

Figure 1.3: III-nitride semiconductor system

Indicative relation between bandgap energy and in-plane lattice constant *a*, for wurtzite AlN, GaN, InN, and their alloys. Taken from [3].

1.3 Efficiency chain

In order to objectively compare the performance of different UV LEDs and also to understand why they perform so poorly compared to visible LEDs, it is important to analyse all the different types of power loss that happen during the conversion of electrical power into light.

The overall efficiency of a light-emitting device is called the Wall Plug Efficiency (WPE), and it is simply defined as the ratio between the optical power emitted by the device over the electrical power supplied to it. The electrical power is spent to force electrons and holes to enter the active region of the device, where they can recombine and, hopefully, produce photons. Unfortunately, not all the power is used for this task: some of it is just lost due to electrical issues. In other words, both the current flowing through the device and the voltage across it are higher than what the active region is actually using. The voltage is higher because of the series resistance due to non-optimized cladding layers and contacts cause an extra voltage drop across the device; the current is higher because part of it leaks through the device without recombining into the active region. The former power loss is described as Electrical Efficiency (EE), the latter as Injection Efficiency (IE).

For each electron-hole pair successfully injected into the active region and recombining there, the probability of obtaining a photon of the wanted wavelength depends on the competition between radiative near-band-edge recombination, and the radiative or non-radiative defect recombinations. This probability is often called Internal Quantum Efficiency[2] (IQE), and strongly depends on the crystal quality of the active region material.

Finally, the term Light Extraction Efficiency (LEE) is used to take into account the losses due to the fact that some of the photons emitted in the active region cannot leave the device, either because they are trapped by total internal reflection or, in general, because they get absorbed somewhere inside the device before they can escape from it.

All the different physical mechanisms of power loss described above contribute to shape the overall WPE, which can hence be seen as the results of an "efficiency chain" of subsequent terms, and whose final value is just their product:

$$WPE = EE \times IE \times IQE \times LEE\ . \tag{1.1}$$

By comparing the corresponding terms of a typical UV LED with those of a state-of-the-art visible device it is then possible to understand the main issues that affect UV LED technology and devise possible strategies to address them.

The EE, which is probably the easiest term to extract, can be obtained by simply comparing the voltage V_F supplied to the device, with the energy $\hbar\omega$ of the photons emitted in this condition. If e is the electron charge, we can write:

$$EE = \frac{\hbar\omega}{eV_F}. \tag{1.2}$$

Partially because of the challenges to obtain a good doping level in high-aluminium-content AlGaN materials, the EE of a typical UV LED is about 30% lower than a state-of-the-art visible LED [29]. This issue also translates into much higher contact resistances, notwithstanding the extensive optimization work about the metallization

[2] Sometimes it is called radiative efficiency instead, and the term Internal Quantum Efficiency is used to indicate its product with the Injection Efficiency.

schemes and the post-deposition annealing treatments that has been carried out in the last few years [30].

While the EE is easy to calculate, separating the other terms is a much more difficult task that requires special measurements and calculations. Considering that the non-radiative recombination channels show a thermally activated behaviour [31], a reasonable estimation of the IQE of the active region can be obtained by comparing the integrated photoluminescence (PL) intensity at the working temperature with the one measured close to 0 K, where all the non-radiative channels are thought to be suppressed [32]. This approach, although very useful, requires specially grown samples without the *p*-type cladding layer, and its results have to be interpreted with great care as the assumptions about the temperature dependence of the recombination-rates are not always met (Cf. [33] and references therein). However, despite these interpretation problems, there is widespread agreement that UV LEDs show a decrease of IQE up to more than 50%, if compared with visible devices [3, 29].

With a similar approach, but using temperature-dependent electroluminescence (EL) instead of PL measurements, it is possible to estimate the product IE × IQE for a full device. However, to extract the actual IE it is still necessary to integrate the measurements with simulations. Although studies on visible devices seem to suggest that the IE approaches 100% at low current densities [34], this does not appear to be necessarily true for UV LEDs [3], in which the asymmetry between electrons and holes in terms of effective mass and mobility that causes some leakage of electron through the active region, is further aggravated by the very poor doping usually present in *p*-type AlGaN materials.

Both in visible and UV LEDs, the method of choice for increasing the recombination rate within the active region is to include in the device a high-bandgap layer in-between the active region and the *p*-type cladding layer, the so-called Electron Blocking Layer (EBL). Unfortunately although the conduction-band offset caused by the EBL can indeed be really effective in impeding the electrons from leaving the active region, the valence-band offset—also present, although smaller—can obstruct the holes in entering it. In addition to that, recently reported simulations and experiments [35, 36] suggest that EBL optimization is particularly problematic in UV LEDs, in which the high internal polarization fields due to the increased Al concentrations may cause them to

excessively bend and consequently severely reduce the hole injection from the *p*-type cladding layer.

The LEE is also estimated indirectly, usually by means of calculations or ray-tracing simulations [37]. The main cause of this type of power loss in high-refractive-index devices is the phenomenon of the total internal reflection at the material interfaces, such as for example in the transition from the semiconductor to the substrate, or from the substrate to air. This happens when the photons reach the material interfaces at angles larger than the critical one, which according to the Snell's law depends only on the ratio between the two refractive indexes. As, at any fixed wavelength, the refractive index is somewhat higher in GaN than in AlN or AlGaN alloys [38], the critical angle in UV LEDs is larger than in their visible counterpart. However, this positive effect is completely nullified by the much larger absorption of light at the metal contacts. Silver, in fact, which is the metal usually employed as a reflective contact in blue LEDs [20], is strongly absorbing in the ultraviolet range below 350 nm [39]; aluminium, on the other hand, is a good UV reflector but usually cannot form ohmic contacts with *p*-doped materials due to its low work-function [40]. Moreover, even using metals with higher work functions, such as palladium or nickel-gold alloys, the only way to achieve reliable ohmic contacts is to deposit the metals not directly to the *p*-AlGaN cladding layer but on top of a few of tens of nanometres of *p*-GaN, as will be discussed in Chapter 3. This layer of material, although very thin, absorbs a significant fraction of the produced UV light.

In addition to these issues, at bandgaps larger than about 5 eV, the structure of the AlGaN valence band changes considerably. Specifically, the crystal-field split-off sub-band starts to have a higher energy than the heavy-hole and the light-hole ones. The effect of this sub-band crossover is that the photons obtained by recombination in these materials shift from being emitted mostly along the direction normal to the semiconductor wafer to being emitted mostly in-plane [39]. This effect further reduces the LEE, which from values higher than 90% in visible devices, goes down to 10% or even less for UVC LEDs [3, 29].

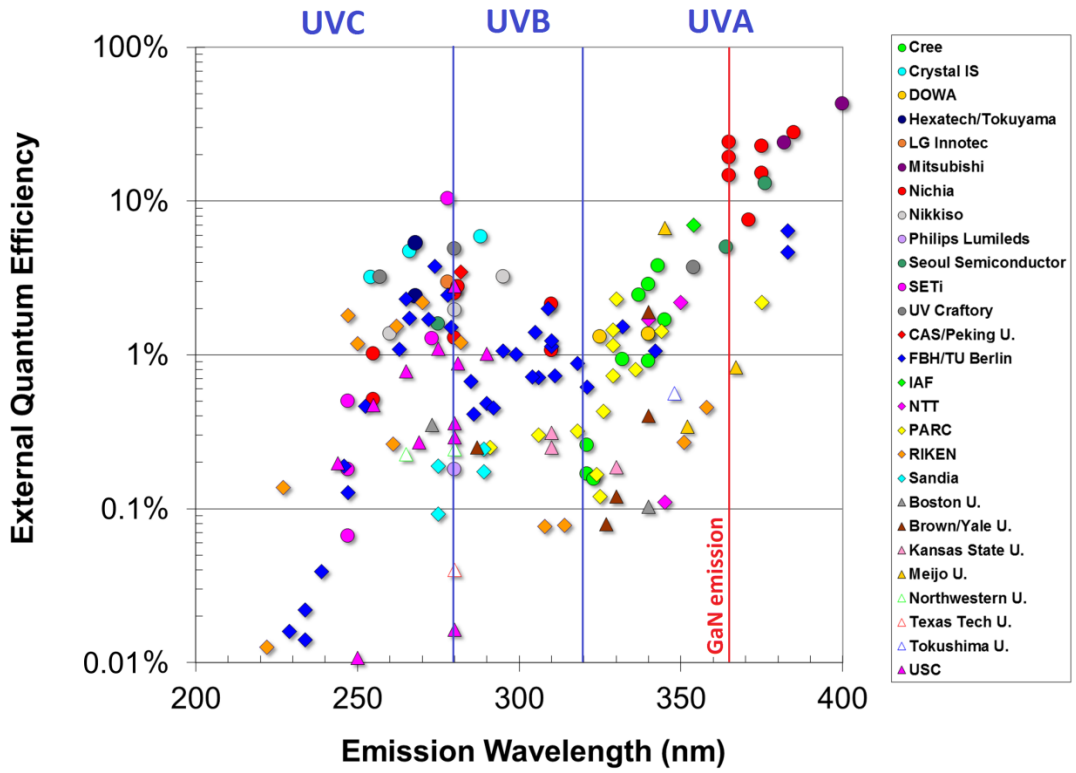

Figure 1.4: EQE of UV LED

External Quantum Efficiencies of the best UV LEDs that were reported by industry and research institutions as of July 2015. The red line indicates the GaN emission and signals the transition from InGaN to AlGaN as the active region material. Adapted from [41].

Although it is difficult to separate their individual contributions, the combined effect of IE, IQE and LEE, i.e. the so-called External Quantum Efficiency (EQE), can be easily measured by comparing the number of photons produced per unit time with the number of carriers flowing through the device:

$$EQE = \left(\frac{P_{OUT}}{\hbar\omega}\right) \Big/ \left(\frac{I}{e}\right), \tag{1.3}$$

where P_{OUT} is the total UV output power, I is the driving current and $\hbar\omega$ is the energy of the emitted photons. The EQEs of the best performing UV LEDs recently reported, both from industry and research institutions, are shown in the Figure 1.4 above. Overall, these values are quite low, not only if compared with the proof-of-concept demonstrations of blue and white LEDs (as e.g. in [42], where an EQE of 84% and a WPE of 81% have been reported) but also with the industrial state-of-the-art, where EQEs of 69% and WPEs of 66% are considered a standard by the US Department of

Energy [43]. However, there are big efficiency variations with the emission wavelength. From 400 nm down to 365 nm (GaN emission) the material used in the QWs can still be an InGaN alloy with only small In concentrations. These devices are based on the same technology of the blue LEDs and for this reason their EQE is only slightly lower. However, as the wavelength becomes shorter and the photon energy exceeds the bandgap of GaN, the EQE drops significantly mostly because of the strong reduction of LEE due to the absorbing *p*-contact issue.

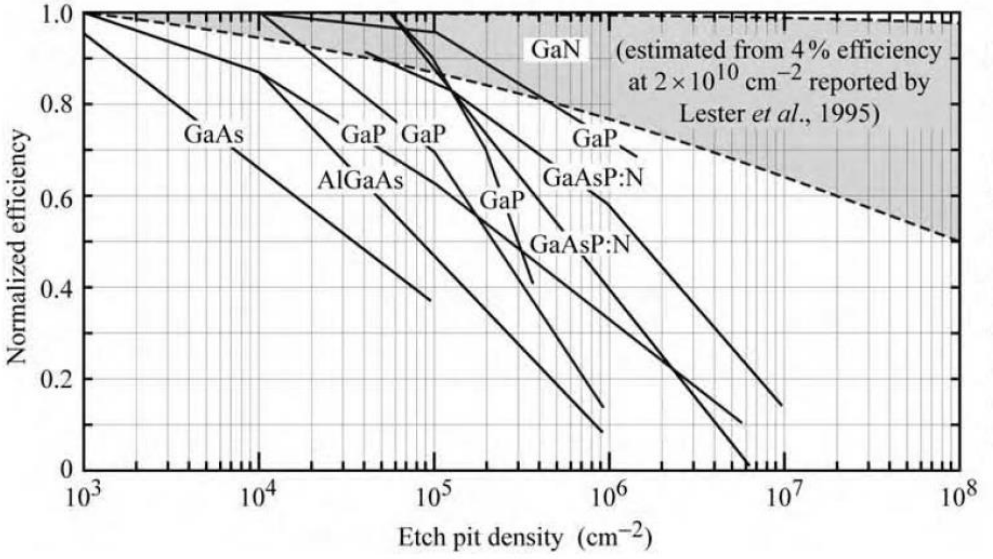

Figure 1.5: Efficiency as a function of defects concentration

Dependence of LED efficiency on dislocation density for devices made with a wide range of III–V materials compared with GaN (shaded region). Taken from [44], p. 231, in turn adapted from [45].

Additionally the IQE also drops as the emission wavelength approaches the UVB range. Firstly, the QW material must be AlGaN, which appears to be much more affected by defects than InGaN. In fact, for years it has been a mystery how the InGaN/GaN active regions could be so efficient notwithstanding the high concentration of defects typical of the III-nitride material system. As can be seen from Figure 1.5, GaN-based devices can still give fair IQEs even at dislocation densities orders of magnitude higher than the maximum permissible limits of other semiconductor material. This fact has been explained as due to the presence of the In atoms in the alloy and, in particular, to their random position within the crystal lattice, which causes the formation of local variations

of the potential that are believed to be large enough to localize[3] the carriers in some regions, preventing them from reaching the dislocations in which they would recombine non-radiatively [48, 49]. This may partially explain why devices based on non-indium-containing AlGaN alloys have such a low IQE [50]. Although the use of InAlGaN can potentially overcome this problem—as evidenced, for example, by the much softer absorption edge and higher apparent IQE of InAlN compared with AlGaN [51, 52], and by the results obtained using InAlGaN with InN concentrations lower than 5% in UVA and UVB LEDs [53]—the very different growth conditions of InN and AlN make these alloys very hard to grow for larger InN concentrations, and further optimization work is needed before this promising approach could actually compete with the use of standard AlGaN-based active regions.

In addition to this effect, the growth of AlN or AlGaN materials is considerably more difficult than GaN because of the much larger sticking coefficient and much lower surface mobility of aluminium adatoms compared to gallium ones [50]. This means that during epitaxial growth the Al atoms are more prone to be incorporated outside their optimal positions, which leads to typical dislocation densities in the range of 10^{10}–10^{11} cm^{-2} for AlN compared with about 10^{8} cm^{-2} for GaN, unless special growth strategies are put in place (Cf. e.g. [3, 50] and references therein).

Moreover, we have to consider that the AlGaN-based devices have to be grown on top of a high quality AlN or (less commonly) GaN template, and the strain due to the different in-plane lattice constant of AlGaN—the active-region material—compared with either templates is another cause of formation of high densities of dislocations. In particular, in case of UVA-emitting devices ($\lambda \gtrsim 360$ nm), the doped AlGaN cladding layers have to be grown pseudomorphically on GaN templates and in fact, as apparent form Figure 1.4, the EQE decreases steadily as the wavelength shortens, as the compromises between Al content increase and strain limits become more severe. In the UVC range, on the contrary, AlN templates have to be used instead of GaN ones. For this reason, an increase of aluminium concentration in the AlGaN material causes, in this range, a reduction of the lattice mismatch and this may explain the slight recovery

[3] This phenomenon is sometimes referred to as In "clustering". However, more precisely, this term should be used to indicate the presence of macroscopic In-rich regions, which were claimed to be observable in TEM images and initially believed to be the origin of the localization effects. It was later reported [46, 47] that these formations can be caused by electron beam damage.

of EQE observed around 280 nm. However, at even shorter wavelengths other issues start to become dominant, namely reduced LEE (due to valence band switching) and IE (due to poor doping), and the EQE drops again of a few orders of magnitude down to efficiencies as low as 0.01%.

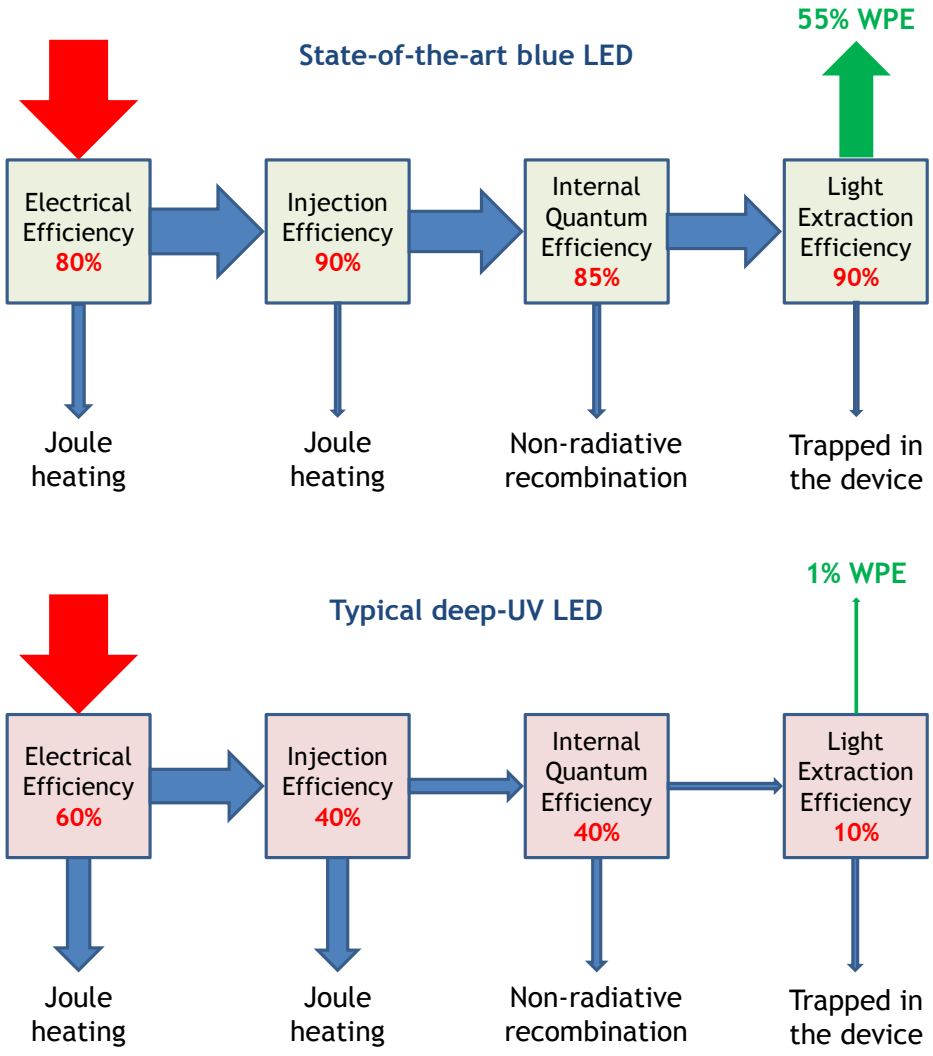

Figure 1.6: Efficiency of nitride-based LEDs

Efficiency comparison of a state-of-the-art visible LED with a typical deep-UV LED. The values of the efficiencies reported here are for indication only, as a significant scatter in the performance of the actual devices is present. The figure concept is taken from [29]; however the data used are modified according to more recent reference [3, 43].

A synoptic comparison of the "efficiency chain" in a typical UVC LED and a state-of-the-art visible LED is shown in Figure 1.6. In the following chapters, the specific challenges alluded to in this section leading to this overall poor efficiency will be

discussed in more detail, and the research aimed at reducing their effects on the efficiency chain will be presented.

1.4 Outline of the thesis

This thesis contains the results of two different projects dealing with UV LEDs. The first one regarded the development of a near-UV LED emitting at 340 nm and based on InAlN materials; the second one, funded by the European Space Agency, focused on the realization of a deep-UV LED that could be used in the discharge system that will control the accumulation of charges in the proof-masses of the LISA space mission [54].

The research activities were aimed at tackling aspects of the UV LED technology such as simulation, growth, fabrication and testing of the devices. Each chapter, which specifically focuses on one of these aspects, aims to provide a deeper insight into some of the loss mechanisms that have been described earlier in this chapter, and reports about the work and the results achieved in the attempt to increase the efficiency of the devices.

Chapter 2 contains the simulation work—mostly performed during the first part of my research—as a preparatory study to help the understanding of the UV LED behaviour and to assist in the design of efficient structures, particularly with respect to the IE. The second part of the chapter focuses on the use of InAlN as an alternative to AlGaN in the QWs of the UV LEDs. As shown in Figure 1.3, this alloy can span the whole range of the III-nitride system including the wavelengths usually obtained with AlGaN. However, the presence of In within the lattice is hoped to induce the same beneficial localization effect that is believed to be present in InGaN. In addition to that, the presence of two different materials in the active region—AlGaN for the barriers and InAlN for the wells—gives a further degree of freedom in the choice of the compositions so that for any given InAlN well it would be possible to have a polarization-matched AlGaN barrier in order to reduce the Quantum Confined Stark Effect (QCSE). These concepts will be discussed in more details and complemented with device simulations performed using the software package SiLENSe.

Chapter 3 focuses on the optimization of the material growth and in particular that of the Al-rich AlGaN cladding layers. The motivations of this study lay in the attempt to improve the EE and the IE of the InAlN based devices, which were found to be quite

poor and responsible for the significant degradation of the overall device efficiency, notwithstanding the high IQE estimated by PL. Material characterization with temperature-dependent Hall-effect measurements showed that the conductivity of the AlGaN alloys with high AlN concentrations can have a significant component due to impurity conduction. This fact makes it hard to interpret the results from the Hall-effect measurements and requires a new model that will be presented and justified in this chapter.

Chapter 4 contains a report about the fabrication activities carried out during my research, which focused on the modification of the μ-LED technology—originally developed for GaN-based visible devices—to make it possible its implementation on the AlGaN-based UV LEDs. The challenges overcome in order to achieve this goal will be described, with a special emphasis on the optimization of the contacts. This was especially important because of the high Al concentration present in the AlGaN cladding-layers of these devices, which makes them very prone to form non-ohmic contacts if the sequence of the evaporated metals and the thermal annealing is not carefully optimized.

Chapter 5 deals with the optical and electrical characterization of the UV LEDs fabricated during my research, and it contains the experimental evaluation of the advantages expected from the adoption of the μ-LED technology. In the first part, the measurement of the optical switching capabilities of the deep-UV LED for space application will be presented, and it will be shown that the device meets the bandwidth requirements set by the European Space Agency for the LISA mission [2]. In the second part, the effects of the fabrication process on the LEE and the far-field emission pattern will be discussed.

Finally, in Chapter 6 the main conclusions of this research will be summarized, and possible future work will be outlined based on this experience.

1.5 Bibliography

[1] P. Mukish, "UV LED Market and Industry Trends," presented at the LED Taiwan, Taipei, Taiwan, 2016. Available: http://www.ledtaiwan.org/zh/sites/ledtaiwan.org/files/data16/docs/2016_LED%20Taiwan_Pars%20MUKISH_UV%20LED%20Market%20and%20Industry%20Trends_For%20Diffusion.pdf [Accessed July 2018].

[2] M. Akhter, P. Pampili, V. Z. Zubialevich, C. Eason, Z. H. Quan, P. P. Maaskant*, et al.*, "Over 20 MHz modulation bandwidth on 250 nm emission of AlGaN micro-LEDs," *Electronics Letters,* vol. 51, pp. 354-355, 2015.

[3] M. Kneissl, "A brief review of III-nitride UV emitter technologies and their applications," in *III-Nitride Ultraviolet Emitters*, vol. 227, M. Kneissl and J. Rass, Eds. Cham: Springer Verlag, 2016, pp. 1-25.

[4] P. J. Parbrook and T. Wang, "Light emitting and laser diodes in the ultraviolet," *IEEE Journal on Selected Topics in Quantum Electronics,* vol. 17, pp. 1402-1411, 5768058, 2011.

[5] B. Guilhabert, D. Massoubre, E. Richardson, J. J. D. McKendry, G. Valentine, R. K. Henderson*, et al.*, "Sub-micron lithography using InGaN micro-LEDs: Mask-free fabrication of LED arrays," *IEEE Photonics Technology Letters,* vol. 24, pp. 2221-2224, 6334416, 2012.

[6] U. Wollina, B. Seme, A. Scheibe, and E. Gutmann, "Application of UV emitters in dermatological phototherapy," in *III-Nitride Ultraviolet Emitters*, vol. 227, M. Kneissl and J. Rass, Eds. Cham (Switzerland): Springer Verlag, 2016, pp. 293-319.

[7] L. Kemény, Z. Csoma, E. Bagdi, A. H. Banham, L. Krenács, and A. Koreck, "Targeted phototherapy of plaque-type psoriasis using ultraviolet B-light-emitting diodes," *British Journal of Dermatology,* vol. 163, pp. 167-173, 2010.

[8] M. A. K. Jansen, V. Gaba, and B. M. Greenberg, "Higher plants and UV-B radiation: Balancing damage, repair and acclimation," *Trends in Plant Science,* vol. 3, pp. 131-135, 1998.

[9] M. Schreiner, I. Mewis, S. Neugart, R. Zrenner, J. Glaab, M. Wiesner*, et al.*, "UV-B elicitation of secondary plant metabolites," in *III-Nitride Ultraviolet Emitters*, vol. 227, M. Kneissl and J. Rass, Eds. Cham (Switzerland): Springer Verlag, 2016, pp. 387-414.

[10] M. A. Lange, T. Kolbe, and M. Jekel, "Ultraviolet Light-Emitting Diodes for Water Disinfection," in *III-Nitride Ultraviolet Emitters*, vol. 227, M. Kneissl and J. Rass, Eds. Cham (Switzerland): Springer Verlag, 2016, pp. 267-291.

[11] E. Gutmann, F. Erfurth, A. Drewitz, A. Scheibe, and M. C. Meinke, "UV fluorescence detection and spectroscopy in chemistry and life sciences," in *III-Nitride Ultraviolet Emitters*, vol. 227, M. Kneissl and J. Rass, Eds. Cham (Switzerland): Springer Verlag, 2016, pp. 351-386.

[12] M. Degner and H. Ewald, "UV emitters in gas sensing applications," in *III-Nitride Ultraviolet Emitters*, vol. 227, M. Kneissl and J. Rass, Eds. Cham (Switzerland): Springer Verlag, 2016, pp. 321-349.

[13] R. J. Drost and B. M. Sadler, "Survey of ultraviolet non-line-of-sight communications," *Semiconductor Science and Technology,* vol. 29, 084006, 2014.

[14] K. X. Sun, B. Allard, S. Buchman, S. Williams, and R. L. Byer, "LED deep UV source for charge management of gravitational reference sensors," *Classical and Quantum Gravity,* vol. 23, pp. S141-S150, 2006.

[15] P. Pampili, M. Akhter, C. Eason, V. Z. Zubialevich, P. P. Maaskant, Z. Quan*, et al.*, "250-nm emitting LED optimized for optical fibre coupling," in *IEEE Summer Topicals Meeting Series (SUM 2015)*, Nassau, Bahamas, 2015, pp. 177-178.

[16] H. Amano, N. Sawaki, I. Akasaki, and Y. Toyoda, "Metalorganic vapor phase epitaxial growth of a high quality GaN film using an AlN buffer layer," *Applied Physics Letters,* vol. 48, pp. 353-355, 1986.

[17] S. Nakamura, "GaN growth using GaN buffer layer," *Japanese Journal of Applied Physics,* vol. 30, pp. L1705-L1707, 1991.

[18] H. Amano, M. Kito, K. Hiramatsu, and I. Akasaki, "P-type conduction in Mg-doped GaN treated with low-energy electron beam irradiation (LEEBI)," *Japanese Journal of Applied Physics,* vol. 28, pp. L2112-L2114, 1989.

[19] S. Nakamura, N. Iwasa, M. Senoh, and T. Mukai, "Hole Compensation Mechanism of P-Type GaN Films," *Japanese Journal of Applied Physics,* vol. 31, pp. 1258-1266, 1992.

[20] D. A. Steigerwald, J. C. Bhat, D. Collins, R. M. Fletcher, M. O. Holcomb, M. J. Ludowise*, et al.*, "Illumination with solid state lighting technology," *IEEE Journal on Selected Topics in Quantum Electronics,* vol. 8, pp. 310-320, 2002.

[21] S. Pimputkar, J. S. Speck, S. P. Denbaars, and S. Nakamura, "Prospects for LED lighting," *Nature Photonics,* vol. 3, pp. 180-182, 2009.

[22] M. T. Hardy, D. F. Feezell, S. P. Denbaars, and S. Nakamura, "Group III-nitride lasers: A materials perspective," *Materials Today,* vol. 14, pp. 408-415, 2011.

[23] *"The Nobel Prize in Physics 2014," Nobelprize.org. Nobel Media AB 2014.* Available: http://www.nobelprize.org/nobel_prizes/physics/laureates/2014/ [Accessed April 2017]

[24] Y. Nanishi, Y. Saito, and T. Yamaguchi, "RF-molecular beam epitaxy growth and properties of InN and related alloys," *Japanese Journal of Applied Physics, Part 1: Regular Papers and Short Notes and Review Papers,* vol. 42, pp. 2549-2559, 2003.

[25] M. Feneberg, M. Rppischer, N. Esser, C. Cobet, B. Neuschl, T. Meisch*, et al.*, "Synchrotron-based photoluminescence excitation spectroscopy applied to investigate the valence band splittings in AlN and $Al_{0.94}Ga_{0.06}N$," *Applied Physics Letters,* vol. 99, 021903, 2011.

[26] M. H. Chang, D. Das, P. V. Varde, and M. Pecht, "Light emitting diodes reliability review," *Microelectronics Reliability,* vol. 52, pp. 762-782, 2012.

[27] DOE SSL Program, "Suggested Research Topics Supplement: Technology and Market Context," U. D. o. Energy, 2017.

[28] Semiconductor TODAY, "UV LED market to grow at 30% to over $115m in 2016," in *Semiconductor TODAY* vol. 6, ed, 2011, p. 79.

[29] M. Shatalov, A. Lunev, X. Hu, O. Bilenko, I. Gaska, W. Sun*, et al.*, "Performance and applications of deep UV LED," *International Journal of High Speed Electronics and Systems,* vol. 21, 1250011, 2012.

[30] G. Greco, F. Iucolano, and F. Roccaforte, "Ohmic contacts to Gallium Nitride materials," *Applied Surface Science,* vol. 383, pp. 324-345, 2016.

[31] P. Michler, T. Forner, V. Hofsäß, F. Prins, K. Zieger, F. Scholz*, et al.*, "Nonradiative recombination via strongly localized defects in quantum wells," *Physical Review B,* vol. 49, pp. 16632-16636, 1994.

[32] A. Hangleiter, D. Fuhrmann, M. Grewe, F. Hitzel, G. Klewer, S. Lahmann*, et al.*, "Towards understanding the emission efficiency of nitride quantum wells," *Physica Status Solidi (A) Applied Research,* vol. 201, pp. 2808-2813, 2004.

[33] J. Mickevičius, G. Tamulaitis, M. Shur, M. Shatalov, J. Yang, and R. Gaska, "Internal quantum efficiency in AlGaN with strong carrier localization," *Applied Physics Letters,* vol. 101, 211902, 2012.

[34] I. E. Titkov, D. A. Sannikov, Y. M. Park, and J. K. Son, "Blue light emitting diode internal and injection efficiency," *AIP Advances,* vol. 2, 032117, 2012.

[35] Y. Y. Zhang, X. L. Zhu, Y. A. Yin, and J. Ma, "Performance enhancement of near-UV light-emitting diodes with an InAlN/GaN superlattice electron-blocking layer," *IEEE Electron Device Letters,* vol. 33, pp. 994-996, 2012.

[36] F. Mehnke, C. Kuhn, M. Guttmann, C. Reich, T. Kolbe, V. Kueller*, et al.*, "Efficient charge carrier injection into sub-250 nm AlGaN multiple quantum well light emitting diodes," *Applied Physics Letters,* vol. 105, 051113, 2014.

[37] Z. Liu, K. Wang, X. Luo, and S. Liu, "Precise optical modeling of blue light-emitting diodes by Monte Carlo ray-tracing," *Optics Express,* vol. 18, pp. 9398-9412, 2010.

[38] U. Tisch, B. Meyler, O. Katz, E. Finkman, and J. Salzman, "Dependence of the refractive index of $Al_xGa_{1-x}N$ on temperature and composition at elevated temperatures," *Journal of Applied Physics,* vol. 89, pp. 2676-2685, 2001.

[39] J. Rass and N. Lobo-Ploch, "Optical polarization and light extraction from UV LEDs," in *III-Nitride Ultraviolet Emitters*, vol. 227, M. Kneissl and J. Rass, Eds. Cham (Switzerland): Springer Verlag, 2016, pp. 137-170.

[40] D. R. Lide, Ed., *CRC Handbook of Chemistry and Physics*. London: CRC Press, 1993.

[41] M. Kneissl. *UV LED Efficiency Mar-2018* (2018). Available: http://www.ifkp.tu-berlin.de/?id=agkneissl [Accessed March 2018]

[42] Y. Narukawa, M. Ichikawa, D. Sanga, M. Sano, and T. Mukai, "White light emitting diodes with super-high luminous efficacy," *Journal of Physics D: Applied Physics,* vol. 43, 354002, 2010.

[43] DOE SSL Program, "Suggested Research Topics," U. D. o. Energy, 2017.

[44] E. F. Schubert, *Light-emitting diodes*. Cambridge (UK): Cambridge University Press, 2006.

[45] S. D. Lester, F. A. Ponce, M. G. Craford, and D. A. Steigerwald, "High dislocation densities in high efficiency GaN-based light-emitting diodes," *Applied Physics Letters,* vol. 66, pp. 1249-1251, 1995.

[46] J. P. O'Neill, I. M. Ross, A. G. Cullis, T. Wang, and P. J. Parbrook, "Electron-beam-induced segregation in InGaN/GaN multiple-quantum wells," *Applied Physics Letters,* vol. 83, pp. 1965-1967, 2003.

[47] T. M. Smeeton, M. J. Kappers, J. S. Barnard, M. E. Vickers, and C. J. Humphreys, "Electron-beam-induced strain within InGaN quantum wells: False indium "cluster" detection in the transmission electron microscope," *Applied Physics Letters,* vol. 83, pp. 5419-5421, 2003.

[48] S. F. Chichibu, A. Uedono, T. Onuma, B. A. Haskell, A. Chakraborty, T. Koyama*, et al.*, "Origin of defect-insensitive emission probability in In-containing (Al,In,Ga)N alloy semiconductors," *Nature Materials,* vol. 5, pp. 810-816, 2006.

[49] D. Watson-Parris, M. J. Godfrey, P. Dawson, R. A. Oliver, M. J. Galtrey, M. J. Kappers*, et al.*, "Carrier localization mechanisms in $In_xGa_{1-x}N$/GaN quantum wells," *Physical Review B - Condensed Matter and Materials Physics,* vol. 83, 115321, 2011.

[50] A. Khan, K. Balakrishnan, and T. Katona, "Ultraviolet light-emitting diodes based on group three nitrides," *Nature Photonics,* vol. 2, pp. 77-84, 2008.

[51] V. Z. Zubialevich, T. C. Sadler, D. V. Dinh, S. N. Alam, H. Li, P. Pampili*, et al.*, "Enhanced UV luminescence from InAlN quantum well structures using two temperature growth," *Journal of Luminescence,* vol. 155, pp. 108-111, 2014.

[52] V. Z. Zubialevich, D. V. Dinh, S. N. Alam, S. Schulz, E. P. O'Reilly, and P. J. Parbrook, "Strongly nonparabolic variation of the band gap in $In_xAl_{1-x}N$ with low indium content," *Semiconductor Science and Technology,* vol. 31, 025006, 2015.

[53] H. Hirayama, "Quaternary InAlGaN-based high-efficiency ultraviolet light-emitting diodes," *Journal of Applied Physics,* vol. 97, 091101, 2005.

[54] *LISA mission, European Space Agency*. Available: https://www.elisascience.org/ [Accessed June 2018]

2 Simulation of UV LEDs

This chapter contains the results of my work regarding device simulation. The purpose of this activity was to gain a better understanding of the basic behaviour of UV LEDs and to guide and support the following experimental work about fabrication and testing of the actual devices. I was particularly interested in how the variation of the typical elements of an LED, such as cladding layers, active region and electron blocking layer can influence its injection and internal quantum efficiency.

The software used for all the simulations described in this chapter is SiLENSe[4], a simulation package distributed by STR, a spin-out company from the Ioffe Institute of Saint Petersburg in Russia. This software, which is quite popular in the field of III-nitride devices, combines all the features of a standard drift-diffusion simulator—acceptable degree of precision at a reasonable computational cost—with the capabilities to model some of the aspects typical of the III-nitride materials, such as the effects of dislocations on the carrier lifetimes, the presence of internal polarization fields, and the carrier localization due to indium inhomogeneities.

2.1 The drift-diffusion model

All drift-diffusion models are based on the assumption that the motion of the carriers in the semiconductor device is determined only by the electric field ($\vec{E}$) and the gradient of the carrier densities ($\vec{\nabla}n$ and $\vec{\nabla}p$), and hence fully described by the following semi-classical equations:

$$\overrightarrow{J_n} = en\mu_n\vec{E} + eD_n\vec{\nabla}n \tag{2.1}$$

$$\overrightarrow{J_p} = ep\mu_p\vec{E} - eD_p\vec{\nabla}p \tag{2.2}$$

where n and p are the carrier densities, J_n and J_p the current densities, μ_n and μ_n the mobilities, D_n and D_p the diffusivity, respectively for electrons and holes; and e is the

[4] SiLENSe 5.4 Laser Edition, STR Group Inc. <www.str-soft.com>

elemental charge. In addition to these equations, the solution has to be consistent with the continuity equations

$$\vec{\nabla} \cdot \overrightarrow{J_n} + e(G - R) = \frac{\partial n}{\partial t} e \tag{2.3}$$

$$-\vec{\nabla} \cdot \overrightarrow{J_p} + e(G - R) = \frac{\partial p}{\partial t} e \tag{2.4}$$

where G and R are the generation and the recombination rates. And finally, the solution also has to be consistent with the first Maxwell equation:

$$\vec{\nabla} \cdot \vec{D} = e(p - n + N_D^+ - N_A^-) \tag{2.5}$$

whose right-hand side represents the total charge density, including not only the free carriers n and p, but also the ionized donors (N_D^+) and acceptors (N_A^-). The bound charges that form within the semiconductor because of the polarization effects are, on the contrary, already taken into account in the electric displacement term $\vec{D}$. In fact, because of the lack of inversion symmetry, wurtzite materials can show piezoelectric and pyroelectric properties and may have significant internal polarization fields that need to be included in the simulation [1]. SiLENSe does this by explicitly including the spontaneous ($\overrightarrow{P_{sp}}$) and piezoelectric ($\overrightarrow{P_{pz}}$) polarization in the left-hand side of Eq. (2.5), in which:

$$\vec{D} = \overrightarrow{P_{sp}} + \overrightarrow{P_{pz}} + \varepsilon_0 \vec{E} \,. \tag{2.6}$$

The spontaneous polarization is taken directly from the internal material-database, whose relevant values are reported in Table 2.1; the piezoelectric polarization is calculated from the elastic deformation of the layers and from the piezoelectric constants, also included in the database. This means that when different layers having different lattice parameters are grown one after the other in the heterostructure device, the degree of strain/relaxation between each couple of layers determines the piezoelectric polarization field. In all the simulations described in this chapter, I have assumed that the first layer grown after the AlN template—i.e. a thick *n*-doped AlGaN layer—is fully relaxed, while all the following ones are completely strained to each

other[5]. In case of alloys, the values of all the parameters are obtained as an average of the data in Table 2.1, weighted with the composition.

		AlN	GaN	InN
Lattice constant *a*	(nm)	0.3112	0.3188	0.3540
Lattice constant *c*	(nm)	0.4982	0.5186	0.5705
Elastic constant C_{11}	(GPa)	395	375	225
Elastic constant C_{12}	(GPa)	140	140	110
Elastic constant C_{13}	(GPa)	115	105	95
Elastic constant C_{33}	(GPa)	385	395	200
Elastic constant C_{44}	(GPa)	120	100	45
Spontaneous polarization	(C/m^2)	-0.081	-0.029	-0.032
Piezoelectric tensor e_{33}	(C/m^2)	1.55	0.65	0.43
Piezoelectric tensor e_{31}	(C/m^2)	-0.58	-0.33	-0.22
Piezoelectric tensor e_{15}	(C/m^2)	-0.48	-0.33	-0.22
Dielectric constant ε_{33}		8.5	8.9	15.3

Table 2.1: Material constants

The parameters relevant to the internal polarization fields in the III-nitride materials are here reported: the values are taken from the material database of SiLENSe.

If we restrict ourselves to mono-dimensional simulations only, and if we use the quasi-Fermi levels F_n and F_p , which are implicitly defined in the equations

$$n = N_C exp\left[-\frac{(E_c - e\varphi) - F_n}{kT}\right] \tag{2.7}$$

$$p = N_V exp\left[-\frac{F_p - (E_V - e\varphi)}{kT}\right] \tag{2.8}$$

with N_C and N_V being the conduction and valence band effective density of states and φ the electric potential, then the Eqs. (2.1), (2.2), and (2.5) can be written, in a much simpler way, as:

[5] Further details about the growth issues will be discussed in Chapter 3.

$$J_n = n\mu_n \frac{dF_n}{dz} \tag{2.9}$$

$$J_p = p\mu_p \frac{dF_p}{dz} \tag{2.10}$$

$$\frac{d}{dz}\left(P_{sp} + P_{pz} - \varepsilon_0\varepsilon_r \frac{d\varphi}{dz}\right) = e(p - n + N_D^+ - N_A^-)\,. \tag{2.11}$$

In narrow bandgap semiconductors, N_D^+ and N_A^-can be considered—with very good approximation—to be equal, respectively, to the total concentration of donors (N_D) and of acceptors (N_A) incorporated into the material. On the contrary, in wide bandgap semiconductor such as the III-nitride materials, N_D^+ and N_A^- have to be calculated from their respective energy levels E_D and E_A, temperature, and level of injection (i.e. the position of the quasi-Fermi levels):

$$N_D^+ = N_D\left[1 + g_D exp\left(\frac{F_n - (E_D - e\varphi)}{kT}\right)\right]^{-1} \tag{2.12}$$

$$N_A^- = N_A\left[1 + g_A exp\left(\frac{(E_A - e\varphi) - F_p}{kT}\right)\right]^{-1} \tag{2.13}$$

where g_D and g_A are the ground-state degeneracy, which for III-V materials are typically $g_D = 2$ and $g_A = 4$.

In addition to the previous equations, to make the problem mathematically solvable we need to incorporate the information about recombination that comes from Eqs. (2.3) and (2.4). In the steady state condition and in case of no generation due to illumination, we have:

$$\frac{dJ_n}{dz} - e(R^{Rad} + R^{SRH} + R^{Auger}) = 0 \tag{2.14}$$

$$\frac{dJ_p}{dz} + e(R^{Rad} + R^{SRH} + R^{Auger}) = 0 \tag{2.15}$$

in which R^{Rad}, R^{SRH} and R^{Auger} are, respectively, the radiative, Shockley-Read-Hall and Auger recombination of the excess carriers. With Eqs. (2.7) to (2.15) we have now a system of nine scalar equations and nine unknown variables: n, p, N_D^+, N_A^-, J_n, J_p, F_n, F_p, and φ. This is basically the full set of differential equations that the numerical solver engine of SiLENSe has to deal with in order to obtain a solution.

Although mathematically well defined, this approach makes use of some assumptions that need to be pointed out in order to be aware of their limit of validity. Firstly, the use of the quasi-Fermi levels is justified by the fact that the phonon-electron interactions in the conduction band and the phonon-hole interactions in the valence band are both much faster than the interactions between the two bands through carrier recombination. For this reason when the device is under positive bias and electrons and holes are injected at the opposite sides of it, even though the device is not under thermal equilibrium, each of the two bands can be considered to be approximately in equilibrium.

Making this assumption, however, means that the effects due to the so-called hot carriers, i.e. electrons or holes injected across a heterojunction that have not yet reached the approximate thermal equilibrium in their respective bands, are completely neglected. Although this might in theory not be acceptable for devices that include thin structures such as QWs, a recent Monte-Carlo study [2] seems to suggest that the hot carriers generally induce significant differences compared to the drift-diffusion model only at bias voltages exceeding the built-in voltage and for structures involving several deep quantum wells. In all the other conditions the differences are negligible.

Another assumption implicit in Eqs. (2.7) and (2.8), which contain the effective density of states:

$$N_C = \frac{1}{\sqrt{2}}\left(\frac{m_e^* kT}{\pi\hbar^2}\right)^{3/2} \tag{2.16}$$

$$N_V = \frac{1}{\sqrt{2}}\left(\frac{m_h^* kT}{\pi\hbar^2}\right)^{3/2} \tag{2.17}$$

is that the dispersion relation of the two bands is almost parabolic in the proximity of the energy minima so that the concept of effective mass (m_e^* and m_h^*) can be introduced.

Moreover, the presence of the exponentials in Eqs. (2.7) and (2.8) means that the Boltzmann statistics is used instead of the Fermi-Dirac one, which is possible only in non-degenerated semiconductor and at low injection levels. Although all these conditions are usually met in standard light-emitting devices, this might not be the case for LEDs driven at very high voltages and currents.

2.1.1 Recombination of excess carriers

The terms R^{Rad}, R^{SRH} and R^{Auger} introduced in Eqs. (2.14) and (2.15) account for the three different types of recombination that carriers can undergo when they are present in excess to their thermal equilibrium concentrations. This excess of carriers, which is the consequence of the current injected into the device and acts as the driving force of the recombination, can be expressed in terms of the difference between the electron and hole quasi-Fermi levels. It is then possible to integrate the explicit expression of the three types of recombination directly into the system of equations (2.7)–(2.15), as no new variable is introduced.

In the radiative recombination, the rate of events is proportional to the excess carriers with a proportionality coefficient B, which can be considered almost independent from the injection level:

$$R^{Rad} = B(np - n_i^2) = Bnp\left[1 - exp\left(-\frac{F_n - F_p}{kT}\right)\right]. \tag{2.18}$$

The values of B used by SiLENSe are: 2.0×10^{-11} cm^3 s^{-1} for AlN, 2.4×10^{-11} cm^3 s^{-1} for GaN, and 6.6×10^{-12} cm^3 s^{-1} for InN; in case of ternary or quaternary alloys, they are calculated as a linear combination of the material values according to the compositions. All these values are very close to what can be found in literature (e.g. in [3, 4]), where values of about 1–2 $\times 10^{-11}$ cm^3 s^{-1} are often reported.

The Shockley-Read-Hall recombination is a non-radiative recombination that is mediated by the presence of defects. Its expression, which was firstly derived by R. Hall [5], and by Shockley and Read [6], is:

$$R^{SRH} = \frac{np - n_i^2}{\tau_p(n + n_D) + \tau_n(p + p_D)}, \tag{2.19}$$

where τ_n and τ_p are the electron and hole radiative lifetimes, and the parameters n_D and p_D are the electron and hole carrier concentrations that would be present, in the conduction and valence bands respectively, if the Fermi level were at the energy level E_D of the defect state:

$$n_D = N_C exp\left(\frac{E_D - E_C}{kT}\right) = n_i exp\left(\frac{E_D - E_{F_i}}{kT}\right) \tag{2.20}$$

$$p_D = N_V exp\left(\frac{E_V - E_D}{kT}\right) = n_i exp\left(\frac{E_{F_i} - E_D}{kT}\right). \tag{2.21}$$

Although the expression (2.19) is quite complicated, the recombination is dominated by the defects whose energy level lies close to the intrinsic Fermi level E_{F_i}, which is when the denominator reaches its minimum. In this case the terms n_D and p_D can be neglected and we can write:

$$R^{SRH} \cong \frac{np - n_i^2}{\tau_p n + \tau_n p} = \left(\frac{\tau_n}{n} + \frac{\tau_p}{p}\right)^{-1} \left[1 - exp\left(-\frac{F_n - F_p}{kT}\right)\right]. \tag{2.22}$$

SiLENSe requires τ_n and τ_p as input data for any layer present in the simulated heterostructure. These values can either be entered manually, if they are known, or estimated by the program using a specific model that will be described in the next Section 2.1.2.

Auger recombination is a non-radiative process in which the energy released from an electron-hole recombination is transferred to a third particle, either another electron or another hole. The explicit expression is:

$$\begin{aligned} R^{Auger} &= \left(C_n n + C_p p\right)(np - n_i^2) \\ &= np\left(C_n n + C_p p\right)\left[1 - exp\left(-\frac{F_n - F_p}{kT}\right)\right], \end{aligned} \tag{2.23}$$

where C_n and C_p are the Auger coefficients for the interaction with two electrons and one hole or two holes and an electron, respectively. Although they can in theory be considered separately, most often an *effective* coefficient C (which is some combination

of C_n and C_p that depends on the actual Auger mechanism) is used in the analysis of this type of recombination [7, 8].

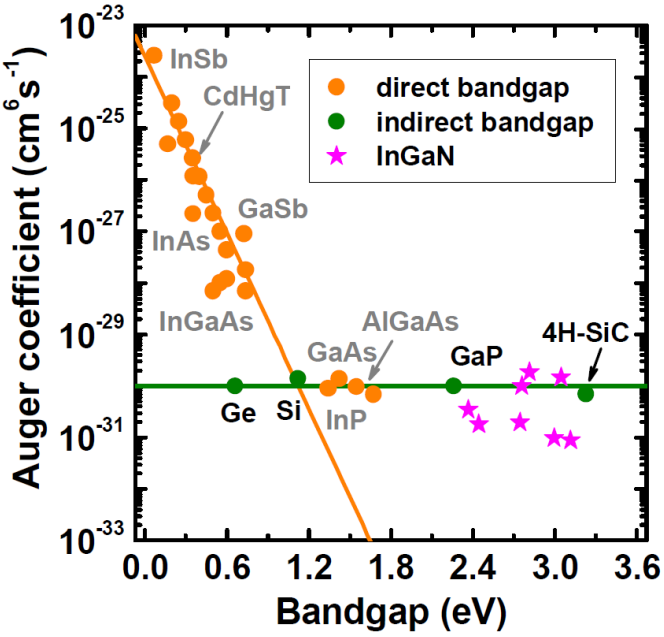

Figure 2.1: Auger Coefficient

Auger recombination coefficients of different semiconductor materials versus their bandgap. The orange line indicates the trend of C in direct bandgap materials, the green line that of indirect or wide bandgap direct materials. Image taken from [9], with some graphical modifications.

The estimation of this coefficient has been extensively debated in literature, especially for InGaN material, for which it has been indicated as the possible main cause for the efficiency droop [10], which affects all the visible LEDs and consist in a reduction of the measured efficiency at current densities above around 3–30 A/cm^2. The validity of this hypothesis strictly depends on the value of C, with a minimum of 10^{-31} cm^6 s^{-1} usually considered necessary to produce any detectable effect on the droop [11].

Notwithstanding the great amount of theoretical and experimental work, there is still not complete agreement about the value of the C coefficient, with proposed values ranging from being in the order of 10^{-30} cm^6 s^{-1} [12] down to 10^{-32} cm^6 s^{-1} or lower [13]. The uncertainty is even greater for AlGaN materials that are much less investigated with respect to this topic. As shown in Figure 2.1, in narrow bandgap semiconductors the Auger coefficient shows a clear exponential dependency with the bandgap, which indicates that this type of recombination should be of negligible relevance in AlGaN

materials on the whole composition range (orange line). However, as discussed in [8, 9], there are experimental results that might seem to indicate the existence of a minimum value for the coefficient C, which is roughly the same for all the indirect and wide-gap direct semiconductors (green line).

In addition to that, it is also possible that Auger recombination rates are significantly higher in QWs than in bulk materials, due to the fact that the conservation of momentum perpendicular to the heterojunctions is removed [14]. We have also to remember that Auger recombination can be either direct or mediated by phonons, defects or alloy scattering. And while the indirect Auger recombination is a second order process, it is expected to be dominant in wide-gap semiconductors because, contrary to the direct one, it does not show any energy threshold (Cf. [11] and references therein).

In SiLENSe both C_n and C_p are set to 2.5×10^{-30} cm^6 s^{-1} for InN, and to zero for GaN and AlN. Although with this choice the Auger coefficients will significantly decrease with the increase of the bandgap in InGaN and InAlN alloys, the values chosen for InN seem nonetheless too high. On the contrary, the fact that in AlGaN materials the Auger recombination is completely ignored might be too simplistic. Luckily, simple calculations that will be shown in Section 2.2, will prove that in the simulations of devices based on highly defective materials—as is the case for UV LEDs based on AlGaN or InAlN alloys—the choice of C is not really critical as the non-radiative recombinations are completely dominated by the Shockley-Read-Hall mechanism.

2.1.2 Influence of the dislocation density on the non-radiative carrier lifetime

As mentioned in the previous section, being a defect-mediated type of recombination, R^{SRH} has a strong dependence on the quality of the material, i.e. on the amount of point and extended defects that are present in the crystal lattice. In the case of III-nitride semiconductors, it is well known from early studies (Cf. e.g. [15]) that it is in particular the presence of dislocations that is responsible for the increase of the non-radiative recombinations, but it was only with the work of Karpov and Makarov [16] that a model was proposed to explicitly connect the carrier lifetimes ($\tau_{n,p}$) with the dislocation concentration (N_{dis}). Apart from its contribution in the understanding of the efficiency problem in III-nitride-based LEDs, this model is briefly described here because it is

used in SiLENSe to calculate the Shockley-Read-Hall coefficients of the different layers of the heterostructure device.

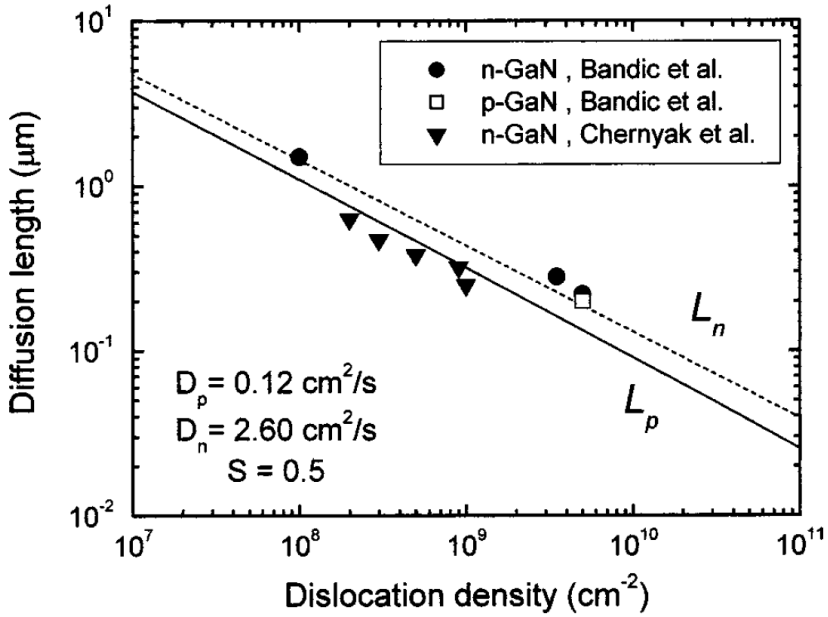

Figure 2.2: Experimental validation of Karpov's model

Minority carrier diffusion length as a function of threading dislocation density. The lines are the computations based on the model proposed in [16]. The symbols are the experimental results obtained by EBIC measurements and reported on Bandić *et al.* [17], and Chernyak *et al.* [18]. Figure taken from [16].

The basic idea behind this model is to consider the material as made of equivalent cylinders of radius $(\pi N_{dis})^{-1/2}$, each of them surrounding a single dislocation. The cylinder is also limited at the centre by the dimensions of the dislocation, whose core is assumed to be of the order of magnitude of the in-plane lattice constant (a). The two-dimensional steady-state diffusion equation for electrons and holes is then solved in this simplified domain. The boundary conditions are set in a way that the dislocation can capture only carriers moving within the cylinder, and the trap rate is limited by the carrier thermal velocity ($V_{n,p}$). The solution found using this approach is:

$$\tau_{n,p} = \frac{1}{4\pi D_{n,p} N_{dis}} \left\{ ln\left(\frac{1}{\pi a^2 N_{dis}}\right) - \frac{3}{2} + \frac{2D_{n,p}}{aV_{n,p}S} \right\} \tag{2.24}$$

where, apart from the parameters already defined above, S is the fraction of electrically active sites on the dislocation core, which was considered to be equal to 0.5 in the cited paper. As shown in Figure 2.2, where experimental diffusion lengths

$$L_{n,p} = \left(D_{n,p}\tau_{n,p}\right)^{1/2} \tag{2.25}$$

are reported as a function of the dislocation density, this model is in good agreement with experimental data for GaN.

2.1.3 Overestimation of the voltage forward drop

A common problem of the software packages based on the drift-diffusion model, is the fact that the simulated IV characteristics tend to have a considerably higher voltage drop than what is usually measured in real devices. One of the possible reasons for this behaviour is due to the fact that, in its original formulation, the model is not able to deal with the transport of carriers across any discontinuity in the band structure. Because all the optoelectronic devices of interest have some heterojunctions with sharp discontinuities in both the conduction and the valence band, some countermeasure has to be taken to circumvent this problem. The usual way is to simply ignore the heterojunctions by choosing the mesh boundaries so that no discontinuity would appear in any cell. In this approach the continuous solutions found in the different parts of the device are connected to each other using some 'reasonable' boundary conditions for the current densities and the quasi-Fermi levels [19], such as:

$$\lim_{z\to z_i^+} J_{n,p}(z) = \lim_{z\to z_i^-} J_{n,p}(z) \tag{2.26}$$

$$\lim_{z\to z_i^+} F_{n,p}(z) = \lim_{z\to z_i^-} F_{n,p}(z) \tag{2.27}$$

where the z_i are the positions of all the heterojunctions.

While (2.26) is indeed a reasonable condition, (2.27) is a hypothesis that, in reality, is not always true and that depends on the actual transport mechanism across the interface, which can be modelled with more precision. This approach was tried for example in [20], where an explicit treatment for the thermionic emission and the tunnelling across all the heterojunctions was included.

In contrast with this approach, another possibility is to take the electric potential inside the device and modify it in a way that would enhance the carrier transmission across the heterojunctions, so that the thermionic/field emission is somehow mimicked. The modified version of the potential—the so-called Bohm potential or simply quantum potential—is then used instead of the real one in a standard drift-diffusion simulation.

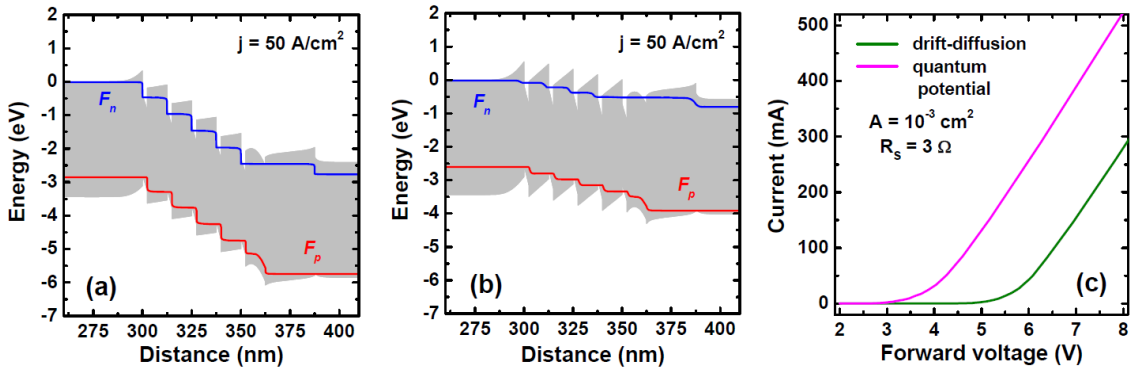

Figure 2.3: Example of a simulation using the quantum potential in SiLENSe
Comparison of the band structure of a blue-green LED in case of (a) standard drift-diffusion model, and (b) with the use of the SiLENSe quantum potential, at the same current density of 50 A/cm^2. The IV characteristics of the two simulations are shown in (c). Taken from [21].

This latter approach has also been implemented in SiLENSe, and is available as an option that can be activated on demand. Although based on a theoretical approach that has been outlined in [21], the presence of two fitting parameters makes this model more of a semi-empirical method. The standard values of these fitting parameters have been chosen to give the best approximation of the current across a triangular barrier obtained using full quantum mechanical calculations from the standard potential. As shown in Figure 2.3 (c), the activation of this option in SiLENSe helps to obtain a more reasonable IV characteristic for GaN/InGaN blue-green LEDs compared with the standard result. The reason of this can be seen in Figure 2.3 (a) and (b), where the two band diagrams are compared. In the quantum potential simulation, it is clearly visible how the improved transport across the QWs of the active region reduces the sharp drops of the quasi-Fermi levels and makes the bands much flatter. In the standard simulation, on the contrary, the presence of layers of the devices almost completely depleted of carriers increases significantly the series resistance and hence the forward voltage drop.

Although the results shown in Figure 2.3 are interesting, the fact that the parameters of the model have been optimized to reproduce the thermal-assisted tunnelling only in a very simple structure such a triangular barrier does not necessarily make it able to provide sensible results for all heterostructures and all materials.

In particular, for structures that have a reduced carrier confinement within the active region (i.e. with low band offsets between QWs and QBs as typical in UV LEDs), the simulations based on the quantum potential often give very unrealistic results. An example of that is reported in Figure 2.4 where the simulations of an AlGaN/AlGaN, five-period multi-QWs structure emitting at 240 nm are briefly summarized. The bandgap difference between QWs and QBs was set here to be only 300 meV, while it can be estimated to be around 1 eV in the example proposed in [21]; not unexpectedly the IV characteristics with and without the use of the quantum potential are, in this case, quite similar to each other as can be seen in Figure 2.4 (a). In fact, the problems due to the transport across the heterojunctions should indeed become less and less important for structures with reduced offsets, making the outcomes of the simulations almost independent of the quantum potential correction; however that should also happen for the IE and the IQE. Instead, the application of the quantum potential to this structure almost completely smears out both the valence and the conduction bands, making the IE—which is only slightly decreased in structures such as in [21]—become suddenly rather poor when the offset becomes too low. As a result of that also the IQE becomes, unrealistically, almost non-existent.

To amend this problem, it would be possible, in principle, to change the fitting parameters used by SiLENSe in order to better describe this type of devices. Unfortunately, it is not clear what would be a practical way to implement that, either experimentally or theoretically, because the fitting parameters do not have any straightforward physical correlation with the type of material used.

A third approach to the issue of the excessive voltage drop has recently been proposed: the so-called percolation conduction [22]. According to this theory, the random variations that naturally occur in any alloy are believed to be large enough to force the movement of the carriers in a random path that follows the bandgap minima within the device. As shown in Figure 2.5, these inhomogeneities would greatly reduce the capability of the quantum barriers to confine the carriers within the QWs and, in the

same time, would considerably decrease the series resistance of the device. Another interesting consequence of this theory is the fact that the inhomogeneities in the composition would cause the carriers to move in a very uneven way, with hot spots of relatively high current density. This might explain how Auger recombination could still cause of the efficiency droop even with relatively low values for the coefficient C.

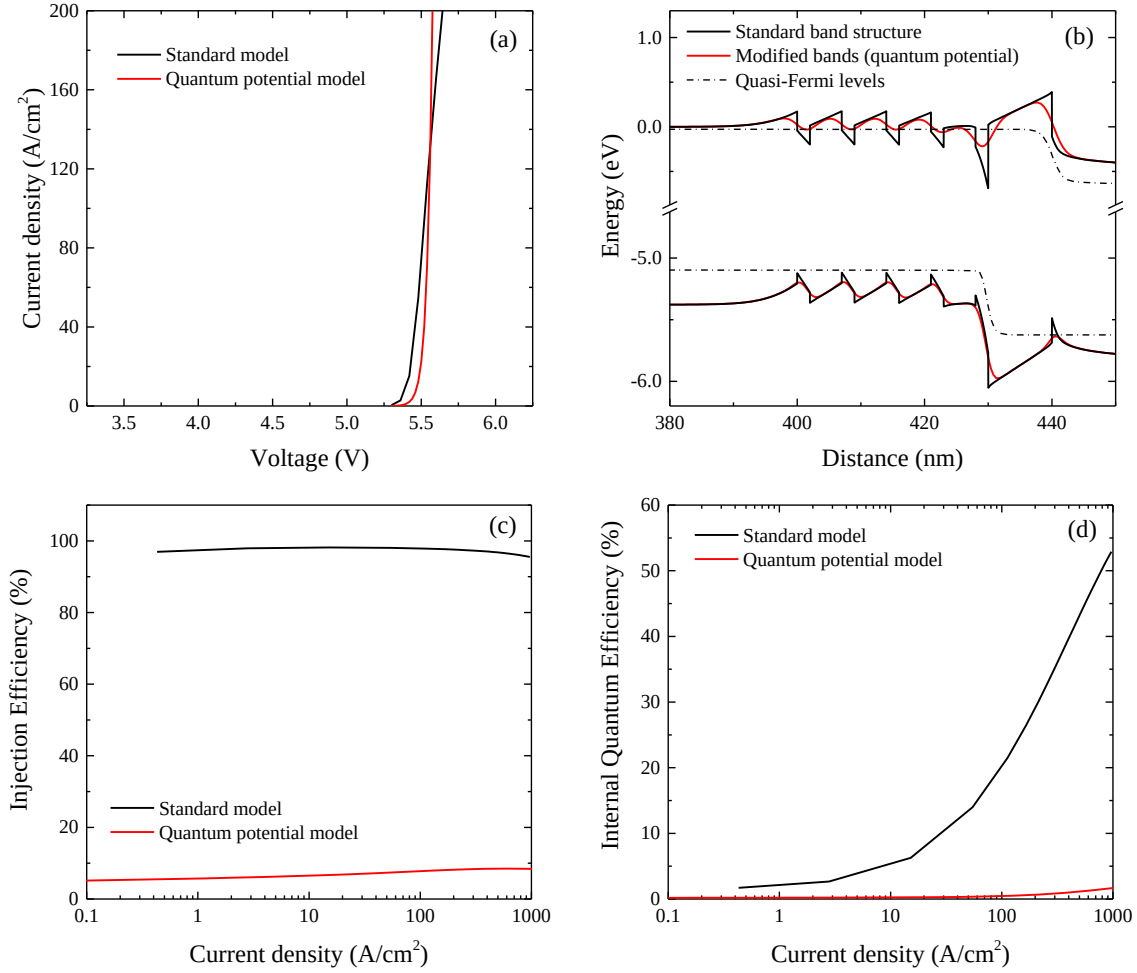

Figure 2.4: Problems of the quantum potential model in UV LEDs

Simulation of an AlGaN/AlGaN UV LEDs with and without the use of the quantum potential model; (a) IV characteristics, (b) structure of conduction-band, (c) IE, and (d) IQE. The poor values of IE and IQE when the quantum potential model is used are consequence of the smearing out of conduction and valence bands.

At the moment this approach is probably the most promising among the three described here. However, being inherently a tri-dimensional phenomenon, it is not possible to implement it using a standard mono-dimensional solver. For this reason, unfortunately, the percolation conduction is completely ignored by SiLENSe.

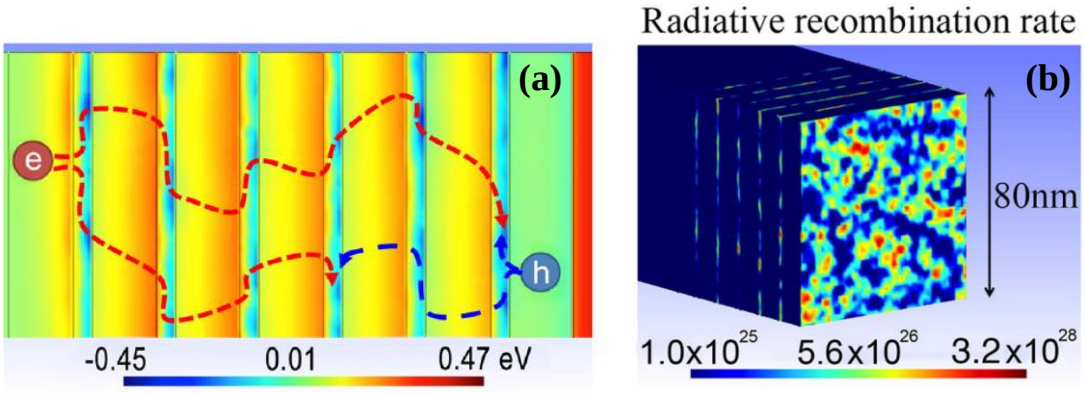

Figure 2.5: Percolation conduction

Illustration of the carrier transport across an LED active region (a); inhomogeneities in the current density and in the radiative recombination due to percolation conduction (b). Taken from [22].

In summary, although SiLENSe addresses the issue of the excessive voltage drop with an option that allows the user to enable a quantum potential model, this solution does not appear to be suitable for the simulations targeting the devices to be considered in this thesis. Particularly because of the unrealistic effects that this approach shows in term of reduced quantum confinement of the carriers within the QWs and the consequent plummeting of the IQE, the option was not activated in any of the simulations presented in this study.

The recent results about the percolation conduction clearly prove that all mono-dimensional simulations are intrinsically limited in their capability of effectively describe any device that contains random alloys, and SiLENSe—notwithstanding its quantum potential model—is no exception to this. For this reason it would appear reasonable to use mono-dimensional models—if one has to—in their original and simpler implementation instead of altering them with *ad hoc* modifications that are not really able to cure their problems but certainly risk undermining their ability to provide any useful information, which they can still do if used with care and awareness of their limits.

2.2 Relative importance of the recombination parameters: the ABC model

As mentioned in Section 2.1.1, the values of the recombination parameters of the III-nitride materials are not fully determined: particularly with regard to the Auger

coefficient C, it is possible that different choices of the values available in literature might produce significant differences in the simulations.

In order to assess that, a few preliminary calculations were performed using the simplified ABC model. According to this approach it is possible, under some assumption, to describe the efficiency of any LED only by making use of three parameters, without going into further details about the actual carrier transport. In fact, if we assume that the recombinations only happen in the quantum wells and in condition of high level of injection, we can neglect the term n_i^2 in the Eqs. (2.18), (2.22), and (2.23). Moreover, if we assume that the non-equilibrium carrier concentrations n and p are equal, and that all the carrier flowing through the device fully recombine in the active region, we have:

$$\frac{J}{e\,d} = An + Bn^2 + Cn^3\,, \tag{2.28}$$

where $A = 1/(\tau_n + \tau_p)$, B, and $C = C_n + C_p$ are the recombination coefficients, which are supposed to be fairly independent from the carrier concentration; J is the current density, and d the total thickness of the active region (i.e. the number of QWs multiplied by their thickness). By solving this cubic equation, it is possible to obtain, for any current density, the amount of non-equilibrium carriers n and, hence, calculate the IQE as:

$$IQE = \frac{Bn}{A + Bn + Cn^2}\,. \tag{2.29}$$

To assess the relative importance of C with respect to A and B, an estimation for the last two parameters is needed. For B the choice is very easy because, as mentioned earlier, most of the sources available in literature use radiative coefficients that are within the small range 1–2 × 10^{-11} cm^3 s^{-1} [3, 4]; to obtain an estimation of the Shockley-Read-Hall coefficient A, the model described in Section 2.1.2 was used instead.

The values calculated with Eq. (2.24) are reported in Table 2.2 for different material qualities with dislocation densities in the range 10^8–10^{10} cm^{-2}, and were obtained using an S coefficient equal to 0.5, as suggested in [16], and with diffusivity coefficients D_n= 2.6 cm^2 s^{-1} and D_p= 0.26 cm^2 s^{-1}, and thermal velocities V_n = 1.95 × 10^7 cm s^{-1} and

V_p = 7.15 × 10^6 cm s^{-1}. In turn, these last values were calculated using the material parameters typical[6] of Al-rich AlGaN alloys: i.e. effective masses m_e= 0.24 m_0 and m_h= 1.8 m_0, mobilities μ_n= 100 cm^2 V^{-1} s^{-1} and μ_n= 10 cm^2 V^{-1} s^{-1}, and in-plane lattice constant a = 0.31 nm.

N_{dis} (cm^{-2})	τ_n (ns)	τ_p (ns)	A (s^{-1})
1 × 10^8	9.4	55.7	1.54 × 10^7
3 × 10^8	3.0	17.4	4.89 × 10^7
1 × 10^9	0.9	4.9	1.74 × 10^8
3 × 10^9	0.3	1.5	5.60 × 10^8
1 × 10^{10}	0.1	0.4	2.02 × 10^9

Table 2.2: Estimation of the *A* coefficient

Calculation based on Eq. (2.24) of the non-radiative electron (τ_n) and hole (τ_p) lifetimes of an Al-rich AlGaN alloy, as a function of the dislocation concentration N_{dis}. The A coefficient was subsequently derived as $A = 1/(\tau_n + \tau_p)$.

Using Eqs. (2.28) and (2.29), and the values of the coefficients A and B justified above, the IQE of a device with a 2 nm single-QW was calculated in the range 0–200 A/cm^2 and for four different values of the coefficient C (i.e. 10^{-35}, 10^{-31}, 3 × 10^{-31}, and 10^{-30} cm^6 s^{-1}); the results are reported in Figure 2.6. As the total non-radiative lifetime ($\tau_n + \tau_p$) goes from 65 ns down to 0.5 ns the IQE drops considerably irrespective of the values of the other coefficients, with efficiencies that are, in the last case, less than 2% in the whole current density range considered.

When the Auger recombination is completely neglected (i.e. with C = 10^{-35} cm^6 s^{-1}) there is no sign of droop. This is not unexpected as carrier leakage, which is the other mechanism responsible for droop that is usually taken into account, was explicitly excluded in the hypotheses used to derive the ABC model. Moreover, as the constants A, B and C were supposed to be independent of the temperature, heating effects were also ignored.

[6] The values reported were calculated, using the SiLENSe material-database, for an $Al_{0.8}Ga_{0.2}N$ alloy; variations of the AlN concentration in the range 50–80% changed the parameters by less than 3%.

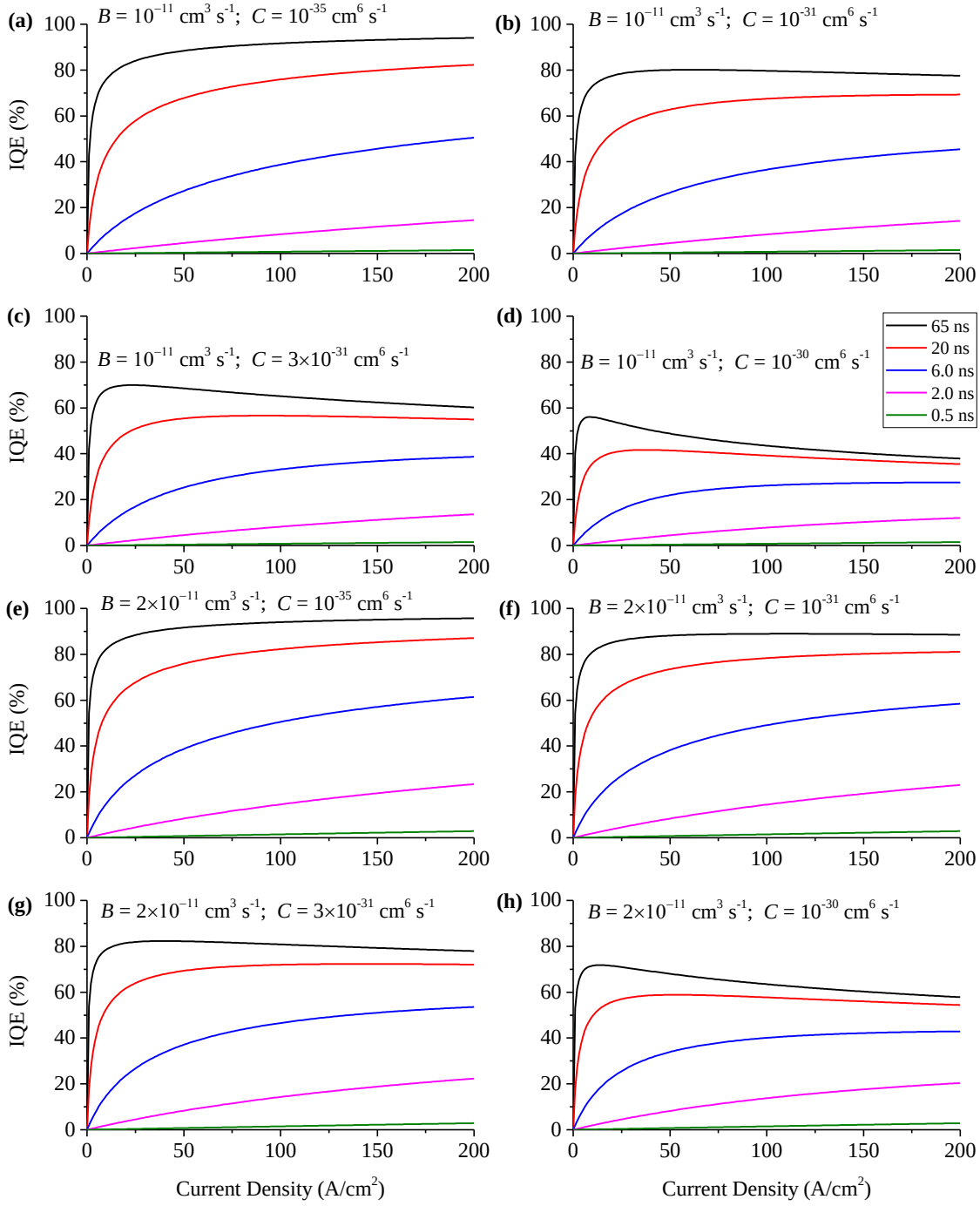

Figure 2.6: IQE curves calculated using the ABC model

Calculation of the IQE as a function of the current density in the range 0–200 A/cm^2, with different radiative recombination coefficient B [i.e. 10^{-11} cm^3 s^{-1} (a-d), and 2×10^{-11} cm^3 s^{-1} (e-h)], and Auger recombination coefficient C [i.e. 10^{-35} cm^6 s^{-1} (a; e), 10^{-31} cm^6 s^{-1} (b; f), 3×10^{-31} cm^6 s^{-1} (c; g), and 10^{-30} cm^6 s^{-1} (d; h)]. The coloured lines refer to different Shockley-Read-Hall non-radiative lifetimes varying in the range 65.0–0.5 ns, which are equivalent to dislocation densities in the range 10^8–10^{10} cm^{-2}, according to the model in [16].

As the C coefficient increases, the onset of an IQE droop is indeed present, with increased intensity as the Auger recombination becomes more and more important. However, this effect is particularly apparent only for the devices with high quality materials, with lifetimes of 65 ns and, to a lesser degree, 20 ns.

For the more defective materials (i.e. 2 and 0.5 ns), the variations of the Auger coefficient in the whole range here considered are not only unable to produce any droop, but they are also insufficient to produce any modification at all in the IQE curve. This proves that the other two recombination channels are largely dominant here. When the same set of calculations was performed with a higher value of the radiative coefficient B (i.e. 2×10^{-11} cm^3 s^{-1}), the results showed an evident increase in the overall IQE, but the shapes of the curves remained almost unchanged.

The calculations here described are, of course, a very rough approximation. In general the QWs are not filled with the same amount of carriers and, in each of them, electron and hole concentrations can be significantly different, with the hole density often being higher in the QWs closer to the *p*-type region. In addition to that, another phenomenon neglected in this analysis is the electron leakage, which in real devices is often significant and has to be included in realistic simulations: all these aspects will be included in the simulations reported in the following sections. However, even with such a limited model, the ABC calculations described here clearly show that the inaccurate knowledge of the actual Auger coefficient will not cause any significant degradation of the accuracy of the simulations in typical UV-LED devices.

The standard values for B and C proposed by SiLENSe were hence used in the following simulations, as well as the Eq. (2.24) for the calculation of A.

2.3 Injection efficiency

2.3.1 Transport asymmetry

As already defined in Chapter 1, the IE is the fraction of injected carriers that recombine in the active region, either radiatively or non-radiatively. The fact that a non-negligible amount of electrons leaks through the device and recombines in the *p*-type region, stems from the asymmetry between holes and electrons, particularly their different concentrations and mobilities. In fact, if we try to simulate an LED made of a fictitious material in which electrons and holes have the same mobility throughout the device, and

if we ensure that the cladding layers have the same amount of free carriers by artificially setting the same dopant concentration, activation energy, and density of states (the latter achieved using the same effective masses), then the IE would be very high, even without any EBL present, as shown in the blue line of Figure 2.7.

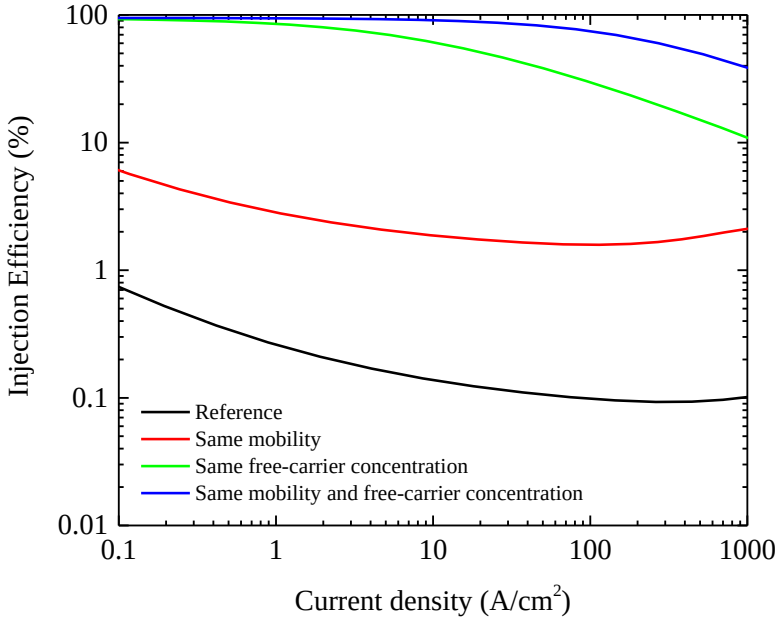

Figure 2.7: Role of electron/hole asymmetry in the IE

Comparison of the IE simulated for different devices that do not have any form of EBL. The level of asymmetry in the hole and electron transport was progressively reduced by artificially changing the parameters summarized in Table 2.3.

In this type of simulation, the reference structure was a five-period multi-QWs AlGaN/AlGaN UV LED emitting at 240 nm, with QBs having their bandgap 200 meV higher than that of the QWs. The standard values of the SiLENSe material-database were used for the 'electron affinity' of all the materials, a choice that ensures a splitting of the bandgap differences so that about 70% of that goes into the conduction-band offset and 30% into the valence-band offset [7], which is commonly assumed in this material system. The donor and acceptor concentrations were both set to 2×10^{18} cm^{-3}; all the other parameters regarding the carrier transport were as in Table 2.3.

Due to the highly asymmetric carrier properties, and to the absence of any form of EBL, it is not surprising that the reference IE is indeed very poor (Cf. black line in Figure 2.7). In the subsequent simulations the parameters were progressively changed to make

the structure more symmetric: in particular, firstly mobility and then activation energy, effective mass and degeneracy factor of holes were set to the same values as those of electrons in Table 2.3. Although the device with electrons and holes of the same mobility had indeed a detectable increase of IE, it was especially the one with the same free-carrier concentrations that showed a significant improvement in the injection. Finally, with the fully symmetric device, the IE increased even further and became very close to 100% in the usual working range of current densities of a typical LED (0–200 A/cm^2). It is clear that the limited IE of real devices is just the result of the intrinsic transport asymmetry present in III-nitride materials, which is also particularly severe in materials containing a high concentration of AlN, as is the case for UV LEDs.

		AlN		**GaN**		**InN**	
		e	*h*	*e*	*h*	*e*	*h*
Mobility	($cm^2\ V^{-1}\ s^{-1}$)	100	10	100	10	100	10
Activation Energy	(meV)	13	470	13	170	13	170
Effective Mass	(m_e)	0.25	1.95	0.20	1.10	0.10	1.35
Degeneracy factor		2	4	2	4	2	4

Table 2.3: Electron/hole asymmetry

The parameters relevant to the carrier transport in the III-nitride materials are here reported: the values are taken from the material database of SiLENSe. The effective masses of the holes are relative to both the heavy and light bands, which—in the direction of the *c*-axis—have the same value; crystal split-off holes have effective masses much similar to electrons, but their contribution to the conductivity is negligible.

As mentioned in Chapter 1, the standard remedy put in place to restore a sufficient level of injection is the use of an EBL, which is a high-bandgap layer in-between the active region and the *p*-type cladding layer. Because of the conduction-band offset, this layer is supposed to reduce the electron current and force it towards levels more similar to the hole current.

A simulation, whose results are reported in Figure 2.8, was done using a similar asymmetric structure as that described in the previous example. However, in this case, an EBL of increasingly higher bandgap was added to the device to study its effect on the IE. Even a small bandgap difference of 200 meV with respect to the cladding layers was enough to bring the IE to values around 60–70%, and it saturated to values close to

100% at around 400 meV. Further increase of the EBL bandgap only degraded the EE by adding a significant series resistance to the device.

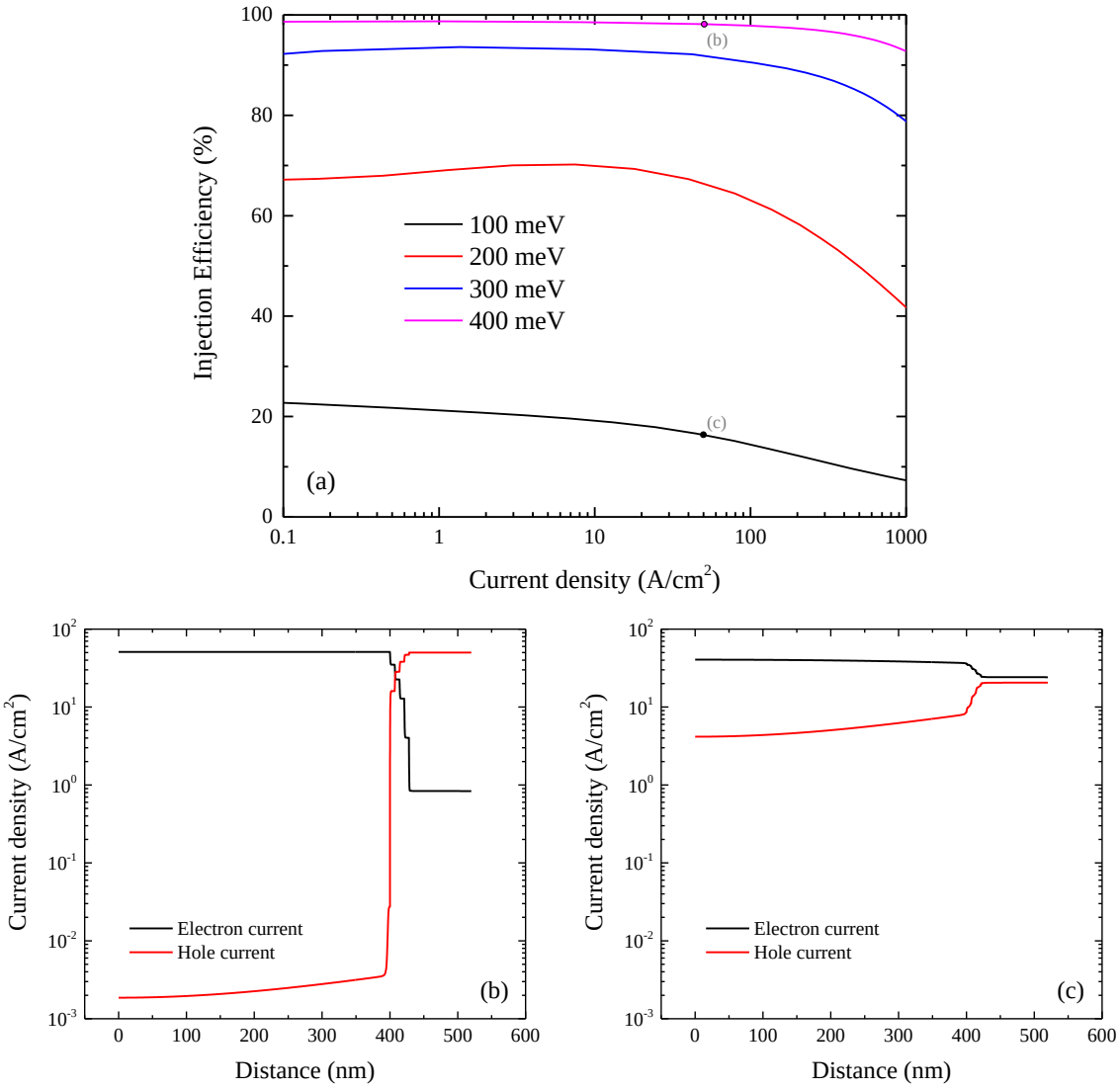

Figure 2.8: The effect of the increase in EBL bandgap

Injection efficiency of UV LEDs having their AlGaN EBL with different AlN concentrations, ranging from 81% to 89% and corresponding to a bandgap difference of 100–400 meV with respect to the cladding layers (a). Variation of the electron and hole current density at 50 A/cm^2 for the device with 400 meV EBL bandgap-difference (b), and the device with 100 meV EBL bandgap-difference (c); the corresponding points in (a) are labelled in gray.

Figure 2.8 (b) and (c) show the variation of electron and hole current densities throughout the device when the total current density is 50 A/cm^2. In (b), which corresponds to the device with the widest-bandgap EBL, the hole current dominates at the right-hand side of the device (*p*-type cladding layer) and the electron current does

the same at the left-hand side (*n*-type cladding layer); the five drops in both types of current correspond to the very high recombination rates happening in the QWs. Although some electrons still leak through the active region, their current in the *p*-type region is about two orders of magnitude lower than the hole current. Instead, the current densities of the device having the lowest-bandgap EBL are shown in (c); in this case the electron current leaking in the *p*-type region is even higher than the hole current.

In devices with a reasonably high IE, at any fixed bias, the amount of electrons injected in the *n*-type region almost exactly matches the amount of holes injected at the *p*-type side of the device. On the contrary, when the leakage of electrons is significant—as in the case depicted in Figure 2.8 (c)—the amount of holes injected is forced to be much lower than that of electrons, as the total current has to be the same throughout the device, and this has a dramatic impact on the IQE. In fact, when the carrier concentrations n and p become too different in the QWs, both the radiative and the Shockley-Read-Hall recombinations greatly reduce even if the total carrier concentration $n + p$ is still high; however, because of the difference in the coefficients, the radiative recombination reduces much more. In other words, a poor IE not only directly contributes to reducing the overall WPE, but also indirectly causes the IQE to significantly drop, regardless of the quality of the material in the active region.

2.3.2 The problem of the last quantum barrier

The leakage of electrons happens as a result of the fact that the hole concentration in the QWs is not high enough to allow a complete recombination of all the electrons flowing through the active region. From this point of view, it is clear that the injection issues can be seen either as an excess of electron current, or as a lack of hole current. Both descriptions are actually the same phenomenon and we cannot have one without the other. This point is crucial as it explains why although a well-designed EBL can indeed help reducing the current leakage, the same EBL may also reduce even further the hole current and restore the transport asymmetry that we were trying to correct in the first place.

In a recent study [23], Mehnke *et al*. highlighted the importance of the optimization of the EBL thickness in deep-UV LEDs. In particular, they showed how an excessive thickness of the EBL causes the appearance of a defect emission in the EL spectrum of the device that has been assigned to an acceptor-mediated recombination in the *p*-type

cladding layer. The presence of this peak was interpreted as the signature of insufficient injection and explained as to be caused by the bending of the EBL.

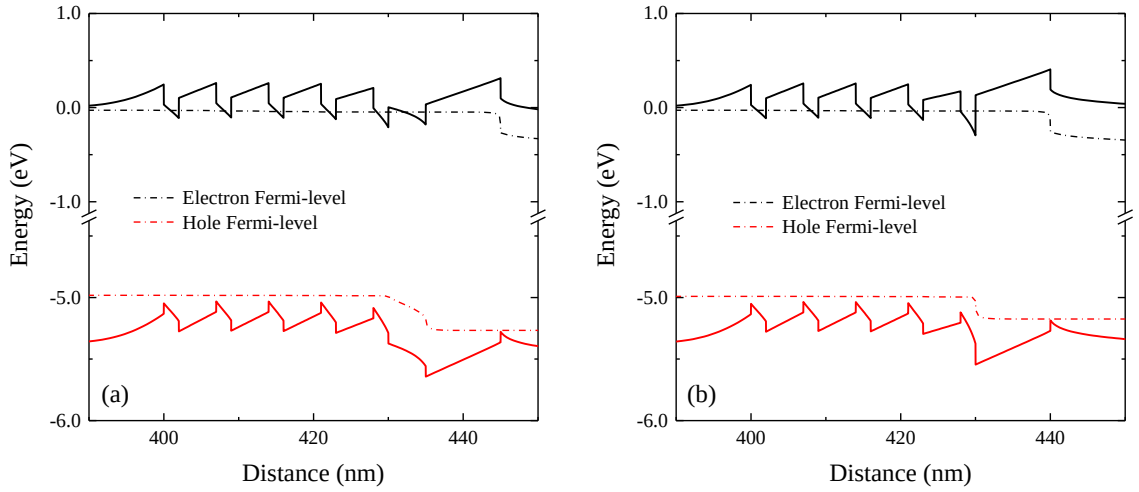

Figure 2.9: The problem of the last QW

Band diagram of a multiple-QW LED with (a) and without (b) the last barrier. Both graphs show the situation at a current density of 50 A/cm^2.

In addition to that, the results of the simulations performed during my doctoral work suggest that it is especially the interaction of the EBL with the last QW-QB that needs to be investigated. In Figure 2.9 the conduction bands of two AlGaN/AlGaN UV LEDs emitting at 240 nm are compared. In the first one the last QB of the active region is followed by an EBL with a bandgap difference of 300 meV. The insertion of a spacer between the last QW and the EBL, either as the presence of a barrier as in this case, or as an extra layer of lower bandgap right after the last barrier is in fact common practice in visible LEDs [11], but also not uncommon in UV devices [23]. In the alternative device here proposed the last barrier of the active region is removed, and the EBL is placed right after the well. As shown in Figure 2.9, the movement of the EBL towards lower energy levels is not just the result of the EBL bending, but it is greatly enhanced by the bending of the last barrier; when this is removed, the IE at the current density of 50 A/cm^2 goes form 63% in the standard structure to 97% in the modified one. The effect is particularly evident in this example because of the relatively thick EBL used (10 nm); however, the same issue is also present—although in a limited way—using

EBLs as thin as 2 nm. Further reductions of the EBL thickness are not practical as would cause the onset of high leakage due to tunnelling (not modelled here).

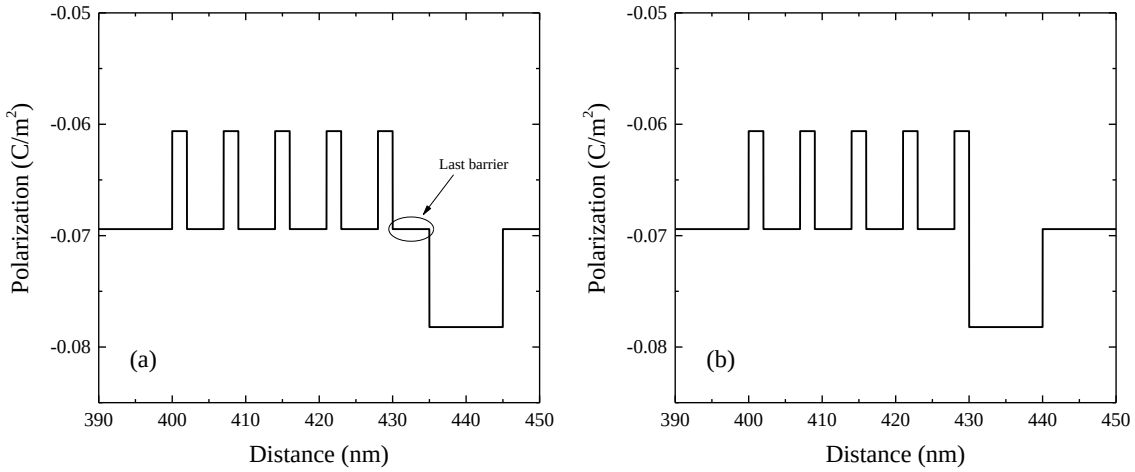

Figure 2.10: Effect of the polarization field on the bending of the last barrier

Comparison of the total polarization field within two UV LEDs with (a) and without (b) the presence of the last barrier before the EBL. The highest-polarization regions are the QWs, the lowest-polarization layer is the EBL

To better understand the reason of the bending of the last QB, the total polarization field—spontaneous plus piezoelectric—of the two devices is shown in Figure 2.10. A sharp increase of polarization corresponds to the appearance of a negative interfacial charge; a drop of it, to a positive charge. The electric fields originated within the device by these charges are the responsible for the bending of the different layers. All the QBs with the exception of the last one are inserted in-between two layers of higher polarization field (the QWs) and this causes them to bend upwards with respect to the direction from the *n*-side to the *p*-side. The last barrier, on the contrary, is followed by a lower polarization layer (the EBL) and retains the same downwards bending of the QWs; as the external bias applied to the device increases, this effect is amplified even further.

2.3.3 The influence of the QW/QB offset

It is not only the height and the thickness of the EBL that has an impact on the IE: the active region geometry can also greatly influence it; in particular the offset between wells and barriers can radically change the amount of electron leakage.

Figure 2.11 shows the results of a series of simulations of devices having increasingly higher QW/QB offsets. The basic structure of the AlGaN/AlGaN devices was similar to that of the previous studies here reported, with no last barrier before the EBL and a 30-nm-thick *p*-GaN contact layer. In order to focus on the influence of the QW/QB offset only, the compositions of the QBs and the EBL were kept fixed and equal to $Al_{0.72}Ga_{0.28}N$ and $Al_{0.81}Ga_{0.19}N$, respectively. The bandgap difference of the QWs with respect to the QBs was varied from 100 meV to 400 meV by reducing the QW bandgap from 5.17 eV down to 4.87 eV.

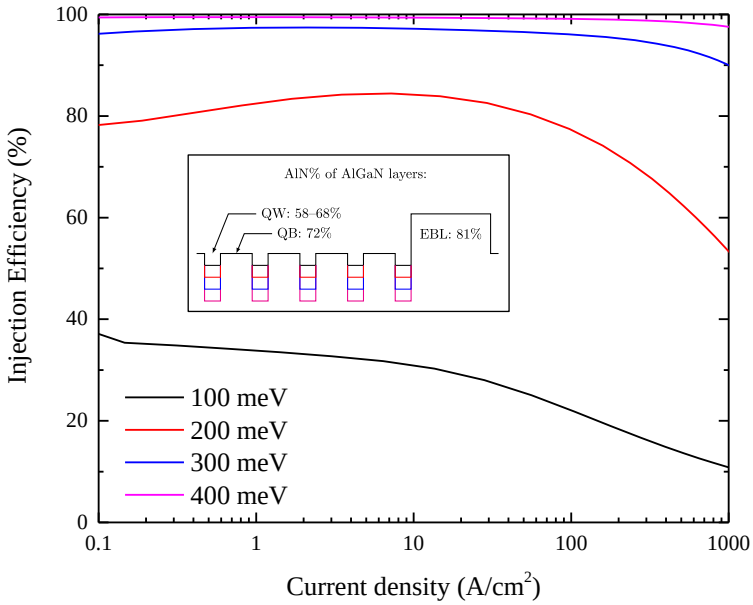

Figure 2.11: Effect of the QW/QB offset on the IE

Injection efficiency of UV LEDs having their QW/QB bandgap differences varying within the range 100–400 meV. Only the QWs were varied, while the QBs and EBL bandgaps were kept constant. The inset contains a schematic of the conduction band of the four devices, and summarizes the compositions of the different AlGaN layers.

The simulations show that the IE increases monotonically with higher QW/QB offsets before approaching 100% at around 400 meV, and suggest that, in the range of offsets here studied, the design of the active region has roughly the same level of impact on the IE as the design of the EBL (Cf. Figure 2.8). Although no sign of degradation of the efficiency was detectable even at much higher levels of QW/QB offset that those shown in Figure 2.11, this result appears to be unrealistic because, as mentioned earlier, when the offset increases too much the drift-diffusion model is not reliable anymore and the

effects of hot carriers have to be included [2], which would cause a reduction of the carrier concentration in the QWs. In case of UV LEDs there is an even more stringent limit to the maximum QW/QB offset that can be achieved as usually an increase of the QB bandgap has to be reflected into an equal increase in the cladding layers, which for Al-rich AlGaN would mean making them even more difficult to dope, with serious consequences in terms of contact resistance and degradation of the EE.

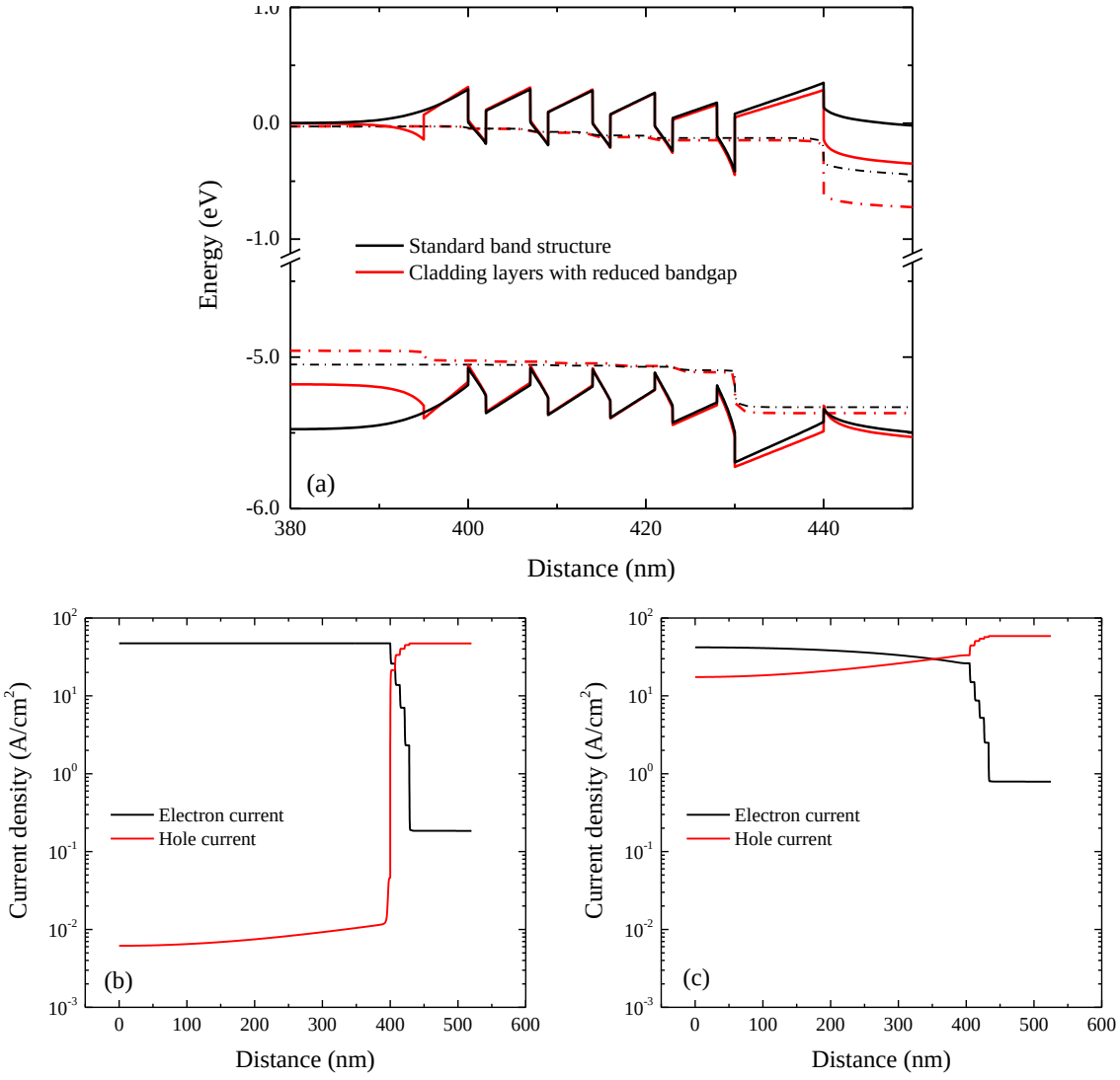

Figure 2.12: LED with cladding layers of reduced bandgap

Band diagrams of two UV LEDs with different cladding-layer bandgaps: same as in the QBs (a), and with a bandgap reduced of 300 meV (b).

In theory it might be possible to circumvent this problem by inserting the active region in-between cladding layers of intermediate bandgap: higher than that of the QWs (to

insure optical transparency), and lower than that of QBs (to facilitate the contacts). However, this approach would lead to serious problems in the electron injection, as summarized in the following set of simulations.

In Figure 2.12 two UV LEDs emitting at 240 nm and having a QW/QB bandgap difference of 400 meV and a QB/EBL difference of 300 meV, but different cladding layers, are compared. The first device follows the standard approach in which the bandgap of both cladding layers is the same as that of the QBs; in the other device their bandgap is 300 meV lower. As can be seen in Figure 2.12, this approach leads to a large reduction in recombination within the active region as a result of the higher recombination rate taking place in the thick *n*-type cladding layer caused by the fact that for the electrons is now much more difficult to overcome the first barrier. In other words, the conduction-band offset between the *n*-type cladding layer and the first barrier acts as an EBL placed just before the active region that stops the electrons from entering in it; in addition to that the valence-band offset is not able to stop the holes from leaking out in the *n*-type region.

2.4 Carrier localization and Urbach energy

As briefly mentioned in Chapter 1, the fact that InGaN/GaN visible LEDs have efficiencies as high as those of devices based on other III-V materials, notwithstanding their much larger dislocation densities, has been explained as due to the beneficial presence of In. Particularly the fact that InN does not easily dissolve in GaN, was believed to cause the formation of macroscopic In-rich regions, with bandgap differences large enough to trap the carriers there and to prevent non-radiative recombination in the dislocations. The presence of these compositional fluctuations was confirmed by several groups using transmission electron microscopy [24], and the phenomenon started to be called ‘indium clustering’. However, O'Neill *et al.* [25] and Smeeton *et al.* [26] reported in 2003 that the exposure of the InGaN samples to an electron beam such as that used in electron microscopy was able to induce damages that might easily be confused with the occurrence of these compositional fluctuations. Finally, Chichibu *et al.* [27] were able to investigate the presence of the clustering at a much shorter scale than what was possible with electron microscopy, and that was possible by using positron annihilation spectroscopy. With this technique, positrons (positively charged antiparticles of electrons) move around in the semiconductor material as if they were holes and, if defects or localization centres are present, they get

trapped there until they annihilate with an electron and emit a γ-ray. By detecting these γ-rays it is possible to measure the diffusion lengths of the positrons—and hence that of electrically injected holes—and a value of about 4 nm was found. This experiment then suggests that the localization effects due to the presence of In indeed exist, only at a much shorter scale.

A model that quantitatively relates the Shockley-Read-Hall lifetime with the amount of localized states present in the material is implemented in SiLENSe, and the physical parameter chosen to parameterize the level of localization is the Urbach energy. In fact, it is well-known that if localized states are present in a material, these would cause the absorption to be significant even at energies lower than the bandgap; in this case the absorption coefficient α is a function of the incoming radiation ($\hbar\omega$), and can be empirically expressed as:

$$\alpha(\hbar\omega) = \alpha_0 exp \frac{\hbar\omega - E_G}{U} \tag{2.30}$$

where U is the Urbach energy, which for high-quality InGaN QWs is in the range 15–30 meV [28]. Although the documentation of the version 5.4 of SiLENSe does not provide the full justification for that, it is claimed that using the approach proposed in [29], it is possible to relate the experimentally measured Urbach energy to the fraction $f_{n,p}$ of the carrier that are completely delocalized and can hence take part in the non-radiative recombination at the dislocation cores. Once the option is activated, the Shockley-Read-Hall lifetime calculated using Eq. (2.24) is then corrected by substituting the carrier lifetimes $\tau_{n,p}$ with the effective values:

$$\tau_{n,p}^{eff} = \frac{\tau_{n,p}}{f_{n,p}} \tag{2.31}$$

where τ_n^{eff} and τ_p^{eff} are the effective Shockley-Read-Hall lifetimes that take into account the localization effects, for electron and holes respectively. In order for SiLENSe to realistically simulate InGaN/GaN blue LEDs, Urbach energies of 30 meV and 15 meV, are suggested by the developers for electrons and holes respectively, which—as mentioned before—are consistent with the experimentally measured values for InGaN QWs [28].

In order to evaluate whether this phenomenon can be extended also to UV LEDs by substituting AlGaN in the QWs with InAlN, and to estimate the potential impact of the localization in these devices, a five-period multi-QW structure was simulated, both with and without taking into account the effects of the localization, and for different material qualities having dislocation densities in the range 10^8–10^{10} cm^{-2}. The QW/QB and QB/EBL bandgap differences were both set to 300 meV in order to insure a high IE; the Urbach energies used—when the model was activated—were the same as suggested for InGaN.

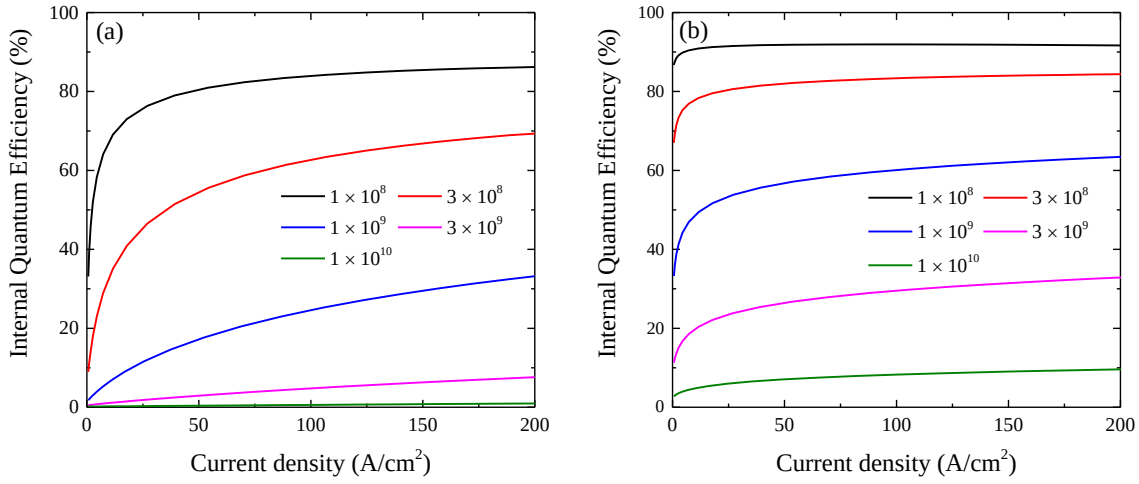

Figure 2.13: Effect of carrier localization on UV LED

The IQE of a near-UV InAlN/AlGaN LED was simulated for different material qualities with dislocation densities in the range 10^8–10^{10} cm^{-2}. The simulations were performed both without (a), or with (b) taking into account the effects of the localization.

As shown in Figure 2.13, the device with In-induced localization effects shows a significant increase of IQE with respect to the reference LED, especially at lower current densities. However, according to these results, both devices proved to be much more affected by the quality of the material, and, at higher current densities, the effects of localization can be completely concealed by an increase of dislocation densities as low as three times.

2.5 Polarization-matched active region

In the previous section, the use of InAlN alloy as an active material for UV LEDs has been investigated only with respect to the reduction of the Shockley-Read-Hall non-

radiative recombination coefficient that the presence of In is supposed to induce. However, the use of this material has also the potential to enhance the IQE by directly increasing the radiative recombination rate.

In fact, one of the main problems that hinder the efficiency of any LED based on the III-nitride materials is the presence of the so-called Quantum Confined Stark Effect (QCSE), which consists in the spatial separation of electron and hole wavefunctions within the QWs caused by the intense internal electric fields that are generated by the polarization mismatch present at the heterojunctions. In standard AlGaN/AlGaN devices it is not possible to independently control emission wavelength, carrier confinement, and polarization field. However, as proposed for example in [30, 31] for visible devices, by using quaternary InAlGaN alloys it would be possible to introduce a further degree of freedom that allows designing active regions with some QW/QB offsets but still no polarization discontinuities. Although in the seminal work [31] the measured increase of efficiency in the polarization-matched devices has been explained in terms of better injection efficiency, the main effect of the absence of polarization charges is the reduction of the radiative lifetime as a result of the increased overlap integral of electrons and holes within the QWs [32].

The aim of the simulation work here described was to demonstrate the feasibility of a polarization-matched near-UV InAlN/AlGaN structure emitting at 340 nm, and to prove that this approach is compatible with the most recent theoretical studies about InAlN. In fact, InAlN is a relatively new material and, due to the very different optimal growth conditions between InN and AlN, also a very difficult one to grow with a reasonable level of crystal quality. Because of that, its physical parameters are still not well known, and especially the bandgap values as a function of the composition are quite scattered in the literature. As for the other III-nitride alloys, it is well-known that the InAlN bandgap does not follow a simple linear Vegard's law and that some form of correction is needed, usually implemented in terms of a bowing parameter b:

$$E_G(In_xAl_{1-x}N) = E_G^{In}x + E_G^{Al}(1-x) - bx(1-x)\,. \qquad (2.32)$$

However, there is no agreement about what bowing parameter should be used, with values ranging from 2.5 eV to 10 eV (Cf. [33] and references therein). This parameter is very critical because from it depends the possibility of realizing a polarization-matched

InAlN/AlGaN structure having sufficient carrier confinement, or even which alloy would act as a barrier and which one as a well.

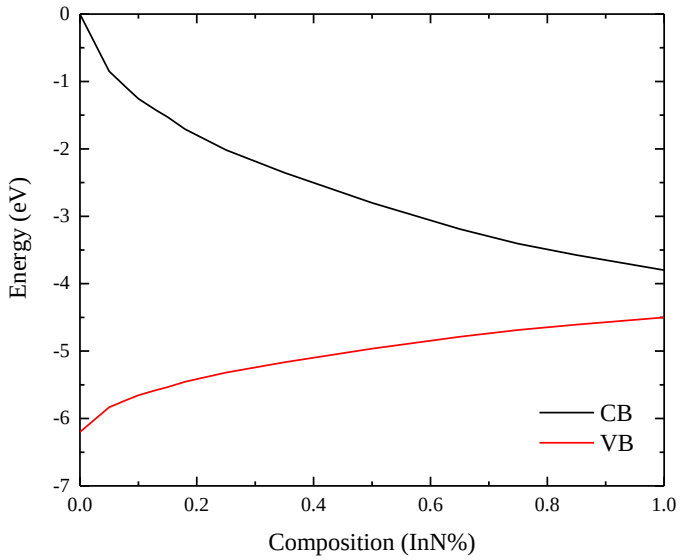

Figure 2.14: InAlN bandgap and band offsets

The graph shows the energy position of the conduction (blue) and valence (red) bands of the InAlN alloy as a function of the InN concentration; the band offsets can be calculated using the vacuum level at 0 eV as the common energy reference (Anderson's rule). These data, which are derived from [34], were used as the basis of the simulations described in this section.

A solution to this problem comes from the most recent work on this subject, both theoretical and experimental [33, 35], which demonstrate that the InAlN bandgap does not have a parabolic dependence on the composition and therefore, if expressed in the form of Eq. (2.32), the bowing parameter has to be strongly composition dependent, which explains the large differences reported in literature. Figure 2.14 shows the energy position of the conduction and valence bands of InAlN with respect to the vacuum level, using the data proposed in [34] but rearranged in a way to have AlN and InN "electron affinities" (as used in SiLENSe) equal to, respectively, 0 eV and 3.85 eV and also so that the contribution from the bowing parameter is split into 70% to the conduction band and 30% to the valence band, as already done in the previous studies reported in this thesis. In order to incorporate these data in the simulations, an algorithm for the interpolation of the bandgap data at any composition and to correspondingly adapt the electron affinity to preserve the band offsets was included in a script for the code interpreter included in the SiLENSe material property editor.

Another reason for this simulation study was to gain some indication about the magnitude of the increase in IQE that a perfectly polarization-matched active-region would be able to provide. The drift-diffusion model implemented in SiLENSe can indeed give some approximate estimation of the QCSE; in fact, although in this semi-classical approach the carriers are treated as point charges, they are free to move within the QWs in response to the electrical field—electrons and holes in the opposite direction—so that the amount of radiative recombination depends on the carrier concentrations, which vary along each QW. However a more satisfying approach would need to treat the carriers as quantum mechanical objects and derive their recombination rate from the overlap integrals of the electron and hole wavefunctions. An optional module also present in SiLENSe can do that by numerically solving the Schrödinger equation for electrons and holes using as input data the shapes of the conduction and valence bands, which in turn come from the solutions of the standard drift-diffusion simulation at any current density. This latter method was used in this study.

Layer	**Material and composition**	**Thickness (nm)**	**N_A or N_D (cm^{-3})**
Contact enhancer	*p*-GaN	30	2×10^{18}
Cladding layer	*p*-$Al_{0.53}Ga_{0.47}N$	70	2×10^{18}
QB	$Al_{0.53}Ga_{0.47}N$	6.5	-
Capping layer	$Al_{0.85}Ga_{0.15}N$	0.5	-
QW	$In_{0.14}Al_{0.86}N$ (alternatively $Al_{0.39}Ga_{0.61}N$)	2	-
QB	$Al_{0.53}Ga_{0.47}N$	9	-
Cladding layer	*n*-$Al_{0.53}Ga_{0.47}N$	500	2×10^{18}

Table 2.4: Summary of the structure simulated

Data used in the simulations of the InAlN/AlGaN near-UV LED emitting at 340 nm and that of a standard AlGaN/AlGaN device emitting at the same wavelength. The only difference in the two structures is the material used for the QW.

Although the actual devices that have been grown and fabricated in this project are multi-QWs structures, the feasibility of the polarization-matched active-region and the increase of the overlap integrals can be studied in single-QW devices all the same, which also have the advantage of greatly reducing the convergence problems that sometimes plague the simulations of more complicated devices.

A reference device, in which the InAlN QW was substituted with an AlGaN-based layer of the same bandgap, was also simulated for comparison; the details of both structures are summarized in Table 2.4. The thin Al-rich capping layer inserted between the QW and the second barrier was included in the sequence because, during the growth of the actual devices, it is indispensable to avoid In desorption from the QW when the temperature is raised to the barrier conditions in a two-temperature growth [36].

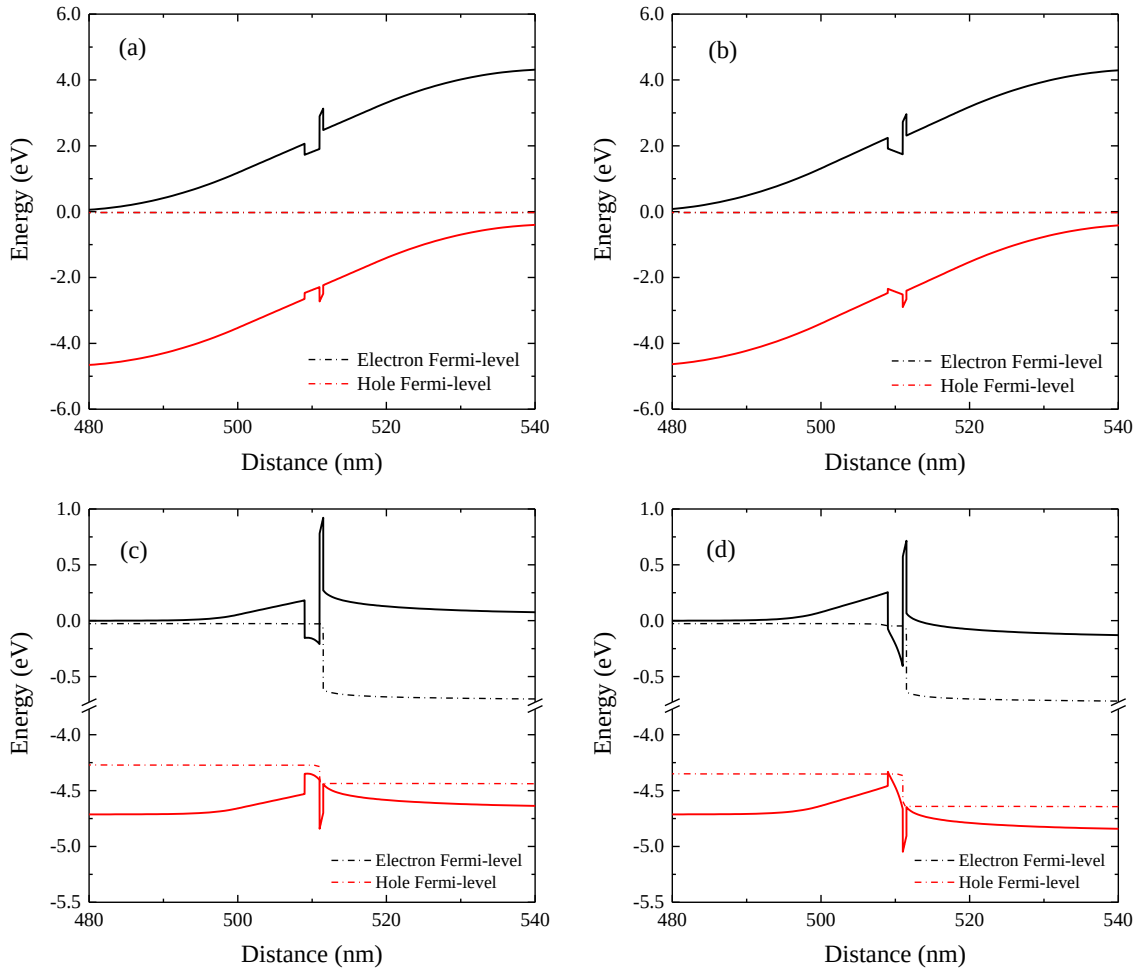

Figure 2.15: Near-UV LED band diagram

Band diagram of the InAlN/AlGaN near-UV LED emitting at 340 nm (a), and that of a standard AlGaN/AlGaN device emitting at the same wavelength (b), when no bias is applied. Close-up of the conduction band at 100 A/cm^2 of the InAlN (c), and the AlGaN-based (d) LEDs.

The band diagrams of the polarization-matched and reference LEDs are shown in Figure 2.15 (a) and (b), respectively, when no bias is applied to the devices. The bending of the barriers in both structures is caused by the built-in potential only, as the polarization

fields are screened by the free carriers. In the reference device, however, the thin QW has an internal polarization that greatly differs from that of the surrounding barriers, and the charges that form at the interfaces cannot be screened. The resulting electric field causes the well to strongly bend downwards. When some bias is applied to the devices, the band diagrams start to flatten and increasingly higher currents to flow through them; when a value of 100 A/cm^2 is reached, both devices have almost completely flat conduction and valence bands. While in the polarization-matched device the bending the QW follows that of the barriers, in the reference structure the external bias only causes the QW to bend even further, Cf. Figure 2.15 (c-d).

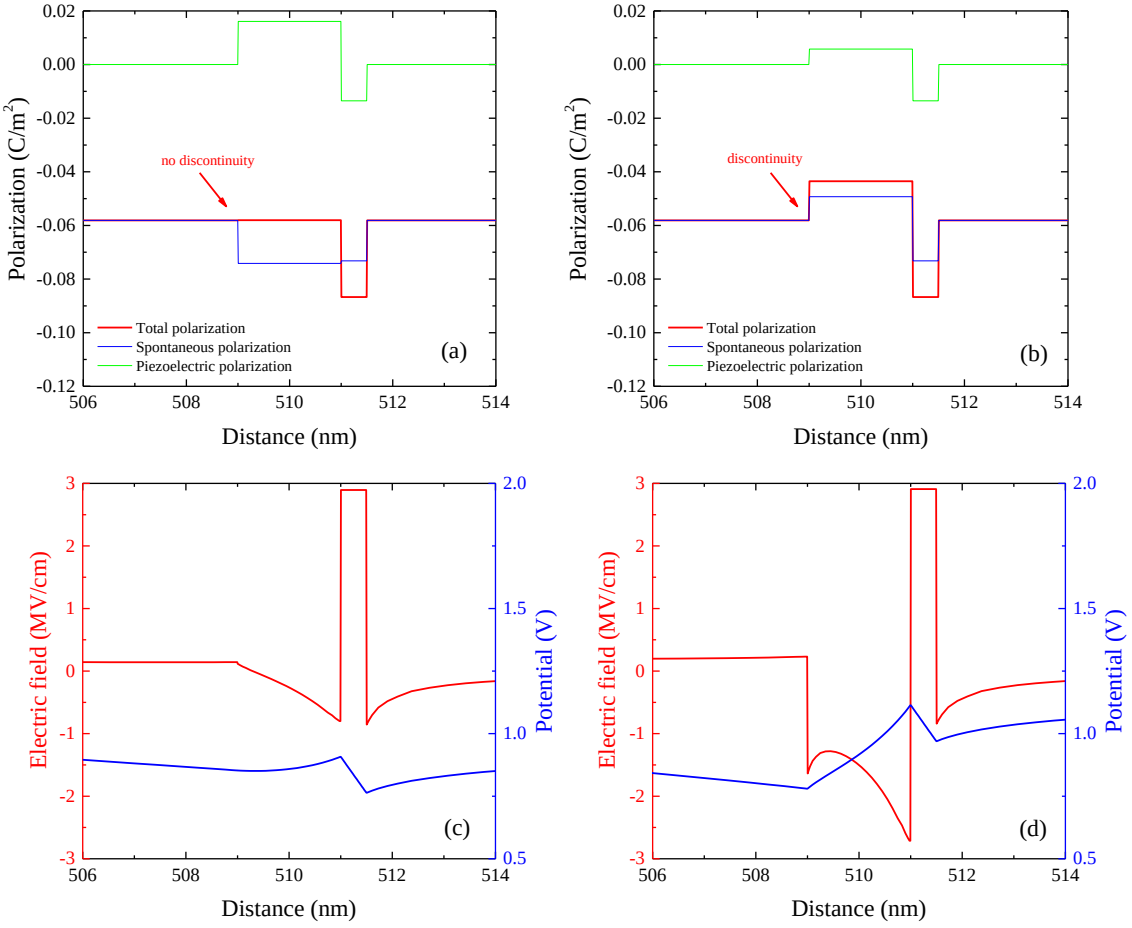

Figure 2.16: Polarization and electric fields

Spontaneous, piezoelectric and total polarization fields of the InAlN/AlGaN near-UV LED emitting at 340 nm (a), and that of a standard AlGaN/AlGaN device emitting at the same wavelength (b). Electric field and potential of the InAlN (c), and the AlGaN-based (d) LEDs.

To better illustrate the reason of this behaviour, the spontaneous, piezoelectric, and total polarization fields present in the two structures are shown in Figure 2.16 (a-b). Assuming that both active regions are fully strained to the cladding layers, the piezoelectric polarization, caused by the elastic deformations necessary to preserve the in-plane lattice constant, is added to the already present spontaneous polarization. However, while in the polarization-matched device the variations of spontaneous and piezoelectric polarization have opposite signs and cancel each other, in the reference device they add up and the discontinuity in the total polarization becomes even stronger. The resulting electric fields are shown in Figure 2.16 (c-d), where the differences in the two QWs are apparent.

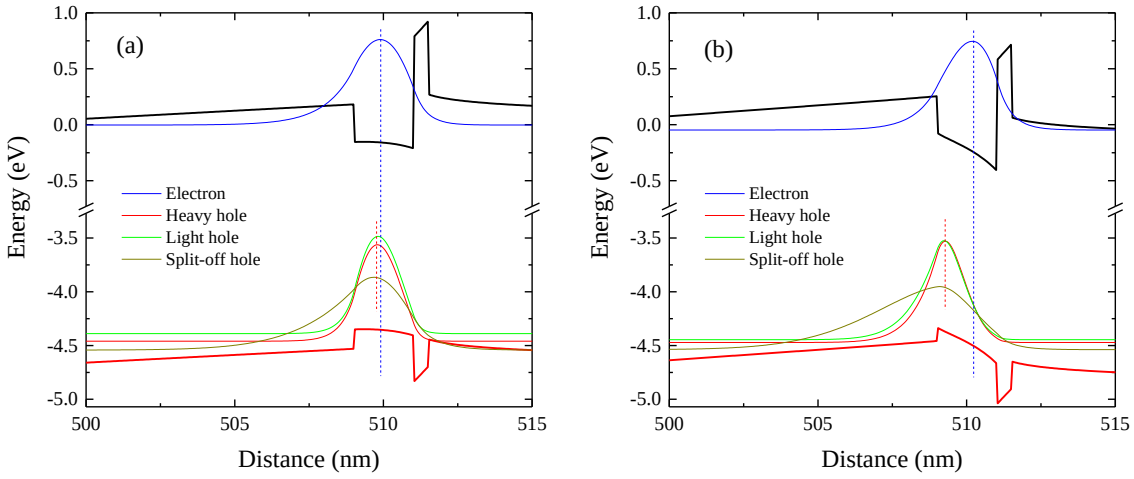

Figure 2.17: Electron and hole wave functions

Carrier wave functions calculated by SiLENSe for the band position at 100 A/cm^2 in the InAlN/AlGaN near-UV LED emitting at 340 nm (a), and in the standard AlGaN/AlGaN device emitting at the same wavelength (b).

Using the band diagrams obtained with a current density of 100 A/cm^2, the wavefunctions of electrons and heavy, light, and split-off holes were calculated as shown in Figure 2.17. Although the presence of the wide-bandgap capping layer is able to partially limit the deformation of the electron wavefunction, the shift in the peak positions of all the hole wavefunctions is clearly visible. The values of the overlap integrals computated by SiLENSe are reported in Table 2.5 and show an increase of the recombination rates from 55% up to 91% with respect to the reference device.

	Electrons/ Heavy holes	Electrons/ Light holes	Electrons/ Split-off holes
InAlN/AlGaN LED	0.9398	0.9300	0.9347
AlGaN/AlGaN LED	0.6045	0.5681	0.4885

Table 2.5: Overlap integrals

Results of the calculations of the overlap integrals of electrons with heavy, light, and crystal split-off holes obtained by SiLENSe at 100 A/cm^2 of current density.

2.6 Conclusions

The characteristics and the problems of the different approaches to the simulation of optoelectronic devices based on III-nitride materials were reviewed, particularly with the aim of supporting the design of UV-LEDs.

The basic elements of UV LEDs—choice of geometry, materials, and relative band offsets for QWs, QBs and EBL—were studied to assess their influence on the performance of the devices. The injection efficiency, which is commonly believed to be a key problem of UV LEDs, not only depends on the choice of the EBL, but it is also significantly affected by the QW/QB offsets. The fact that the bandgap of the barriers cannot be set higher than that of the cladding layers, in turn limited by doping issues, seriously limits the IE of the devices emitting in the UVC range.

The interaction of the last QB and the EBL caused by the polarization discontinuities has been investigated and proved to be able to significantly reduce the effectiveness of the latter. The simulation of a structure with the EBL placed immediately after the last QW showed an increase of the IE that varied from 63% of the standard structure to 97% of the modified device.

The effects of the carrier localization occurring in In-containing alloys were investigated using the same model and material parameters that are usually used for InGaN-based devices. A significant increase of the IQE was present in the simulations, especially at low current densities; however such an improvement could be nullified by a simultaneous decrease of the material quality. In order to have devices able to withstand an increase of the dislocation densities of more than 3 times and still show an improved IQE, materials with Urbach energies higher than 30 and 15 meV are required for electrons and holes, respectively.

The simulation of a proof-of-concept device showed that the realization of a polarization-matched InAlN/AlGaN near-UV LED is consistent with the more recent findings about the material characteristics of the InAlN alloy. The reduced QCSE present in this structure causes the overlap integrals to greatly increase with respect to a non-polarization-matched traditional AlGaN/AlGaN structure emitting at the same wavelength.

2.7 Bibliography

[1] F. Bernardini, V. Fiorentini, and D. Vanderbilt, "Spontaneous polarization and piezoelectric constants of III-V nitrides," *Physical Review B - Condensed Matter and Materials Physics,* vol. 56, pp. R10024-R10027, 1997.

[2] P. Kivisaari, T. Sadi, J. Li, P. Rinke, and J. Oksanen, "On the Monte Carlo Description of Hot Carrier Effects and Device Characteristics of III-N LEDs," *Advanced Electronic Materials,* 2017.

[3] Y. C. Shen, G. O. Mueller, S. Watanabe, N. F. Gardner, A. Munkholm, and M. R. Krames, "Auger recombination in InGaN measured by photoluminescence," *Applied Physics Letters,* vol. 91, 141101, 2007.

[4] J. Piprek, "Efficiency droop in nitride-based light-emitting diodes," *Physica Status Solidi (A) Applications and Materials Science,* vol. 207, pp. 2217-2225, 2010.

[5] R. N. Hall, "Electron-hole recombination in germanium," *Physical Review,* vol. 87, p. 387, 1952.

[6] W. Shockley and W. T. Read, "Statistics of the recombinations of holes and electrons," *Physical Review,* vol. 87, pp. 835-842, 1952.

[7] J. Piprek, *Semiconductor optoelectronic devices. Introduction to physics and simulation*. USA: Academic Press, 2003.

[8] K. A. Bulashevich and S. Y. Karpov, "Is Auger recombination responsible for the efficiency rollover in III-nitride light-emitting diodes?," vol. 5, pp. 2066-2069, 2008.

[9] S. Y. Karpov, "Modeling of III-nitride light-emitting diodes: Progress, problems, and perspectives," San Francisco, CA, 2011.

[10] J. Iveland, L. Martinelli, J. Peretti, J. S. Speck, and C. Weisbuch, "Direct measurement of auger electrons emitted from a semiconductor light-emitting diode under electrical injection: Identification of the dominant mechanism for efficiency droop," *Physical Review Letters,* vol. 110, 177406, 2013.

[11] G. Verzellesi, D. Saguatti, M. Meneghini, F. Bertazzi, M. Goano, G. Meneghesso*, et al.*, "Efficiency droop in InGaN/GaN blue light-emitting diodes: Physical mechanisms and remedies," *Journal of Applied Physics,* vol. 114, 2013.

[12] K. T. Delaney, P. Rinke, and C. G. Van De Walle, "Auger recombination rates in nitrides from first principles," *Applied Physics Letters,* vol. 94, 191109, 2009.

[13] F. Bertazzi, M. Goano, and E. Bellotti, "A numerical study of Auger recombination in bulk InGaN," *Applied Physics Letters,* vol. 97, 231118, 2010.

[14] A. S. Polkovnikov and G. G. Zegrya, "Auger recombination in semiconductor quantum wells," *Physical Review B - Condensed Matter and Materials Physics,* vol. 58, pp. 4039-4056, 1998.

[15] T. Sugahara, H. Sato, M. S. Hao, Y. Naoi, S. Kurai, S. Tottori*, et al.*, "Direct evidence that dislocations are non-radiative recombination centers in GaN," *Japanese Journal of Applied Physics Part 2-Letters,* vol. 37, pp. L398-L400, Apr 1998.

[16] S. Y. Karpov and Y. N. Makarov, "Dislocation effect on light emission efficiency in gallium nitride," *Applied Physics Letters,* vol. 81, pp. 4721-4723, 2003.

[17] Z. Z. Bandić, P. M. Bridger, E. C. Piquette, and T. C. McGill, "Values of minority carrier diffusion lengths and lifetimes in GaN and their implications for bipolar devices," vol. 44, pp. 221-228, 2000.

[18] L. Chernyak, A. Osinsky, and A. Schulte, "Minority carrier transport in GaN and related materials," *Solid-State Electronics,* vol. 45, pp. 1687-1702, 2001.

[19] K. Horio and H. Yanai, "Numerical Modeling of Heterojunctions Including the Thermionic Emission Mechanism at the Heterojunction Interface," *IEEE Transactions on Electron Devices,* vol. 37, pp. 1093-1098, 1990.

[20] K. Yang, J. R. East, and G. I. Haddad, "Numerical modeling of abrupt heterojunctions using a thermionic-field emission boundary condition," *Solid State Electronics,* vol. 36, pp. 321-330, 1993.

[21] K. A. Bulashevich, O. V. Khokhlev, I. Y. Evstratov, and S. Y. Karpov, "Simulation of light-emitting diodes for new physics understanding and device design," in *Proc. SPIE 8278, Light-Emitting Diodes: Materials, Devices, and Applications for Solid State Lighting XVI*, 2012.

[22] T. J. Yang, R. Shivaraman, J. S. Speck, and Y. R. Wu, "The influence of random indium alloy fluctuations in indium gallium nitride quantum wells on the device behavior," *Journal of Applied Physics,* vol. 116, 113104, 2014.

[23] F. Mehnke, C. Kuhn, M. Guttmann, C. Reich, T. Kolbe, V. Kueller*, et al.*, "Efficient charge carrier injection into sub-250 nm AlGaN multiple quantum well light emitting diodes," *Applied Physics Letters,* vol. 105, 051113, 2014.

[24] O. Brandt and K. H. Ploog, "The benefit of disorder," *Nature Materials,* vol. 5, pp. 769-770, 2006.

[25] J. P. O'Neill, I. M. Ross, A. G. Cullis, T. Wang, and P. J. Parbrook, "Electron-beam-induced segregation in InGaN/GaN multiple-quantum wells," *Applied Physics Letters,* vol. 83, pp. 1965-1967, 2003.

[26] T. M. Smeeton, M. J. Kappers, J. S. Barnard, M. E. Vickers, and C. J. Humphreys, "Electron-beam-induced strain within InGaN quantum wells: False indium "cluster" detection in the transmission electron microscope," *Applied Physics Letters,* vol. 83, pp. 5419-5421, 2003.

[27] S. F. Chichibu, A. Uedono, T. Onuma, B. A. Haskell, A. Chakraborty, T. Koyama*, et al.*, "Origin of defect-insensitive emission probability in In-containing (Al,In,Ga)N alloy semiconductors," *Nature Materials,* vol. 5, pp. 810-816, 2006.

[28] M. Piccardo, C. K. Li, Y. R. Wu, J. S. Speck, B. Bonef, R. M. Farrell*, et al.*, "Localization landscape theory of disorder in semiconductors. II. Urbach tails of disordered quantum well layers," *Physical Review B,* vol. 95, 144205, 2017.

[29] M. A. Jacobson, D. K. Nelson, O. V. Konstantinov, and A. V. Matveentsev, "The tail of localized states in the band gap of the quantum well in the In0.2Ga0.8N/GaN system and its effect on the laser-excited photoluminescence spectrum," *Semiconductors,* vol. 39, pp. 1410-1414, 2005.

[30] W. C. Lai, S. J. Chang, M. Yokoyam, J. K. Sheu, and J. F. Chen, "InGaN-AlInGaN multiquantum-well LEDs," *IEEE Photonics Technology Letters,* vol. 13, pp. 559-561, 2001.

[31] M. F. Schubert, J. Xu, J. K. Kim, E. F. Schubert, M. H. Kim, S. Yoon*, et al.*, "Polarization-matched GaInNAlGaInN multi-quantum-well light-emitting diodes with reduced efficiency droop," *Applied Physics Letters,* vol. 93, 041102, 2008.

[32] Y. K. Kuo, M. C. Tsai, and S. H. Yen, "Numerical simulation of blue InGaN light-emitting diodes with polarization-matched AlGaInN electron-blocking layer and barrier layer," *Optics Communications,* vol. 282, pp. 4252-4255, 2009.

[33] S. Schulz, M. A. Caro, L. T. Tan, P. J. Parbrook, R. W. Martin, and E. P. O'Reilly, "Composition-dependent band gap and band-edge bowing in AlInN: A combined theoretical and experimental study," *Applied Physics Express,* vol. 6, 121001, 2013.

[34] S. Schulz, Private communication, March 2013

[35] V. Z. Zubialevich, D. V. Dinh, S. N. Alam, S. Schulz, E. P. O'Reilly, and P. J. Parbrook, "Strongly nonparabolic variation of the band gap in $In_xAl_{1-x}N$ with low indium content," *Semiconductor Science and Technology,* vol. 31, 025006, 2015.

[36] V. Z. Zubialevich, T. C. Sadler, D. V. Dinh, S. N. Alam, H. Li, P. Pampili*, et al.*, "Enhanced UV luminescence from InAlN quantum well structures using two temperature growth," *Journal of Luminescence,* vol. 155, pp. 108-111, 2014.

3 Growth optimization

This chapter focuses on the various aspects of the epitaxial growth of the material that have an impact on the performance of the final device. In particular, the cladding-layer optimization of the UV LEDs has been investigated, and the main results are here reported and discussed.

All the growth activities described in this chapter were carried out by Metal-Organic Vapour Phase Epitaxy (MOVPE) in our reactor. The actual growth runs were conducted by Dr. Vitaly Zubialevich, Dr. Duc Van Dinh and Dr. Haoning Li with whom I collaborated; the material characterization by Hall-effect measurements, the analysis and interpretation of the data here reported are the result of my own independent work. The design of the experiments was discussed and finalized together.

The general introduction on III-nitride epitaxy (Section 3.1.1) and the literature review (Section 3.2.4) are based on the review paper "Doping of III-nitride materials" [1], which I co-authored with Prof. Peter Parbrook.

3.1 Epitaxial growth of III-nitride materials

3.1.1 Introduction

Because of their extremely high melting temperatures and high decomposition pressures, single crystalline III-nitride materials cannot be obtained by methods such as Czochralski or Bridgman growth. More advanced methods have consequently been investigated for bulk growth of GaN and AlN, such as ammonothermal crystal growth, sodium flux, physical vapour transport and sublimation–recondensation [2]. However, the resulting material is very expensive, usually available only in small sizes, and contains impurities that reduce its transparency in the visible and also in the deep UV [3].

For all these reasons, the most practical solution available to obtain III-nitride-based optoelectronic devices is by vapour phase epitaxy on foreign substrates such as silicon, silicon carbide or sapphire. In particular, the three main epitaxial techniques are: Hydride Vapour Phase Epitaxy (HVPE), MOVPE, and Molecular Beam Epitaxy (MBE). The first two are both chemical deposition methods that only differ in the mode

of transport of the group-III elements to the reactor and resulting growth chemistry; the last one is a vacuum technique in which the precursor atoms are evaporated and travel to the substrate as a 'beam' due to the long mean free path for atom interaction in the growth chamber. These techniques are extensively described in literature in specific review papers such as [4, 5] for HVPE, [4-6] for MOVPE, and [4, 7] for MBE.

The first technique used to grow GaN was HVPE [8, 9], originally developed for silicon and germanium epitaxy, and afterwards for conventional III-V materials such as gallium arsenide (GaAs) and gallium phosphide (GaP). In HVPE growth, group-III atoms are brought into the reactor as halides (hence the name of '*Halide* Vapour Phase Epitaxy' sometimes used as a synonym), and group-V atoms are introduced as hydrides. In case of GaN growth, the halide precursor is usually in the form of gallium chloride, produced when pure metallic gallium, melted in a heated crucible, is exposed to hydrogen chloride. These molecules are then carried by a flow of hydrogen gas into the reactor where they react with ammonia, the nitrogen-carrying hydride, to form GaN with gaseous reaction by-products (H_2, HCl). Using this technique at the RCA Laboratories in 1969, Markusa and Tietjen [10] were able to demonstrate, for the first time, the growth of monocrystalline GaN; and soon afterwards Pankove *et al.* [11] produced the first GaN-based LED. As a consequence of these results, several research groups in the US and in Japan built their own HVPE reactors and the approach became quite popular for a while. Nevertheless, few years later most of them, including RCA, eventually moved to the new emerging MOVPE method in the hope of better quality material, and HVPE was mostly abandoned. Nowadays, the modern versions of HVPE are still in use and, because of their fast growth-rate (typically 10–100 μm/h), they are particularly suitable for the growth of thick, high quality free-standing GaN substrates [2].

In MOVPE growth, the metal precursors are organic compounds such as trimethylgallium (TMGa), trimethylaluminium (TMAl) and trimethylindium (TMIn); while ammonia is still the nitrogen source. Within the reactor chamber, ammonia and precursors transported by a carrier gas (hydrogen or nitrogen) decompose because of the high temperature at which the substrate is kept (typically 1000 °C or more). Group-III and nitrogen atoms are then adsorbed into the substrate and, some of them, are eventually incorporated into the epitaxial film. The chemical reactions involved in the process are more complicated than in HVPE and great care has to be taken, at reactor design level, to minimize any pre-reactions outside the substrate surface that might lead

to the formation of non-volatile compounds. In the first years of development, MOVPE-grown films did not show any major improvement in quality compared with the HVPE system, but in 1986 Amano *et al.* [12] proposed the use of an AlN nucleation buffer-layer that significantly improved the crystalline quality and the uniformity of the subsequently grown GaN epilayers; in 1991 Nakamura [13] reported a similar approach using GaN buffer-layers. At the moment, virtually all MOVPE growth of III-nitride epilayers are based on some evolution of this approach, which consists of a high-temperature nitridation of the substrate with ammonia, a low-temperature deposition of a thin nucleation layer, followed by a high-temperature growth in which the increased mobility of the adsorbed adatoms contributes to a higher crystalline quality of the film [5, 14, 15]. If required, doping can be obtained during growth by introducing into the reactor controlled amounts of dopant-containing gases, such as silane (SiH_4), disilane (Si_2H_6), or bis-cyclopentadienylmagnesium (Cp_2Mg) that undergo thermal dissociation and release the dopant species in the reactor chamber (i.e. silicon or magnesium, in these examples).

In MBE growth, group-III metal and dopant atoms come from high-purity solid sources contained in Knudsen effusion cells that, heated in high-vacuum chambers, produce a stream of non-interacting particles that impinge into the substrate, typically heated at around 800 °C, where they are adsorbed and, eventually, incorporated. The fluxes of the different atomic species can be controlled by varying the temperatures of the Knudsen cells, and can also be quickly stopped by means of mechanical shutters, a feature that allows MBE-grown devices to have structures with very sharp interfaces. Nitrogen, on the contrary, cannot be supplied through effusion cells, and must come from other sources in the form of reactive radicals able to be effectively incorporated into the epitaxial layer. The most widespread version of MBE is the so-called Plasma Assisted MBE in which the nitrogen radicals are produced by radio-frequency (RF) or electron cyclotron resonance (ECR) plasma sources [4, 7]. Ammonia-based MBE systems also exist and have recently attracted considerable attention for the high quality of their materials [16]. They require more complex types of chamber in order to be able to maintain a high-vacuum level even with relatively large flows of ammonia, but they can take advantage from higher growth temperatures that are not only necessary to ensure the thermal cracking of the ammonia molecules, but are also beneficial in improving the quality of the epilayer.

In any type of III-nitride epitaxy, the major problem that hinders the quality of the epilayers, is the already mentioned lack of suitable, low-cost substrates for homoepitaxy. Notwithstanding the great deal of optimization in the growth techniques so far achieved, the large lattice mismatch between the foreign substrates and the III-nitride materials inevitably leads to high dislocation concentrations that are not only detrimental to the optoelectronic device performance (they act as non-radiative recombination centres), but they also affect the quality of the doping, as will be discussed in the following sections.

III-nitride epilayers are grown much more easily with their hexagonal c-axis perpendicular to the substrate surface, but because of the presence of spontaneous and piezoelectric polarization fields along this direction, this causes the quantum wells typically used in optoelectronic devices, to be subjected to strong electric fields that bend their potential profiles and shift holes and electrons in opposite directions, greatly reducing the recombination efficiency. In order to overcome this issue, different growth directions have also been studied, either with no polarization (nonpolar directions) or with reduced fields (semipolar directions) [17]. The resulting material often shows different electrical characteristics, if compared to polar epilayers subjected to the same doping conditions. The electrical characterization of our *n*-type $(11\bar{2}2)$ semipolar AlGaN material—grown to study its potential application in UV LEDs—is reported on Section 3.5.

3.1.2 The Aixtron reactor

All the samples in this thesis were grown using an AIXTRON 3×2FT vertical reactor, which uses the so-called closed-coupled showerhead technology, originally developed by the British company Thomas Swan. In this approach, a silicon carbide coated graphite susceptor containing the substrates is placed at close distance to the lid of the reactor chamber, through which the gases are flown. This lid is shaped in the form of a ‘showerhead’ with small tubes through which the gases are uniformly spread around the susceptor surface (Cf. Figure 3.1). Moreover, in order to minimize pre-reactions, nitrogen and metalorganic precursors flow from different tubes in alternate positions, and come into contact only in the close vicinity of the substrates. To further increase the uniformity, the susceptor can also rotate up to a maximum speed of 300 rpm; both rotation speed and the gap between showerhead and susceptor can be finely adjusted; nevertheless, in our experiments, they were fixed to 60 rpm and 11 mm, respectively.

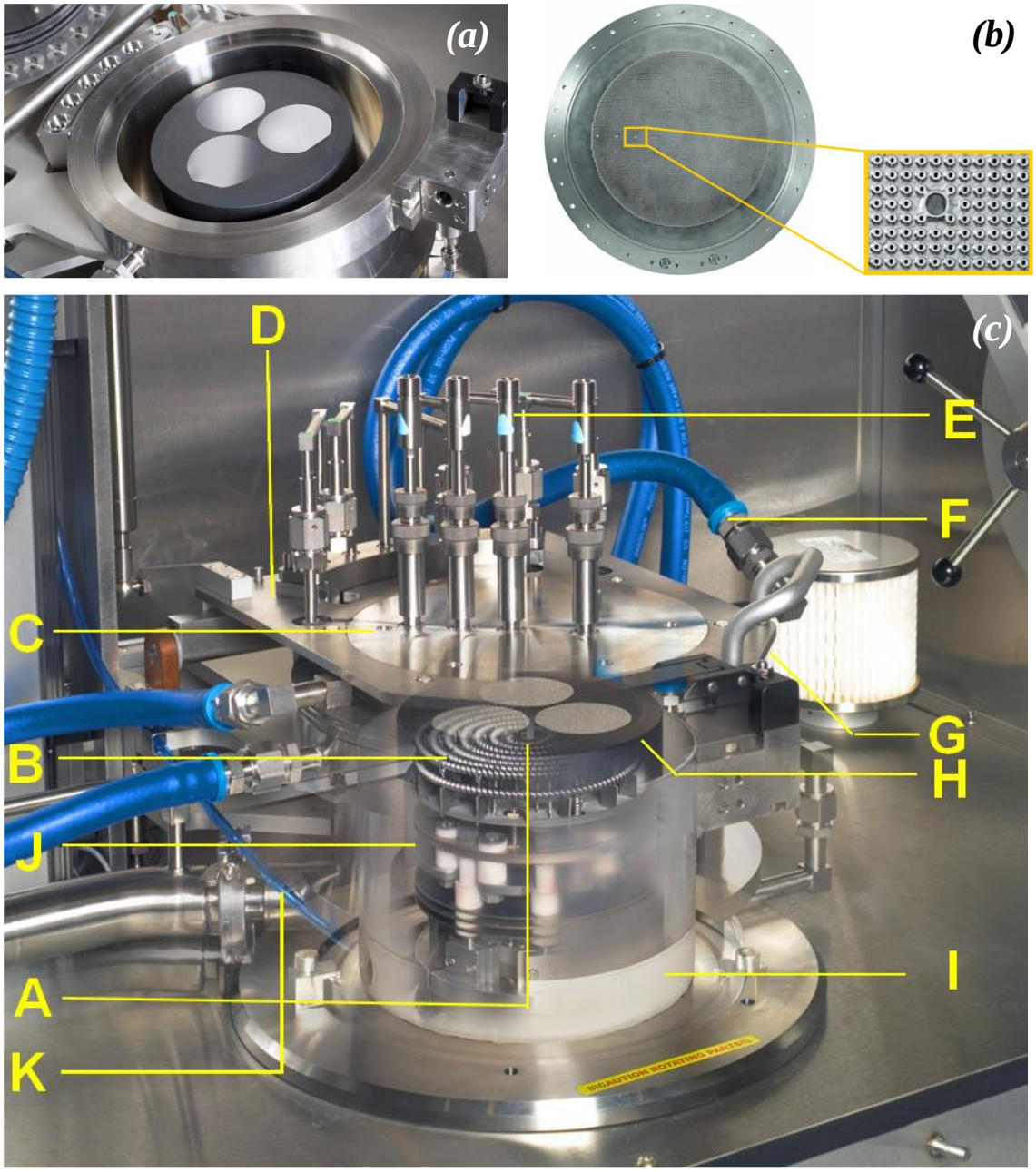

Figure 3.1: Details of the AIXTRON 3x2FT reactor

From the AIXTRON manual, ref. [12].

a) Susceptor for three two-inch wafers

b) Showerhead with close-up of the injection tubes

c) Main parts of the reactor:

A	Thermocouple	G	Double O-ring seal
B	Tungsten heater	H	Susceptor
C	Showerhead	I	Quartz liner
D	Reactor lid	J	Susceptor support
E	Optical probe	K	Exhaust

To induce thermal cracking of the gas molecules and obtain the active radicals needed for the chemical deposition, the surface temperature of the susceptor can be raised up to a maximum of 1300 °C by means of a tungsten heater located inside the susceptor holder. The system controls the temperature using the feedback from a thermocouple placed at the centre of the susceptor just below its surface; infrared pyrometry is also used for temperature calibration.

The sources of nitrogen and group-III atoms are, as standard, NH_3, TMAl, TMGa and TMIn. While NH_3 is a gas directly supplied into the reactor from a cylinder, the metalorganic precursors are either liquid (TMAl and TMGa) or solid (TMIn) and need to interact with a carrier gas so that their vapours can be brought into the reactor. For this purpose they are stored in special container called "bubblers" that have an inlet for the carrier gas and an outlet through which the vapours dissolved into the gas go to the reactor chamber.

The amount of metalorganic moles extracted from a bubbler is proportional to the inlet gas flow-rate and, according to Dalton's law, the proportionality constant is the partial pressure of the precursor (vapour pressure) over the total pressure in the bubbler. If, as customary, the volume flow-rate of the gas entering the bubbler is expressed in terms of standard cubic centimetres per minutes (sccm), the practical formula for the metalorganic molar flow-rate is:

$$\Phi_{MO}(mol/min) = \frac{\Phi_{carrier}(sccm)}{22400}\,\frac{P_{vapour}}{P_{bubbler}}. \tag{3.1}$$

which uses the fact that the molar volume of an ideal gas at standard conditions is 22400 cm^3/mol.

In order to keep the metalorganic molar flow proportional to the inlet gas flow-rate, the vapour pressure has to remain constant during the whole growth run and, for this reason, the bubblers are kept in a thermal bath and their temperatures constantly regulated. In the case of TMAl, it has also to be noted that, at bubbler conditions, this substance is dimeric, i.e. the unit particles contained in any molar quantity of TMAl are molecule pairs, not just single molecules as for TMGa and TMIn. At reactor conditions, the molecule pairs split and the molar flow doubles; a fact that has to be taken into account when growing AlGaN alloys.

In our reactor, the precursor used for *p*-type doping is the standard Cp_2Mg, which is a solid contained in a bubbler. For *n*-type doping, on the contrary, instead of the more common alternative SiH_4, we use Si_2H_6 from a cylinder containing a 50 ppm gas mixture in an inert gas. The reason for preferring disilane over silane dates back to the 1980s when it was proposed for the doping of GaAs materials [18], because of its much higher reactivity. Silicon incorporation into GaAs by means of silane, was shown to be quite temperature dependent, leading to inefficient incorporation at low growth temperatures, and to substantial doping inhomogeneities resulting from any substrate temperature variation. As shown in Figure 3.2, doping by means of disilane leads to an almost constant silicon incorporation into GaAs in the whole range of temperatures tested.

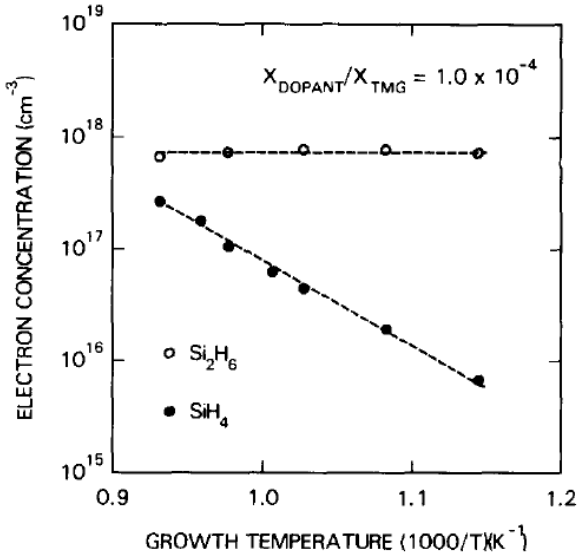

Figure 3.2: Silane vs disilane doping efficiency

Comparison between silane and disilane incorporation in GaAs growth. Taken from [12].

For nitride materials there are not many reports in literature that compare silane and disilane doping, apart from the review paper from Sheu and Chi [19], which basically indicates that both gases can be effectively used to induce the formation of free electrons and that in both cases their concentrations are linear with the molar flow rate. Although in the cited reference disilane doping efficiency was claimed to be one order of magnitude lower than silane, it is not really possible to fairly compare those results as the two experiments were performed in different reactors and different growth

conditions (the data from Sheu and Chi about the use of disilane [19], were compared with those from Nakamura *et al.* who used silane [20]). Whatever the case here, given the higher growth temperatures required for GaN compared to GaAs it is not surprising that both provide an effective solution. However, to compare our doping results with those of other groups—which almost generally use silane—it is important to remember that the molar flow of the dopant gas being equal, the amount of silicon atoms introduced into the reactor is, in our case, double.

An essential prerequisite of III-nitride MOVPE is the preparation of suitable high-quality AlN or GaN templates to be used as crystal seeds for the actual material growth. This preliminary step, usually done in separate growth runs and based on the aforementioned seminal work of Amano, Akasaki and Nakamura [12, 13], is of fundamental importance for the crystal quality of the subsequently grown epitaxial film. In the approach developed by our group, the growth of AlN templates on sapphire was optimized in a three-step process as described in [21] (and later adapted to semipolar materials in [22]). Using this method, templates with sub-nanometre surface roughness and high crystalline quality were demonstrated, with dislocation concentrations in line with the results achieved by other groups, which confirms that our material is of sufficient quality for the analysis of the charge transport reported in this chapter. A few more details about the determination of the material quality will be discussed in the next section.

For the subsequent growth of the actual epitaxial films a trial and error optimization process of the different growth parameters is required, the most important of which are temperature, pressure, and partial pressure ratio between ammonia and metalorganic precursors (V/III ratio). Ideal values for these parameters are shown in Table 3.1 for GaN, AlN, and InN; in case of alloys, the optimal growth conditions are at somewhat intermediate values between those of the constituting materials. The detailed description of this optimization work and of the resulting recipes is out of the scope of this thesis as I was not directly involved in this activity. For this reason, although the relevant growth conditions will be summarized in the experimental sections of this chapter, the focus will be more on the aspects of growth that are related to the doping of the materials.

	carrier gas	temperature (°C)	pressure (mbar)	V/III ratio
GaN	H_2	~1050	~100	~1000
AlN	H_2	1100–1300	~50	~50
InN	N_2	~500	>400	>10 000

Table 3.1: Typical MOVPE growth parameters

Summary of the most important parameters for MOVPE growth of III-nitride materials. The values reported are for general indication only: growth recipes developed by different groups in different reactors may significantly differ from each other.

3.1.3 Characterization of the material with X-ray diffraction

X-ray diffraction (XRD) is a non-destructive technique used to analyse the structure of crystals, and is the primary tool for post-growth characterization of epilayers. The technique exploits the fact that crystal samples hit by X-ray radiations—which have wavelengths comparable to the interatomic distances—generate diffraction patterns as a result of the interference from the radiation reflected by individual atoms. It is customary to define the diffraction geometry as in Figure 3.3, where ω is the angle between the incident beam and the sample surface, and 2θ is the one between the prolongation of the incident beam and the detector. For any choice of the angles ω and 2θ, the detector will collect the reflection from all the crystal planes that have an offset[7] $\omega - \theta$ with respect to the sample surface, provided they exist. If the interplanar distance d and the X-ray wavelength λ satisfy the Bragg's law for some integer number n:

$$2d \sin\theta = n\lambda\,, \tag{3.2}$$

a constructive interference of all the planes will cause a maximum in the diffracted intensity.

One of the most common applications of XRD is the measurement of the average lattice parameters of the epilayers, which can be especially useful to determine the material composition of alloys with the Vegard's law. In fact, this technique was used to estimate the composition of all the materials discussed in this thesis.

[7] If the offset is zero the reflection is said to be symmetric, and asymmetric otherwise.

Because of the high penetration depth of the X-rays, it is also possible to obtain information from complex hererostructures, including composition, thickness and strain of each of its layers. However, in this case the diffraction patterns are much more complicated and the data can only be analysed with special software packages for simulation and fitting.

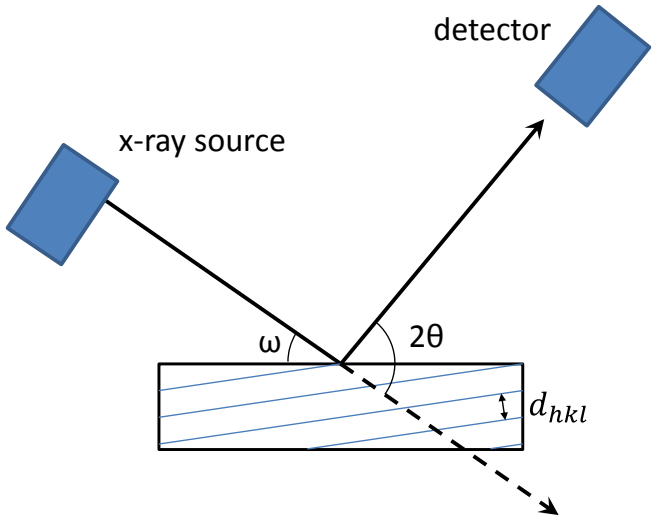

Figure 3.3: Diffraction geometry

Schematics of the diffraction geometry used in XRD measurements. The blue lines in the sample schematize the crystal planes (hkl) probed in this particular configuration. These planes have an offset angle $\omega - \theta$ with respect to the surface of the sample, and form an angle θ with the detector. The plan of the figure, which contains both incident and reflected beams is called "diffraction plane".

Ideally, the maxima in the diffracted radiation should have the form of delta functions occurring at some geometrical configurations, with the intensity that immediately goes to zero when the angles are changed. In real samples, however, many factors contribute to the broadening of the peaks, so that the intensity as a function of the scanning angle most often assumes a Gaussian shape with values of the full width at half maximum (FWHM) that can reach a few hundreds of arcsec in III-nitride epilayers. Any deviation from the ideal case of a perfectly regular, infinite lattice such as the presence of wafer curvature, variations in strain and composition, limited size of the coherently diffracting domains, and lattice rotations present at the dislocations will cause some broadening.

It is usually difficult to separate the effects of the different sources of broadening. However, for relatively highly defective films such as the III-nitride materials,

dislocations are the dominant contributor, so that the FWHM of selected scans can be used to estimate their concentration. In fact, epilayers grown on substrates with large lattice mismatches usually exhibit a mosaic structure, which means that they consist of subgrains slightly misoriented with respect to each other and the underlying substrate [23]. In this framework, threading dislocations of screw type accommodate tilts among these mosaic subgrains and cause broadening in all symmetric and asymmetric scans, while edge dislocations accommodate twists and are responsible for broadening in the direction perpendicular to the diffraction plan shown in Figure 3.3. Although the former effect can be easily estimated through the FWHM of any ω-scan, the latter is much more difficult to measure, as in-plane scans—theoretically the ideal method—are usually not possible for thin epitaxial films, and the broadening of the scans performed on samples rotated by 90° around their axis and subsequently tilted with respect to the diffraction plane—the so-called skew-symmetric reflections—are in general affected by both tilts and twists of the subdomains and might be difficult to analyse. However, experimental studies on III-nitride materials [23, 24] have shown that the FWHM of skew-symmetric ω-scans that have very large angles from the normal, such as $(10\bar{1}1)$, $(10\bar{1}2)$ and $(12\bar{3}1)$, are—in most cases—a very good approximation of the in-plane broadening caused solely by the presence of edge dislocations.

For this reason, we routinely check the FWHM of (0002) ω-scans to estimate the screw and mixed dislocations, and FWHM of $(10\bar{1}1)$ skew-symmetric ω-scans to estimate edge and mixed dislocations. Our standard AlN templates discussed in the previous section typically show FWHMs as low as ≈250 arcsec and ≈500 arcsec for the (0002) and $(10\bar{1}1)$ reflections, respectively. Although our group originally reported FWHM of only 350 arcsec for the (0002) reflection and 760 arcsec for the $(10\bar{1}1)$ (Cf. ref. [21]), subsequent studies proved that the quality of the templates can in fact be improved even further if they are grown after a long series of AlN growths, as the reactor behaviour tends to be influenced by previous runs.

Commercial templates that allow the growth of high-quality AlN without the need of the complex procedure required by our standard templates were also used in some of the experiments described in this chapter. XRD ω-scans of the AlN epilayers show typical FWHMs of 20–100 arcsec for the (0002) reflection and ≈1000 arcsec for the $(10\bar{1}1)$. This means that although they have a lower concentration of screw and mixed dislocations, the concentration of edge dislocations is much higher.

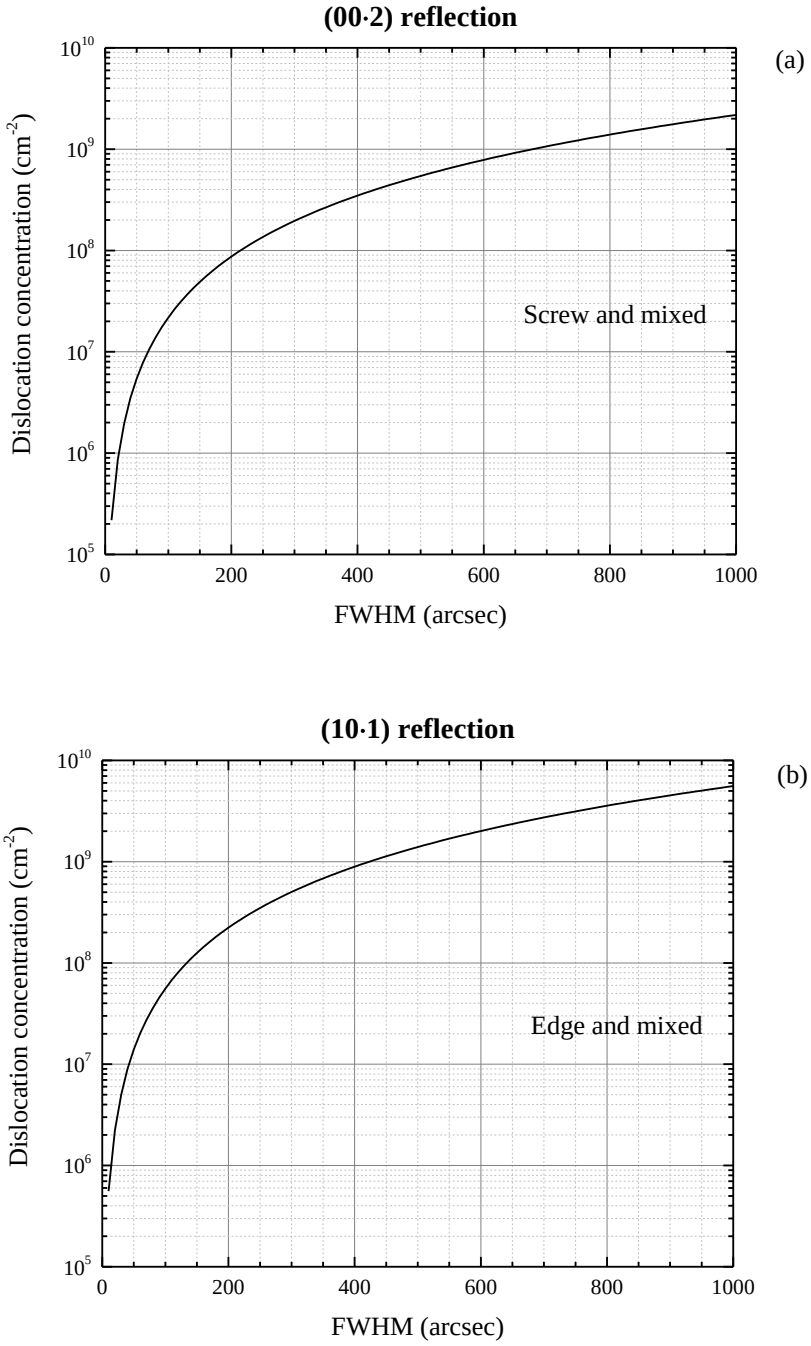

Figure 3.4: Relation with FWHM and dislocation density

Estimation of the dislocation density with Eq. (3.3) as a function of the FWHM of the XRD ω-scans for (a) the (0002) reflection, which only detects screw and mixed dislocations; and (b) the $(10\bar{1}1)$ reflection, which is substantially determined by edge and mixed dislocations only.

The method described above is mostly used to compare the relative material quality of different epilayers, and to qualitatively assess the result of a growth run. However, under certain conditions, it also allows a quantitative estimation of the actual concentration of dislocations that are accessible to that reflection. There are many

different formulae that can be used to do this calculation, although in most cases they give quite similar results; one of the most used in the evaluation of III-nitride materials is the one originally proposed by Dunn and Koch for Si–Fe crystals:

$$N_{dis} = \frac{(FWHM)^2}{3.45\, b^2}, \tag{3.3}$$

in which b is the Burgers vector of the dislocation. A critical discussion of all the possible formulae and their limit of validity can be found in the review paper by Moram and Vickers [25]. In Figure 3.4 the dislocation density as a function of the FWHM calculated using Eq. (3.3) is reported for the two reflections used in this thesis; the lattice parameters *c* and *a* of AlN were used to estimate the Burgers vectors of the screw and edge dislocations, respectively.

3.2 Elements of doping and transport in AlGaN

3.2.1 Hydrogenic theory of shallow impurities

As shown in Figure 3.5, the donor states of moderately doped semiconductors lie at an energy level E_D slightly below the bottom of the conduction band E_C; the difference E_d between these two levels is called either ionization energy or activation energy and, as the name suggests, is the amount of energy required to free an electron bound to the impurity and allow its transfer to the conduction band. The acceptor states E_A, on the other hand, lie above the upper edge of the valence band E_V, and similarly as for the donors, the difference E_a between these two levels is the energy necessary to release a hole in the valence band.

The simplest way to model the behaviour of shallow substitutional impurities in a semiconductor host is by the so-called hydrogenic theory—also referred to as effective-mass theory—which is based on Bohr's model of the atom. In this approach the electrons bound to an impurity are treated as if they were part of a modified hydrogen atom, in which the electron effective-mass (m^*) and the semiconductor permittivity ($\varepsilon_0\varepsilon_r$) are used in place of the free-electron mass (m_e) and the vacuum permittivity (ε_0). The use of these parameters, which describe macroscopic properties of the semiconductor, is justified by the fact that the electron wavefunctions extend over many lattice cells.

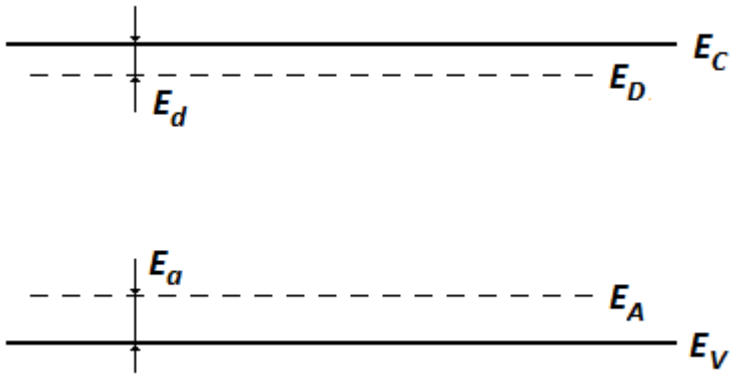

Figure 3.5: Definition of terms: donor and acceptor states in the bandgap
Schematic illustration of the position of the donor and acceptor states (E_D and E_A), with respect to the conduction and the valence band (E_C and E_V).

In order to estimate the donor activation energy of a *n*-type semiconductor, the expression of the Rydberg energy [26]

$$E_{Ryd} = \frac{e^4 m_e}{2(4\pi\varepsilon_0\hbar)^2} = 13.6\ eV\ , \tag{3.4}$$

which corresponds to the ionization energy of an isolated hydrogen atom, needs to be modified with the relevant semiconductor parameters m^* and ε_r:

$$E_d = \frac{m^*}{m_e}\frac{1}{(\varepsilon_r)^2} \times 13.6\ eV\ . \tag{3.5}$$

This model does not differentiate among donor species as it gives the same activation energy for all of them. A more precise calculation would require the introduction of a correction to the $1/r$ impurity potential to take into account also the deformations present in the lattice cell that hosts the impurity, which depend on the particular dopant species. However, adding this contribution is, in many cases, not really necessary and Eq. (3.5), despite its simplicity, can estimate with amazing precision the activation energy of real shallow donors. For acceptor dopants the calculation is slightly more complicated because of the degenerate valence-band structure, but the approach is very similar.

In some conditions, the deformations of the crystal around the dopants might nonetheless induce lattice relaxations through the movement of some of the impurities

from a substitutional into an interstitial position. In this case the donor is said to have undergone a DX transition and its energy levels shifts closer to the centre of the forbidden gap. Deep states have much more localized wavefunctions and the hydrogenic theory cannot be used to model them. Both O and Si are suspected to cause DX states in Al-rich AlGaN [27-29]. Similar transitions can happen also for acceptor impurities, and in this case they are referred to as AX states. Although these were originally believed to be present in Mg-doped GaN [30], a later theoretical study disproved this hypothesis, and assigned the persistent photoconductivity results previously reported as due to bistability of the N-vacany [28].

3.2.2 Semiconductor statistics

The activation energy, together with the temperature, are the main parameters that control the amount of free carriers and consequently the conductivity of the doped layers. While in narrow-bandgap materials the values of the activation energy are usually so small that at room-temperature all the impurities can be considered fully ionized, this assumption does not hold for the wide-bandgap III-nitride materials. A realistic calculation of the free-carrier concentration as a function of the temperature will be here derived for AlGaN alloys and briefly discussed.

Because the experimental activities reported in this thesis mostly regard the study of partially compensated *n*-type materials—although the calculations for *p*-type materials are very similar—a donor concentration N_D higher than the acceptor concentration N_A will be assumed here. In this case, all the acceptor states can be considered to be occupied by an electron coming from a donor impurity; the remaining donors that still have an electron localized around them can release it to the conduction band if enough thermal energy is available. Due to the charge neutrality, the free-electron concentration n can hence be expressed as:

$$n = N_D^+ - N_A^- = N_D^+ - N_A \,. \tag{3.6}$$

The concentration of ionized donors can be determined using the Fermi-Dirac statistics

$$N_D^+ = N_D[1 - f_F(E_D)] \,, \tag{3.7}$$

where $f_F(E)$ is the probability that the state of energy E is occupied with an electron. Substituting Eq. (3.7) in Eq. (3.6), one obtains

$$n = N_D \left[1 + g\, exp\left(\frac{E_F - E_C}{kT}\right) exp\left(\frac{E_d}{kT}\right)\right]^{-1} - N_A\,, \tag{3.8}$$

where g is the degeneracy factor of the ground-state of the hydrogen-like system. The equation (3.8) was derived without the use of any approximation but, in order for this expression to be useful, the reference to the Fermi level E_F must be substituted with some function of the carrier concentration n. The strategy usually followed in most textbooks (Cf. e.g. [26, 31, 32]), is to use the Boltzmann approximation for non-degenerate semiconductor, according to which:

$$exp\left(\frac{E_F - E_C}{kT}\right) = \frac{n}{N_C}\,, \tag{3.9}$$

where N_C is the effective density of states. In this case, substituting Eq. (3.9) into Eq. (3.8), one obtains the following well-known equation:

$$\frac{n(n + N_A)}{N_D - N_A - n} = \frac{N_C}{g} exp\left(-\frac{E_d}{kT}\right). \tag{3.10}$$

This expression, which is a quadratic polynomial in n, can be used to derive an explicit expression for the carrier concentration. However, if

$$n \ll N_A\,, \tag{3.11}$$

a simpler expression can be derived:

$$n \cong \frac{N_C}{g}\ \frac{N_D - N_A}{N_A} exp\left(-\frac{E_d}{kT}\right), \tag{3.12}$$

which has the advantage of being much easier to interpret. Having an exponential part multiplied by a coefficient only slowly varying with temperature, the effect of the activation energy can be clearly determined by the slope of n if displayed in a semi-logarithmic graph with respect to the inverse of the temperature. Although this approach is sometimes found in literature, it is important to realize that this method gives sensible results only when the data extend over a large range of temperatures so that the exponential part is really dominant over the effective density of states, which is also dependent on the temperature:

$$N_C = \frac{1}{\sqrt{2}}\left(\frac{m_e^* k}{\pi\hbar^2}\right)^{3/2} T^{3/2} \tag{3.13}$$

Moreover, close to the saturation regime in which the carrier concentration approaches $N_D - N_A$, the approximation (3.11) does not hold anymore and the fitting with the simplified Eq. (3.12) would lead to large errors. However, for the extraction of the activation energy, the limitations of the Eq. (3.12) do not constitute a problem anymore: the widespread availability of non-linear regression tools often present in modern software packages such as Origin or Excel, allows fitting the experimental data directly with Eq. (3.10), without the need of any simplification.

Another, more subtle, source of errors might derive from the failure of the Boltzmann statistics—implicit in Eq. (3.9)—which would happen, as a result of high dopant concentrations, when the Fermi level approaches or crosses the conduction-band edge. The exact expression of the free-carrier concentration involves the use of the Fermi-Dirac integral of order $1/2$

$$n = N_C \mathcal{F}_{1/2}\left(\frac{E_F - E_C}{kT}\right), \tag{3.14}$$

but unfortunately an analytic expression of $\mathcal{F}_{1/2}$ does not exist. In Figure 3.6, two different approximate expressions are compared: the commonly used Boltzmann approximation, which is valid only until the Fermi energy is at least one kT below the bottom of the conduction band, and the Ehrenberg approximation, which can be used if the Fermi energy is not more than $2kT$ above the conduction band edge.

The latter approximation is based on the expression [26]:

$$exp\left(\frac{E_F - E_C}{kT}\right) = \frac{4n}{4N_C - n}, \tag{3.15}$$

which can be substituted in Eq. (3.8), in place of Eq. (3.9), to obtain

$$\frac{4gn(n + N_A)}{4N_C(N_D - N_A) - n(N_D - N_A + 4N_C - n)} = exp\left(-\frac{E_d}{kT}\right). \tag{3.16}$$

This formula is more complicated that Eq. (3.10), but its validity is extended to a wider range of doping levels and activation energies. Because our material showed a significantly reduced activation energy with respect to the values expected from the hydrogenic model—most likely due to free-carrier screening effects— the results from Eq. (3.10) were compared with those of Eq. (3.16) to check the applicability of the Boltzmann statistics. Although some deviations were indeed noticed, the results obtained with the two approaches showed only limited differences.

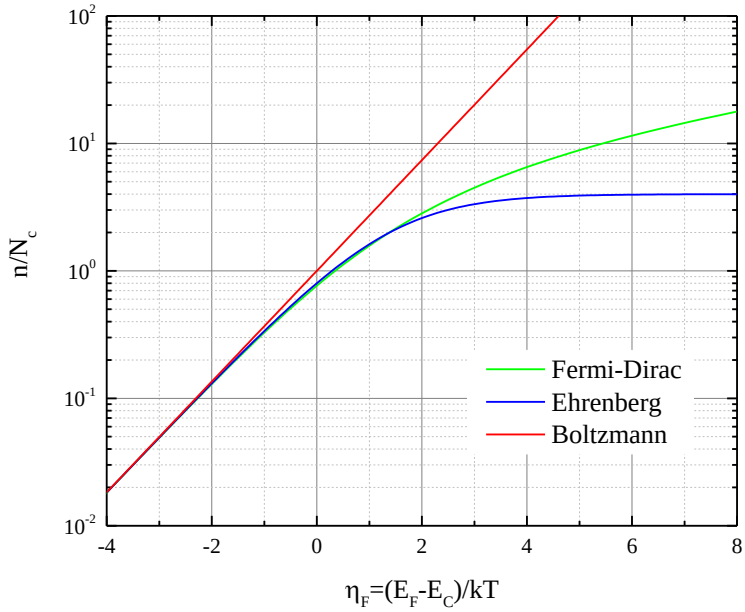

Figure 3.6: Approximation of the Fermi-Dirac statistics

The Boltzmann and the Ehrenberg approximations are compared with the Fermi-Dirac expression calculated using the Joyce-Dixon power expansion, which—in this scale—is almost indistinguishable from the exact values [26, 31].

In addition to the activation energy, the fitting of the experimental data using Eq. (3.10) or Eq. (3.16) can be used to estimate also N_D and N_A, but experimental errors can make this calculation very imprecise if the data are collected far from the saturation regime. It is also important to notice that when the dopant concentration is very high, even in case of activation energies as low as 1 meV, the saturation regime might not be visible even at relatively high temperatures. This is what happens, for example, in case of highly-doped AlGaN materials close to the Mott transition.

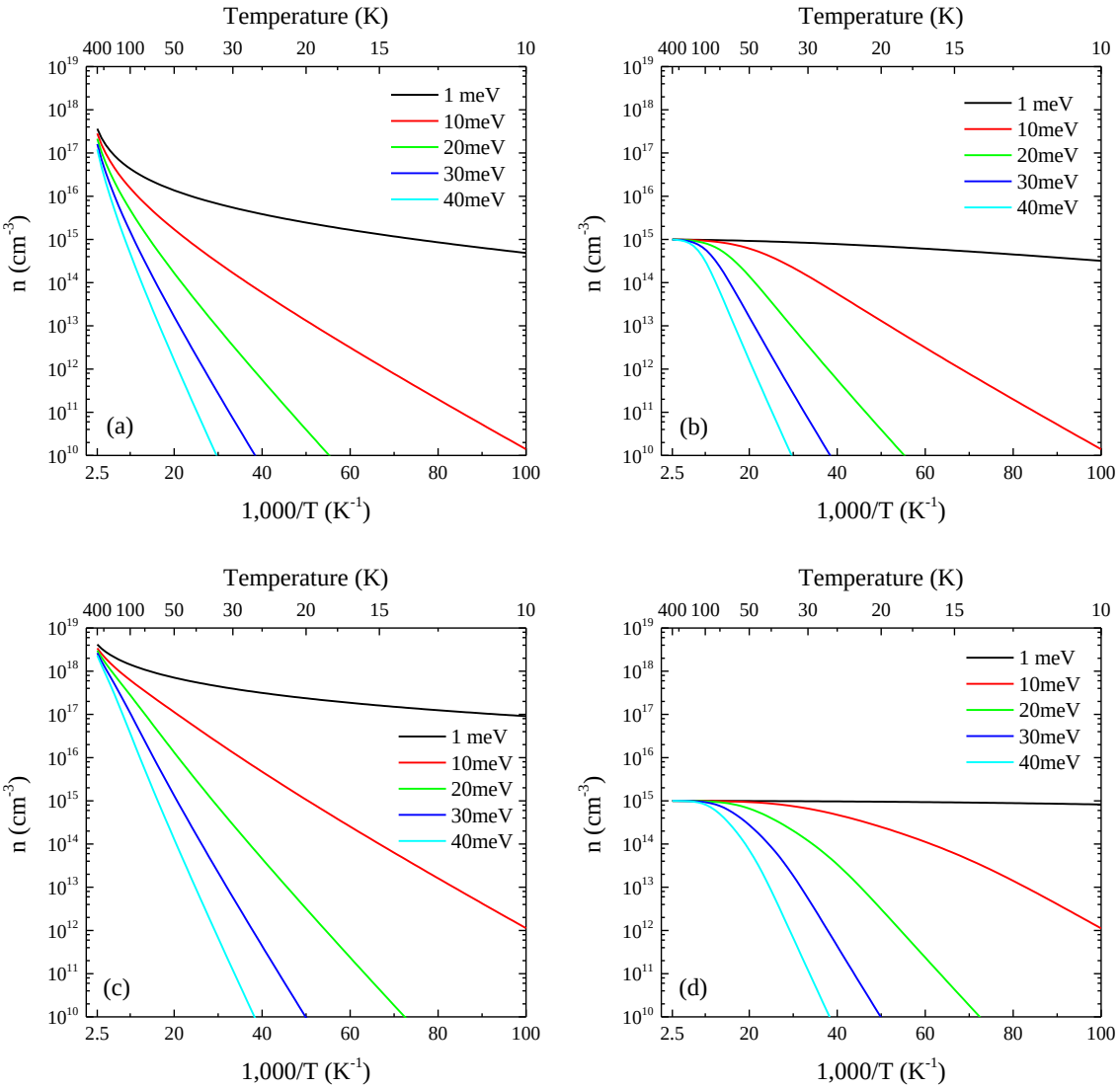

Figure 3.7: Calculation of the free-carrier concentration

The variation of the free-electron concentration with the temperature was calculated using Eq. (3.16) for $Al_{0.6}Ga_{0.4}N$ at different conditions: $(N_D - N_A)$ equal to 10^{19} cm^{-3} (a; c), or 10^{15} cm^{-3} (b; d); compensation degree (N_A/N_D) equal to 10% (a; b), or 90% (c; d). The coloured lines refer to different activation energies in the range 1–40 meV.

To illustrate this point, the results of calculations performed using Eq. (3.16) with an effective density of states of $(8.9 \times 10^{14}) \times T^{3/2}$ cm^{-3}, which corresponds to an $Al_{0.6}Ga_{0.4}N$ alloy [33], are reported in Figure 3.7. Although in the low temperature range the slope of the carrier density depends only on the activation energy, the net doping $(N_D - N_A)$ and the compensation degree (N_A/N_D) greatly influence the high-temperature range. If the doping is high enough, as in Figure 3.7 (a) and (c), the saturation regime of AlGaN materials cannot be reached even at temperatures as high as 400 K, which are the limit of our experimental apparatus.

3.2.3 Hall-effect measurements

In order to investigate the free-carrier concentrations at different temperatures, a Lake Shore Model 8404 Hall Effect Measurement System was used in this study. This piece of equipment consists in a high-power magnet capable of reaching a maximum magnetic field of 1.7 T, a programmable unit that controls the measurements and collects the data, and a cryostat able to set the temperature in the range 10–400 K with a precision of ±1 K. Before the commissioning of this equipment, preliminary measurements were performed with an old Keithley 920 series Hall Test Equipment, which has a fixed magnetic field of 0.32 T and can only be used for experiments at room or liquid-nitrogen temperatures.

According to the Hall effect, when a conductor of thickness t carrying a current I is subject to a magnetic field B applied perpendicularly to the direction of the current, a transverse[8] voltage V_H develops in a direction perpendicular to both the current and the magnetic field. The output of a Hall-effect measurement then consists in the evaluation of the Hall coefficient defined as

$$R_H = \frac{V_H t}{I\,B}, \tag{3.17}$$

which can then be used to extract information about the free-carrier concentration and the mobility of the sample, provided some assumptions about the transport are met and using specific models based on these assumptions.

If only one type of carrier is present, the Hall coefficient is

$$R_H = -\frac{r}{ne} \tag{3.18}$$

for *n*-type materials, and

$$R_H = \frac{r}{pe} \tag{3.19}$$

[8] In case of a sample with van der Pauw geometry, V_H is the voltage across one diagonal when the current is flowing through the other one.

for *p*-type materials [31]. The factor r present in these equations depends on the type of scattering mechanisms to which the carriers are subject: it is usually close to unity, but its actual value can be very difficult to estimate and, for this reason, the deviation from unity is often neglected. In this case, the carrier concentration obtained with (3.18) and (3.19) should more precisely be called the *Hall* carrier-concentration to highlight the fact that it might differ by a factor r to the actual value.

An independent measurement of the conductivity (σ) of the material can be used to extract the mobility of the carrier (μ_e or μ_h for electrons or holes, respectively) from the Hall coefficient:

$$\mu_{e,h} = \frac{\sigma |R_H|}{r}. \tag{3.20}$$

The situation in which the conductivity is actually dominated by the transport of just one type of carrier is so common that often the software of the Hall systems automatically performs the calculations of carrier concentration and mobility assuming that Eqs. (3.18), (3.19) and (3.20) are valid. As will be detailed in Section 3.6, this is not the only possible situation: if the carriers that contribute to the conduction belong to two independent channels with different types of transport mechanisms and mobilities, the resulting Hall coefficient will be [34]

$$R_H = \frac{r}{e}\frac{n_1\mu_1^2 + n_2\mu_2^2}{(n_1\mu_1 + n_2\mu_2)^2} = \frac{\sigma_1^2 R_1 + \sigma_2^2 R_2}{(\sigma_1 + \sigma_2)^2} \tag{3.21}$$

in which the subscript 1 or 2 indicates which of the two independent channels the parameters are referring to. As shown in Figure 3.8, if the two channels have individual Hall coefficients R_1 and R_2 very different from each other, the combined Hall coefficient of Eq. (3.21) will follow the lowest of them or, in other words, the channel with the highest carrier concentration. If the activation energies are different, it is possible that the highest populated channel will be overtaken by the other one as the temperature changes, so that one channel will be dominant at low temperatures and one at high temperatures. If the conductivity in the two channels is similar, the transition will be quite soft; however, if there is a significant difference between the two mobilities, the switchover is delayed and, in the intermediate temperature range, the value of R_H will remain close to the one of the two channels that has lower carrier

concentration but still higher mobility. The effect of this behaviour is the appearance of a local maximum in the Hall coefficient as the one shown in the example of Figure 3.8.

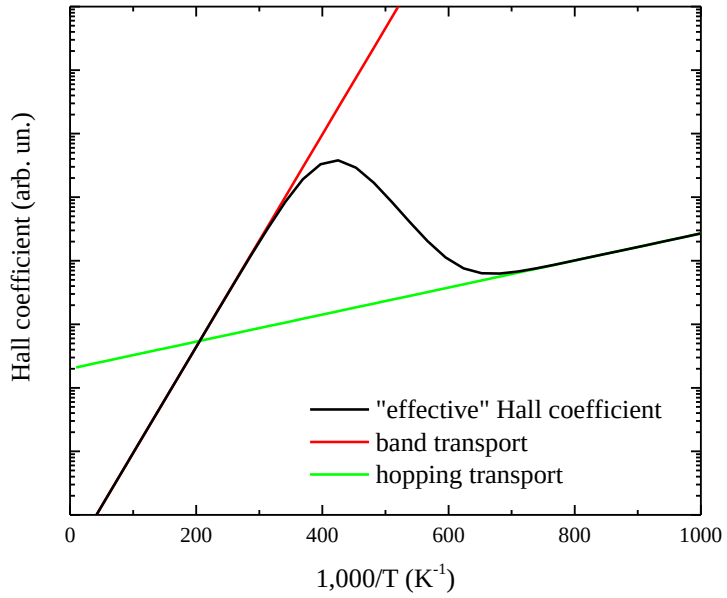

Figure 3.8: Illustration of the two-channel model

The graph shows the qualitative behaviour of an arbitrary material with two conductivity channels due to band and hopping transport, with the latter having much smaller activation energy and mobility. The red and green lines represent their respective Hall coefficients in the ideal case of activation energies and mobilities of both channels independent of the temperature; the black line represents the combined Hall coefficient as obtained from Eq. (3.21).

3.2.4 Hopping transport in highly-doped materials

With respect to the type of charge transport, the conductivity of any doped semiconductor material can be roughly divided in four temperature ranges, as schematically shown in Figure 3.9. In the highest-temperatures range A (intrinsic region) the transport is dominated by thermally-generated electron-hole pairs, and the doping level is uninfluential. Because of the large bandgap of the III-nitride materials typical in optoelectronic devices, this type of conduction is usually not observable, as the temperatures would be so high to completely destroy the material. In the range B (saturation region) the conductivity stays almost constant to a value that depends on the dopant concentration; a slight increase at the lower end of the temperature range is due to reduced phonon scattering. As the temperature decreases to the range C (freeze-out region), which is the type of conduction usually explored in III-nitride materials, more

and more electrons are trapped in the localized dopant states and the conductivity keeps decreasing. If the temperature is further decreased, eventually, a sharp reduction of the temperature dependence of the conductivity appears as we enter the range D, where the conduction is dominated by hopping among localized states. Almost all materials have a certain amount of conduction due to hopping, but that is usually visible only at very low temperatures when all other transport mechanisms are suppressed. However, in some materials, either because of the high dopant or defect concentrations, or because of the presence of potential fluctuations due to alloy disorder, this type of transport can be significant even at room-temperature or above. One of the results of this thesis is the demonstration that Al-rich AlGaN alloys are such type of material.

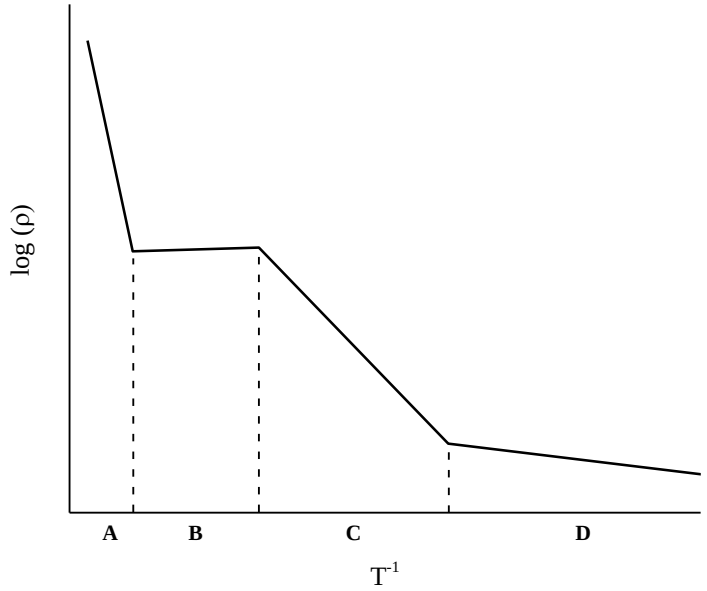

Figure 3.9: Schematic temperature dependence of the conductivity
The conductivity of a doped semiconductor can be divided in four regions: (A) intrinsic conduction, (B) saturation, (C) freeze-out region, and (D) hopping conduction.

As it was shown in Figure 3.5, in lightly doped semiconductors all the dopant states are roughly at the same energy level (i.e. E_D or E_A). However, when the doping concentration becomes higher, the Coulomb interactions make the energy levels to split so that an impurity band such as those illustrated in Figure 3.10 starts to appear. These are not real bands with delocalized carrier wavefuntions such as the usual valence or conduction band; instead they have to be considered as statistical energy distributions of all the localized states present in that particular material. Because of the energy

differences among states, any single hopping act from one state to another requires that a phonon is either absorbed or released, and this explains the thermally-activated behaviour that, although much less evident than in the freeze-out region, is still present in hopping transport. The exact calculation of the activation energy is quite complicated (Cf. [34] for a full review on this topic); however, its general trend is strongly dependent on the dopant concentration: as this increases the activation energy initially also increases because of stronger Coulomb interactions, but if the dopant concentration increases even further, suddenly the activation energy significantly drops because of higher overlap among the wavefunctions. If the dopant concentration reaches an even higher critical value, the superposition of the states becomes so large that delocalized states start to appear at the centre of the impurity band and, if the Fermi level lies within these states, the charge transport in the impurity band becomes purely diffusive with no thermally-activated behaviour as in metals. This is the so called Mott transition[9] of the doped semiconductors.

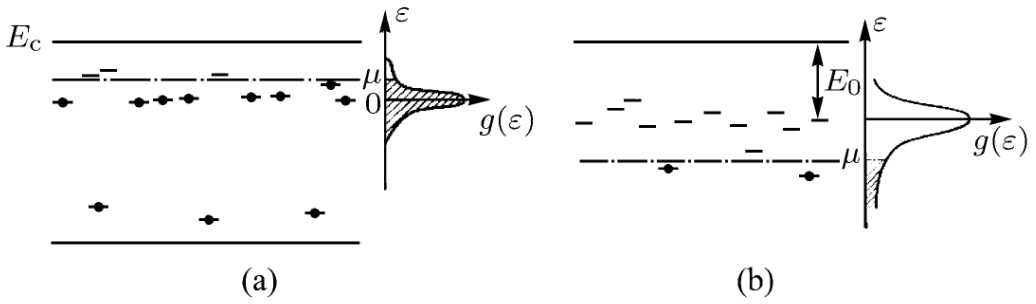

Figure 3.10: Impurity bands

Schematic illustration of donor impurity bands in case of: (a) low degree of compensation, and (b) high degree of compensation. The symbol μ indicates the position of the Fermi level. Taken from [34].

The first type of hopping conduction that starts to appear at relatively higher temperatures is the so-called nearest-neighbour hopping (NNH), which takes place among states that are spatially closer to each other. This means that only the states whose energy lies near the peak of the impurity band can contribute significantly to this mechanism. In the special case in which the degree of compensation is either very weak

[9] Because this transition is not only the result of electron-electron interactions but it is also influenced by the disordered distribution of the impurities, the name of Mott-Anderson transition is also, and more correctly, used.

or very strong, as shown in Figure 3.10 (a) and (b) respectively, the activation energy is expected to stay almost constant for a large range of temperatures. This happens because the states near the peak are either fully occupied or fully empty and hence not yet suitable to sustain any conduction. Only a transition of some electrons from the energy peak to the Fermi level, in case of weak compensation, or the opposite transition from the Fermi level to the peak, in case of strong compensation, can make it possible to have both empty and occupied states near the peak. In either case the activation energy experimentally measured can be physically interpreted as the energy difference $|E_F - E_{peak}|$.

At much lower temperatures, the NNH has to transition into some other type of hopping mechanisms due to the fact that the resistivity is forced to diverge as the temperature approaches 0 K, because localized states cannot produce any conductivity if no phonons are available to assist the hopping. At 0 K only metals can have some finite—although not necessarily low—resistivity. Semiconductors, on the other hand, at low temperatures behave as insulators unless the dopant concentration is so high to induce the Mott transition. However, because our equipment limited the low-temperature investigations to a minimum of 10 K, no long-range hopping could be observed in our material.

Although hopping conduction has been demonstrated in many different materials (Cf. e.g. [35]), most of the experimental work has been done especially on Si and Ge, which are well-known semiconductor materials, with high crystal quality and for which it is possible to precisely control both the doping level and the compensation degree [36]. On the other hand, the AlGaN alloys investigated in this thesis are much more complicated materials. In addition to the random distribution of dopant impurities, it is particularly the presence of potential fluctuations due to the alloy disorder that add another level of complexity to the system. These fluctuations cause the sharp band-edges of the conduction and valence band to be replaced by tails of the density of states that extend within the forbidden gap. These states induced by the disorder are localized and cannot support diffusion-like transport anymore: only if the doping is high enough to raise the Fermi level above the so-called mobility edge—i.e. the level that separates localized from delocalized states—the conduction in the band can be restored (Cf. Figure 3.11). This type of behaviour has indeed been observed in AlGaN materials

[37], in which a threshold doping concentration exists that needs to be overcome in order to achieve any conductivity.

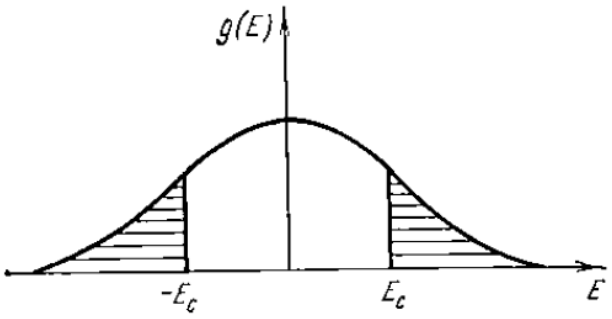

Figure 3.11: Density of states in the Anderson model
The region of localized states is shaded. Energy E_C and $-E_C$, which separate the regions of localized and delocalized states, represent the mobility edges. Taken from [34].

If the disorder is further increased, the mobility edges shift towards the centre of the band and, eventually, all the states become localized and no diffusion-like conduction is possible anymore in the conduction or valence bands. This is the so-called Anderson transition.

Although the carriers occupying localized states cannot contribute to the usual diffusion transport, they can still take part in hopping conduction. In materials such as highly doped AlGaN alloys, in which localized states are present because of both alloy and impurity-band disorder, it is very difficult to understand which of the two types of hopping would be the dominant at low temperatures; in some conditions the two region can even overlap. As a general indication, a variation of the doping level can affect both types of hopping conductions because of the consequent shifting of the Fermi level position; however, in case of the hopping conduction within the impurity band, this would also change the shape and the structure of the band, with exponential reduction of the resistivity with increase of the doping concentration [38].

3.3 Literature review

3.3.1 Recent results in *n*-type doping of AlGaN

Early studies regarding *n*-AlGaN were limited to aluminium concentrations of only few percent with the purpose of using these materials as cladding layers of electrically-

injected blue laser-diodes, and because of the large differences in bandgap and refractive index between GaN and AlN, they were still able to provide sufficient optical confinement and were also relatively easy to grow and dope [39]. However, AlGaN materials with even fairly moderate (20–30%) aluminium concentrations were historically considered as insulating [40-42].

More recently, with the research moving towards shorter wavelength emitters, increasingly larger bandgap cladding layers have become necessary. The first attempts to intentionally dope AlGaN materials with an AlN concentration higher that 60% were undertaken, roughly in the same period, by Jiang and co-workers [37, 43, 44], and by Taniyasu and co-workers [45, 46]; in particular these latter two works led to the demonstration of the first working AlN-based light-emitting diode [47].

The main conclusions that Jiang and co-workers were able to draw from their experience, is that the presence of silicon atoms in the material initially just reduces the localization effects within the alloy, and only when the localization is sufficiently overcome (which was evaluated to happen at a silicon concentration of about 1×10^{18} cm^{-3}), does *n*-conductivity occur. They also conjectured that residual oxygen impurities could play an important role in the difficulties of achieving a reasonable level of doping, not only because of a DX transition, but also because, together with a high concentration of dislocations, oxygen can enhance the formation of cation vacancies that act as compensation centres [43]. For this reason they stressed the importance of achieving a good material quality as the key element that allowed them to obtain *n*-type conductivity in the whole composition range of the AlGaN alloy, up to pure AlN. They also reported some flattening in the dependence of the resistivity with temperature for the optimized materials with higher dopant concentrations, and they interpreted this as compatible with an onset of metallic behaviour due to the Mott transition. As a consequence of that, they concluded that this condition is favourable for a good conductivity, and they suggested increasing the dopant concentration as much as possible in order to push the material closer to the transition.

In contrast, Taniyasu and co-workers reported clear signs of self-compensation effects in their material and they thought this was the first cause of the difficulties in achieving a good doping level. Even though SIMS measurements revealed that the silicon incorporation was linear in the whole range of silane flow-rates examined, the room-

temperature free-carrier density was at least one order of magnitude lower, and when the concentrations of incorporated atoms were 6×10^{19} cm^{-3} for $Al_{0.49}Ga_{0.51}N$, or 3×10^{19} cm^{-3} for pure AlN, the materials reached their maximum values of free carrier concentrations (4.5×10^{18} cm^{-3} and 9.5×10^{16} cm^{-3}, for $Al_{0.49}Ga_{0.51}N$ and AlN respectively). Any further attempt to increase the silane flow rate, led to a fully compensated and insulating material.

Both groups reported some estimation of the activation energies as a function of Al concentration, calculated from the Hall-effect measurements at different temperatures, which are shown in Figure 3.12 and compared with the results from other works. These data were of fundamental importance in order to try to settle a controversy that is still very much on-going now, and that regards the origin of the increase of the activation energy for high-aluminium-content AlGaN alloys. One proposed reason of this behaviour only invokes the increase of the electron effective masses and the decrease of the dielectric constant when shifting the AlGaN composition towards AlN. In a simple application of the hydrogenic model of the doping impurities, this would lead to a linear (or almost linear) increase of the activation energies from a few tens up to about 75–95 meV [48]. The other possible explanation involves a DX transition of the silicon dopant and a sudden, non-linear, increase of the binding energy. This latter hypothesis was firstly proposed by Bogusławski *et al.* [27] and by Park *et al.* [28] in 1997, and claimed to be experimentally proved by Zeisel *et al.* [29] making use of persistent photoconductivity measurements in 2000.

As apparent in Figure 3.12, all the datasets show some form of higher-than-linear behaviour, but this effect appears to be somewhat limited in the results from Jiang [43] and Taniyasu groups [45]. For this reason, both teams concluded that their data supported the fact that silicon most likely remained a shallow donor in the whole alloy range, up to pure AlN. In particular Taniyasu proposed that the observed moderate superlinear increase of the activation energy could be explained as due to the coexistence of shallow silicon donors and other deeper donors, possibly related to oxygen DX-levels.

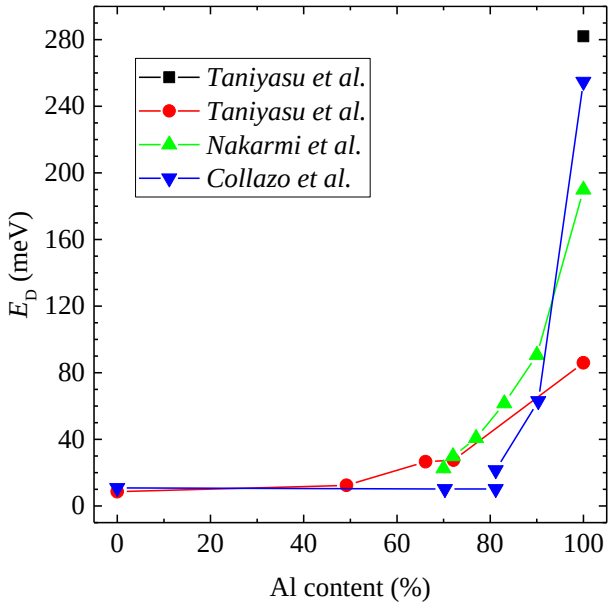

Figure 3.12: AlGaN activation energy

Comparison of the activation energies of silicon doped AlGaN materials experimentally obtained by a few groups. While the data from Nakarmi *et al.* [43] and from Taniyasu *et al.* [45] show only a slightly higher than linear behaviour, the data from Collazo *et al.* [48], present a very sharp increase of the activation energy for AlN contents higher than 80%. A second work from Taniyasu *et al.* [47] includes data for pure AlN only.

These conclusions were most likely influenced by Van de Walle and his co-workers, who, following the same approach already used for GaN, theoretically studied the doping of AlN and AlGaN. According to their results [49-51], the only type of defect that can influence the *n*-type doping is the aluminium vacancy, which is a compensating acceptor, and whose formation energy decreases with the increase of the Fermi level towards the conduction band. Moreover, in his 1998 paper [52], Van de Walle reported that according to his first-principles calculations, only oxygen, but not silicon, can undergo a DX transition in the whole range of AlGaN compositions. The reason for this claim is that silicon, contrary to oxygen, which is a nitrogen substitution impurity, is almost exclusively present as a cation substitution (either as Si_{Ga} or Si_{Al}) and hence, because of its position in the lattice and of the fact that in the DX state it would be negatively charged, the coulombic repulsion from its third-nearest-neighbour anion is able to suppress the DX formation. As a result they proposed that the difficulties in doping high-aluminium-content AlGaN could only be explained by the presence of a residual background of oxygen impurities that after the DX-transition become deep

acceptors and, together with aluminium vacancies, heavily compensate the shallow silicon donors.

The controversy is still not conclusively settled, partially because Hall-effect measurements of the activation energy are quite scattered due to the fact that they are affected by screening effects and vary considerably with the free carrier concentration [53-55]. At the moment the most recent experimental works available in this area of research are those from Kakanakova-Georgieva's group [56, 57], who tested AlGaN materials having aluminium content higher than 63%, with a silicon concentration of 2×10^{18} cm^{-3}, specifically chosen because it is a high enough value to allow good conductivity, but sufficiently low to avoid any degradation of the material quality. The concentrations of residual oxygen and carbon impurities measured with SIMS were at the detection limit of the equipment, i.e. 2×10^{17} cm^{-3}, one order of magnitude lower than silicon concentration, which excluded that they were able to cause any major compensation effects. Frequency dependent C–V measurements performed on this material for an aluminium composition higher that 79% seemed to prove that the silicon DX transition does indeed occur. Moreover electron paramagnetic resonance measurements showed that, starting from an aluminium concentration of 84%, two DX configurations of the Si donor are detectable: one with ionization energy remaining close to the shallow level, and the other one with energy increasing linearly and drastically with the Al content.

As already pointed out by Jiang and co-workers, the quality of the material has a profound impact on the outcomes of the doping, and this is true not only with respect to the concentrations of residual impurities, but also in term of the concentration of threading dislocations. From this perspective, it is particularly interesting the work of Collazo *et al.* [48] in which AlGaN thin films in the whole range from GaN to AlN were grown both on standard sapphire substrates and free-standing AlN single-crystal substrates. Up to an AlN concentration of about 80%, the materials grown on the two substrates showed comparable results, both in term of carrier concentrations and mobilities. However, for higher aluminium concentrations, the resistivity of the materials grown on sapphire became significantly higher: up to 5 orders of magnitude for 90% AlN concentration, and with no conduction at all for pure AlN. Hall-effect measurements indicated that this increase of resistivity is mostly due to the reduction of

free carrier concentration rather than due to the decrease on mobility, which is nonetheless present.

It should be noted that for UV-LEDs the optimization of the *n*-doping is quite critical. For nearly all III-nitride optoelectronic devices the *n*-contact is placed to the side of the device requiring lateral conduction of electrons. For visible LEDs, GaN is fairly easily doped *n*-type and typical mobilities are around 200–300 $cm^2\ V^{-1}\ s^{-1}$ [20]; in addition to that, the resistance from the active region to the lateral *n*-contact can also be improved by simply making the *n*-GaN layer thicker. However, due to alloy scattering, typical *n*-type mobilities for AlGaN are about one order of magnitude lower; furthermore there is a degradation in AlGaN quality with thickness that is still poorly controlled [58]. Thus to minimize the device resistance the *n*-AlGaN layer must be carefully optimised.

To obtain such low-resistivity *n*-type materials two conflicting requirements need to be achieved: a sufficiently high dopant concentration in order to push the material close to the metallic transition, and to ensure that the dopant concentration is insufficient to cause the onset of any major self-compensation effects. This trade-off is well summarized in the work of Mehnke *et al.* [59] where they report on the growth by MOVPE of *n*-AlGaN materials with AlN concentrations higher than 80% with different doping conditions obtained by varying the silane flow rates into the reactor. Their results clearly show the existence of an optimum doping concentration expressed in term of the ratio between the partial pressure of silane gas over the sum of those of the metalorganic precursors (Si/III ratio). Moreover, the trade-off between the two conflicting requirements was shown to be increasingly difficult for higher aluminium compositions as the window of suitable doping conditions with no under- or over-doping became considerably narrower, with a shift of the optimum condition towards reduced doping levels.

3.3.2 Recent results in *p*-type doping of AlGaN

Compared to *n*-type, the *p*-doping of AlGaN materials has received much less attention in the last few years, and it is still considered quite challenging, especially in the high-aluminium-content range of the alloy. After the fundamental breakthroughs of Amano, Akasaki and Nakamura [60, 61] that were able to solve the long-standing issue of the hydrogen passivation of magnesium, this element has become the acceptor impurity of choice for all the III-nitride materials including AlGaN alloys. However, obtaining

satisfactory *p*-type epitaxial layers has proven to be so difficult that, at device level, some mitigation strategies had to be developed to in order to compensate for their low conductivity or poor contacts. For example in UV LEDs it has become standard solution to grow a thin layer of about 10–50 nm of *p*-GaN on top of the *p*-AlGaN cladding layer [62-64]; notwithstanding its strong absorption at the emission wavelengths, which considerably reduces the light extraction efficiency, it is often the only way to achieve a reasonably good contact and ensure some hole injection into the device. More recently Rajan and co-workers at the Ohio State University have developed devices that make use of polarization-engineered tunnel junctions in order to reduce both absorption and electrical losses [65, 66].

Magnesium is practically the only dopant used and, according to first-principles calculations [51], it does not tend to form any AX deep level. Consequently any form of self-compensation would most likely be caused by the creation of nitrogen vacancies, whose formation energy is considerably lower in AlN than in GaN. Beryllium has also been considered as a possible acceptor because of its comparable (possibly lower) binding energy, but the calculations suggest that it may also be incorporated on interstitial sites, where it acts as a donor [51]. Very few experimental attempts were undertaken and, at present, it is hard to conclude whether or not it may be a suitable alternative.

As for the *n*-type material, the early reports of *p*-doping in AlGaN were aimed to obtain a suitable material for cladding layers and optical confinement in blue laser-diodes. The attempted aluminium concentrations were limited to the range 8–15%, but a marked reduction of the free carrier concentrations was already noticeable, and was attributed to the increased activation energies of the dopants [67-69]. With the work of Li *et al.* [70], the alloy range was extended up to $Al_{0.3}Ga_{0.7}N$ and both Hall-effect and photo-luminescence (PL) measurements were performed from this alloy composition down to pure GaN. The activation energy as a function of the aluminium concentration was calculated by the variation of free-carrier concentrations and the PL intensity of the band-acceptor transition at different temperatures, and both methods gave the same results. In a later work from the same group, Nam *et al.* [71] for the first time reported magnesium doping of pure AlN. The material did not show any sign of conductivity, neither before nor after thermal annealing, but making use of the technique elaborated in [70], they were still able to optically estimate the Mg activation energy to be 510 meV,

a value that fits well with calculations based on hydrogenic model (Cf. [72] and reference therein). After careful optimization of the growth parameters, Taniyasu *et al.* [47] were eventually able to produce a conductive *p*-AlN material, with a free-hole concentration at room temperature in the order of 10^{10} cm^{-3} and an activation energy of 630 meV. Used as the *p*-cladding-layer in the first AlN-based LED, this material was able to effectively inject holes into the device as proved by a clear electro-luminescence peak at 210 nm.

Other studies of note include: Jeon *et al.* [73] who reported evidence of a marked self-compensation for a magnesium concentration higher than 3.5×10^{19} cm^{-3} for 30% AlN content and, more recently, Chakraborty *et al.* [74] and Kinoshita *et al.* [75] who focused on further optimizing the growth conditions, and the effect of Mg doping on $Al_{0.7}Ga_{0.3}N$ material. These two papers report rather different results. Chakraborty *et al.* have samples that are quite resistive at room temperature (about 10^4 Ω cm) and showed a strong reduction in resistivity with increasing temperature, consistent with a high acceptor binding energy as theoretically expected. In contrast Kinoshita *et al.* claim that under optimal conditions a room temperature resistivity of 50 Ω cm with a very low activation energy can be achieved. This they attribute to a hopping conduction in the material, which might suggest that scope exists to improve doping through very careful growth optimization.

3.4 Room-temperature measurements of polar AlGaN

3.4.1 Optimization of the *n*-type material

$Al_{0.5}Ga_{0.5}N$ alloy

Our initial experimental work focused on the relatively low AlN-content *n*-$Al_{0.5}Ga_{0.5}N$ material. Two sets of five samples each were grown at different Si/III ratio conditions in the range $1.4–3.6 \times 10^{-4}$. The first set was grown on AlN templates obtained with our standard approach [21]; in the second group—grown in parallel with the first one—the commercial templates described in Section 3.1.3 were used instead. The XRD analysis of the AlN templates showed ω-scan FWHMs of 311–356 arcsec for the (0002) reflection and 478–677 arcsec for the $(10\bar{1}1)$ reflection. The same measurements on the AlN material grown on the commercial templates gave FWHMs of 94–145 arcsec and 762–829 arcsec for the (0002) and $(10\bar{1}1)$ reflections, respectively.

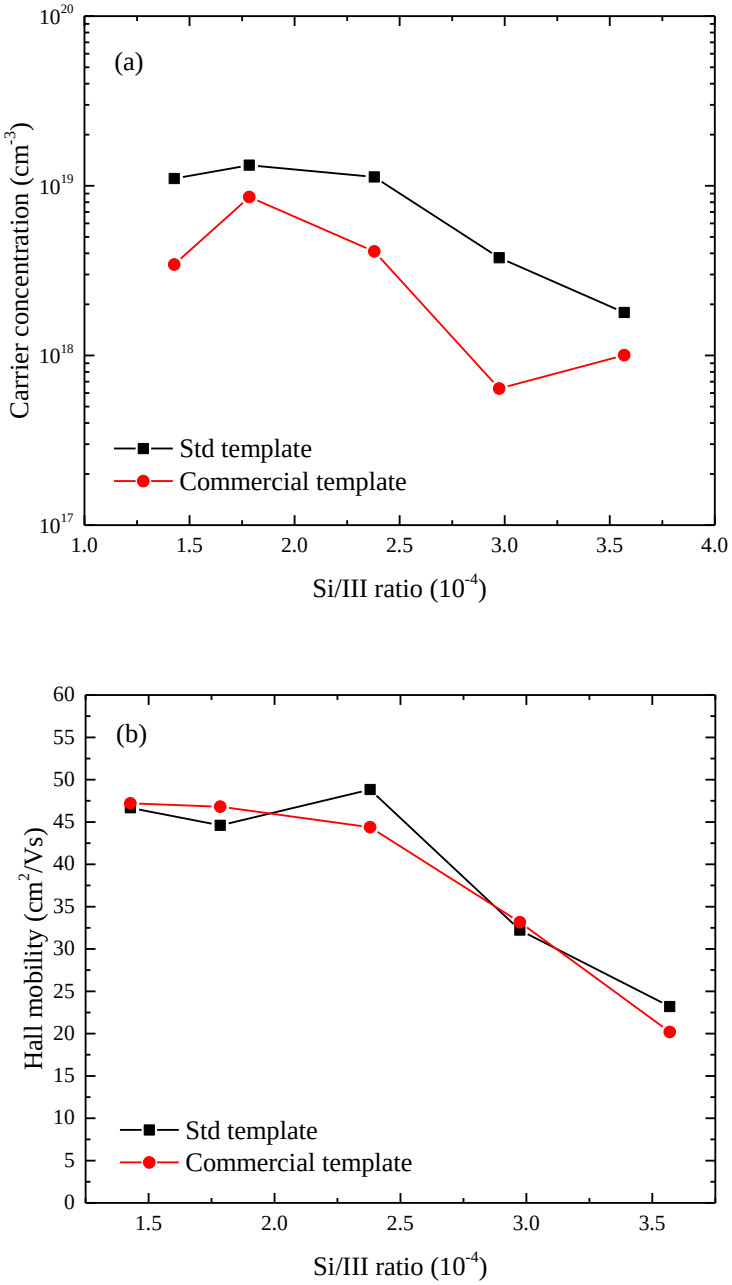

Figure 3.13: AlGaN:Si series with 50% AlN content

Results of the room-temperature Hall-effect measurements: (a) carrier concentration, and (b) mobility; the two series were grown on different types of template. All the samples showed *n*-type conductivity and linear IV characteristics.

The growth conditions were set to a V/III ratio of 800, growth temperature of 1110 °C, and pressure of 50 mbar; the nominal thickness of the doped film was 1 µm. The material was first cut in squares of about 7 × 7 mm^2 and then a contact metal stack (Ti/Al/Ti/Au with 20/170/5/100 nm of thickness) was evaporated on the corners to form van der Pauw samples. Rapid thermal annealing at 600 °C for 1 minute in N_2 environment was performed to ensure ohmic contacts. Room-temperature Hall-effect

measurements were performed with a magnetic field of 0.36 T on a Keithley 920 series Hall Test Equipment; the results are reported in Figure 3.13.

In both sets of samples the carrier concentration showed a clear maximum at a Si/III ratio of 1.8×10^{-4}, with carrier concentrations of 1.3×10^{19} cm^{-3} and 8.6×10^{18} cm^{-3} for the material grown on the standard and commercial templates, respectively. In the low-doping range—including the doping levels that lead to carrier concentrations close to the maximum—the mobility of both series remained quite stable at about 45 cm^2 V^{-1} s^{-1}, before eventually starting to decrease at Si/III ratios higher than 2.4×10^{-4}. Although the material was sufficiently conductive in the whole range of doping levels here explored, our standard conditions for the *n*-type cladding layers—corresponding roughly to the centre of the range—proved to be slightly in the overdoped region.

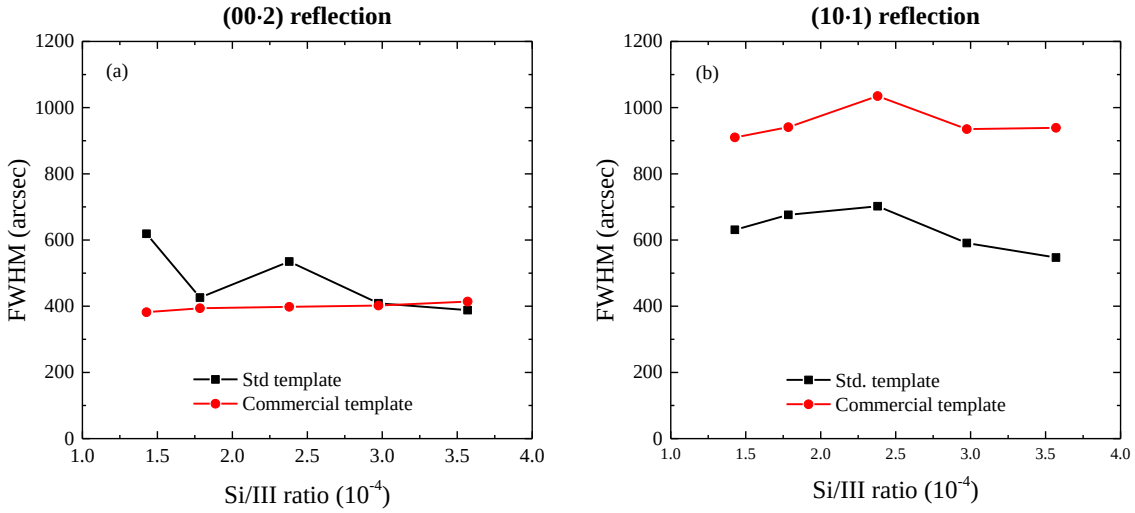

Figure 3.14: Material quality of the two *n*-$Al_{0.5}Ga_{0.5}N$ series

FWHM of the ω-scan of (a) the (0002) reflection, and (b) of the $(10\bar{1}1)$ reflection. The black and red datasets refer to the material grown on standard and commercial templates, respectively.

The fact that the samples grown on standard and commercial templates differ significantly in their carrier concentration, but not in their mobility, suggests that the increase in the edge-dislocation density apparent in Figure 3.14 (b), although insufficient to noticeably increase the scattering of the free-carriers—which is probably dominated by alloy scattering—is nonetheless able to largely enhance the incorporation of compensating defects, possibly charged cation vacancies complexes bounded with oxygen (Cf. [43] and references therein). This is consistent with other studies present in

literature, which report a dramatic increase of resistivity correlated with the degradation of the crystal quality of the material [48, 76]. However, in contrast with the latter of the two cited works [76], in which the increased incorporation of compensating detects was detected in the regions surrounding dislocations with a screw components (by cathodoluminescence and electron channelling contrast imaging), our results seem to indicate that pure edge dislocations also have an impact on the doping of AlGaN materials. In fact, as can be seen in Figure 3.14, while our samples grown on commercial templates have higher FWHMs in all the $(10\bar{1}0)$ reflections, they also have very similar—or even lower—FWHMs in the (0002) reflections, if compared with those grown on standard templates.

$Al_{0.6}Ga_{0.4}N$ alloy

We then extended our investigations to the optimization of *n*-$Al_{0.6}Ga_{0.4}N$ material, which was closer to the composition we planned to use for the cladding layers of the InAlN-based near-UV LED. The growth conditions were the same used for the material with 50% AlN-content, with the exception of the V/III ratio, which was lowered to 585. The explored range of Si/III ratios was extended to $1.1–5.6 \times 10^{-4}$.

Unfortunately, the metallization scheme that was previously developed for the samples with lower Al-content proved to be unsuitable to ensure reliable ohmic contacts. As a consequence of that, the Hall-effect measurements showed often inconsistent results, especially on the samples grown on the commercial templates, which, for this reason, are not shown here. The carrier concentration and the mobility of the samples grown on standard templates that notwithstanding the poor contacts could still be successfully tested are reported in Figure 3.15. Although the measurements are affected by large experimental errors, the data clearly show that, similarly as for the *n*-$Al_{0.5}Ga_{0.5}N$ material, there is evidence of overdoping in the higher Si/III ratio range, which include the condition previously used for the growth of the devices.

With the purpose of investigating the effects of lower doping levels, a second series of *n*-$Al_{0.6}Ga_{0.4}N$ materials was grown on standard templates with Si/III ratios in the range $0.28–3.3 \times 10^{-4}$. The growth conditions were the same as in the first attempt, with the exception of the growth temperature which was slightly decreased to 1100 °C. The material was cut in squares of about 1×1 cm^2 and a stack of Ti/Al/Ti/Au (20/170/50/100 nm) was evaporated on the corners to form van der Pauw samples. It

has to be noticed that, although the metal sequence was the same as in the previous attempts, the thickness of the second Ti layer was increased from 5 nm to 50 nm. This thicker layer was able to provide a better separation between the Al and the Au layers and was able to prevent the intermixing of these two metals—also known as the highly resistive 'purple plague' [77]—during the post-evaporation high-temperature treatment. The contacts could then be annealed at 800 °C (i.e. 100 °C higher than in the previous attempt) for 1 minute in N_2 environment and proved to be ohmic even at temperatures as low as 10 K. Further details on the contact formation will be discussed in Chapter 4.

In addition to the improved metallization scheme, the use of the new Lake Shore Hall Effect Measurement System, which has a much higher sensitivity and magnetic field allowed us to obtain much more precise and reliable measurements in the whole range of doping. The results of the room-temperature measurements at a magnetic field of 1.7 T are also reported in Figure 3.15; temperature-dependent measurements will be discussed in Section 3.6. The samples of the previous series were also remeasured with the new equipment, confirming the previous data and also allowing the extraction of carrier concentration and mobility from a few more samples. However, the 'geometry inconsistency' errors often shown during the measurements proved that, due to the non-optimized metallization scheme, the contacts on the four corners of the samples were often too different from each other, making them very hard to measure even with the new equipment.

Similarly as in the *n*-$Al_{0.5}Ga_{0.5}N$ series, the carrier concentration first increased and then decreased with higher doping levels and showed a maximum of 4.2×10^{18} cm^{-3} at a Si/III ratio of 1.1×10^{-4}. As expected from a slightly reduced alloy scattering, this material showed a higher maximum mobility of 62 cm^2 V^{-1} s^{-1} for the least doped sample. However, in contrast with the *n*-$Al_{0.5}Ga_{0.5}N$ materials, the *n*-$Al_{0.6}Ga_{0.4}N$ samples showed an earlier onset of the decrease of the mobility, which happened while the carrier concentration was still increasing.

Although the two 60% series were grown in very similar conditions, a decrease of both the carrier concentration and the mobility of the more recently grown set of samples is apparent. One possible source of this difference could be related to the higher experimental errors that—as already mentioned—are due to the non-optimized metallization scheme of the first attempt. However, the fact that one series is showing

consistently lower values of both the carrier concentration and the mobility suggests that the higher density of dislocation present in the second series might be the most important factor in explaining these differences. In fact, as shown in Figure 3.16, probably because of an unintentional use of templates with lower quality, the material of the second series shows consistently higher FWHM of the XRD ω-scans, particularly in the $(10\bar{1}1)$ reflection.

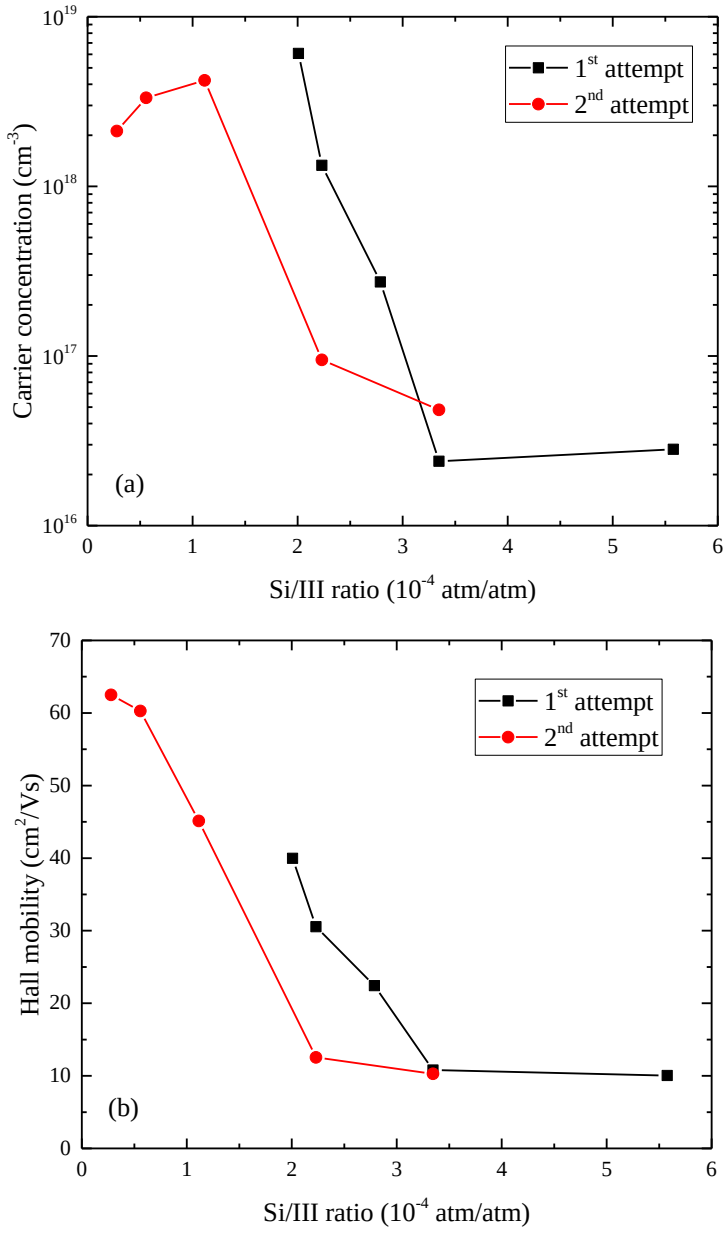

Figure 3.15: AlGaN:Si series with 60% AlN content

Results of the room-temperature Hall-effect measurements: (a) carrier concentration, and (b) mobility; both series were grown on standard templates. All the samples showed *n*-type conductivity and linear IV characteristics. It is worth noting that the carrier concentrations in the low Si/III ratio are in good agreement with the theoretical values shown for $Al_{0.6}Ga_{0.4}N$ at 300 K in Figure 3.7 (c).

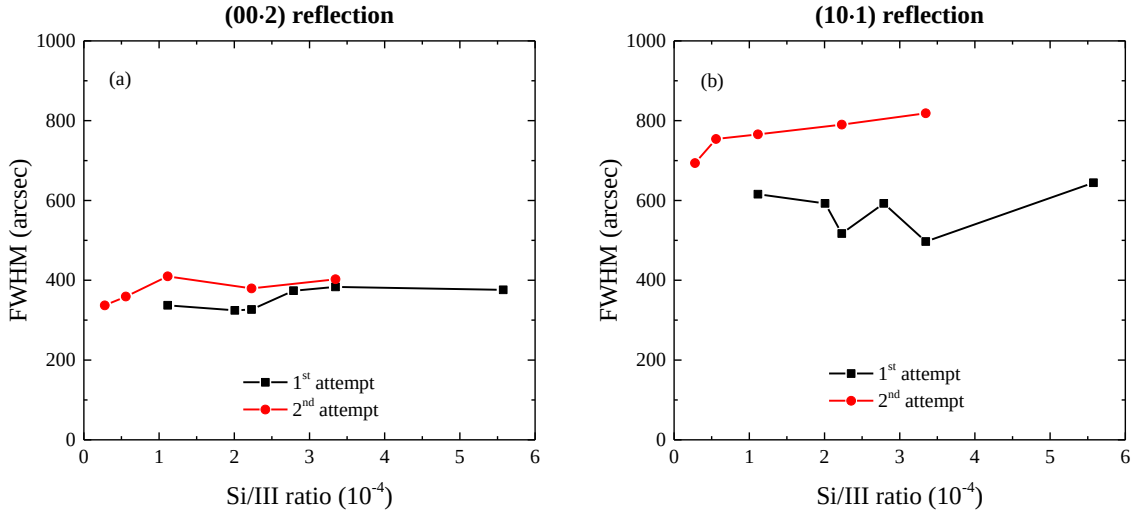

Figure 3.16: Material quality of the two *n*-$Al_{0.6}Ga_{0.4}N$ series

FWHM of the ω-scan of (a) the (0002) reflection, and (b) of the $(10\bar{1}1)$ reflection. The black and red datasets refer to the first and second attempt, respectively.

$Al_{0.85}Ga_{0.15}N$ alloy

In order to understand the behaviour of materials with potential application in the cladding layers of the deep-UV devices, we moved our investigations to alloys with higher AlN content. In particular we focused our attention to the study of *n*-$Al_{0.85}Ga_{0.15}N$ grown at the same conditions that were used to obtain the first deep-UV LEDs, at the early stages of the project: a V/III ratio of 460, growth temperature of 1115 °C, pressure of 50 mbar, and Si/III ratio of 1.5×10^{-4}. A few samples grown with this or similar doping levels resulted to be fully insulating and it was not possible to estimate either their carrier concentration or mobility. Although unexpected at that time, this is in agreement with the findings of Mehnke *et al.* [59], who—as mentioned before—showed that with increasing AlN concentration the window for optimal doping becomes narrower and shifts to lower Si/III ratio.

A series of five samples on standard templates was then grown in the Si/III ratio range $1.3–6.6 \times 10^{-5}$. The material was cut in 1×1 cm^2 squares and van der Pauw samples were formed using the same metal stack and annealing procedures that were optimized for the *n*-$Al_{0.6}Ga_{0.4}N$ materials; all of them showed good resistivity and could be reliably measured. The carrier concentrations and the mobility acquired at room-temperature by Hall-effect measurements at a magnetic field of 1.7 T are reported in Figure 3.17; temperature-dependent measurements will be discussed in Section 3.6.

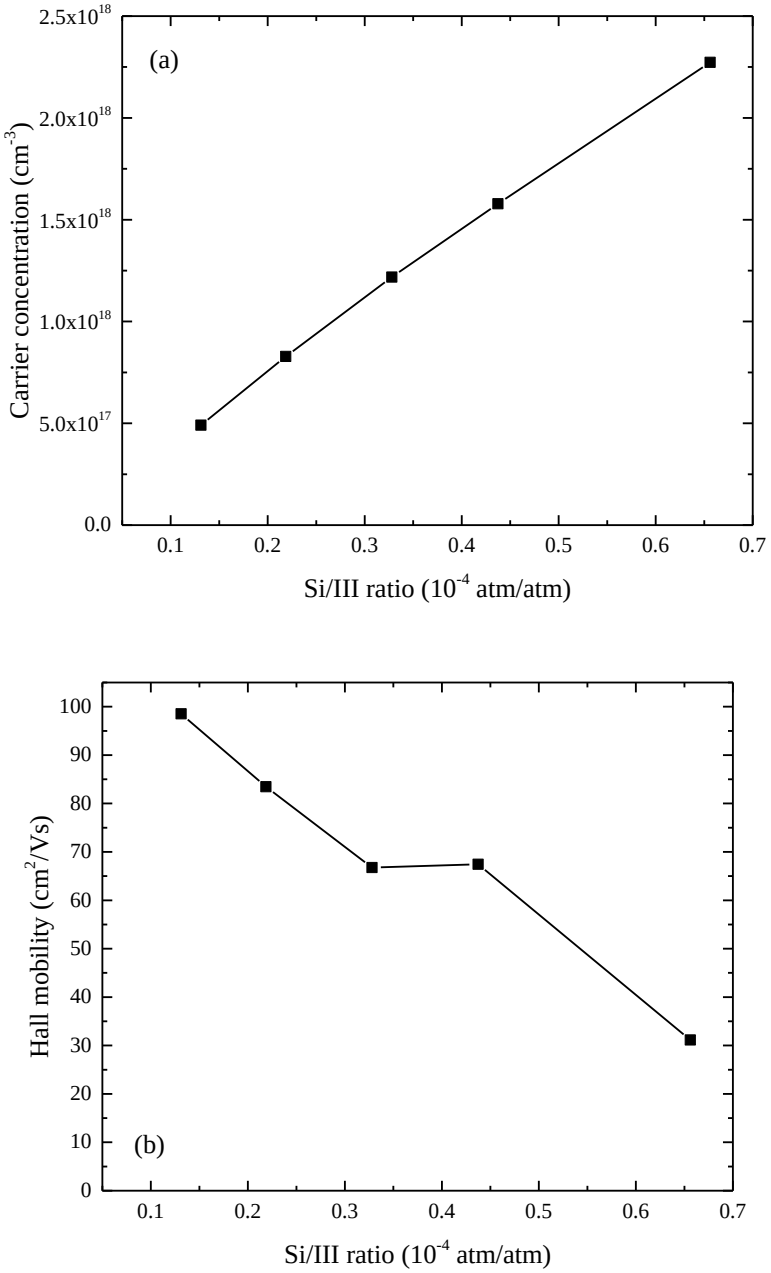

Figure 3.17: AlGaN:Si series with 85% AlN content

Results of the room-temperature Hall-effect measurements: (a) carrier concentration, and (b) mobility. All the samples showed *n*-type conductivity and linear IV characteristics.

Because of the much smaller range of Si/III ratios able to make the material sufficiently conductive for the formation of ohmic contacts, it was not possible to see the maximum of carrier concentration, which monotonically increased from 4.9×10^{17} cm^{-3} to 2.3×10^{18} cm^{-3}, nor that of the mobility, which decreased from 98.5 cm^2 V^{-1} s^{-1} to 31 cm^2 V^{-1} s^{-1}. Although the mobility at the lowest doping level was the highest of all the samples here discussed, as the Si/III ratio increased a very rapid and almost linear

decrease of the mobility was present, which was the cause of the early degradation of the resistivity before the carrier concentration could reach its maximum.

Conclusions

The combined effect of carrier concentration and mobility in all the three AlGaN compositions studied in this work[10] is summarized in Figure 3.18, which shows the variation of their resistivity with the doping level; the results from the paper of Mehnke *et al.* [59] are also shown for comparison. Although the study from Kneissel's group focused on higher AlN contents, our results show that the same trend is clearly present in our material, down to 50% AlN concentration, and seems to be a general feature of MOVPE-grown AlGaN, independent of the particular growth conditions. On the other hand, the discrepancies in the absolute values of the resistivities can be explained by the different dislocation concentrations due to the type of substrate used: i.e. patterned sapphire for lateral overgrowth in Kneissel's group approach, and AlN templates on standard sapphire in our work.

In addition to that, our analysis also suggests a possible explanation of the narrowing of the Si/III ratio window of optimal doping when the AlN content is increased. At lower Al concentrations the minimum of the resistivity is mostly the result of a maximum in the carrier concentration, with almost no contribution from the mobility. In turn the presence of this maximum is most likely due to the onset of compensation due to the incorporation of oxygen/cation-vacancy complexes enhanced by the presence of dislocations. However, at higher AlN concentrations, the mobility starts to play a crucial role. In the series with 60% AlN concentration, the reduction of the mobility due to impurity scattering starts now slightly before the carrier concentration maximum is reached and, although does not significantly affect the position of the resistivity minimum, it is responsible for the larger degradation of the conductivity at higher Si/III ratios. Finally, in the series with 85% AlN concentration the drop of the mobility starts much earlier, when the carrier concentration is still increasing and it is what causes the much earlier increase of the resistivity.

[10] For the *n*-$Al_{0.6}Ga_{0.4}N$ materials only the second of the two series was included in the graph.

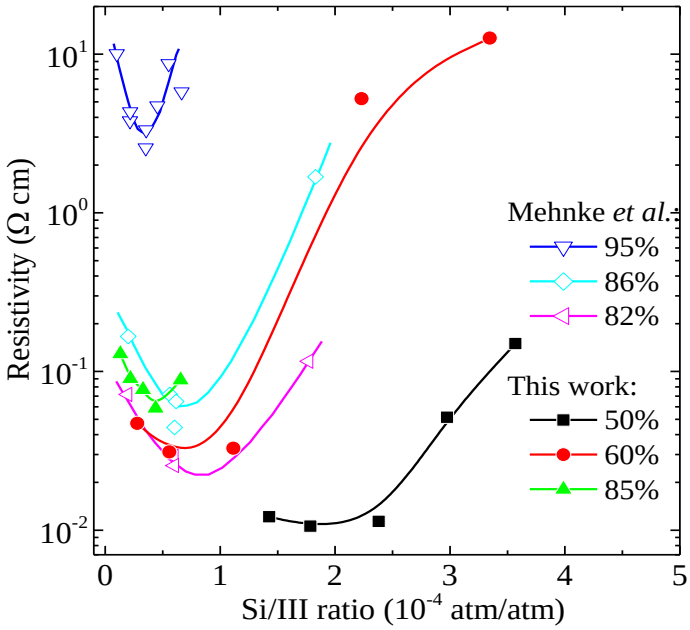

Figure 3.18: Doping optimization in AlGaN

Variation of resistivity as a function of the Si/III ratio. Comparison between the results reported in Mehnke *et al.* [59] and these of this work [78].

Although this sudden degradation of the mobility is what causes the doping of AlGaN materials with compositions close to pure AlN to be so hard to achieve, the significantly reduced alloy scattering present in these materials is what still allows some reasonable conductivity in the low doping regime. On the other hand, the causes of this much sharper decrease of the mobility with doping in Al-rich AlGaN are not fully understood. It is reasonable to assume that dislocation scattering might have a dominant role in this behaviour, as these are expected to be present in higher concentrations in Al-rich materials, and also this effect might possibly be increased even further by the antisurfactant effect of Si [79]. However, further experiments would be needed to confirm this hypothesis.

3.4.2 Optimization of the *p*-type material

As mentioned in the literature review, obtaining good *p*-type conductivity in III-nitride materials is even more difficult than for *n*-type doping. Not only the higher effective mass of holes compared to electrons causes the activation energy of the Mg acceptors to increase up to 500–600 meV for pure AlN, but also the fact that a thermal activation step is required to remove the hydrogen passivation from the impurities adds another free parameter to the process that needs to be optimized. In addition to that, it is almost impossible to obtain ohmic contacts on *p*-type AlGaN materials without the use of a

thin *p*-GaN layer underneath the metal pads, which would short-circuit the current from the AlGaN layer if not appropriately removed.

In this experiment a series of three AlGaN samples with a target AlN content of 60% was grown with Mg/III ratios of 4.8×10^{-3}, 9.6×10^{-3}, and 1.4×10^{-2}. The growth conditions were set to a V/III ratio of 585, growth temperature of 1100 °C, and pressure of 50 mbar; the nominal thickness of the doped *p*-AlGaN was 160 nm: although thicker epilayers would have been beneficial for the Hall-effect measurements, this would have significantly decreased the crystal quality of the material. A nominally 50-nm-thick *p*-GaN layer was subsequently grown with a Mg/III ratio of 1.0×10^{-2}, a V/III ratio of 3670, a growth temperature of 1045 °C, and a pressure of 150 mbar. The thermal activation of the Mg impurities was performed *in-situ*, at a pressure of 300 mbar while the temperature linearly decreased from the growth temperature of the *p*-GaN layer down to 500 °C in 5.6 min. The material was first cut in squares of about 1×1 cm^2 and then 40 nm of Pd were evaporated on the corners to form van der Pauw samples; no thermal treatment was performed on the contacts, which already exhibited ohmic behaviour.

A preliminary set of Hall-effect measurements were performed at room-temperature and with a magnetic field of 1.7 T. Because the conduction was the result of current flowing both through the *p*-AlGaN and the *p*-GaN layers, it was not possible to extract any reliable estimation of the carrier concentration and mobility in either material; however, the measurements confirmed that the sample had *p*-type conductivity. The sheet resistivity of the three samples were in the very narrow range 1.47–1.88 MΩ/□, which is consistent with the conductivity being dominated by the nominally identical *p*-GaN layers.

In order to remove the *p*-GaN layer, a shallow dry-etch was performed in an Oxford Plasmalab 200 Induction-Coupled Plasma (ICP) equipment, using our standard recipe for etches of III-nitride materials. This process, which is based on chlorine-chemistry plasma, has a nominal etch rate of 680 nm/min for GaN, and is routinely used to expose the buried *n*-type layers during the fabrication of our LEDs. The previously deposited Pd contacts acted as a mask and were able to protect the *p*-GaN underneath them so that a good ohmic contact was still present after the etch. A profilometer measurement along

the normal of the metal-contact edges showed that about 60–80 nm of material were removed, leaving only *p*-AlGaN material in the entire region outside the corners.

A new set of resistivity and Hall-effect measurements were performed at room-temperature and with a magnetic field of 1.7 T; the results before and after the dry-etch are summarized in Table 3.2. Although the sheet resistivity showed a clear trend with a significant reduction at higher doping levels, the Hall-effect measurements revealed that the conductivity had turned to *n*-type as a results of the donor defects introduced in the material by the plasma treatment. The large differences in the sheet resistivity values, which are shown in Figure 3.19 together with the values measured before the dry-etch, suggests that the trend is probably due to real differences in the doping levels of the *p*-AlGaN layers subjected to plasma treatment more than the effect of random variation of the process. The defects introduced during the dry-etch are most likely nitrogen vacancies, whose formation energy in *p*-AlGaN materials is the lowest among all defects, and decreases even further as the Fermi level approaches the conduction band [51]. The fact that the conductivity has become *n*-type means that the concentration of donor defects after etch is the dominant one and the material is only partially compensated by the intentionally introduced acceptor impurities. This suggests that the material with the highest sheet resistivity is the one with the highest degree of compensation or, in other words, the one that had the highest *p*-type doping-level before being exposed to the plasma. If that is true, this would mean that the range of Mg/III ratios here explored is in the over-doped region; however more experimental work would be needed to confirm this hypothesis.

	before dry-etch		**after dry-etch**	
Mg/III ratio	sheet resistivity	sheet carrier concentration	sheet resistivity	sheet carrier concentration
4.8×10^{-3}	1.52 MΩ/□	1.0×10^{12} cm^{-2}	23.3 MΩ/□	2.8×10^{12} cm^{-2}
9.6×10^{-3}	1.47 MΩ/□	8.1×10^{11} cm^{-2}	13.6 MΩ/□	8.3×10^{11} cm^{-2}
1.4×10^{-2}	1.88 MΩ/□	3.9×10^{12} cm^{-2}	7.85 MΩ/□	2.5×10^{12} cm^{-2}

Table 3.2: Results of the Hall-effect measurements

Summary of the measurements performed before and after the dry-etch used to remove the GaN contact-layer. The conductivity of the samples was *p*-type before the etch, and *n*-type after.

Although these preliminary results were interesting, because of time constraints we could not investigate any further the issue of *p*-type doping. In order to improve the experiment, apart from extending the analysis also to lower Mg/III ratios, the next step would have been to develop a different dry-etch recipe that could be able to remove the *p*-GaN layer without inducing high concentrations of defects. An outline of this approach, together with other fabrication aspects, will be discussed in Chapter 4.

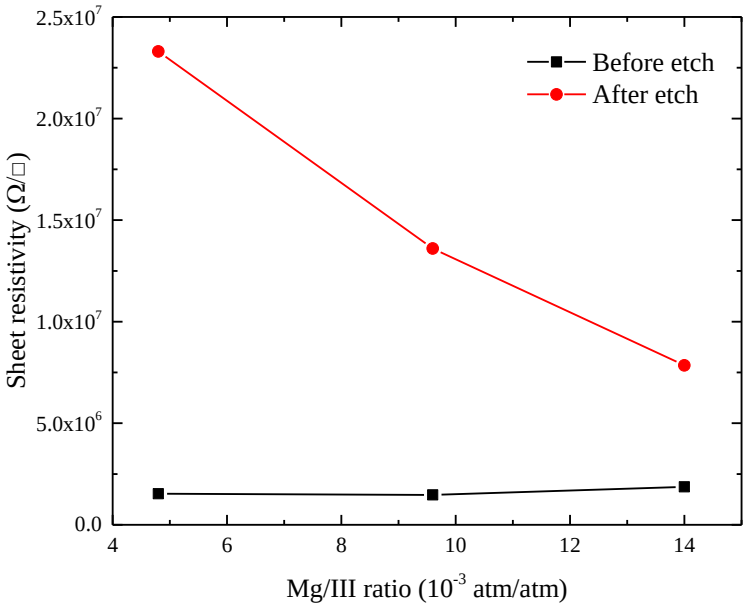

Figure 3.19: Sheet resistance

Sheet resistance measured on the three samples before (black line), and after (red line) the dry etch.

3.5 Room-temperature measurements of *n*-type semipolar AlGaN

As mentioned earlier, the use of nonpolar or semipolar orientations would allow the reduction of the QCSE, which significantly hinders the IQE of the active regions grown on the standard *c*-plane direction. The first attempts date back to the late 1970s, but it was not before 2000 that the first successful results were eventually reported [17]. The electron concentrations were not substantially different from those of standard polar epilayers, but the mobilities were often considerably lower as a result of the much higher defect concentrations typical of these materials [80]. Another interesting feature that has often been reported is the variation of resistivity along different planar directions [81, 82]; because electrons have almost the same effective masses along these directions [83, 84], the observed behaviour has been often attributed to anisotropic

scattering from defects. In particular, stacking faults—i.e. inclusions of monolayers of zincblende-phase perpendicular to the *c*-direction—have been thought to be the most likely cause: due to the band offset between zincblende and wurtzite structures and to the discontinuities in the polarization field at their interfaces, electrons that flow in the *c*-direction have to overcome regions with bent conduction-band edges, while those moving perpendicularly do not; a quantitative model based on this hypothesis has also been proposed by Konar *et al.* [85].

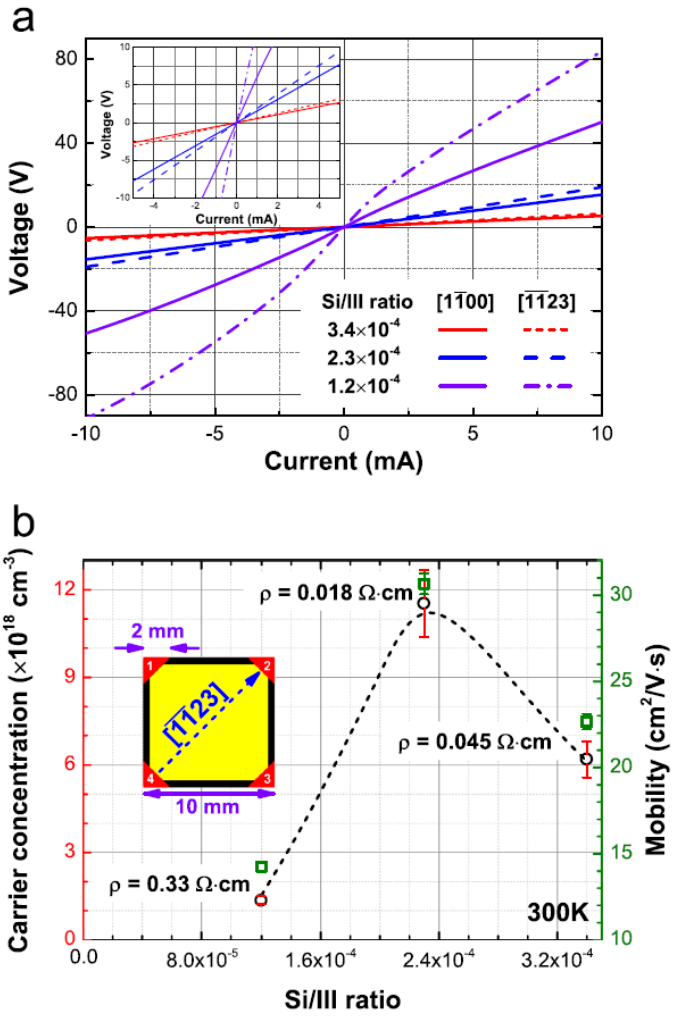

Figure 3.20: Semipolar AlGaN:Si series with 50–55% AlN content

Figure taken from our recently published paper [86].

Even though ultraviolet-LEDs based on nonpolar or semipolar AlGaN have already been demonstrated [87, 88], there are few systematic studies about doping of those materials. In a recent work from our group [86], we have reported *n*-type doping of

semipolar $(11\bar{2}2)$ AlGaN with an aluminium concentration close to 50%, grown at different disilane flow rates with Si/III ratios in the range 0.56–3.3 × 10^{-4}. The samples were grown in parallel with the polar *n*-$Al_{0.6}Ga_{0.4}N$ materials already described in Section 3.4.1, and the differences in AlN concentration are due to an increased GaN incorporation on semipolar orientation. As previously reported, the growth condition were set to a V/III ratio of 585, growth temperature of 1100 °C, and pressure of 50 mbar; the nominal thickness of the doped film was 1 µm. The material was cut in squares of about 1 × 1 cm^2 and metal contacts were evaporated on the corners to form van der Pauw samples using the same procedure previously described in Section 3.4.

The electrical characterization of the samples (which was my contribution to that article) is summarized in Figure 3.20. For the sample grown with a Si/III ratio of 5.6 × 10^{-5}, at a current of 10 µA the voltage values already reached/exceeded the maximum compliance voltage of 100 V, indicating that the sample is very resistive, and hence it was not included in the analysis. The IV curves measured along the $[\bar{1}\bar{1}23]$ and $[1\bar{1}00]$ directions of the three samples grown with the highest Si/III ratios are reported in Figure 3.20 (a), and clearly show the signs of anisotropy in the resistivity along different planar directions, with values along $[\bar{1}\bar{1}23]$ larger than along $[1\bar{1}00]$. Voltage-drop differences along the two directions at 10 mA were estimated to be 45%, 15%, and 20% for the samples grown with Si/III ratios of 1.1 × 10^{-4}, 2.2 × 10^{-4}, and 3.3 × 10^{-4}, respectively. Although the sample grown with a Si/III ratio of 1.1 × 10^{-4} showed IV curves with somewhat nonlinear behaviour—indicating that a Schottky barrier exists between the contacts and the layer surface—for the samples grown with Si/III ratios ≥ 2.3 × 10^{-4}, the IV curves along $[\bar{1}\bar{1}23]$ and $[1\bar{1}00]$ exhibited ohmic behaviours.

Figure 3.20 (b) shows the room-temperature carrier concentration, mobility, and resistivity of the three most doped samples, which showed carrier concentrations in excess of 1.3 × 10^{18} cm^{-3}. The carrier concentration reached a maximum of 1.2 × 10^{19} cm^{-3} at a Si/III ratio of 2.2 × 10^{-4}, giving a minimum resistivity of ρ = 0.018 Ω cm, and then decreased as the ratio further increased indicating the onset of strong compensation, as already reported in this thesis for the other materials. However, the fact that also the mobility showed a maximum of 30.7 cm^2 V^{-1} s^{-1} at the intermediate doping level was not reported for polar samples, in which this parameter was almost constant in the whole low-doping region.

The reason for this unusual mobility behaviour is currently unclear. However, one possible explanation is that the mobility at low carrier concentrations is dominated by the scattering of negatively charged dislocations, while at higher carrier concentrations the free carriers can screen this effect. At higher concentrations the mobility starts to decrease again with the doping level, this time as a consequence of ionized impurity scattering as typical in all doped semiconductors. This mechanism, which has been reported for *n*-type GaN by Ng *et al.* [89], would explain the bell-shaped behaviour of the mobility we report. However, the semipolar material here investigated in this experiment is much more complicated than GaN given the presence of both high alloy scattering and high basal stacking fault scattering; hence further experimental work is required to investigate this problem.

3.6 Temperature-dependent Hall-effect measurements of polar AlGaN materials

In order to get a better understanding of the polar samples with 60% and 85% AlN composition described in the previous sections, a set of temperature-dependent Hall-effect measurements in the range 10–400 K were performed. Because of the larger space between the poles of the magnet required to accommodate the special sample-holder for low-temperature measurements, the magnetic field was reduced to 0.9 T; the injected current varied from 100 μA to 10 mA depending on the resistivity of the samples.

The logarithm of the Hall coefficient (R_H) vs the inverse of temperature is shown in Figure 3.21 (a) and (b) for $Al_{0.6}Ga_{0.4}N$ and $Al_{0.85}Ga_{0.15}N$, respectively. In case of the $Al_{0.6}Ga_{0.4}N$ material, apart from the two most highly doped samples, which showed a very different behaviour and will be discussed separately, three regimes are clearly apparent: a high temperature one, in which R_H increases exponentially with 1/T as expected in case of conductivity whereby electrons are thermally activated into the conduction band; an intermediate temperature one in which R_H reaches a maximum and then decreases; and finally a low temperature one in which R_H stays almost constant with 1/T showing a very small, although well defined, thermal activation behaviour, with energies that decrease as the doping level increases. For the $Al_{0.85}Ga_{0.15}N$ set of samples, it was not possible to have reliable measurements at temperatures lower than 60–70 K as the contacts became non-ohmic. However, in the range of temperatures

explored, the presence of a maximum in R_H was also clearly visible in all the samples apart from the least doped one. Moreover, the samples showed the same trend as in $Al_{0.6}Ga_{0.4}N$, in which the R_H maximum shifts towards higher temperatures as the doping level is increased.

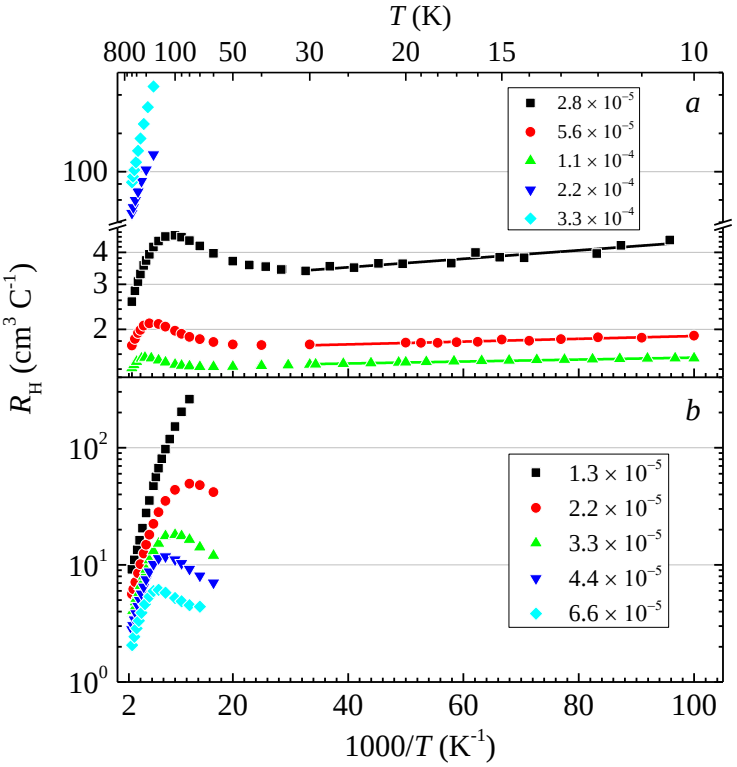

Figure 3.21: Hall coefficient

Temperature dependence of Hall coefficient for (a) *n*-$Al_{0.6}Ga_{0.4}N$ and (b) *n*-$Al_{0.85}Ga_{0.15}N$ doped with different Si/III ratios.

A variation of the Hall coefficient with temperature similar to that shown in Figure 3.21 has previously been reported for germanium [90], and gallium nitride [55, 91, 92], and was explained as due to the simultaneous presence of two conduction channels: the usual band transport and some form of impurity conduction with a much lower mobility. The Hall coefficient can then be fitted using the formula (3.22) as discussed in Section 3.2.3:

$$R_H = \frac{R_{con}\sigma_{con}^2 + R_{hop}\sigma_{hop}^2}{\left(\sigma_{con} + \sigma_{hop}\right)^2}, \tag{3.22}$$

in which R_{con} and R_{hop} are the Hall coefficients of the band-like channel and the low-mobility channel, respectively; and σ_{con} and σ_{hop} are their respective conductivities. While at high and low temperatures this formula simply reduces to R_{con} and R_{hop}, respectively, at intermediate temperatures the switchover from one channel to the other as the dominant transport mechanism can be delayed if the ratio of the two mobilities is high and a maximum might indeed appear as in the data of Figure 3.21.

Even though this behaviour of R_H is not new in other highly-doped semiconductor materials, to the best of our knowledge this is the first time that it has been reported for AlGaN. Moreover, because of the particularities of this alloy, none of the methods proposed in the previously cited works regarding Ge and GaN [55, 90, 91] can be used with our material to separate the contributions of the two channels.

In the work of Hung and Gliessman [90] the authors suggest that R_{con} and R_{hop} can be simply isolated at high and low temperatures. While this seems to be reasonable in order to isolate R_{hop} at low temperatures (i.e. in the 10–30 K range), in which we can assume no significant band conduction, the same is not necessarily true for R_{con} as we cannot rule out the possibility of having considerable impurity conduction even at temperatures as high as those we have explored here. Specifically in order to respond to this objection, Molnar *et al.* [91] and later Look *et al.* [55] have developed more elaborate models that can effectively be used to separate the two contributions in GaN samples, provided some initial assumptions are met. In particular, the Molnar model assumes that the total number of carriers in the two bands is constant, which implies that the impurity band must be completely degenerate with no possible sign of thermally activated behaviour. The Look model assumes that the uncorrected mobility calculated using a single-channel model should asymptotically approach the almost constant impurity-band mobility at low temperature. However, neither of those two assumptions holds for our material as thermally activated behaviour is clearly present in the impurity conduction, and the uncorrected mobility keeps decreasing as the temperature is lowered without stabilizing to any asymptotic value, as will be shown later (Cf. Figure 3.25).

To overcome these problems and effectively estimate the contributions of the two conductivity channels in our material, a new method is proposed. The fact that at low temperature the logarithm of R_H is a linear function of the inverse of the temperature,

suggests that the term R_{hop} in Eq. (3.22) is associated with a channel whose carrier concentration, n_{hop} has an exponential dependence with temperature, and a well-defined activation energy, ε_{hop}:

$$R_h = \frac{r_{hop}}{en_{hop}} \propto exp\left(\frac{\varepsilon_{hop}}{k_B T}\right), \tag{3.23}$$

where r_{hop} is the Hall factor, which, although not known and possibly significantly different from unity in this almost-degenerate channel, remains constant in the whole low-temperature range. Assuming that this also holds at higher temperatures, I propose to extract R_{hop} by fitting R_H in the low temperature range, and then calculate R_{con} by inverting Eq. (3.22), which is possible provided we know how to split the total conductivity into the two components σ_{con} and σ_{hop}.

This information can be extracted by plotting the logarithm of the measured conductivities as a function of the inverse of the temperature, as shown in Figure 3.22 for the samples of the $Al_{0.6}Ga_{0.4}N$ series. It then becomes evident that the experimental data of the three samples are well fitted by a sum of two exponentials,

$$\sigma = \sigma_1 exp\left(-\frac{\varepsilon_1}{k_B T}\right) + \sigma_3 exp\left(-\frac{\varepsilon_3}{k_B T}\right), \tag{3.24}$$

where the activation energies ε_1 and ε_3, and the asymptotic conductivities σ_1 and σ_3 are the fitting parameters. The former of the two terms, with subscript 1, accounts only for the band conduction and the slight deviation of the data from pure exponential dependence close to the 400 K limit is, most likely, due to an increased phonon interaction with the free carriers. The latter term (which following the convention of Shklovskii and Efros [34] is indicated with subscript 3) is attributed to NNH conduction. The term usually indicated with the subscript 2 and attributed to the hopping among neutral donors is, as often the case, not detectable in our material.

The attribution of the low-temperature conductivity to the NNH mechanism is based on the fact that the activation energy ε_3 remains extremely stable in this temperature range for each sample. This is a typical feature of this type of transport that can be explained as being due to the large energy difference between the Fermi level and the peak of the density of states in the impurity band [34], as discussed in Section 3.2.4. It is possible

that in extending the analysis to lower temperatures, some form of variable-range hopping conduction might become apparent; but, for the scope of this study, this can be ignored without introducing any significant error in the model. Moreover, the observation that the low temperature conductivity increased by an order of magnitude (Cf. Figure 3.22) when the dopant atoms supplied during growth increased by only a factor of two (from a Si/III ratio of 2.8×10^{-5} to 5.6×10^{-5}, before the channel became almost completely degenerate at 1.1×10^{-4}) is also consistent with hopping conduction [38]. In addition to that, the reduction of the activation energy with increased doping can be explained as the effect of an increased superposition among the localized state wavefunctions.

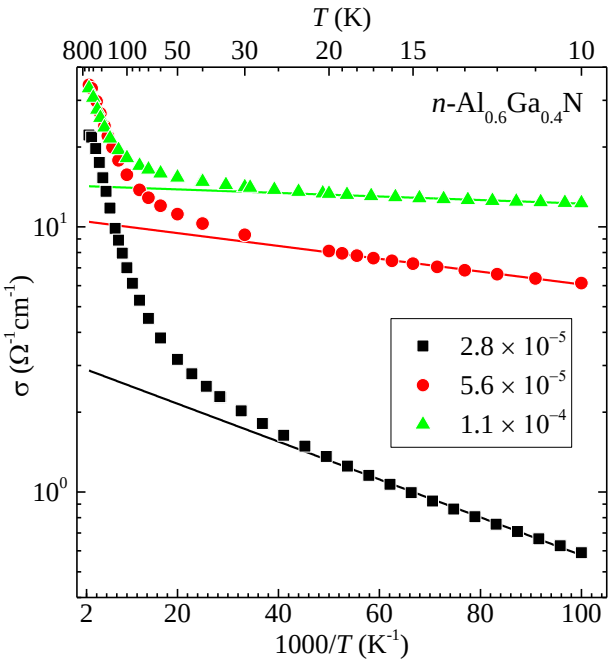

Figure 3.22: Conductivity

Temperature dependence of conductivity for the *n*-$Al_{0.6}Ga_{0.4}N$ samples doped with different Si/III ratios. The straight lines show the exponential fitting at low temperatures extrapolated to higher temperatures.

Potential fluctuations due to alloy disorder are also expected to be present in AlGaN materials, and are known to induce tails of localized states into the gap. It is very possible that these states also contribute to the hopping transport observed in our material; however, because of the typical features of NNH, the low-mobility channel in our material is most likely dominated by hopping in the impurity band.

As a result of those considerations, σ_{hop} in Eq. (3.22) can be identified with the second exponential term of Eq. (3.24), and because ε_3 is orders of magnitude lower that ε_1, extract it by fitting the experimental data in the low temperature range (10–20 K); finally, by subtracting the so obtained σ_{hop} from the total conductivity σ_{con} can be obtained. Apart from its use in retrieving R_{con} and R_{hop} from Eq. (3.22), the splitting of the conductivity into σ_{con} and σ_{hop} allowed me to extrapolate the contribution of the hopping channel at room-temperature, which was estimated to be 13%, 32% and 46% for the samples with 2.8×10^{-5}, 5.6×10^{-5} and 1.1×10^{-4} Si/III ratio, respectively. This result further confirms that the simple interpretation of our Hall-effect measurements based on a standard single-band approach is not reliable, even at room-temperature, and justifies the need for method of separation here introduced.

The separate values of the Hall carrier concentrations in the conduction-band and in the hopping channel as a function of temperature, which were obtained using the equations

$$n_{con} = \frac{1}{eR_{con}}, \tag{3.25}$$

$$n_{hop} = \frac{1}{eR_{hop}}, \tag{3.26}$$

are presented in Figure 3.23. For comparison, the combined effect of the two transport mechanisms interpreted with the standard single-channel model is also shown, with the apparent dip caused by the discrepancies in the mobilities of the two channels.

It is worth mentioning that these values have to be taken with care as we do not have any information about the Hall factors (r_{con} and r_{hop}), and while we can assume it is close to 1 for the diffusion transport in the conduction band, this might not be true for the impurity band of localized states. Nonetheless, even though this model is only meant to give an approximate estimation of R_{con} and R_{hop}, and it becomes inaccurate in the low temperature range where σ_{con} approaches zero and relative errors increase significantly, still a great deal of information can be extracted. In particular, the model suggests that although the uncorrected room-temperature carrier concentration appears to increase with the dopant concentration (up to 4.2×10^{18} cm^{-3} in the range explored) the actual free-carrier concentration in the conduction band has already reached its

maximum of 1.6×10^{18} cm^{-3} at a Si/III ratio of 2.8×10^{-5}, and any further increase of dopant atoms supplied during growth only enhances the hopping conduction with concentrations of the carriers participating in this type of transport that increase from 2.1×10^{18} cm^{-3} up to 4.3×10^{18} cm^{-3}. This process eventually stops when a critical Si/III ratio is reached and the band-like channel starts to degrade (i.e. at 2.2×10^{-4} and above, as will be discussed later).

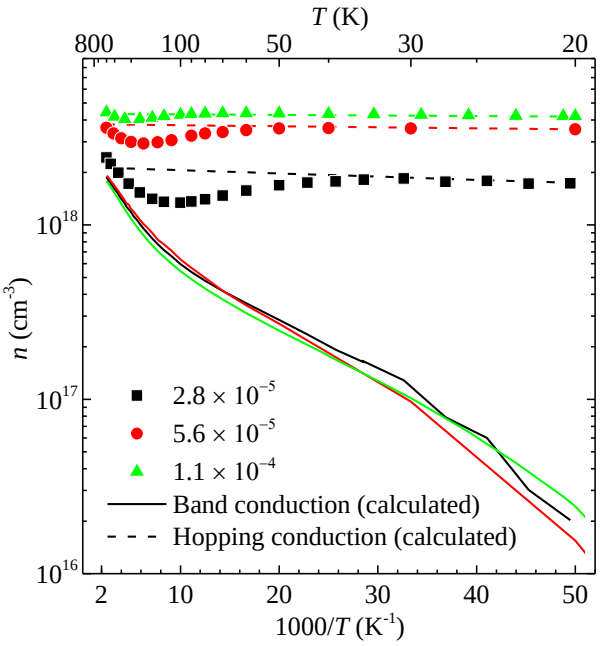

Figure 3.23: Calculated carrier concentrations

Temperature dependence of carrier concentration for the *n*-$Al_{0.6}Ga_{0.4}N$ samples doped with different Si/III ratios. The discrete data-points represent the uncorrected values obtained with the standard single-channel model; the solid and dashed lines are the concentrations calculated for the conduction-band and the hopping channel, respectively, with the model here described.

The free carrier concentrations in the conduction band, which, as shown in Figure 3.23, are virtually the same in all the reported $Al_{0.6}Ga_{0.4}N$ samples, can be fitted using the charge neutrality equation:

$$\frac{n(n+N_A)}{N_D - N_A - n} = \frac{N_C}{g} exp\left(-\frac{E_d}{kT}\right) \tag{3.27}$$

in which, apart from the symbols already defined, N_D and N_A are, respectively, the concentrations of donor and acceptor impurities, $g = 2$ the ground state degeneracy,

$N_C = (8.9 \times 10^{14}) \times T^{3/2}$ cm^{-3} the effective density of states, and E_d the activation energy. This gives a very low E_d of about 1 meV, which is consistent with the presence of large screening effects due to the high concentration of free carriers, as already reported in literature [48, 93, 94]. Although the net dopant concentrations ($N_D - N_A$) in the three samples are most likely different, it was not possible to estimate them because, in this range of temperatures far from the saturation regime, the variations of n with $N_D - N_A$ are minimal. However the compensation degree (N_A/N_D) could be estimated as being around 27% for all the three samples. The fitting of the data calculated with the two-channel model is shown in Figure 3.24; on the contrary, the uncorrected data could not be fitted with Eq. (3.27) for any choice of the parameters N_D, N_A, and E_d, which once again confirms the importance of the method here described.

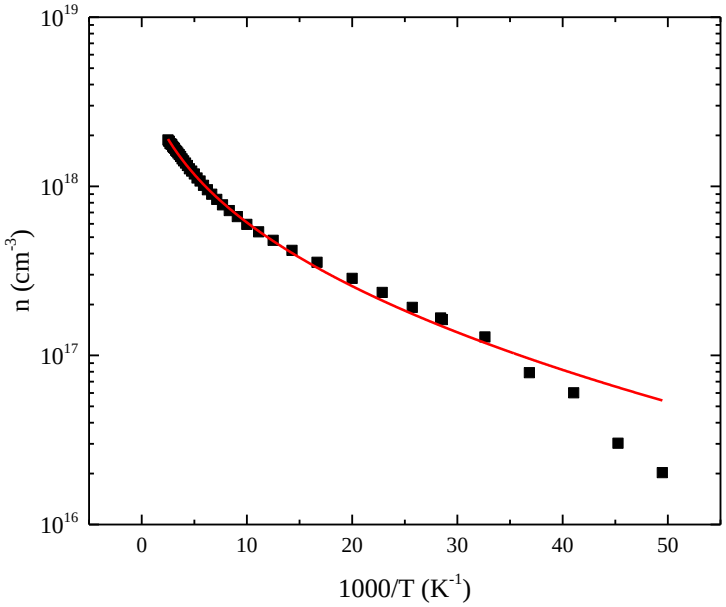

Figure 3.24: Fitting of the carrier concentration vs temperature

Fitting of the carrier concentration in the conduction-band for the *n*-$Al_{0.6}Ga_{0.4}N$ samples. The discrete data-points represent the values obtained with the model here proposed; the red line is the best fitting obtained with Eq. (3.27).

The model also allows the separation of the Hall mobilities of the two channels:

$$\mu_{con} = \sigma_{con} R_{con} \,, \tag{3.28}$$

$$\mu_{hop} = \sigma_{hop} R_{hop} \,, \tag{3.29}$$

as shown, for the sample with a Si/III ratio of 2.8×10^{-5}, in Figure 3.25. The trend is very similar in all the samples of the $Al_{0.6}Ga_{0.4}N$ series, with a hopping conduction mobility almost constant in the range of temperature explored, and free-carrier mobility that shows the typical bell-shaped curve due to ionized impurity scattering dominating at lower temperatures and phonon scattering at higher temperatures.

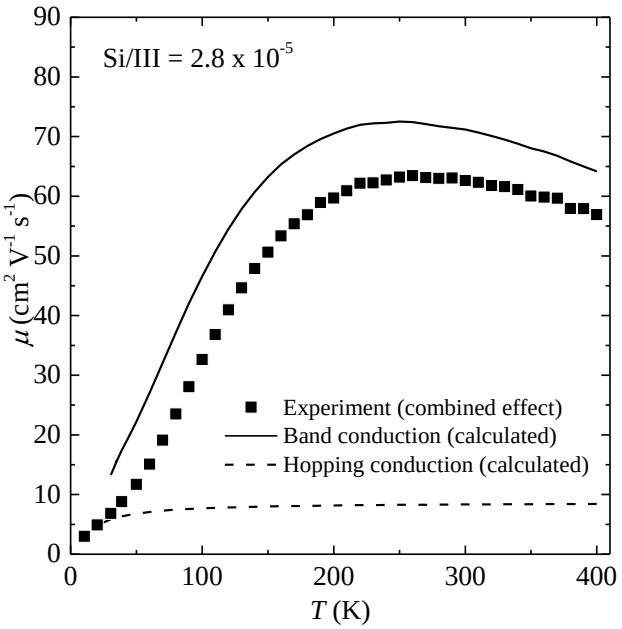

Figure 3.25: Example of calculated carrier mobility

Typical Hall mobility for the samples of the *n*-$Al_{0.6}Ga_{0.4}N$ series; the sample shown here has a Si/III ratio of 2.8×10^{-5}. The squares represent the uncorrected values obtained with the standard single-channel model, which do not converge to any asymptotic value at low temperature. Solid and dashed lines are the calculated Hall mobilities for the free carriers and in the hopping channel, respectively.

In contrast with the analysis of the first three samples of the *n*-$Al_{0.6}Ga_{0.4}N$ series so far detailed, these with higher doping levels (Si/III ratios 2.2×10^{-4} and 3.3×10^{-4}) showed a very different behaviour, with only one conductivity channel clearly apparent. Although it is not possible to exclude the presence of some hopping conduction at low temperature, this form of transport seems to be much less important for these samples because at temperatures lower than 160 K both of them became so resistive that neither Hall-coefficient nor resistivity could be measured. Their carrier concentrations were hence calculated using the standard single-channel expression

$$n = \frac{1}{eR_H}, \tag{3.30}$$

instead of the two Eqs. (3.25) and (3.26) as previously done for the other samples. When the carrier concentrations at different temperatures were fitted with Eq. (3.27), the degree of compensation was found to be, in both cases, close to 95%, while the activation energy noticeably increased, up to 17.8 meV for the most doped sample. This suggests that the large decrease of the hopping contribution to the total conductivity is due to the depletion of electrons from the impurity band as a result of the very high degree of compensation. Moreover, the consequent reduction of the screening effects due to the much lower free-carrier concentration explains the increase of the activation energy.

3.7 Conclusions

The results discussed in Section 3.6 show that, in the doping range explored, hopping transport in the *n*-$Al_{0.6}Ga_{0.4}N$ material was not only dominant at low temperature, but also significant at room-temperature, with contributions to the total conductivity up to 46% for the most conductive sample. As a consequence of this fact, the measurements of Hall carrier concentration and Hall mobility using the usual single-channel approach are not reliable, even at high temperatures. I have proposed a method to separate the contributions of the two channels, which—although only approximate—can be used to gain insight into the doping mechanism. Particularly it shows that the room temperature free-electron concentration in the $Al_{0.6}Ga_{0.4}N$ material reaches its maximum at about 1.6×10^{18} cm^{-3}, well below the value that would have been obtained with the standard single-channel analysis of the data. This maximum is already achieved at dopant concentrations lower than the one that gives the best conductivity. However, further increase of the doping levels will enhance the hopping channel, with concentrations of the carriers participating in this type of transport increasing from 2.1×10^{18} cm^{-3} up to 4.3×10^{18} cm^{-3}. For the $Al_{0.85}Ga_{0.15}N$, even though it was not possible to estimate the actual carrier concentrations, our measurements suggest that a significant hopping conduction channel is present also in this material.

Because the contacts of most of the samples analysed in this chapter became non-ohmic in the range 10–30 K where the activation energy of the hopping channel can be isolated, it was not possible to perform the required correction to the room-temperature

data reported and discussed in Section 3.4, where the standard single-channel model was used instead. However, although the presence of a hopping channel significantly affects the absolute values of the carrier concentration and the mobility, their trends with the doping level are still reliable and show that the variations of the mobility play a particularly important role in the degradation of the conductivity with increased doping levels in Al-rich materials.

The study of semipolar $(11\bar{2}2)$ *n*-AlGaN close to 50% AlN content also showed the existence of an optimum Si/III ratio condition that leads to a maximum in carrier concentration. However, in contrast with the material grown on *c*-plane, this doping condition also gives a maximum value for the mobility. Future work would be necessary to investigate this aspect, which might be due to dislocation scattering at low doping levels. In particular the application of the same methodology used for the analysis of the temperature-dependent measurements of the polar material would be highly beneficial also for this material.

Preliminary results on the *p*-type doping seem to suggest that the doping conditions of the cladding layers used in the growth of our devices might lead to overdoping. However, to continue the investigation of this issue, the development of a dry-etch recipe with high selectivity between GaN and AlGaN would be necessary in order to avoid the introduction of high concentrations of compensating donor defects.

3.8 Bibliography

[1] P. Pampili and P. J. Parbrook, "Doping of III-nitride materials," *Materials Science in Semiconductor Processing,* vol. 62, pp. 180-191, 2017.

[2] J. A. Freitas Jr, "Properties of the state of the art of bulk III-V nitride substrates and homoepitaxial layers," *Journal of Physics D: Applied Physics,* vol. 43, 073001, 2010.

[3] B. E. Gaddy, Z. Bryan, I. Bryan, J. Xie, R. Dalmau, B. Moody*, et al.*, "The role of the carbon-silicon complex in eliminating deep ultraviolet absorption in AlN," *Applied Physics Letters,* vol. 104, 202106, 2014.

[4] O. Ambacher, "Growth and applications of group III-nitrides," *Journal of Physics D: Applied Physics,* vol. 31, pp. 2653-2710, 1998.

[5] P. Gibart, "Metal organic vapour phase epitaxy of GaN and lateral overgrowth," *Reports on Progress in Physics,* vol. 67, pp. 667-715, 2004.

[6] I. M. Watson, "Metal organic vapour phase epitaxy of AlN, GaN, InN and their alloys: A key chemical technology for advanced device applications," *Coordination Chemistry Reviews,* vol. 257, pp. 2120-2141, 2013.

[7] X. Wang and A. Yoshikawa, "Molecular beam epitaxy growth of GaN, AlN and InN," *Progress in Crystal Growth and Characterization of Materials,* vol. 48-49, pp. 42-103, 2004.

[8] I. Akasaki, "Key inventions in the history of nitride-based blue LED and LD," *Journal of Crystal Growth,* vol. 300, pp. 2-10, 2007.

[9] H. P. Maruska and W. C. Rhines, "A modern perspective on the history of semiconductor nitride blue light sources," *Solid-State Electronics,* vol. 111, pp. 32-41, 2015.

[10] H. P. Maruska and J. J. Tietjen, "The preparation and properties of vapor-deposited single-crystal-line GaN," *Applied Physics Letters,* vol. 15, pp. 327-329, 1969.

[11] J. I. Pankove, E. A. Miller, and J. E. Berkeyheiser, "GaN blue light-emitting diodes," *Journal of Luminescence,* vol. 5, pp. 84-86, 1972.

[12] H. Amano, N. Sawaki, I. Akasaki, and Y. Toyoda, "Metalorganic vapor phase epitaxial growth of a high quality GaN film using an AlN buffer layer," *Applied Physics Letters,* vol. 48, pp. 353-355, 1986.

[13] S. Nakamura, "GaN growth using GaN buffer layer," *Japanese Journal of Applied Physics,* vol. 30, pp. L1705-L1707, 1991.

[14] I. Akasaki, H. Amano, Y. Koide, K. Hiramatsu, and N. Sawaki, "Effects of AlN buffer layer on crystallographic structure and on electrical and optical properties of GaN and $Ga_{1-x}Al_xN$ ($0 < x \leqq 0.4$) films grown on sapphire substrate by MOVPE," *Journal of Crystal Growth,* vol. 98, pp. 209-219, 1989.

[15] M. Lada, A. G. Cullis, and P. J. Parbrook, "Effect of anneal temperature on GaN nucleation layer transformation," *Journal of Crystal Growth,* vol. 258, pp. 89-99, 2003.

[16] E. C. H. Kyle, S. W. Kaun, P. G. Burke, F. Wu, Y. R. Wu, and J. S. Speck, "High-electron-mobility GaN grown on free-standing GaN templates by ammonia-based molecular beam epitaxy," *Journal of Applied Physics,* vol. 115, 193702, 2014.

[17] T. Paskova, "Development and prospects of nitride materials and devices with nonpolar surfaces," *Physica Status Solidi (B) Basic Research,* vol. 245, pp. 1011-1025, 2008.

[18] T. F. Kuech, B. S. Meyerson, and E. Veuhoff, "Disilane: A new silicon doping source in metalorganic chemical vapor deposition of GaAs," *Applied Physics Letters,* vol. 44, pp. 986-988, 1984.

[19] J. K. Sheu and G. C. Chi, "The doping process and dopant characteristics of GaN," *Journal of Physics Condensed Matter,* vol. 14, pp. R657-R702, 2002.

[20] S. Nakamura, T. Mukai, and M. Senoh, "Si- and Ge-Doped GaN Films Grown with GaN Buffer Layers," *Japanese Journal of Applied Physics,* vol. 31, pp. 2883-2888, 1992.

[21] H. Li, T. C. Sadler, and P. J. Parbrook, "AlN heteroepitaxy on sapphire by metalorganic vapour phase epitaxy using low temperature nucleation layers," *Journal of Crystal Growth,* vol. 383, pp. 72-78, 2013.

[22] D. V. Dinh, M. Conroy, V. Z. Zubialevich, N. Petkov, J. D. Holmes, and P. J. Parbrook, "Single phase ($112\bar{2}$) AlN grown on ($101\bar{0}$) sapphire by metalorganic vapour phase epitaxy," *Journal of Crystal Growth,* vol. 414, pp. 94-99, 2015.

[23] V. Srikant, J. S. Speck, and D. R. Clarke, "Mosaic structure in epitaxial thin films having large lattice mismatch," *Journal of Applied Physics,* vol. 82, pp. 4286-4295, 1997.

[24] H. Heinke, V. Kirchner, S. Einfeldt, and D. Hommel, "X-ray diffraction analysis of the defect structure in epitaxial GaN," *Applied Physics Letters,* vol. 77, pp. 2145-2147, 2000.

[25] M. A. Moram and M. E. Vickers, "X-ray diffraction of III-nitrides," *Reports on Progress in Physics,* vol. 72, 036502, 2009.

[26] E. F. Schubert, *Doping in III-V Semiconductors*. Cambridge (UK): Cambridge University Press, 1993.

[27] P. Bogusławski and J. Bernholc, "Doping properties of C, Si, and Ge impurities in GaN and AlN," *Physical Review B - Condensed Matter and Materials Physics,* vol. 56, pp. 9496-9505, 1997.

[28] C. H. Park and D. J. Chadi, "Stability of deep donor and acceptor centers in GaN, AlN, and BN," *Physical Review B - Condensed Matter and Materials Physics,* vol. 55, pp. 12995-13001, 1997.

[29] R. Zeisel, M. W. Bayerl, S. T. B. Goennenwein, R. Dimitrov, O. Ambacher, M. S. Brandt*, et al.*, "DX-behavior of Si in AlN," *Physical Review B,* vol. 61, pp. R16283-R16286, Jun 15 2000.

[30] J. Z. Li, J. Y. Lin, H. X. Jiang, A. Salvador, A. Botchkarev, and H. Morkoc, "Nature of Mg impurities in GaN," *Applied Physics Letters,* vol. 69, pp. 1474-1476, 1996.

[31] R. A. Smith, *Semi-conductors*. Cambridge (UK): Cambridge University Press, 1968.

[32] S. M. Sze and K. N. Kwok, *Physics of semiconductor devices* John Wiley & Sons, 2007.

[33] *Semiconductors on NSM*. Available: http://www.ioffe.ru/SVA/NSM/Semicond/index.html [Accessed February 2017]

[34] B. I. Shklovskii and A. L. Efros, *Electronic Properties of Doped Semiconductor* Springer-Verlag, 1984.

[35] H. Böttger and V. V. Bryksin, *Hopping Conduction in Solids* VCH, 1985.

[36] I. Shlimak, *Is Hopping a Science? Selected Topics of Hopping Conductivity* World Scientific Publishing, 2015.

[37] K. B. Nam, J. Li, M. L. Nakarmi, J. Y. Lin, and H. X. Jiang, "Achieving highly conductive AlGaN alloys with high Al contents," *Applied Physics Letters,* vol. 81, pp. 1038-1040, 2002.

[38] H. Fritzsche and M. Cuevas, "Impurity conduction in transmutation-doped p-type germanium," *Physical Review,* vol. 119, pp. 1238-1245, 1960.

[39] H. Morkoç, S. Strite, G. B. Gao, M. E. Lin, B. Sverdlov, and M. Burns, "Large-band-gap SiC, III-V nitride, and II-VI ZnSe-based semiconductor device technologies," *Journal of Applied Physics,* vol. 76, pp. 1363-1398, 1994.

[40] S. Yoshida, S. Misawa, and S. Gonda, "Properties of $Al_xGa_{1-x}N$ films prepared by reactive molecular beam epitaxy," *Journal of Applied Physics,* vol. 53, pp. 6844-6848, 1982.

[41] Y. Koide, H. ltoh, N. Sawaki, and I. Akasakf, "Epitaxial Growth and Properties of $Al_xGa_{1-x}N$ by MOVPE," *Journal of the Electrochemical Society,* vol. 133, pp. 1956-1960, 1986.

[42] V. Adivarahan, G. Simin, G. Tamulaitis, R. Srinivasan, J. Yang, M. Asif Khan*, et al.*, "Indium-silicon co-doping of high-aluminum-content AlGaN for solar blind photodetectors," *Applied Physics Letters,* vol. 79, pp. 1903-1905, 2001.

[43] M. L. Nakarmi, K. H. Kim, K. Zhu, J. Y. Lin, and H. X. Jiang, "Transport properties of highly conductive *n*-type Al-rich $Al_xGa_{1-x}N$ (x≥0.7)," *Applied Physics Letters,* vol. 85, pp. 3769-3771, 2004.

[44] K. Zhu, M. L. Nakarmi, K. H. Kim, J. Y. Lin, and H. X. Jiang, "Silicon doping dependence of highly conductive *n*-type $Al_{0.7}Ga_{0.3}N$," *Applied Physics Letters,* vol. 85, pp. 4669-4671, 2004.

[45] Y. Taniyasu, M. Kasu, and N. Kobayashi, "Intentional control of *n*-type conduction for Si-doped AlN and $Al_xGa_{1-x}N$ (0.42≤x<1)," *Applied Physics Letters,* vol. 81, pp. 1255-1257, 2002.

[46] Y. Taniyasu, M. Kasu, and T. Makimoto, "Electrical conduction properties of *n*-type Si-doped AIN with high electron mobility (>100 $cm^2 V^{-1} s^{-1}$)," *Applied Physics Letters,* vol. 85, pp. 4672-4674, 2004.

[47] Y. Taniyasu, M. Kasu, and T. Makimoto, "An aluminium nitride light-emitting diode with a wavelength of 210 nanometres," *Nature,* vol. 441, pp. 325-328, 2006.

[48] R. Collazo, S. Mita, J. Xie, A. Rice, J. Tweedie, R. Dalmau*, et al.*, "Progress on n-type doping of AlGaN alloys on AlN single crystal substrates for UV optoelectronic applications," *Physica Status Solidi (C) Current Topics in Solid State Physics,* vol. 8, pp. 2031-2033, 2011.

[49] C. Stampfl and C. G. Van De Walle, "Doping of $Al_xGa_{1-x}N$," *Applied Physics Letters,* vol. 72, pp. 459-461, 1998.

[50] C. Stampfl, J. Neugebauer, and C. G. Van De Walle, "Doping of $Al_xGa_{1-x}N$ alloys," *Proceedings of the 1998 Symposium L: on Nitrides and Related Wide Band Gap Materials (E-MRS Meeting),* vol. 59, pp. 253-257, 1999.

[51] C. G. Van De Walle, C. Stampfl, J. Neugebauer, M. D. McCluskey, and N. M. Johnson, "Doping of AlGaN alloys," *MRS Internet Journal of Nitride Semiconductor Research,* vol. 4, 1999.

[52] C. G. Van De Walle, "DX-center formation in wurtzite and zinc-blende $Al_xGa_{1-x}N$," *Physical Review B - Condensed Matter and Materials Physics,* vol. 57, pp. R2033-R2036, 1998.

[53] W. Götz, J. Walker, L. T. Romano, N. M. Johnson, and R. J. Molnar, "Thickness dependence of electronic properties of GaN epilayers," in *Proceedings of the 1996 MRS Fall Symposium*, Pittsburgh, PA, United States Boston, MA, USA, 1997, pp. 525-530.

[54] W. Götz, L. T. Romano, J. Walker, N. M. Johnson, and R. J. Molnar, "Hall-effect analysis of GaN films grown by hydride vapor phase epitaxy," *Applied Physics Letters,* vol. 72, pp. 1214-1216, 1998.

[55] D. C. Look and R. J. Molnar, "Degenerate layer at GaN/sapphire interface: Influence on Hall-effect measurements," *Applied Physics Letters,* vol. 70, pp. 3377-3379, 1997.

[56] X. T. Trinh, D. Nilsson, I. G. Ivanov, E. Janzén, A. Kakanakova-Georgieva, and N. T. Son, "Stable and metastable Si negative-U centers in AlGaN and AlN," *Applied Physics Letters,* vol. 105, 162106, 2014.

[57] D. Nilsson, X. T. Trinh, E. Janzén, N. T. Son, and A. Kakanakova-Georgieva, "On the behavior of silicon donor in conductive $Al_xGa_{1-x}N$ (0.63 ≤x≤ 1)," *Physica Status Solidi (B) Basic Research,* vol. 252, pp. 1306-1310, 2015.

[58] K. Forghani, L. Schade, U. T. Schwarz, F. Lipski, O. Klein, U. Kaiser*, et al.*, "Strain and defects in Si-doped (Al)GaN epitaxial layers," *Journal of Applied Physics,* vol. 112, 093102, 2012.

[59] F. Mehnke, T. Wernicke, H. Pingel, C. Kuhn, C. Reich, V. Kueller*, et al.*, "Highly conductive n-$Al_xGa_{1-x}N$ layers with aluminum mole fractions above 80%," *Applied Physics Letters,* vol. 103, p. 212109, 2013.

[60] H. Amano, M. Kito, K. Hiramatsu, and I. Akasaki, "P-type conduction in Mg-doped GaN treated with low-energy electron beam irradiation (LEEBI)," *Japanese Journal of Applied Physics,* vol. 28, pp. L2112-L2114, 1989.

[61] S. Nakamura, N. Iwasa, M. Senoh, and T. Mukai, "Hole Compensation Mechanism of P-Type GaN Films," *Japanese Journal of Applied Physics,* vol. 31, pp. 1258-1266, 1992.

[62] A. Khan, K. Balakrishnan, and T. Katona, "Ultraviolet light-emitting diodes based on group three nitrides," *Nature Photonics,* vol. 2, pp. 77-84, 2008.

[63] C. Pernot, S. Fukahori, T. Inazu, T. Fujita, M. Kim, Y. Nagasawa*, et al.*, "Development of high efficiency 255-355 nm AlGaN-based light-emitting diodes," *Physica Status Solidi (A) Applications and Materials Science,* vol. 208, pp. 1594-1596, 2011.

[64] H. Hirayama, N. Maeda, S. Fujikawa, S. Toyoda, and N. Kamata, "Recent progress and future prospects of AlGaN-based high-efficiency deep-ultraviolet light-emitting diodes," *Japanese Journal of Applied Physics,* vol. 53, 100209, 2014.

[65] S. Krishnamoorthy, D. N. Nath, F. Akyol, P. S. Park, M. Esposto, and S. Rajan, "Polarization-engineered GaN/InGaN/GaN tunnel diodes," *Applied Physics Letters,* vol. 97, 203502, 2010.

[66] Y. Zhang, S. Krishnamoorthy, J. M. Johnson, F. Akyol, A. Allerman, M. W. Moseley*, et al.*, "Interband tunneling for hole injection in III-nitride ultraviolet emitters," *Applied Physics Letters,* vol. 106, 141103, 2015.

[67] T. Tanaka, A. Watanabe, H. Amano, Y. Kobayashi, I. Akasaki, S. Yamazaki*, et al.*, "*p*-type conduction in Mg-doped GaN and $Al_{0.08}Ga_{0.92}N$ grown by metalorganic vapor phase epitaxy," *Applied Physics Letters,* vol. 65, pp. 593-594, 1994.

[68] L. Sugiura, M. Suzuki, J. Nishio, K. Itaya, Y. Kokubun, and M. Ishikawa, "Characteristics of Mg-doped GaN and AlGaN grown by H_2-ambient and N_2-ambient metalorganic chemical vapor deposition," *Japanese Journal of Applied Physics, Part 1: Regular Papers and Short Notes and Review Papers,* vol. 37, pp. 3878-3881, 1998.

[69] M. Suzuki, J. Nishio, M. Onomura, and C. Hongo, "Doping characteristics and electrical properties of Mg-doped AlGaN grown by atmospheric-pressure MOCVD," *Journal of Crystal Growth,* vol. 189-190, pp. 511-515, 1998.

[70] J. Li, T. N. Oder, M. L. Nakarmi, J. Y. Lin, and H. X. Jiang, "Optical and electrical properties of Mg-doped *p*-type $Al_xGa_{1-x}N$," *Applied Physics Letters,* vol. 80, pp. 1210-1212, 2002.

[71] K. B. Nam, M. L. Nakarmi, J. Li, J. Y. Lin, and H. X. Jiang, "Mg acceptor level in AlN probed by deep ultraviolet photoluminescence," *Applied Physics Letters,* vol. 83, pp. 878-880, 2003.

[72] F. Mireles and S. E. Ulloa, "Acceptor binding energies in GaN and AlN," *Physical Review B - Condensed Matter and Materials Physics,* vol. 58, pp. 3879-3887, 1998.

[73] S. R. Jeon, Z. Ren, G. Cui, J. Su, M. Gherasimova, J. Han*, et al.*, "Investigation of Mg doping in high-Al content p-type $Al_xGa_{1-x}N$ (0.3 < x < 0.5)," *Applied Physics Letters,* vol. 86, 082107, Feb 21 2005.

[74] A. Chakraborty, C. G. Moe, Y. Wu, T. Mates, S. Keller, J. S. Speck*, et al.*, "Electrical and structural characterization of Mg-doped p-type $Al_{0.69}Ga_{0.31}N$ films on SiC substrate," *Journal of Applied Physics,* vol. 101, 053717, 2007.

[75] T. Kinoshita, T. Obata, H. Yanagi, and S. Inoue, "High p-type conduction in high-Al content Mg-doped AlGaN," *Applied Physics Letters,* vol. 102, 012105, Jan 7 2013.

[76] G. Kusch, M. Nouf-Allehiani, F. Mehnke, C. Kuhn, P. R. Edwards, T. Wernicke*, et al.*, "Spatial clustering of defect luminescence centers in Si-doped low resistivity $Al_{0.82}Ga_{0.18}N$," *Applied Physics Letters,* vol. 107, 072103, 2015.

[77] E. Philofsky, "Intermetallic formation in gold-aluminum systems," *Solid State Electronics,* vol. 13, pp. 1391-1394, 1970.

[78] P. Pampili, V. Z. Zubialevich, D. V. Dinh, H. Li, and P. J. Parbrook, "Optimization study of *n*-type doping of $Al_xGa_{1-x}N$ (0.50≤x≤0.85)," *in preparation*.

[79] T. Markurt, L. Lymperakis, J. Neugebauer, P. Drechsel, P. Stauss, T. Schulz*, et al.*, "Blocking growth by an electrically active subsurface layer: The effect of si as an antisurfactant in the growth of GaN," *Physical Review Letters,* vol. 110, 036103, 2013.

[80] R. Armitage, Q. Yang, and E. R. Weber, "P- and N-type doping of non-polar A-plane GaN grown by molecular-beam epitaxy on R-plane sapphire," *MRS Internet Journal of Nitride Semiconductor Research,* vol. 8, 2003.

[81] M. McLaurin, T. E. Mates, F. Wu, and J. S. Speck, "Growth of p-type and n-type m-plane GaN by molecular beam epitaxy," *Journal of Applied Physics,* vol. 100, 063707, 2006.

[82] K. H. Baik, Y. G. Seo, S. K. Hong, S. Lee, J. Kim, J. S. Son*, et al.*, "Effects of basal stacking faults on electrical anisotropy of nonpolar a-plane (11$\bar{2}$0) GaN light-emitting diodes on sapphire substrate," *IEEE Photonics Technology Letters,* vol. 22, pp. 595-597, 5419048, 2010.

[83] A. Kasic, M. Schubert, S. Einfeldt, D. Hommel, and T. E. Tiwald, "Free-carrier and phonon properties of n- and p-type hexagonal GaN films measured by infrared ellipsometry," *Physical Review B - Condensed Matter and Materials Physics,* vol. 62, pp. 7365-7377, 2000.

[84] I. Vurgaftman and J. R. Meyer, "Band parameters for nitrogen-containing semiconductors," *Journal of Applied Physics,* vol. 94, pp. 3675-3696, 2003.

[85] A. Konar, T. Fang, N. Sun, and D. Jena, "Charged basal stacking fault scattering in nitride semiconductors," *Applied Physics Letters,* vol. 98, 022109, 2011.

[86] D. V. Dinh, P. Pampili, and P. J. Parbrook, "Silicon doping of semipolar (11-22) $Al_xGa_{1-x}N$ (0.50≤x≤0.55)," *Journal of Crystal Growth,* vol. 451, pp. 181-187, 2016.

[87] K. Balakrishnan, V. Adivarahan, Q. Fareed, M. Lachab, B. Zhang, and A. Khan, "First demonstration of semipolar deep ultraviolet light emitting diode on m-plane sapphire with AlGaN multiple quantum wells," *Japanese Journal of Applied Physics,* vol. 49, pp. 0402061-0402063, 2010.

[88] C. Chen, V. Adivarahan, J. Yang, M. Shatalov, E. Kuokstis, and M. A. Khan, "Ultraviolet light emitting diodes using non-polar a-plane GaN-AlGaN multiple quantum wells," *Japanese Journal of Applied Physics, Part 2: Letters,* vol. 42, pp. L1039-L1040, 2003.

[89] H. M. Ng, D. Doppalapudi, T. D. Moustakas, N. G. Weimann, and L. F. Eastman, "The role of dislocation scattering in n-type GaN films," *Applied Physics Letters,* vol. 73, pp. 821-823, 1998.

[90] C. S. Hung and J. R. Gliessman, "Resistivity and Hall Effect of Germanium at Low Temperatures," *Physical Review,* vol. 96, pp. 1226-1236, 1954.

[91] R. J. Molnar, T. Lei, and T. D. Moustakas, "Electron transport mechanism in gallium nitride," *Applied Physics Letters,* vol. 62, pp. 72-74, 1993.

[92] C. Mavroidis, J. J. Harris, M. J. Kappers, C. J. Humphreys, and Z. Bougrioua, "Detailed interpretation of electron transport in *n*-GaN," *Journal of Applied Physics,* vol. 93, pp. 9095-9103, 2003.

[93] P. P. Debye and E. M. Conwell, "Electrical properties of N-type germanium," *Physical Review,* vol. 93, pp. 693-706, 1954.

[94] W. Götz, R. S. Kern, C. H. Chen, H. Liu, D. A. Steigerwald, and R. M. Fletcher, "Hall-effect characterization of III-V nitride semiconductors for high efficiency light emitting diodes," *Materials Science and Engineering B: Solid-State Materials for Advanced Technology,* vol. 59, pp. 211-217, 1999.

4 Fabrication of UV LEDs

This chapter focuses on the fabrication work carried out to manufacture UV LEDs. The initial part of the work was supported by Dr. Mahbub Akhter, with whom I collaborated in particular during the transfer of the μ-LED process from the GaN-based visible devices—for which it was originally developed—to the AlGaN-based UV LEDs object of my research.

Later devices and their optimization were carried out independently, including all fabrication on UV LED devices based on InAlN active regions. This entailed personally performing all the fabrication steps, including photolithography, dry etches, deposition of passivation layers, chemical pre-treatment and post-deposition thermal annealing of the contacts. In compliance with our clean-room regulations, the actual metal evaporation runs were instead performed by Tyndall personnel according to our recipes, which I also contributed to optimize.

Although I had the chance to oversee the whole fabrication flow of different types of devices, most of the work that I have done has focused on the study of the μ-LED emitters and, most especially, on the optimization of their contacts. Both of these topics will be detailed in the next two sections of this chapter; the introductory parts, including literature research and some theoretical preambles, are based on a book chapter on UV LEDs that I co-authored with Prof. Peter Parbrook, which is currently under review by the editors.

4.1 The μ-LED concept

The use of micron-sized emitters is a well-established fabrication approach that was originally developed for visible devices in the early 2000s, especially by the work of Jiang and Lin at the Kansas State University [1, 2]. Devices consisting of clusters of closely-packed μ-LEDs were compared with standard flat LEDs having the same dimensions and, despite the reduced effective area, μ-LED clusters showed a significantly increased efficiency, which was attributed to a more efficient distribution of the current, and to an enhancement of LEE. In addition to that, other beneficial features of this approach are the reduced parasitic capacitance, which leads to faster turn-on and turn-off times [3], and the lowering of strain, which reduces the internal piezoelectric field

partially responsible for the spatial separation of electrons and holes in the QWs [4], the already cited QCSE (Cf. Section 2.5)

Based on these promising results, other groups also started to work on μ-LED emitters, further improving some of their potentialities. As a result of these extensive research efforts a few patents were also filed relative to different implementations of this concept [5-7]. In particular, the work of Corbett and co-workers here at the Tyndall National Institute proved to be particularly useful in order to achieve an enhancement of LEE while at the same time allowing a good coupling with optical components having reduced acceptance angles [8]. With this implementation, the individual μ-LEDs that compose the final device have smooth, reflective, and quasi-parabolically shaped sidewalls that are obtained by a specially optimized dry-etch process, a configuration that allows the light emitted at larger angles to be reflected back, at almost perpendicular angles, towards the sapphire substrate. As shown in Figure 4.1, this not only allows extraction of a significant part of the light that would otherwise be trapped because of total internal reflection, but also changes the far-field pattern so that most of the UV radiation is emitted perpendicularly.

Due to the success of this approach with visible devices, it was decided to implement this fabrication concept for UV LEDs, the object of this thesis. In particular with regard to the deep-UV LED designed for the charge management system of the LISA space mission [9], it was thought that shaping the devices in the form of μ-LED clusters would have helped increasing the coupling efficiency with the optical fibre necessary to transfer the UV radiation to the proof-mass [10], and also would have been beneficial for achieving the high optical-bandwidth required by the application [11].

The effectiveness of these two design choices will be discussed with more details in Chapter 5, where the experimental characterization of the devices will be reported. This chapter, on the contrary, focuses more on the description of the fabrication strategies adopted, and the related issues.

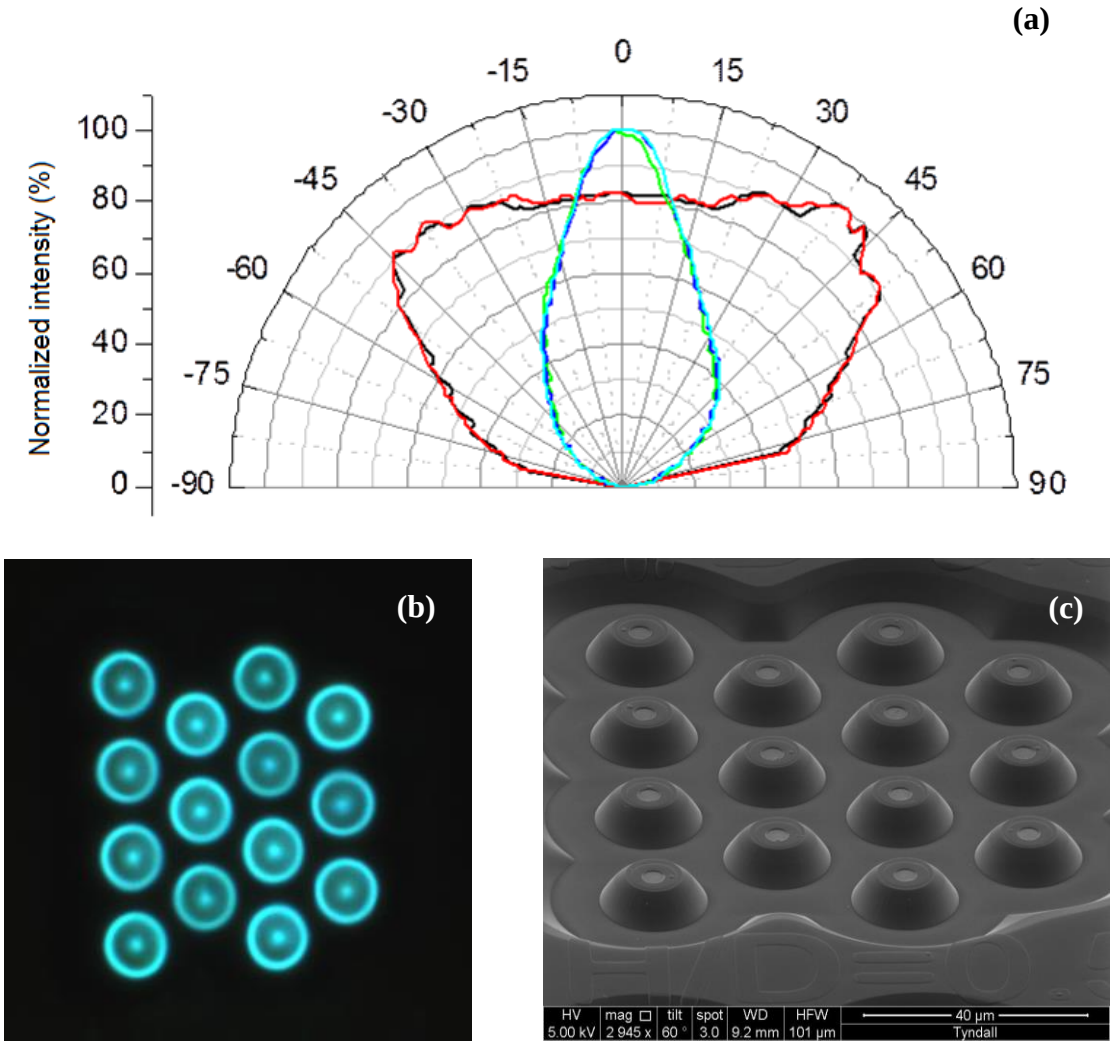

Figure 4.1: Near- and far-field patterns of µ-LED clusters

The normalized far-field patterns of a few µ-LED clusters (blue, cyan and green lines), and non-shaped standard devices (red and black lines) are compared to show the reduction in the emission angles (a). From the near-field image of one of the µ-LED clusters (b), the increased intensity at the circular sidewalls of each µ-LED is also apparent; an SEM image of a similar cluster is also shown for reference (c). The graph and the images are relative to visible LEDs from previous projects, and are shown with the permission of Dr. M. Akhter.

4.1.1 Fabrication of µ-LED emitters

The *standard* fabrication flow as it was designed at the beginning of the project, before any further optimization, is here briefly outlined.

The process starts with a cleaning of the samples in room-temperature Buffered Oxide Etch (BOE) and HCl for five minutes each, followed by a 30 s dip in a solution of KOH in deionized water (45 wt%) at 90 °C. This is our standard procedure to remove oxides,

metal and organic contaminants from the samples, which we routinely use as the first step of all our fabrication activities. The fact that AlGaN materials—particularly those with a high AlN content—oxidise much faster than GaN [12], suggests that this chemical pre-treatment has to be considered an essential part of the process, especially in case of deep-UV devices.

After the cleaning, the samples are immediately prepared for the first photolithography step, which was decided to be the *p*-type contact definition. The rationale behind this choice was to deposit the *p*-metal, a critical step for the device, when the surface is still perfectly cleaned, before it had undergone any other process that might have caused its degradation. The drawback of this solution is that the following thermal treatments—particularly any possible annealing of the *n*-contacts—are limited by the maximum temperature that the *p*-contacts can withstand without being damaged, which for the *p*-metal of our choice (40 nm of Pd) is no more than about 600 °C, well below the optimal annealing temperatures required by high-quality *n*-contact schemes to Al-rich AlGaN materials, as will be detailed in Section 4.2.4. The Pd film is then deposited by e-beam evaporation in a Temescal FC2000 equipment and, after the lift-off of excess metal, the contacts left on the sample consist of clusters of dots having a diameter of 8 μm each that will become the tops of the μ-LED emitters. No annealing is included at this stage.

The following step is the dry etch necessary to expose the *n*-type cladding-layer, which is achieved using a standard, Cl_2-based recipe on an Oxford plasmalab System 100. This is subsequently followed by the deposition, again by e-beam evaporation, of a sequence of Ti/Al/Ti/Au metals, with thicknesses of 20, 170, 5 and 100 nm, respectively. Due to the already mentioned temperature constraints, no annealing was included in the standard fabrication flow also for the *n*-contacts.

The next step, the most critical one in the whole μ-LED process, is the definition of the sidewalls by dry etch. Initially a thick resist—e.g. AZ4562, which has a target thickness of about 7 μm at 3,000 rpm—is spin-coated on the sample, and then exposed to form sets of "cylinders" in correspondence of the *p*-contact dots. After photolithography, the resist "cylinders", which have their diameter equal to the basal diameter of the final μ-LED, are reflown in oven at 140 °C for 3 to 4 hours in order to obtain the parabolic sidewalls shown in Figure 4.2 (a). The shape so obtained is then transferred into the material by means of a carefully optimized, BCl_3-based, dry-etch step implemented on an STS

Multiplex ICP etcher, which is able to provide an etch selectivity between the resist and the AlGaN material of roughly 1:1, as well as very smooth surfaces. The final μ-LED emitter, and a schematic of this process are shown in Figure 4.2 (b) and (c), respectively.

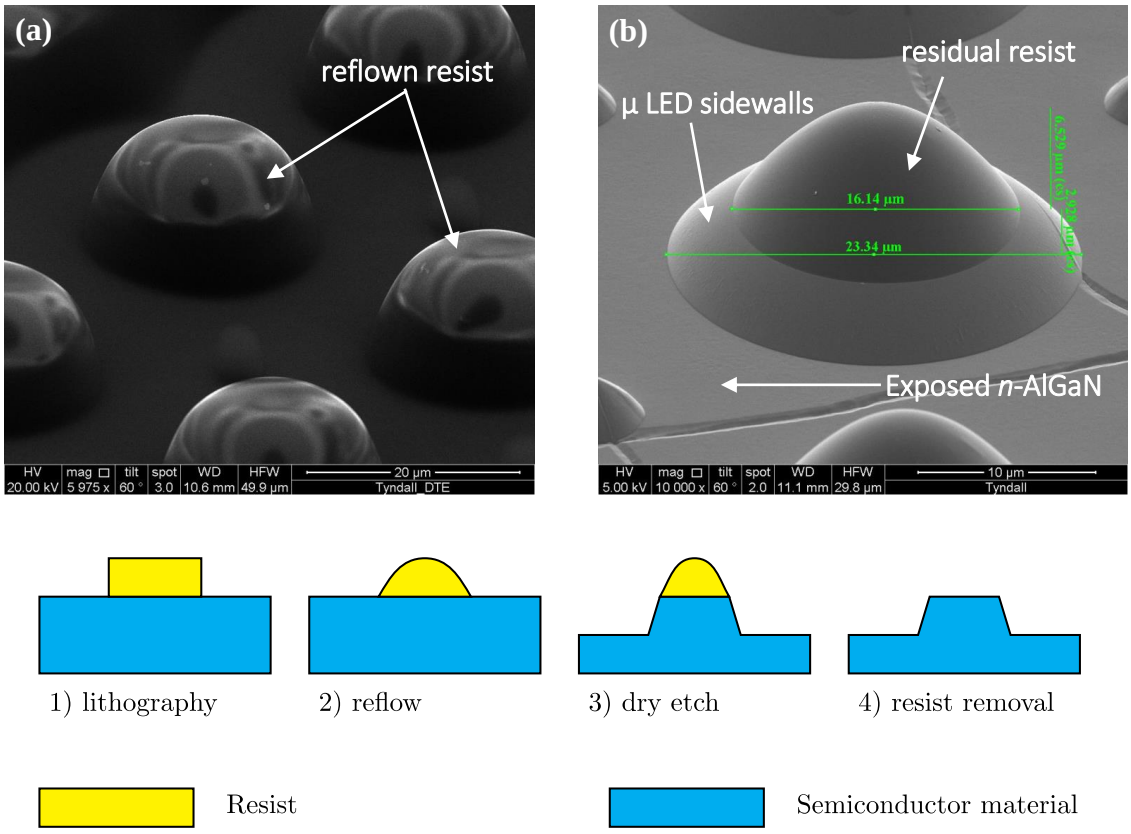

Figure 4.2: Formation of the sidewalls

The formation mechanism of the μ-LED sidewalls is illustrated with two SEM images taken before and after the dry etch. Thank to the high-temperature reflow of the resist, the area of the sample where the emitters will be formed is covered with resist domes having roughly the same shape as the final μ-LEDs (a). By means of a dry etch with a resist/AlGaN selectivity close to 1:1, the shape of the resist domes is transferred into the semiconductor material (b). From the measurements reported on the image, a sidewall angle of 39° can be calculated. For clarity, a schematic of the whole μ-LED fabrication sequence is also shown (c). SEM images by Dr. M. Akhter.

Because the sidewall-shaping etch also exposes the edges of the active region, to avoid any risk of contamination, a passivation step is performed as soon as possible after having removed all the resist residues from the sample: typically 300 nm of SiO_2 are hence blanket-deposited using an Oxford plasmalab 400 magnetron sputterer.

Openings on the passivation layer are then created in correspondence of the contacts, by a standard F-based dry etch on an STS Multiplex ICP etcher. A final photolithographic step and subsequent evaporation of Ti/Au (30 and 300 nm, respectively) is necessary to electrically connect the *p*-contacts of all the µ-LEDs present in each cluster, and to define the metal pads necessary for wire-bonding or *on-chip* testing of the devices.

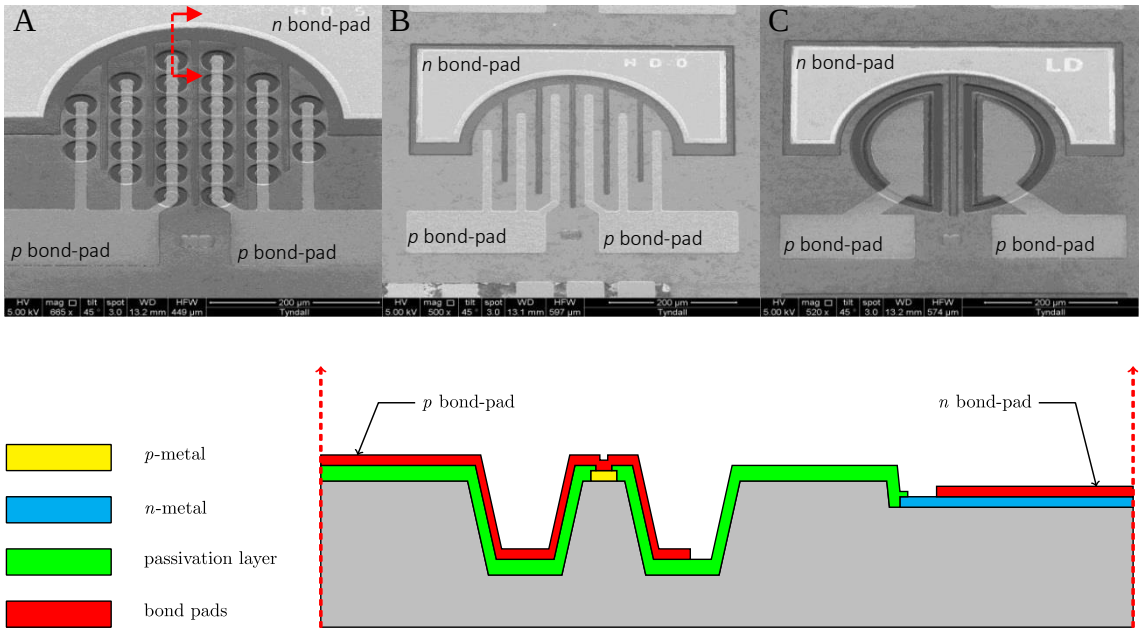

Figure 4.3: Type of devices

SEM images of the three types of devices fabricated. Type A consists of two clusters of 15 µ-LED emitters each; the *p*-contacts have a diameter of 8 µm. Type B has the same geometry as type A, except that the semiconductor around each emitter has not been shaped to form separated µ-LEDs. Type C consists of two half-disc emitters having a diameter of 270 µm. A cross section of one µ-LED emitter of the type-A device is also included for clarity. SEM images by Dr. M. Akhter.

The final appearance of the device is shown in Figure 4.3 (a), where two clusters of 15 µ-LEDs each are clearly visible at the centre of the image, together with two independent *p*-contact pads and a common *n*-contact pad, respectively below and above the emitters. The presence of two independently controllable µ-LED clusters in each final device is due to redundancy reasons, a solution that was deemed necessary for the reliability of the whole charge management system during the space mission. In order to evaluate the effectiveness of the µ-LED shaping, two other types of devices were also fabricated, in parallel with the target one, for comparison. The first one, shown in Figure 4.3 (b), has the exact same geometry, but do not present any sidewall shaping nor any mesa

definition; the second one, shown in Figure 4.3 (c), consists of two standard large-area LEDs that occupy the same area as the μ-LED clusters.

4.1.2 Discussion of the critical points of the process

Although the process briefly described in the previous section is mostly the result of experience in the fabrication of visible LEDs, its transfer to the AlGaN-based UV LEDs required some adaptation work.

First, the sidewall-shaping etch, which in order to obtain the high aspect-ratio necessary to achieve the ideal far-field emission shown in Figure 4.1 (a) should be extended to depths up to 10 μm [8], is constrained by the much reduced thickness of the *n*-type cladding layers present in UV LEDs compared with those of visible devices. As discussed in Section 3.3.1, *n*-doped AlGaN epilayers grown on AlN templates can only extend for a few μm before they start to relax forming cracks or dislocations that propagate through the active region, greatly reducing the IQE of the device. However, a highly conductive layer must be present below the base of the μ-LEDs to allow the current injected at the *n*-contact to enter freely inside each shaped emitter. Although, as shown in Figure 4.2 (b), we did manage to obtain sidewall angles very close to the target value of 45°, this was possible for etch depths of about 3 μm, which are still too large to allow satisfactory injection of current in the μ-LEDs. In shallower etches, the sidewall angles are much less controllable.

Another important consequence of the limited depth of the sidewall-shaping etch is that the flat region at the top of each μ-LED was somewhat larger than what was originally anticipated. As can be seen in Figure 4.2 (b), the upper diameter of the μ-LED is about 16 μm, while the Pd metal dot through which the current is injected has a diameter of only 8 μm. In addition to the significant underutilization of the area available for current injection, the fact that the 50-nm-thick *p*-GaN contact-layer extends even outside the small metal dot over the whole μ-LED top, causes an unnecessarily large UV absorption.

In order to estimate the effects of this absorption and partially mitigate problem, the excess *p*-GaN outside the contact was then removed. Using the metal dots as a hard mask to protect the *p*-GaN below the contacts from the effects of the dry etch, about 70 nm of material was removed after the formation of the μ-LEDs and before the deposition of the passivation layer. While the shaping of the sidewalls was not significantly affected, this etch was still able to completely remove the unused *p*-GaN material not protected by the

metal. The EL data reported in Figure 4.4 show a ~50% increase of the UV peak emission in the device that was subject to this extra etch. Although this modification of the standard fabrication flow was made necessary by the presence of *p*-contacts that were significantly smaller than the flat area on top of the μ-LEDs, even with a new and optimized mask with larger contacts, this step might still be useful as the actual depth of the sidewall-shaping etch—and hence the dimensions of the flat area—can slightly change from run to run due to small variations of the etch rate caused by changes in the material composition or by instabilities of the dry-etch equipment. In addition to that, because the tolerances relative to the photolithographic alignment can be estimated—with the equipment available in our fab—to be around a couple of μm, the metal dots cannot in any case cover the entire μ-LED flat-tops.

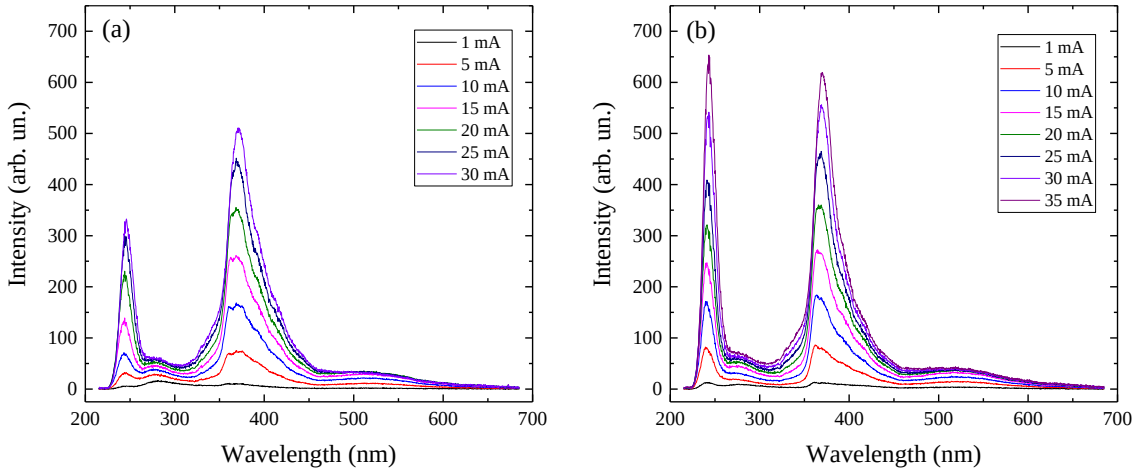

Figure 4.4: Removal of the excess *p*-GaN

EL measurements, at different injection currents, of a μ-LED fabricated according to the standard process (a), and with the removal of excess *p*-GaN by shallow dry etch (b). Both data were recorded from a device of type A (Cf. Figure 4.3).

The fact that the area covered by the metal dots, which can be thought as the effective area of the device, only accounts for less than 3% of the total area occupied by the μ-LED clusters is another important limitation of the current design. This was not an issue with the ESA-funded project, in which—for reliability reasons—the focus was to optimize the extraction and coupling of UV radiation rather than its actual power. However, in order to extend this approach to other applications and to be able to compete with traditional large-area LEDs also in terms of total power, the available area needs to be used much more efficiently. In addition to extending the metal dots so that they can cover most of the

flat tops, this can be achieved especially by making the μ-LED cluster much denser. Although the presence of the slanted sidewalls poses a limit on the minimum pitch distance between μ-LEDs, there is still room for a large improvement, especially considering that being shallower than the visible ones, our UV μ-LEDs are also thinner and can be packed more closely.

The other major issue with the standard fabrication process was the fact that the non-annealed *p*- and *n*-contacts were both rather poor. While we managed to achieve a somewhat ohmic behaviour from the *p*-contacts (Cf. Section 4.2.5), the *n*-contacts always showed some degree of non-ohmic behaviour, despite all the efforts made to improve their quality. In addition to that, the fully fabricated devices showed very high forward-drop voltages, in some cases as high as 50 V at 14 mA. While, as discussed in Chapter 3, this problem was certainly exacerbated by the sub-optimal doping of both cladding layers, the choice of depositing the *n*-contact after the *p*-contact and the consequent impossibility to perform an adequate thermal annealing as common for Al-rich AlGaN materials, proved to be a serious limitation of the standard fabrication approach.

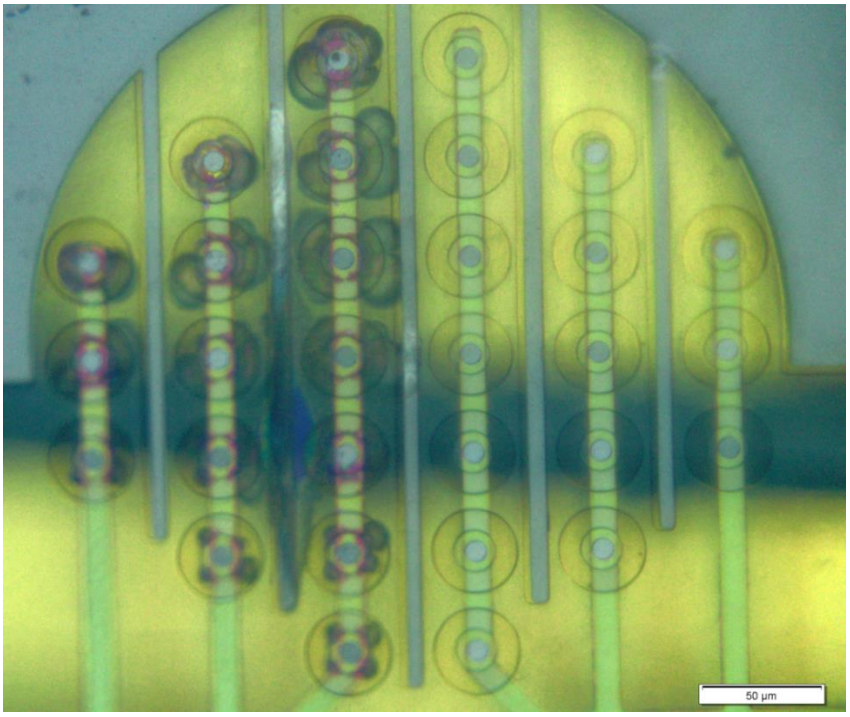

Figure 4.5: Degradation of the passivation layer

Optical microscopy image of a μ-LED device after a lifetime test of 100 h; only the left-hand-side cluster was used for the test.

In addition to causing a significant reduction of the EE, the high operating voltage of the μ-LEDs have also important consequences on the reliability of the device. As shown in Figure 4.5, which was taken after a 100-h-long lifetime-test, the presence of discolorations around the μ-LED emitters of the left-hand-side cluster, clearly indicate a degradation of the passivation layer that needs to be addressed. While an improvement of the *p*-contacts might be sufficient to solve this problem, the passivation layer—whose thickness was decided based on the experience from visible μ-LEDs—might also require further optimization work, which—due to time constraints—was not possible to include at this stage of the development.

Although all these considerations suggest that there is room for a great deal of optimization in many aspects of the process flow, the main factor limiting the performance of our device, for its consequences both in terms of EE and reliability, appeared to be the quality of the contacts. This justifies the line of research that I have decided to undertake, which is discussed in the remaining of this chapter.

4.2 Optimization of the contacts

4.2.1 Schottky-Mott theory

The first theory about carrier transport across metal–semiconductor junctions was independently proposed by Schottky [13] and Mott [14], and is based on the assumption that the vacuum levels of the metal and the semiconductor simply align with each other as shown in Figure 4.6 (a), even after the two materials are brought into close contact. This level, which corresponds to the rest energy of an electron that has been extracted from the material and brought just outside its surface, can also be used as a common reference to express other energy quantities. In particular, the difference with the Fermi level of the metal is indicated as the metal work function (Φ_M), while the one with the bottom of the conduction band is indicated as the electron affinity of the semiconductor (χ). According to the Schottky-Mott theory, these are the only two quantities that affect the band alignment at the interface, which in turn influences the transport across the junction.

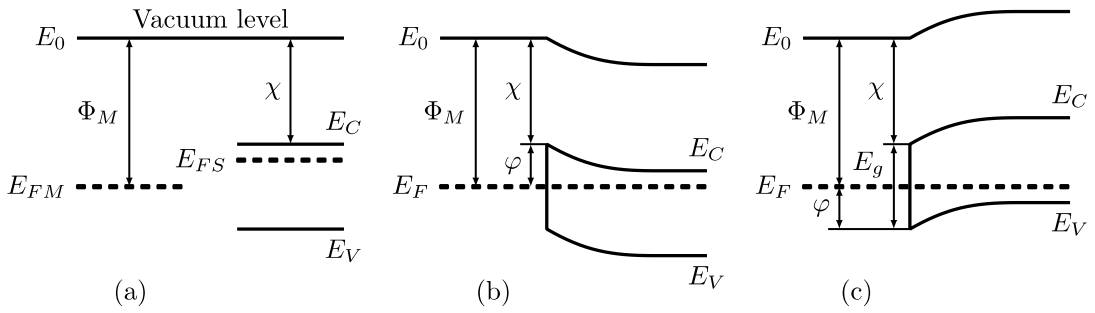

Figure 4.6: Formation of the Schottky barrier

Alignment of the vacuum level in the metal and in the semiconductor (a); formation of a Schottky barrier in *n*-type (b) and *p*-type (c) semiconductors with depletion of majority carriers in the area close to the junction with the metal. The symbols E_{FM}, E_{FS} and E_F indicate the Fermi levels of the metal, the semiconductor and the metal–semiconductor system, respectively; E_V the top edge of the valence band; E_C the bottom edge of the conduction band; E_0 the vacuum level. The other symbols are explained in the text.

In case of an LED, the metal–semiconductor junctions must be able to efficiently inject electrons from the metal into the *n*-type cladding layer, as well as holes into the *p*-type one. Because the carriers that take part in the metallic transport are those close to the Fermi level, this one should ideally be aligned with the bottom of the conduction band or with the top of the valence band of the semiconductor, for an optimal injection into *n*-type and *p*-type semiconductors, respectively. Unfortunately these conditions are practically never met and, as evident from Figure 4.6, a potential barrier φ most often appears at the interface, whose height can be calculated as:

$$\varphi = \Phi_M - \chi\,, \tag{4.1}$$

for *n*-type semiconductors, or as:

$$\varphi = \chi + E_g - \Phi_M\,, \tag{4.2}$$

for the *p*-type ones, where E_g is the bandgap of the semiconductor. Although some electrons may still overcome this so-called Schottky barrier by thermionic emission, its presence greatly hinders the carrier injection and should be kept as low as possible by choosing metals with low work functions when they are used as *n*-contacts and, conversely, metals with high work functions in case of *p*-contacts.

In thermodynamic equilibrium the Fermi level must be constant throughout the whole metal–semiconductor system, thus after the metal deposition some rearrangement of carriers across the junction also inevitably happens. This charge redistribution causes an accumulation or a depletion of electrons or holes in a small region of the semiconductor close to the junction, which is responsible for the band bending shown e.g. in Figure 4.6 (b) for a depletion of electrons, and Figure 4.6 (c) for a depletion of holes; accumulations of carriers, although theoretically possible, rarely happen in practice for real contacts. The thickness of this depletion region is the other key parameter that affects the transport across the junction. In fact, because the thickness is strictly dependent on the doping level of the semiconductor, if this is sufficiently increased the depletion region might shrink enough for the transport due to tunnelling to become comparable with thermionic emission (thermionic–field emission regime), and eventually even become the dominant mechanism (field emission).

Unfortunately, this very simple and elegant model fails to accurately describe the contact formation in many semiconductor materials, as the height of the Schottky barrier has often been found to be only weakly dependent on the work function of the metal. This phenomenon, which is often referred to as the *pinning* of the Fermi level, is generally believed to be caused by the formation of states localised at the metal–semiconductor interface, whose energy levels lie in the bandgap of the semiconductor. They were initially attributed to generic surface states of the semiconductor, and the mechanism of pinning also involved the presence of a thin separation gap (possibly due to an oxide layer) between metal and semiconductor [15, 16]. This assumption, which was somehow justified by the technology available in the early stages of research in this field, was eventually relaxed in more advanced models subsequently proposed, which instead invoke the presence of the so-called Metal Induced Gap States (MIGS) [17, 18].

Irrespective of the origin of the pinning effect, many researchers focused their work on trying to find a correlation between some properties of the semiconductors and the degree of pinning experimentally detected in the height of the Schottky barriers. With this regard, the work of Kurtin *et al*. [19] is often cited in the field of III-nitride materials, as the justification for the use of the Schottky-Mott theory in this semiconductor system. In fact, based on the analysis of the experimental results available in literature at that time, the authors concluded that the pinning effect shows a very strong correlation with the degree of "ionicity" of the semiconductor, and while it is very strong in covalent

semiconductors such as Si and Ge, it significantly decreases in highly-ionic compound semiconductors, the category to which III-nitride materials belong.

However, notwithstanding all these arguments, the details of the Schottky barrier formation are still far from being fully understood; the very existence of the pinning effect has even been recently put in doubt altogether [20], as new experimental evidence suggests that epitaxial contacts do not actually show any form of it. In addition to that, the presence of large spatial inhomogeneities in the Schottky barriers of conventional, non-epitaxial contacts was also experimentally proven, which might be the reason for the weak dependence on the metal work function of their *apparent* barrier-height. Whatever the case, the Schottky-Mott theory can still be considered a useful approximation of the physics of metal–semiconductor junctions and, certainly for the III-nitride materials, it is at least able to explain the general trend in the available experimental data, as summarized for example in Figure 4.7 for the case of GaN.

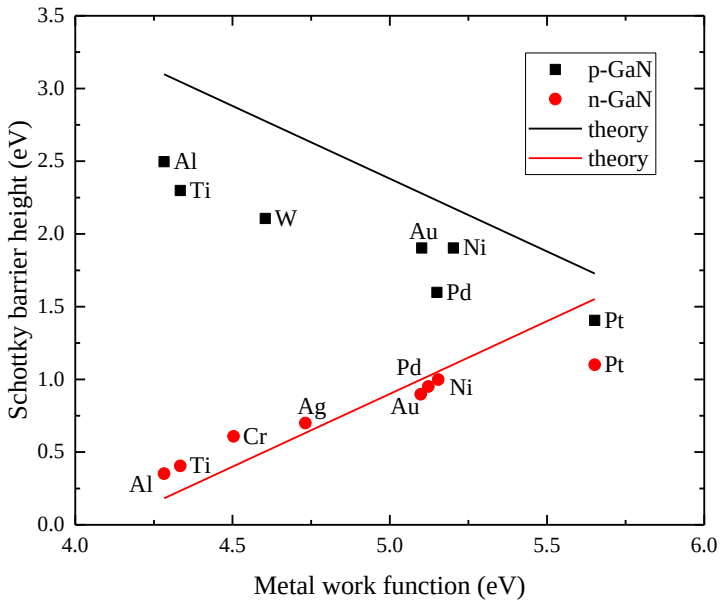

Figure 4.7: Validity of the Schottky-Mott model in GaN

Height of the Schottky barriers formed by different metals with GaN; the data were taken from the list of the most significant works present in the literature of ohmic contact to GaN, as from the review paper by Greco *et al.* [21]. The lines indicate the theoretical values according the Schottky-Mott model; an electron affinity of 4.1 eV and a bandgap of 3.4 eV were assumed for GaN.

4.2.2 Fabrication of the metal contacts

In order to obtain these metal–semiconductor junctions in real devices, thin metallic films—often consisting of multiple layers of different of high-purity metals—need to be deposited in a controllable way on the surface of the semiconductor materials. This can be achieved in many different ways, most notably by vacuum evaporation and sputtering.

In vacuum evaporation, the different metals required by the metallisation scheme are sequentially heated up in an evaporation chamber in which a high vacuum level ($< 10^{-5}$ Torr) is initially obtained. Because of their reduced interaction, the metal particles evaporated from the source impinge into the sample almost in straight lines; this leads to a poor conformal coverage and a pronounced shadow effect, a feature that might be problematic for some applications, but it is also the reason that makes this technique the most preferred one in lift-off fabrication. The metals can be melted in a crucible by means of a resistance, or by RF induction; alternatively, a focused electron beam can be used to heat up and melt only a small portion of the metal, hence reducing the contamination from the heater or the crucible [22]. Apart from these purity issues, the e-beam evaporation is also the only deposition technique with which it is possible to achieve temperatures well above 1800 °C, which are necessary to evaporate refractory metals such as W, Mo, Ti, or V.

In metal sputtering, a plasma is struck inside the equipment chamber in order to make the gas contained there conductive, and generate ions that are accelerated by the DC electric field formed between the cathode (made by high-purity metals) and the sample holder, which acts as anode. When they hit against the cathode, these highly energetic ions are able to extract some metal atoms and project them against the sample at very high speed. Compared with the evaporation, the pressure inside the chamber is much higher because of the relatively high flow of gases necessary to sustain the plasma (typically in the range 1–100 mTorr); as a consequence of that, the trajectories of the metal atoms are much less directional, which might severely affect lift-off processes. The grain size is usually smaller than in the metal layers deposited by evaporation, which translates into an increased grain-boundary area and into a possible increase of unwanted elemental diffusion across the deposited layers; this also tends to reduce the mechanical hardness of the layers. However, sputtering of metals produces films with very good adhesion (due to the high energy of the impinging particles), it has a more reproducible deposition control, and also the waste of precious metals deposited outside the sample is limited if compared

with evaporation; for all these reasons sputtering is also widely used, particularly in industry [23].

Very frequently, metal films require post-deposition thermal annealing in order to alloy the different metal layers, or to trigger some chemical reactions. This processing step can be performed both in conventional furnaces and with the use of Rapid Thermal Annealing (RTA) equipment, with the latter being usually the most preferred solution. This is because, when the two methods are compared at the same process temperature, RTA gives a much lower thermal budget (i.e. the overall time–temperature integral), a feature that greatly limits the occurrence of any unwanted reactions that might have different activation energies from the target one. In fact, with the use of halogen lamps and pyrometer-based control systems, typical heating rates in the range 30–500 °C/s and cooling rates around 50 °C/s can be easily reached with RTA equipment. During annealing, the ambient atmosphere also plays a very crucial role on the outcome of the process; typical alternatives are vacuum (down to 10^{-2} mbar), inert gases (N_2 or Ar), reducing (H_2 diluted in N_2 at a few percent concentrations, the so-called forming gas), and oxidising (air or O_2) environments.

4.2.3 Characterisation of the contacts

When current is made to flow into the semiconductor through a metal contact, there inevitably is some extra voltage drop that forms at the metal–semiconductor interface, which adds to the part already caused by the finite conductivity of the materials. Ideally the former contribution should be much lower than the latter so that the energy dissipation in the contacts can be neglected. However, this is not always the case, and it is very important to estimate its actual value. In particular, in order to compare contacts with different geometries, the quantity that is often measured and reported in literature is the so-called specific contact resistance ρ, which is defined as:

$$\rho = \left.\frac{\partial V}{\partial J}\right|_{V=0}, \tag{4.3}$$

where V is the voltage drop across the contact as a function of the current density J. The presence in this definition of a limit for $V \to 0$ allows assigning specific contact resistance values even when the contacts do not show ohmic behaviour; however, the

presence of a linear IV characteristic—at least within the working range of the device—is often considered to be an essential requirement for the reliability of the contacts.

As any possible measurement of the voltage drop in real devices inevitably includes the contributions due to both the contacts and the semiconductor, the separation of the two effects is not a trivial task. The two most used methods developed for this purpose are the Transmission Line Measurement (TLM)—sometimes also called Transfer Length Measurement and referred to using the same acronym—and its circular implementation (cTLM). Both of them are based on collecting a series of voltage measurements between pairs of contacts having different separation distances, while keeping the driving current fixed. Assuming that the contribution due to the contacts does not change and the one due to the semiconductor increases with the distance, the former can be estimated by extrapolating the measured values down to a separation distance of zero. These methods are also able to estimate the real dimensions of the effective contact area, which due to limited current spreading below the contacts is usually only a small fraction of the actual metal pad area. Specific contact resistances lower that 10^{-4} Ω cm^2 are considered to be fairly good, but values as low as 10^{-7} Ω cm^2 are not infrequently reported in literature, although the subsistence of the accuracy of these claims can be questioned if the material sheet resistivity is insufficiently low [24].

The estimation of the Schottky barrier height is also often included in the characterization of the contacts, especially to compare the transport before and after thermal annealing. These measurements can be done with standard CV or IV techniques, whose details are outside the scope of this thesis. An extensive review of all the electrical characterization methods here mentioned can be found e.g. in the book by Schroder [25].

In addition to electrical characterization, very often studies about contact formation also contain some form of chemical, or physical structural characterization. The surface of the contact can be analysed by optical microscopy, Scanning Electron Microscopy (SEM), or Atomic Force Microscopy (AFM), often with the purpose of detecting any sign of degradation of the contacts after high-temperature annealing, such as lack of uniformity, change of colour, blistering, etc. The use of Transmission Electron Microscopy (TEM) is also very common to detect any sign of inter-diffusion of the metal layers into each other, or the semiconductor. Analytical techniques such as Energy Dispersive x-ray Spectroscopy (EDS), Auger Electron Spectroscopy (AES), and X-ray Photoelectron

Spectroscopy (XPS) can also be used to detect any possible chemical change at the sample surface due to predeposition treatments or thermal annealing. Structural characterisation of the interior of the metal films, e.g. by X-Ray Diffraction (XRD), are also sometimes reported in literature, but they are much more difficult because of the thinness of the metal layers, which cause the signal intensity to be often below detection limits. More information about these characterisation techniques can be found in the introductory sections of the book chapter by Cole and Joshi [26], and in the references therein.

4.2.4 Literature review

n-type contacts

The standard metallisation scheme used to obtain ohmic contacts in *n*-type GaN consists in a multilayer stack of metals deposited according to the sequence Ti/Al/X/Au, in which X can be chosen from among a variety of different alternatives such at Ti [27], Ni [28], Mo [29], Pd [30], or Pt [31]. Usually the contacts need to be annealed at high temperatures (typically within the range 600–800 °C) to achieve ohmic behaviour, and the thicknesses of the single layers need to be optimized on a case-by-case basis as they are very dependent on the materials and the annealing procedure used. This approach has proven to be very effective for both GaN and low-aluminium-content AlGaN alloys and, for this reason, it is also the natural starting point for the development of any *n*-type contact scheme in UV LEDs. There are many different mechanisms that are believed to be essential in the success of this approach on GaN and, in order to extend its scope of application to Al-rich AlGaN materials, they need to be examined in detail.

First of all, it appears to be very important to have metals with low work-function in close contact with the semiconductor. This is, as previously discussed, in agreement with the Schottky-Mott theory and the supposedly reduced pinning effect present in highly-ionic compound semiconductors [19]; it also seems to be confirmed by the fact that, in certain conditions, ohmic contacts to GaN can also be achieved simply by using single layers of low-work-function metals such as Al [32] or Ti [33], or with non-annealed Ti/Al-based structures [34], in which the interaction of the two metals is hence negligible. Although the use of these metals may indeed be very important, this cannot certainly be the only mechanism involved in the contact formation as, contrary to experience, they should also be able to guarantee ohmic behaviour in AlN or Al-rich AlGaN materials, which have lower electron affinities than GaN.

The fact that annealing considerably and consistently improves the contact resistances of both Ti- and Al-based contacts means that some type of reaction involving either the metals or the semiconductor must play an important role in the contact formation. Both Ti and Al are known to reduce GaN and AlN oxides, thus one possible explanation of the effect of annealing is that it removes the native oxides present on the semiconductor surfaces and brings the metals to intimate contact with the semiconductor. This type of explanation has been proposed e.g. by Luther *et al.* [35] who reported results on Al and Ti/Al contacts deposited on samples both with and without removal of the native oxides. While the contacts with no (or reduced) native oxide often showed ohmic behaviour even before annealing, the as-deposited samples with a thick native oxide were initially rectifying and only became fully ohmic after a thermal-annealing step.

The issue due to the presence of an insulating layer on top of the semiconductor surface is not only caused by the existence of native oxides, but can also be exacerbated by any fabrication process that requires the samples to be exposed to plasma, which is known to favour the formation of oxides on III-nitride materials [36]. In particular, this inevitably happens with the dry etch necessary to expose the *n*-type layer in LEDs grown on non-conductive substrates such as sapphire. The fact that different chemical treatments performed on the samples after plasma exposure give quite different results in terms of oxide removal [36], suggests that the surface of the samples before metal deposition, if not properly treated, might still have too thick an insulating layer for the above-mentioned reducing effect of Ti and Al to work. In addition to that, the fact that the oxidation of AlGaN materials seems to increase with the Al content [12], may in part explain why the formation of contacts in deep-UV LEDs is so challenging.

Another mechanism often claimed to be crucial for the formation of ohmic contacts after post-deposition annealing, is the high increase of the doping level in the proximity of the semiconductor surface. In fact, even in the presence of high Schottky barriers—either due to Fermi-level pinning or high-work-function metals—a very high doping level in the first few nm of the semiconductor would be sufficient to reduce the thickness of the depletion region enough to allow the current to flow by tunnelling (field emission). In *n*-type III-nitride materials, this superficial increase of doping is believed to be caused by a high concentration of N vacancies, in turn produced by the reaction of the N present in the GaN with either Ti or Al to form TiN [28] or AlN [37]. These reactions are indeed energetically possible as the enthalpies of formation of GaN, TiN, and AlN are,

respectively, −110.9, −265.5, and −318.1 kJ/mol [38], and hence the energy required to dissolve GaN bonds is lower than that released by the formation of either TiN or AlN. The fact that TiN is a semi-metal, whereas AlN is a wide bandgap material that carriers can only overcome by tunnelling, has been often considered the reason of the superiority of the contacts in which Ti is in close contact with the semiconductor over the ones that only use Al. However, AlN and not TiN was reported to be present in some Ti/Al contacts [37] when the contacts had become ohmic by annealing, which suggests that different reactions may happen in different implementations of the same metallisation scheme as a result of variations in the layers thickness and thermal annealing process.

In addition to being semi-metallic, TiN has also a lower work function (3.74 eV) than both Ti and Al (4.33 and 4.28 eV, respectively)—Cf. the paper by Luther *et al.* [39] and references therein—and, for this reason, in addition to inducing N vacancies in the semiconductor, its presence in close contact with the semiconductor material should be able to lower the height of the Schottky barrier, further improving the current transport across the contact. There has been a long debate about whether this effect is real or not, with different researchers claiming one or the other mechanism to be the dominant one. For example, Jeon *et al.* [40] reported that directly deposited, non-annealed TiN/Al contacts had a lower Schottky barrier than Ti/Al. In contrast, Lin *et al.* [41] observed that after the formation of TiN by annealing the contacts, a significant increase of the Schottky barrier was actually present together with the reduction of the depletion layer thickness. Subsequently, a study by Iucolano *et al.* [42] was able to demonstrate the presence of both effects, confirming once more that similar approaches might still lead to quite different results.

In addition to the beneficial effects of annealing, there also seems to be quite a widespread consensus that Ti/Al-based metallisation is, both in term of contact resistance and reliability, much better than Ti-only and Al-only contacts. One explanation, proposed by Liu *et al.* [43], is that during the annealing of these metals the intermetallic alloy Al_3Ti forms, which is less prone to oxidation than either Al or Ti and this can effectively protect the contacts from degradation. Oxidation is indeed a serious issue for all annealed contacts and is the main reason for the inclusion of a final Au layer in most metallisation schemes; however, another mechanism might also play an important role here: as observed by Van Daele *et al.* [38], the reaction of Ti with GaN that leads to the formation of TiN is so strong that it can result in the creation of large voids at the interface between

the semiconductor and the metals as shown in Figure 4.8. These voids are detrimental to both the contact resistance and its reliability and must be avoided. The presence of metallic Al in close contact with the Ti seems to be able to significantly reduce its reactivity and it allows the formation of a uniformly thin layer of TiN on top of the GaN. This suggests that the thickness of the Al layer is quite a critical parameter: too much of it can consume all Ti and completely prevent the formation of TiN, but too little can lead to the formation of the voids discussed above. In addition to that, Van Daele and co-workers observed that even the Al already present in AlGaN alloys can reduce the reactivity of Ti as does the deposited one, which might explain why metallisation schemes that work on GaN devices cannot simply be transferred to UV LEDs without further optimisation.

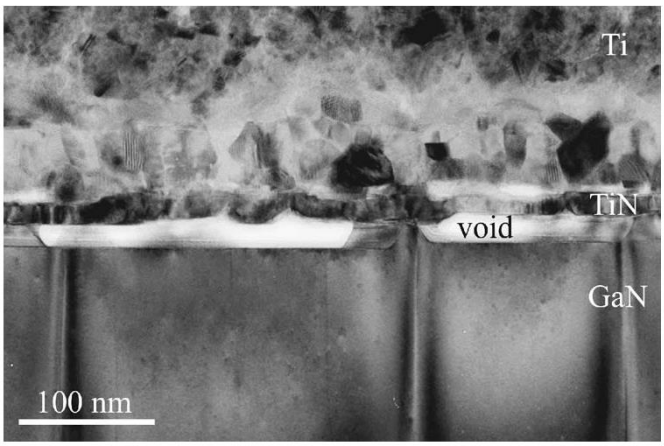

Figure 4.8: Presence of voids in Ti-based contacts to *p*-GaN and *p*-AlGaN
SEM images taken after annealing of Ti on GaN at 991 °C for 90 s in N_2 ambient. Two large voids are clearly visible in-between the GaN material and the thin TiN layer formed as a result of the annealing. From [38].

As mentioned earlier, oxidation of the metals during annealing is a very important issue that needs to be addressed [44]. The use of a reducing atmosphere (e.g. forming gas) was proposed, for example, in the early attempts of annealing at high temperatures [35]. Although the use of Ti/Al bilayer contacts could mitigate the problem through the formation of an oxidation-resisting Al_3Ti layer [43], a much more effective protection was achieved with the deposition of a noble metal—usually Au—as the top layer of the metal sequence. However, for this solution to work, the presence of a diffusion-preventing layer in-between Au and Al is very critical [27-31], as without it Al and Au would form highly resistive intermetallic alloys such as Al_2Au, the so-called "purple

plague" [45]. Because the optimal annealing temperature required to achieve ohmic contacts to AlGaN alloys significantly increases with Al content [46], the issue with interdiffusion of Au might be particularly severe in UV LEDs, and the optimisation of the diffusion-preventing layer requires special care especially with these devices [47].

Although a significant body of work has been devoted to improve the quality of *n*-type metallisation schemes in UV LEDs, the difficulties in achieving a satisfactorily high doping level in Al-rich AlGaN—which has been discussed in Chapter 3—makes the realisation of ohmic contacts in these devices an inherently difficult job. However, there are interesting results that give rise to a moderate optimism. Following the principle of having a metal with low work function in close contact with the semiconductor, France *et al.* [46] showed that the use of V as a replacement for Ti makes it possible to achieve, after annealing of the contacts, ohmic behaviour in the whole composition range of AlGaN up to pure AlN. Similarly as with the Ti-based schemes, the formation of ohmic contacts is believed to involve a reaction of V with AlGaN, and the consequent formation of VN, which has the lowest work function among Ti, TiN, and V; however, still more work is needed to fully understand this mechanism.

Another interesting field of research regards the study of the appropriate chemical pre-treatment necessary, before metal deposition, to remove either the oxides natively present on the semiconductor surface or those caused by plasma treatments [36, 48, 49]. It is also important to notice that, in addition to the formation of oxides, exposure of the semiconductor to plasma has the ability to introduce high concentrations of defects on its surface. Although this has proven to be beneficial in GaN and low-Al-content AlGaN [50, 51], in which it results in the creation of nitrogen vacancies able to further increase the superficial doping, it has been shown to be highly detrimental on AlGaN materials having an AlN content higher than 30% [51]. For this reason, in the UV LEDs that require the exposure of the *n*-doped layer by dry etch, the development of special etch recipes able to minimize the introduction of unwanted defects appears to be a worthwhile research area to pursue.

***p*-type contacts**

As metals with low work function proved to be essential in achieving ohmic contacts with *n*-type GaN and AlGaN materials, those with large work function (such as Au, Pd, Ni, and Pt) are the natural candidates for the contact formation to *p*-doped III-nitride

materials, and have been extensively studied for this purpose. Although there are reports in literature that ohmic behaviour can be achieved using as-deposited, not annealed, metal films [52-54], the specific contact resistance usually shows a marked reduction if the contacts undergo some form of thermal treatment. This is shown for example by Jang *et al.* [53], who reported a decrease of more than an order of magnitude in the specific contact resistance of Pt/Ni/Au contacts after annealing. A very extensive list of the most relevant results reported in literature for ohmic contacts to GaN can be found in the recent review paper by Greco *et al.* [21]. As shown in Figure 4.9, which summarizes these results, the typical annealing temperatures used for the formation of *p*-type contacts are, in most cases, significantly lower than for their *n*-type counterparts.

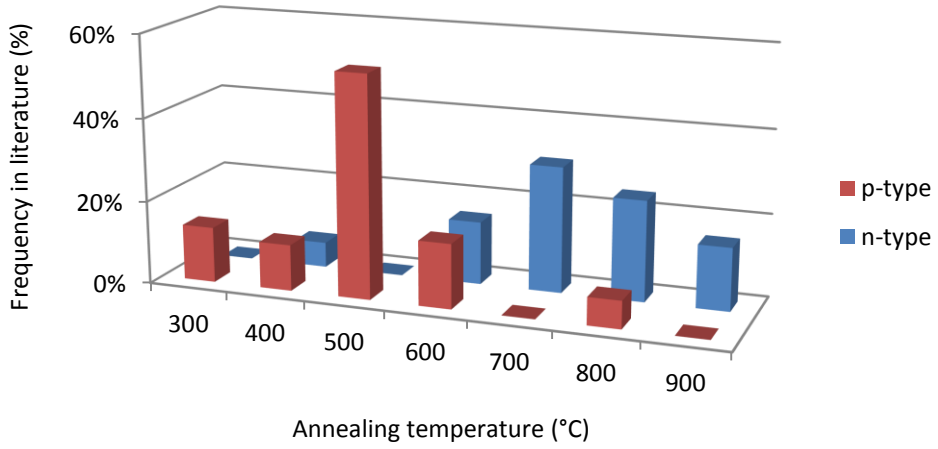

Figure 4.9: Annealing temperatures

Comparison of the annealing temperatures of different processes used to obtain ohmic contacts to GaN, for both *n*- and *p*-type doped materials. The data were taken from the list of the most significant works present in the literature of ohmic contact to GaN, as from the review paper by Greco *et al*. [21].

Whether the contacts are annealed or not, there seems to be widespread consensus that cleaning the semiconductor surface from native oxides and contaminants before the metal deposition is a very critical part of the process. Aqua regia (i.e. a mixture of HNO_3 and HCl, usually in the molar ratio 1:3) has often been reported as the most effective surface treatment [54]; however, the use of many other chemicals such as HCl, BOE, dilute HF, KOH, and $(NH_4)_2S_x$ has also been reported. A critical discussion of all the attempted approaches can be found in the paper by Song *et al.* [55] and references therein.

Among all the different metallisation schemes to *p*-GaN reported in literature, annealed Ni/Au is probably the most used and can be considered the standard approach, more or less as the previously discussed Ti/Al/X/Au is the standard one for *n*-type contacts. Although both contact schemes require a post-deposition thermal treatment to obtain the best results, there are significant differences in the two cases. In particular, apart from the much lower temperature, an oxidising process atmosphere—such as pure O_2 or air—is virtually always required for the formation of *p*-type contacts. Even small amounts of oxygen contamination in otherwise inert gases are able to induce a detectable decrease of the contact resistance [56], a finding that is in striking contrast to the case of *n*-type contacts for which, as previously discussed, the oxidation of the metals was the major cause of contact resistance deterioration.

Although the importance of an oxidising atmosphere is widely recognized, the actual mechanism of ohmic contact formation is still not fully understood, which might explain the insurmountable difficulties so far faced by the researchers in trying to extend this approach to Al-rich AlGaN materials. Among the many different theories investigated, Sheu *et al.* [57] proposed that the formation of ohmic contacts should be related to the presence of the Ga–Ni and Ga–Au intermetallic alloys that were clearly detected by AES, Rutherford backscattering spectrometry and XRD analysis. Some authors—Cf. the review paper by Song *et al.* [55]— have argued that this can be due to the formation of Ga vacancies, which are known to act as acceptors in III-nitride materials, and the consequent reduction of the depletion region thickness. A very similar mechanism was also proposed by Lee *et al.* [58], with the only difference that the metal vacancies were instead claimed to be induced by the formation of Ga oxides.

In contrast, Koide *et al.* [59] proposed that the doping concentration increase was instead the result of an enhanced extraction of H from the *p*-GaN during annealing in air or oxygen. In fact, it is well-known that the Mg atoms, introduced as *p*-type dopants during the MOVPE growth of III-nitride materials, are not immediately active as acceptors because they find themselves bonded to the H atoms naturally present in the reactor chamber, both as a carrier gas and as by-product of the reaction. It was only after the seminal works of Amano, Akasaki and Nakamura [60, 61], that it became known how to release H from the *p*-GaN and achieve *p*-type conductivity. In their work, Koide and co-authors claim that during annealing in an oxygen containing environment the formation of H_2O can further enhance this H extraction and increase the superficial hole concentration.

Based on this mechanism, the authors also reported that the use of Ta/Ti instead of Ni/Au can be equally effective in removing H atoms and increasing the doping level [62, 63].

Because XRD and TEM studies have consistently detected the presence of NiO after the annealing of Ni/Au contacts, the formation of this material has also been extensively investigated by many authors for its possible function in the attainment of ohmic contacts. Although most of the TEM studies recognize the presence of NiO both as scattered patches at the semiconductor interface and as a coating grown on top of the Au layer, there is still not agreement about which of the two formations is the one actually linked to the improvement of the contact resistance. According to Ho *et al.* [64, 65] the key point is the presence of the NiO patches at the interface, which are able to lower the height of the Schottky barrier, while the function of Au, which has a higher conductivity than NiO, is limited to the reduction of the overall series-resistance of the contact. In the second of their two papers on this subject [65], they also proposed a way to estimate the height of this highly-reduced potential barrier, and obtained an incredibly low value of 55 mV. However, this calculation was later criticized by Yu and Qiao [66], who using the same theoretical approach obtained instead a value of 2.28 V.

In contrast with the conclusions of Ho and co-workers, other authors argue that, whatever the actual height of the *p*-GaN/NiO Schottky barrier might be, considering that most of the NiO revealed by TEM is present as an inversion layer on top of the Au, it is most likely the intimate contact of this latter metal with the semiconductor that ensures the achievement of an ohmic behaviour [67, 68]. From this perspective, the only function of Ni is to allow the removal of any native oxide and contaminants from the surface of the semiconductor before diffusing through the Au layer and reaching the surface, where the NiO inversion layer forms as the annealing continues. In addition to that, Greco *et al.* [68] have shown how the presence of an oxidising atmosphere facilitates the formation of this superficial NiO layer, which in turn is crucial in enhancing the extraction of Ni from the Au layer and in ensuring that the one initially present at the interface keeps being dissolved until it is fully consumed together with all native oxides and surface contaminants (Cf. Figure 4.8).

Unfortunately, despite the reasonable effectiveness of this metallisation scheme on visible devices, its implementation in the UV LEDs has not produced the expected results. From the point of view of the Schottky-Mott theory, moving from *p*-GaN to *p*-AlGaN material

should have two opposite consequences on the height of the potential barrier that forms at the metal–semiconductor junction: on the one hand increasing the bandgap from the 3.4 eV of GaN up to the 6.0 eV of pure AlN would cause an increase while from the other hand the reduction of the electron affinity from the 4.1 eV of GaN down to the almost 0 eV of AlN should fully compensate this effect. However, most likely due to the fact that *p*-type doping of AlGaN alloys is still very challenging, good ohmic contacts obtained directly to *p*-AlGaN have not been demonstrated yet.

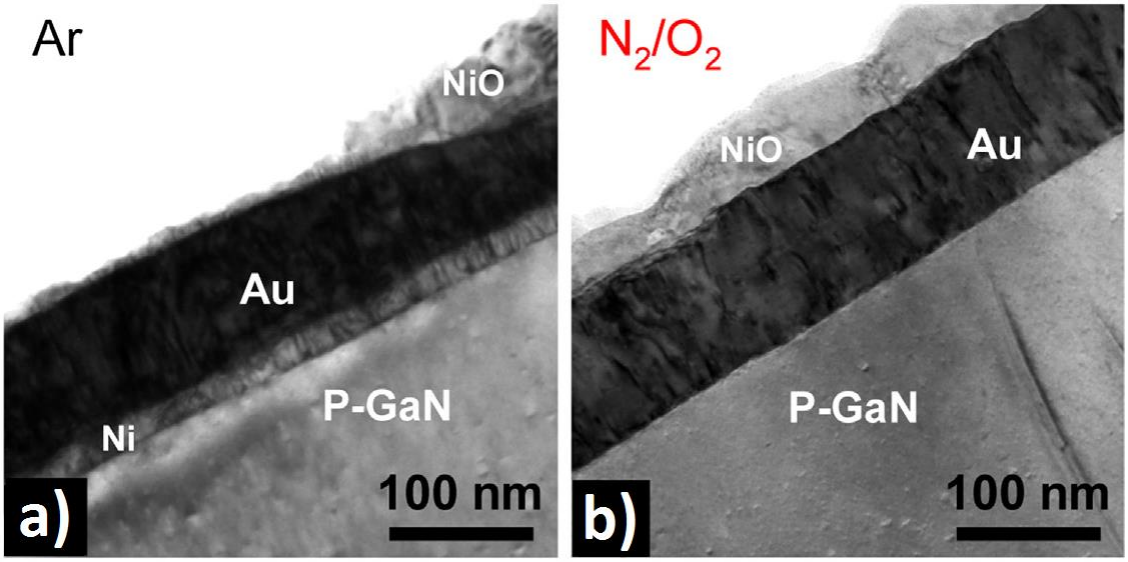

Figure 4.10: Role of oxidizing environment in Ni/Au-based contacts
SEM images of Ni/Au contacts annealed at 600 °C in inert (a), and oxidizing (b) ambient. While in the first case there is still a thin Ni layer at Au/GaN interface, in the second case Ni has been fully consumed and, after having diffused through the Au layer, it forms a NiO layer on top of the sample. From [21].

To overcome this problem, the standard solution at the moment adopted in virtually all the UV LEDs fabricated in industry as well as in research, is the use of a thin layer of highly doped *p*-GaN grown on top of the *p*-AlGaN cladding layer, to form an intermediate layer between this and the subsequently deposited metal contacts. Although this solution does allow the formation of an electrically satisfying contact, its repercussions in terms of LEE reduction are huge. As a matter of fact, because of the strong absorption of GaN in the deep-UV range, even a thin layer of only a few tens of nm causes the loss of a great amount of the UV radiation emitted by the active region of the device.

Apart from their good electrical performance, another advantage of using Ni/Au contacts in visible devices is the fact that, after annealing, they become semi-transparent allowing a significant increase in light extraction. For the same reason, fully-transparent contacts—particularly those based on indium tin oxides—are also very commonly used [55], even though they are electrically poorer. Unfortunately, because neither of these solutions are UV transparent, they do not guarantee any particular advantage in terms of LEE of UV LEDs. On the contrary, provided the *p*-GaN layer is somehow greatly reduced or even completely removed, the presence of reflective contacts could be advantageous in devices having the so-called flip-chip configuration, in which the light is collected from the substrate side. However, this approach can be considered more of an attempt to increase the LEE to the detriment of the EE than a form of real progress in the formation of ohmic contacts. In fact, although the optimization of contacts and cladding layers is indeed very critical to the overall efficiency of UV LEDs, the strategies used to increase electrical and injection efficiencies may be so detrimental to the extraction of UV radiation that some researchers have studied the opportunity of sacrificing them in exchange of a significant enhancement in LEE.

For example, to reduce the UV absorption due to the presence of the *p*-GaN contact layer, Inazu *et al.* [69] proposed the use of mesh contacts, in which the *p*-GaN is partially removed by the opening of windows in which the *p*-AlGaN beneath is exposed by dry etch. In this way the actual contact surface is considerably reduced and the voltage drop of the LED necessarily increases; however, because these previously opened windows can be coated with a reflective metal, some of the light emitted towards the *p*-contact can be reflected back without being absorbed. By including a similar process also for the *n*-contact, the authors were able to report a 55% increase of the UV power of a sub-300-nm LED. A similar concept was previously proposed, for longer-wavelength devices, by Lobo *et al.* [70].

In an alternative approach, Hirayama and co-workers proposed to completely remove the *p*-GaN layer, and also make the *p*-AlGaN cladding layer as much transparent to the UV radiation as possible by increasing the Al content of the alloy [71, 72]. Although the injection of holes is highly reduced, which might require redesigning the EBL to at least partially mitigate the problem, the LEE results significantly increased. In addition to that, the *p*-contact can be obtained using a Ni/Al metallization scheme, which reflects about

70% of the UV, instead of the more conventional Ni/Au, which only reflects 20% of it, so that the extraction efficiency can be increased even further.

These results are indeed very interesting, and clearly show that there is room for a great deal of improvement with the LEE of UV LEDs. However, none of the cited studies provide a thorough analysis of the performance of these alternative contacts, in terms of specific contact resistance, height of the Schottky-barrier and carrier transport mechanism. Considering also how intertwined EE, IE and LEE are it is very difficult to evaluate whether this type of approach is actually effective in enhancing the overall WPE of the device, based on the currently published information.

4.2.5 Experimental

This last section summarizes the most relevant experimental investigations about the UV LED contacts performed during my research.

p-type contacts

The first analysis of the *p*-contacts was undertaken, at the beginning of the project, when the first fabrication run of the deep-UV μ-LED was completed. As described in Section 4.1.1, the *p*-contact was deposited as the first step of the process. After standard cleaning, the samples were subject to a thermal activation of the Mg dopants in an RTA equipment at 850 °C in N_2 ambient for 1 min at the target temperature. After photolithography, the samples were dipped for 10 s in hot aqua regia to remove any oxide before loading into the evaporation chamber. To increase the adhesion of the metals to the semiconductor surface, a high temperature baking of the chamber at 80 °C was performed for 30 min before the actual deposition. Subsequently, 40 nm of Pd were evaporated with a deposition rate of about 0.5 Å/s, with a chamber pressure lower than 2×10^{-7} Torr.

As shown in Figure 4.11 (a), not only the IV characteristics of the contacts measured across the cTLM test features were non-linear, but the reduction of the contact separation does not always correspond to a reduction of the measured total resistance, a clear sign of the non-uniformity of the specific contact resistance across the sample surface. The fact that the *p*-contact was still non-ohmic notwithstanding the presence of a 25-nm-thick *p*-GaN contact layer, proves that the material quality of the *p*-GaN grown on top of the *p*-$Al_{0.85}Ga_{0.15}N$ layer of our deep-UV LED was significantly poorer than the *p*-GaN typically present in the cladding layers of visible devices.

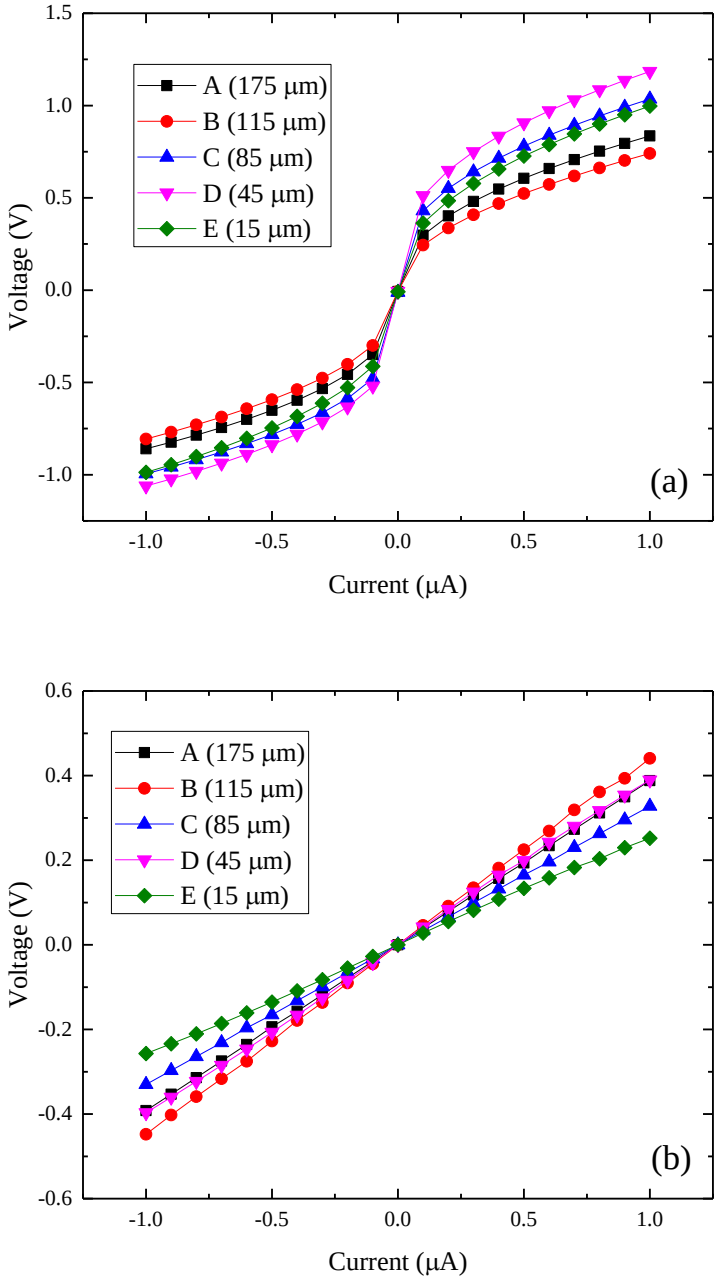

Figure 4.11: IV analysis of the *p*-contacts

IV characteristics measured across five different cTLM test structures, from the largest (type A: with a separation of 175 µm) to the smallest (type E: with a separation of 15 µm). The data were collected before (a), and after (b) the optimization work.

The initial fabrication work was then focused on the improvement of the quality of the *p*-contacts. After a series of runs performed over a few months of work, we were eventually able to obtain ohmic behaviour of the *p*-contacts by increasing the temperature of the Mg-dopant activation to 900 °C before the cleaning. All other fabrication steps were kept the same as in the first run. However, in addition to the fabrication process, it

was also found necessary to increase the thickness of the *p*-GaN contact layer to 50 nm, and to grow this critical layer at higher pressure to improve its surface morphology.

As can be seen in Figure 4.11 (b), the IV characteristics became eventually linear for all the tested cTLM features. However, the sequence of the contact separations does still not monotonically correspond to a reduction of the measured resistance. In Figure 4.12 the measured resistances (R_T) are shown as a function of the different cTLM contact separation and compared with the theoretical model:

$$R_T = \frac{R_{sheet}}{2\pi}\left[ln\left(\frac{R_1}{R_0}\right) + \frac{L_T}{R_0}\frac{I_0\left(\frac{R_0}{L_T}\right)}{I_1\left(\frac{R_0}{L_T}\right)} + \frac{L_T}{R_1}\frac{K_0\left(\frac{R_1}{L_T}\right)}{K_1\left(\frac{R_1}{L_T}\right)}\right], \tag{4.4}$$

where R_0 and R_1 are the internal and external radii of the cTLM structure, I_0, I_1, and K_0, K_1 the modified Bessel functions[11] of first and second kind, respectively. The sheet resistance (R_{sheet}) and the transfer length (L_T) are then used as fitting parameters and calculated by minimising the errors. In particular, using the formula:

$$\rho_C = R_{sheet}\,(L_T)^2\,, \tag{4.5}$$

a value of 3.5 $\Omega\,cm^2$ for the specific contact resistance (ρ_C) was estimated, which although still very large, was enough to ensure reliable hole injection in our device.

The same type of metallization scheme was then transferred to the near-UV LED. Apart from the thermal activation of the Mg dopants in the cladding layers, which in the *p*-$Al_{0.6}Ga_{0.6}N$ material used in this device was already possible at 850 °C, all the other parameters were kept the same, including thickness and growth conditions of the *p*-GaN contact layer. The final contacts showed specific contact resistances comparable to those of the deep-UV devices.

[11] The subscript indicates the function order.

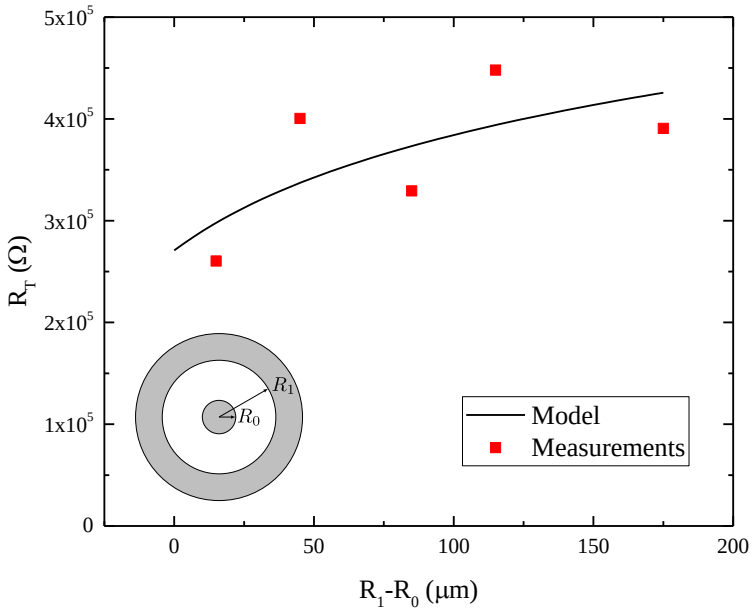

Figure 4.12: cTLM analysis of the *p*-type contacts

This graph shows the measured total resistance as a function of the contact separation ($R_1 - R_0$) of different cTLM test features (discrete data-points). The solid line is the best fit according to Eq. (4.4).

n-type contacts

In parallel with the analysis of the *p*-contacts of the devices fabricated in the initial part of this research, the *n*-contacts were also studied, and—not unexpectedly—they also showed non-ohmic behaviour. In order to separate the effects of the dry-etch from the choice of the metal stack and the post-deposition treatments, I then decided to perform a preliminary optimization using *ad hoc* samples consisting in thin *n*-type doped AlGaN films grown on commercial and AlN templates.

The first samples investigated were based on AlGaN films with an AlN concentration of 50% and a thickness of 800 nm. A photolithographic step was used to cover the samples with cTLM test structures. The metal sequence adopted in these initial attempts was the standard Ti/Al/Ti/Au with thicknesses of 20, 170, 5, and 100 nm, respectively. After the lift-off of the excess metal, the as-grown contacts showed, as expected, a clear non-ohmic behaviour. Following the literature research reported in Section 4.2.4, I then decided to include a thermal annealing step of the contacts at high temperature in inert atmosphere. Different annealing temperatures were preliminary investigated in the range 150–900 °C, and while below 600 °C no significant change in the contact behaviour nor in the surface morphology of the contacts was detected, starting from the temperature of 700 °C and, more evidently, at even higher temperatures, a clear degradation of the surface

morphology was present. For these reasons, in the actual experiment, the samples were annealed at 600 °C in N_2 atmosphere for 60 s.

An example of the cTLM fitting of these samples is shown in Figure 4.13, where, in contrast to the case of the *p*-type contacts discussed in the previous section (Cf. Figure 4.12), the resistances of the different cTLM spots align much better with the theoretical model of Eq. (4.4).

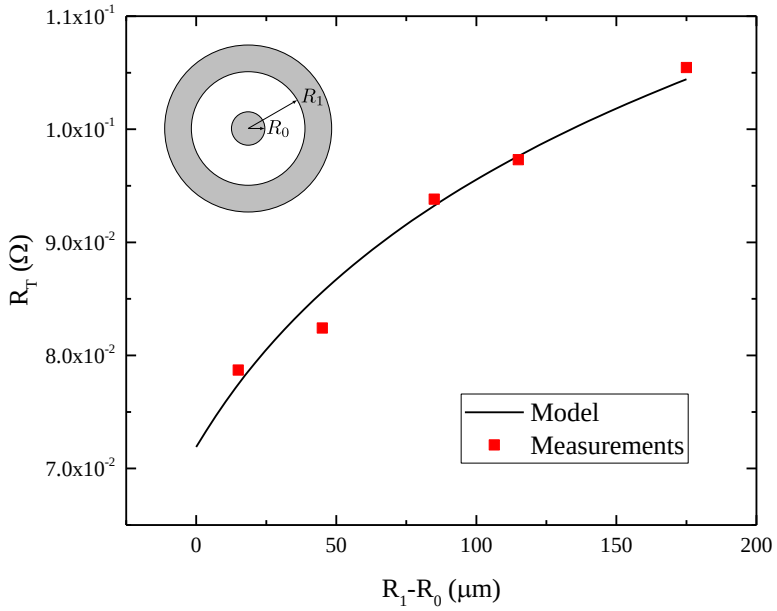

Figure 4.13: cTLM analysis of the *n*-type contacts
This graph shows an example of the measured total resistance as a function of the contact separation ($R_1 - R_0$) of different cTLM test features (discrete data-points). The solid line is the best fit according to Eq. (4.4).

As shown in Figure 4.14 (a), the quality of the contacts is reasonable, with specific contact resistances as low as 2 x 10^{-4} Ω cm^2 for the sample grown on commercial template, and 5 x 10^{-4} Ω cm^2 for those grown on standard AlN template. The sheet resistance measured by cTLM shows the same trend present in the data obtained by Hall-effect measurements (Cf. Chapter 3) but with some differences in the absolute values, as reported in Figure 4.14 (b). These differences are, most likely, due to growth inhomogeneities and statistical variations of the contact quality, which can introduce large errors in the estimation of the sheet resistivity by cTLM. In addition to that, both methods assume that the conductive film is homogeneously doped along its thickness, which might

not necessarily be true for the samples here studied. Although both methods would give an "effective" average sheet resistance, this value may be different for the two methods.

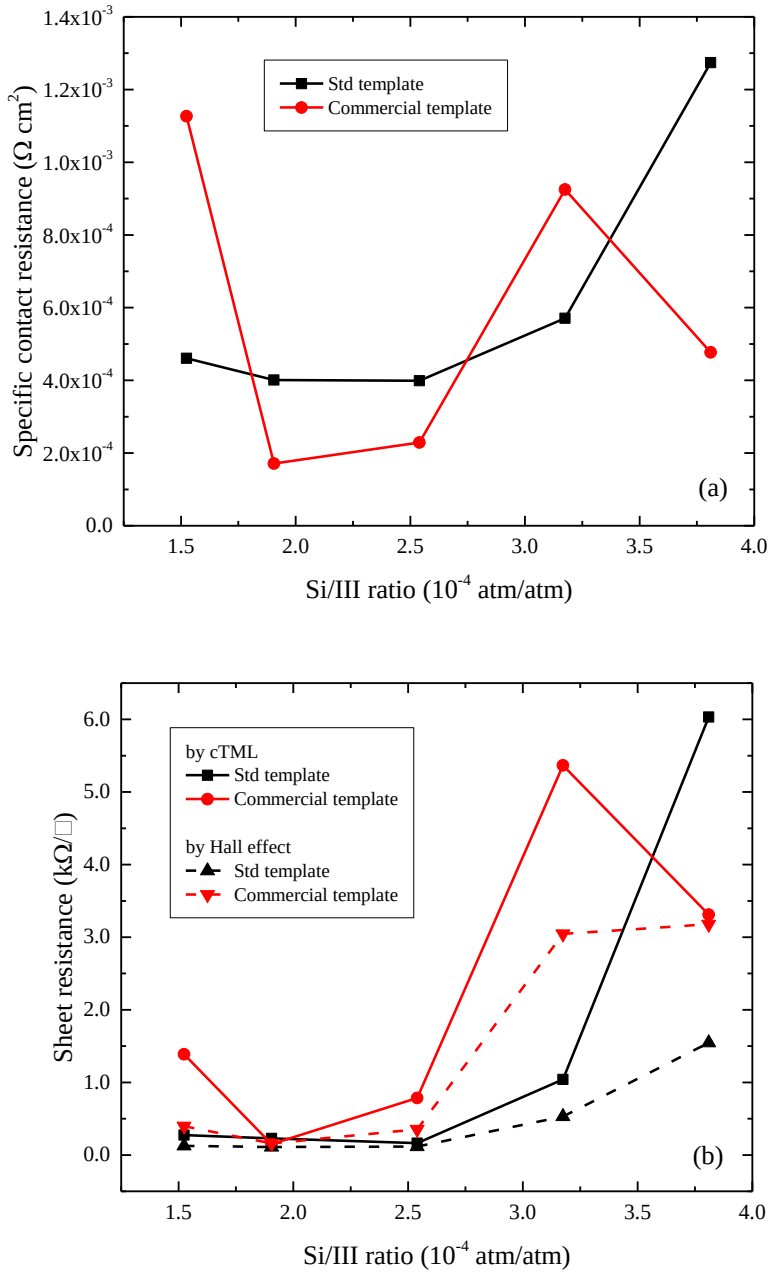

Figure 4.14: Characterization of the *n*-contacts on *n*-$Al_{0.5}Ga_{0.5}N$

(a) Specific contact resistance of the *n*-contacts as a function of the doping level of the *n*-AlGaN, obtained by cTLM measurements. (b) Comparison of the sheet resistance measured by cTLM (solid line) and by Hall effect (dashed line). In both graphs the values obtained for material grown on commercial (red), and AlN (blue) templates are reported.

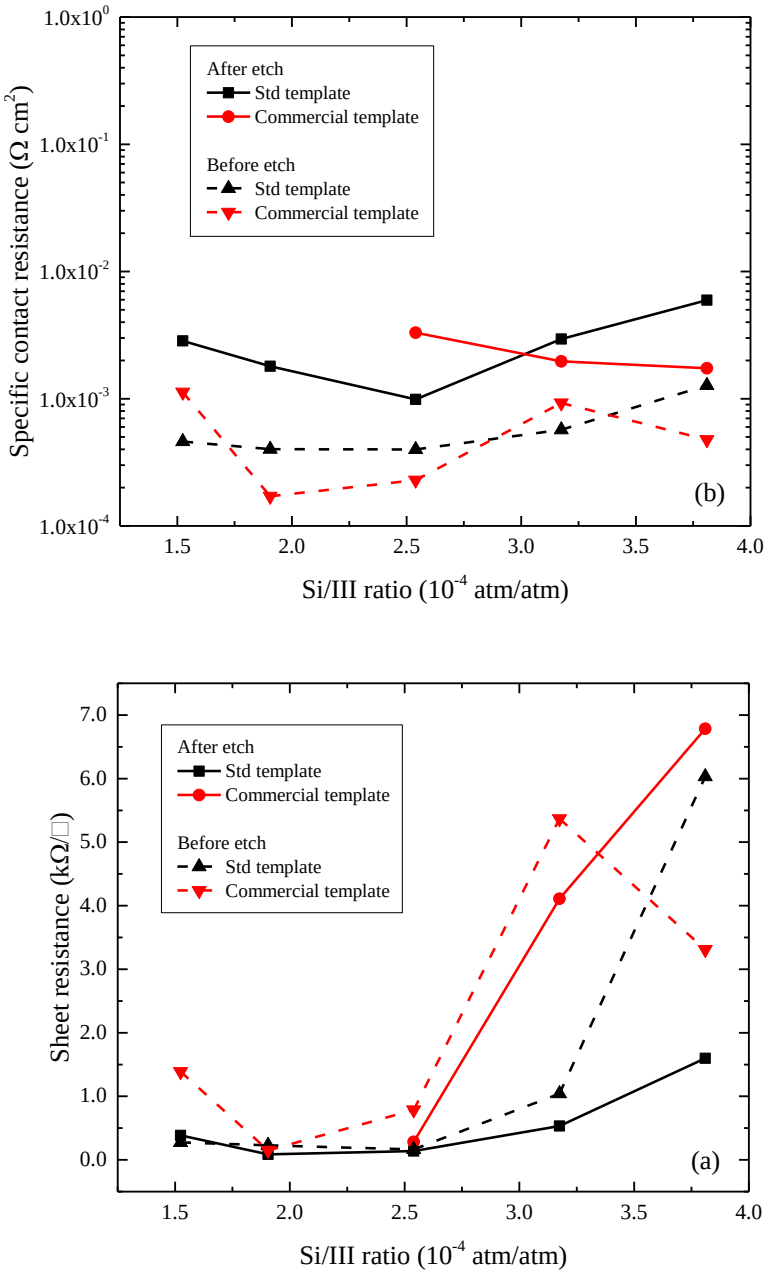

Figure 4.15: Effect of dry etch on the contact resistance of *n*-$Al_{0.5}Ga_{0.5}N$

Comparison of specific contact resistance (a), and sheet resistance (b), of the contacts obtained with dry-etched (solid lines) or non-dry-etched (dashed lines) material. In both cases the data are estimated by cTLM measurements, and are shown as a function of the doping level of the *n*-AlGaN material.

In order to study the effects of dry etch on this *n*-$Al_{0.5}Ga_{0.5}N$ material, another experiment was conducted on twin samples that were previously used for Hall-effect measurements. These samples, which—apart from the corners—had most of their surface still untouched and free from annealed metal residues, were initially subject to a blanket dry etch with a

target depth of 100 nm at the same conditions used for exposing the *n*-type cladding layers in the actual devices. Subsequently, cTLM test features were deposited and annealed using the same metal stack and conditions as in the cTLM samples with no dry etch.

As shown in Figure 4.15, despite a slight decrease in the sheet resistivity present in the samples after dry etch, the specific contact resistance showed a degradation of about one order of magnitude. Although these results refer to a metallization scheme that was still not fully optimized for high-Al-content AlGaN materials, this experiment suggests that our standard dry-etch recipe used for exposing the *n*-type cladding layer of the devices can indeed significantly degrade the quality of the contacts.

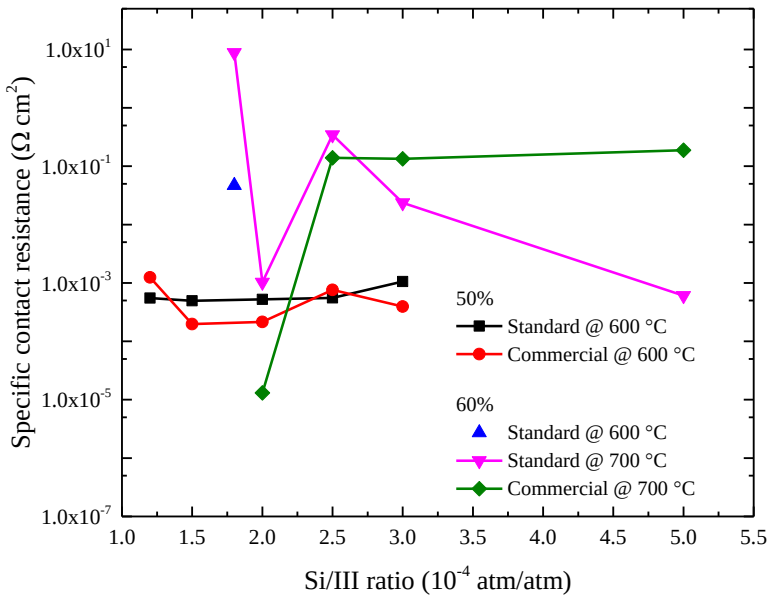

Figure 4.16: Characterization of the *n*-contacts on *n*-$Al_{0.6}Ga_{0.4}N$

Specific contact resistance of the *n*-contacts as a function of the doping level of the *n*-AlGaN, obtained by cTLM measurements. The single blue data-point was measured after annealing at 600 °C, while the pink and green lines represent the data obtained after a second annealing at 700 °C. The black and red lines are the data for the *n*-$Al_{0.5}Ga_{0.5}N$ material, which are reported for comparison.

The same type of optimization was then attempted for the contacts deposited on AlGaN material with an AlN concentration of 60%. As shown in Figure 4.16, after the annealing at 600 °C, only one sample showed ohmic behaviour and its specific contact resistance could be measured; its value was found to be about two orders of magnitude worse than in the case of $Al_{0.5}Ga_{0.5}N$. A further attempt to obtain ohmic contacts was made by

performing a second annealing step at 700 °C. Although after this further thermal treatment at higher temperature it was possible to induce ohmic behaviour in almost all samples (Cf. Figure 4.16), the surface morphology became very poor and the specific contact resistances estimated by cTLM became quite scattered.

The results of the previous experiment clearly suggested that a higher annealing temperature was indeed required for achieving ohmic contacts to AlGaN materials with increased Al content. However, the evident degradation of the surface morphology already present at 700 °C was a clear sign that the thicknesses of the different layers in the metal stack was not optimal. Considering that in the literature it is often stressed the importance of the second Ti layer in the Ti/Al/Ti/Au metal sequence for its role as a barrier able to prevent excessive diffusion of Au into Al, I decided to focus my attention on this aspect.

After a series of tests at different temperatures and thicknesses, I found that the best results were obtained with a diffusion-preventing Ti layer increased to 50 nm (i.e. with a metal stack of Ti/Al/Ti/Au having thicknesses of 20, 170, 50, and 100 nm), and a thermal annealing in N_2 ambient for 1 minute at 800 °C. Notwithstanding the use of a temperature much higher than the previous experiment, the samples with this modified metallization scheme did not show any severe sign of surface morphology degradation and ohmic behaviour was present even at currents as high as 100 mA, and not only for the *n*-$Al_{0.6}Ga_{0.4}N$ but also for materials with AlN concentrations as high as 85%. The ohmic behaviour was also present in samples with sub-optimal doping levels and for temperatures as low as 10 K, which was crucial result in order to make it possible to perform the Hall-effect measurements already described in Chapter 3.

This contact scheme was then applied to actual UV LED devices. In order to preserve the quality of the *p*-contacts, the fabrication flow was slightly modified, with the *n*-contacts deposited right after the exposure of the *n*-type cladding layer by dry etch, and then annealed according to the procedure previously described. Although the subsequently deposited *p*-contacts did not undergo any thermal treatment, it was not possible to repeat the standard cleaning of the sample immediately before the evaporation of Pd, and the only possible pre-deposition treatment that was a short dip in aqua regia for 10 s. Although the photolithographic step was slightly more complicated because of the reduced contrast and definition of the alignment marks previously obtained with the dry

etch and the annealed *n*-contacts, the *p*-contact itself did not show any significant degradation compared with the standard fabrication flow. The IV characteristics of deep-UV devices fabricated with the modified and the standard processes are compared in Figure 4.17.

Although there is a significant improvement of the IV characteristics in the devices produced according to the new approach, with a reduction of the voltage forward drop of about 67% of the original value, the results were not as good as we would have expected from the high quality of the contacts achieved on the *ad hoc* samples. We think this behaviour is most likely caused by the damages introduced on the material by the dry etch necessary to expose the *n*-type doped material in the device material, similarly as to what previously discussed for the *n*-$Al_{0.5}Ga_{0.5}N$ material.

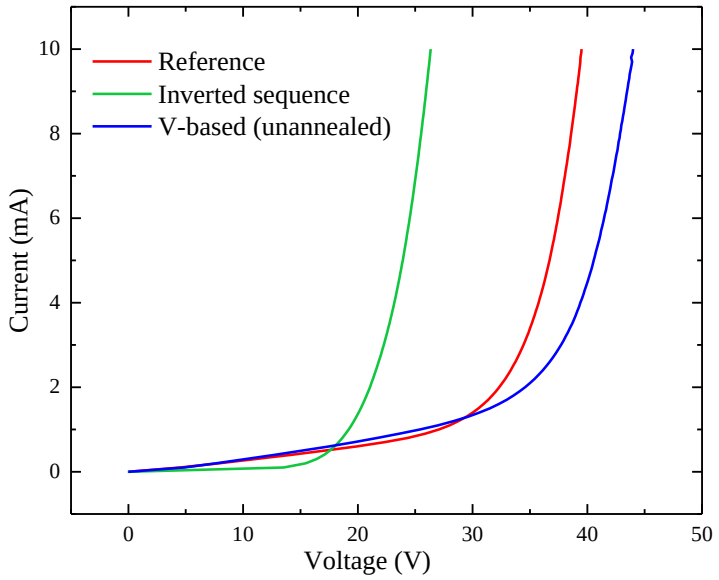

Figure 4.17: Comparison of standard vs inverted contact LED

IV characteristics of a deep-UV μ-LED fabricated according to the standard process (red), and with the *n*-contacts deposited before the *p*-contacts and the introduction of an annealing step at 800 °C (green). The data relative to a non-annealed V-based contact (blue) are also reported for comparison.

4.3 Conclusions

The μ-LED fabrication process developed for visible devices was successfully transferred to both the deep- and near-UV devices object of study in this thesis. The most critical aspects of this optimization were highlighted, and the problems caused by the specific characteristics of the AlGaN-based devices were mitigated. In particular, the theoretical

and experimental investigations relative to the mechanism of ohmic contact formation to Al-rich AlGaN materials led to the development of more reliable metallization schemes. In addition to that, the optimized *n*-contacts were also an essential prerequisite necessary for the analysis of the doping based on Hall-effect measurements that was previously discussed in Chapter 3.

Although the quality and reliability of the contacts was sufficient for the purpose of the characterization work described in Chapter 5, the results discussed in this chapter suggest that there is still room for further optimization. In particular, the dry etch necessary for the exposure of the *n*-type cladding layers could be significantly improved as our preliminary results suggest. The introduction of a thermal annealing step also for the *p*-contacts is another area of further research that appears to be worth investigating.

4.4 Bibliography

[1] S. X. Jin, J. Li, J. Z. Li, J. Y. Lin, and H. X. Jiang, "GaN microdisk light emitting diodes," *Applied Physics Letters,* vol. 76, pp. 631-633, 2000.

[2] S. X. Jin, J. Li, J. Y. Lin, and H. X. Jiang, "InGaN/GaN quantum well interconnected microdisk light emitting diodes," *Applied Physics Letters,* vol. 77, pp. 3236-3238, 2000.

[3] S. X. Jin, J. Shakya, J. Y. Lin, and H. X. Jiang, "Size dependence of III-nitride microdisk light-emitting diode characteristics," *Applied Physics Letters,* vol. 78, pp. 3532-3534, 2001.

[4] L. Dai, B. Zhang, J. Y. Lin, and H. X. Jiang, "Comparison of optical transitions in InGaN quantum well structures and microdisks," *Journal of Applied Physics,* vol. 89, pp. 4951-4954, 2001.

[5] H. X. Jiang, J. Y. Lin, S. X. Jin, and J. Li, "Micro-size LED and detector arrays for minidisplay, hyper-bright light emitting diodes, lighting, and UV detector and imaging sensor applications," US 6410940 B1, 2002.

[6] M. D. Dawson, H. W. Choi, and C. W. Jeon, "MICRO-LEDs," EP 1590834 B1, 2012.

[7] P. Maaskant, E. A. O'Carroll, P. M. Lamkin, and B. Corbett, "Light emitting diodes and the manufacture thereof," European Patent EP 1620902 B1, 2010.

[8] P. P. Maaskant, H. Shams, M. Akhter, W. Henry, M. J. Kappers, D. Zhu*, et al.*, "High-speed substrate-emitting micro-light-emitting diodes for applications requiring high radiance," *Applied Physics Express,* vol. 6, 022102, 2013.

[9] *LISA mission, European Space Agency*. Available: https://www.elisascience.org/ [Accessed June 2018]

[10] P. Pampili, M. Akhter, C. Eason, V. Z. Zubialevich, P. P. Maaskant, Z. Quan*, et al.*, "250-nm emitting LED optimized for optical fibre coupling," in *IEEE Summer Topicals Meeting Series (SUM 2015)*, Nassau, Bahamas, 2015, pp. 177-178.

[11] M. Akhter, P. Pampili, V. Z. Zubialevich, C. Eason, Z. H. Quan, P. P. Maaskant*, et al.*, "Over 20 MHz modulation bandwidth on 250 nm emission of AlGaN micro-LEDs," *Electronics Letters,* vol. 51, pp. 354-355, 2015.

[12] X. L. Wang, D. G. Zhao, J. Chen, X. Y. Li, H. M. Gong, and H. Yang, "Effect of oxidation on the optical and surface properties of AlGaN," *Applied Surface Science,* vol. 252, pp. 8706-8709, 2006.

[13] W. Schottky, "Zur Halbleitertheorie der Sperrschicht- und Spitzengleichrichter," *Zeitschrift für Physik,* vol. 113, pp. 367-414, 1939.

[14] N. F. Mott, "The Theory of Crystal Rectifiers," *Proceedings of the Royal Society of London. Series A, Mathematical and Physical Sciences,* vol. 171, pp. 27-38, 1939.

[15] J. Bardeen, "Surface states and rectification at a metal semi-conductor contact," *Physical Review,* vol. 71, pp. 717-727, 1947.

[16] A. M. Cowley and S. M. Sze, "Surface states and barrier height of metal-semiconductor systems," *Journal of Applied Physics,* vol. 36, pp. 3212-3220, 1965.

[17] V. Heine, "Theory of surface states," *Physical Review,* vol. 138, pp. A1689-A1696, 1965.

[18] W. Mönch, "Metal-semiconductor contacts: electronic properties," *Surface Science,* vol. 299-300, pp. 928-944, 1994.

[19] S. Kurtin, T. C. McGill, and C. A. Mead, "Fundamental transition in the electronic nature of solids," *Physical Review Letters,* vol. 22, pp. 1433-1436, 1969.

[20] R. T. Tung, "The physics and chemistry of the Schottky barrier height," *Applied Physics Reviews,* vol. 1, 011304, 2014.

[21] G. Greco, F. Iucolano, and F. Roccaforte, "Ohmic contacts to Gallium Nitride materials," *Applied Surface Science,* vol. 383, pp. 324-345, 2016.

[22] K. S. Sree Harsha, *Principles of Vapor Deposition of Thin Films* Elsevier Ltd, 2006.

[23] J. D. Plummer, M. D. Deal, and P. Griffin, *Silicon VLSI Technology*. Upper Saddle River, New Jersey (USA): Prentice Hall, 2000.

[24] L. Lewis, P. P. Maaskant, and B. Corbett, "On the specific contact resistance of metal contacts to p-type GaN," *Semiconductor Science and Technology,* vol. 21, pp. 1738-1742, 041, 2006.

[25] D. K. Schroder, *Semiconductor material and device characterization*, Third ed. Hoboken, New Jersey (USA): John Wiley & Sons, 2006.

[26] M. W. Cole and P. C. Joshi, "Ohmic Contacts to GaN," in *III-V nitride semiconductors applications and devices*, vol. 16, E. T. Yu and M. O. Manasreh, Eds. London: Taylor and Francis books, 2003, pp. 1-66.

[27] A. Motayed, R. Bathe, M. C. Wood, O. S. Diouf, R. D. Vispute, and S. Noor Mohammad, "Electrical, thermal, and microstructural characteristics of Ti/Al/Ti/Au multilayer Ohmic contacts to *n*-type GaN," *Journal of Applied Physics,* vol. 93, pp. 1087-1094, 2003.

[28] S. Ruvimov, Z. Liliental-Weber, J. Washburn, K. J. Duxstad, E. E. Haller, Z. F. Fan*, et al.*, "Microstructure of Ti/Al and Ti/Al/Ni/Au Ohmic contacts for n-GaN," *Applied Physics Letters,* vol. 69, pp. 1556-1558, 1996.

[29] V. Kumar, L. Zhou, D. Selvanathan, and I. Adesida, "Thermally-stable low-resistance Ti/Al/Mo/Au multilayer ohmic contacts on n-GaN," *Journal of Applied Physics,* vol. 92, pp. 1712-1714, 2002.

[30] E. F. Chor, D. Zhang, H. Gong, G. L. Chen, and T. Y. F. Liew, "Electrical characterization and metallurgical analysis of Pd-containing multilayer contacts on GaN," *Journal of Applied Physics,* vol. 90, pp. 1242-1249, 2001.

[31] C. T. Lee and H. W. Kao, "Long-term thermal stability of Ti/Al/Pt/Au Ohmic contacts to *n*-type GaN," *Applied Physics Letters,* vol. 76, pp. 2364-2366, 2000.

[32] J. S. Foresi and T. D. Moustakas, "Metal contacts to gallium nitride," *Applied Physics Letters,* vol. 62, pp. 2859-2861, 1993.

[33] Y. F. Wu, W. N. Jiang, B. P. Keller, S. Keller, D. Kapolnek, S. P. Denbaars*, et al.*, "Low resistance ohmic contact to *n*-GaN with a separate layer method," *Solid-State Electronics,* vol. 41, pp. 165-168, 1997.

[34] M. E. Lin, Z. Ma, F. Y. Huang, Z. F. Fan, L. H. Allen, and H. Morkoç, "Low resistance ohmic contacts on wide band-gap GaN," *Applied Physics Letters,* vol. 64, pp. 1003-1005, 1994.

[35] B. P. Luther, S. E. Mohney, T. N. Jackson, M. Asif Khan, Q. Chen, and J. W. Yang, "Investigation of the mechanism for Ohmic contact formation in Al and Ti/Al contacts to *n*-type GaN," *Applied Physics Letters,* vol. 70, pp. 57-59, 1997.

[36] D. Selvanathan, F. M. Mohammed, J. O. Bae, I. Adesida, and K. H. A. Bogart, "Investigation of surface treatment schemes on *n*-type GaN and $Al_{0.20}Ga_{0.80}N$," *Journal of Vacuum Science and Technology B: Microelectronics and Nanometer Structures,* vol. 23, pp. 2538-2544, 2005.

[37] B. P. Luther, J. M. DeLucca, S. E. Mohney, and R. F. Karlicek Jr, "Analysis of a thin AlN interfacial layer in Ti/Al and Pd/Al ohmic contacts to *n*-type GaN," *Applied Physics Letters,* vol. 71, pp. 3859-3861, 1997.

[38] B. Van Daele, G. Van Tendeloo, W. Ruythooren, J. Derluyn, M. R. Leys, and M. Germain, "The role of Al on Ohmic contact formation on *n*-type GaN and AlGaN/GaN," *Applied Physics Letters,* vol. 87, 061905, 2005.

[39] B. P. Luther, S. E. Mohney, and T. N. Jackson, "Titanium and titanium nitride contacts to n-type gallium nitride," *Semiconductor Science and Technology,* vol. 13, pp. 1322-1327, 1998.

[40] J. W. Jeon, T. Y. Seong, H. Kim, and K. K. Kim, "TiN/Al Ohmic contacts to N-face *n*-type GaN for high-performance vertical light-emitting diodes," *Applied Physics Letters,* vol. 94, 042102, 2009.

[41] Y. J. Lin, Y. M. Chen, T. J. Cheng, and Q. Ker, "Schottky barrier height and nitrogen-vacancy-related defects in Ti alloyed Ohmic contacts to *n*-GaN," *Journal of Applied Physics,* vol. 95, pp. 571-575, 2004.

[42] F. Iucolano, F. Roccaforte, A. Alberti, C. Bongiorno, S. Di Franco, and V. Raineri, "Temperature dependence of the specific resistance in Ti/Al/Ni/Au contacts on *n*-type GaN," *Journal of Applied Physics,* vol. 100, 123706, 2006.

[43] Q. Z. Liu, L. S. Yu, F. Deng, S. S. Lau, Q. Chen, J. W. Yang*, et al.*, "Study of contact formation in AlGaN/GaN heterostructures," *Applied Physics Letters,* vol. 71, pp. 1658-1660, 1997.

[44] L. L. Smith, R. F. Davis, M. J. Kim, R. W. Carpenter, and Y. Huang, "Microstructure, electrical properties, and thermal stability of Al ohmic contacts to *n*-GaN," *Journal of Materials Research,* vol. 11, pp. 2257-2262, 1996.

[45] E. Philofsky, "Intermetallic formation in gold-aluminum systems," *Solid State Electronics,* vol. 13, pp. 1391-1394, 1970.

[46] R. France, T. Xu, P. Chen, R. Chandrasekaran, and T. D. Moustakas, "Vanadium-based Ohmic contacts to n-AlGaN in the entire alloy composition," *Applied Physics Letters,* vol. 90, 062115, 2007.

[47] K. Mori, K. Takeda, T. Kusafuka, M. Iwaya, T. Takeuchi, S. Kamiyama*, et al.*, "Low-ohmic-contact-resistance V-based electrode for n-type AlGaN with high AlN molar fraction," *Japanese Journal of Applied Physics,* vol. 55, 05fl03, 2016.

[48] R. Sohal, P. Dudek, and O. Hilt, "Comparative study of NH_4OH and HCl etching behaviours on AlGaN surfaces," *Applied Surface Science,* vol. 256, pp. 2210-2214, 2010.

[49] F. L. M. Khir, M. Myers, A. Podolska, T. M. Sanders, M. V. Baker, B. D. Nener*, et al.*, "Synchrotron-based XPS studies of AlGaN and GaN surface chemistry and its relationship to ion sensor behaviour," *Applied Surface Science,* vol. 314, pp. 850-857, 2014.

[50] H. W. Jang, C. M. Jeon, J. K. Kim, and J. L. Lee, "Room-temperature Ohmic contact on n-type GaN with surface treatment using Cl_2 inductively coupled plasma," *Applied Physics Letters,* vol. 78, pp. 2015-2017, 2001.

[51] X. A. Cao, H. Piao, S. F. LeBoeuf, J. Li, J. Y. Lin, and H. X. Jiang, "Effects of plasma treatment on the Ohmic characteristics of Ti/Al/Ti/Au contacts to n-AlGaN," *Applied Physics Letters,* vol. 89, 082109, 2006.

[52] H. Ishikawa, S. Kobayashi, Y. Koide, S. Yamasaki, S. Nagai, J. Umezaki*, et al.*, "Effects of surface treatments and metal work functions on electrical properties at p-GaN/metal interfaces," *Journal of Applied Physics,* vol. 81, pp. 1315-1322, 1997.

[53] J. S. Jang, I. S. Chang, H. K. Kim, T. Y. Seong, S. Lee, and S. J. Park, "Low-resistance Pt/Ni/Au ohmic contacts to p-type GaN," *Applied Physics Letters,* vol. 74, pp. 70-72, 1999.

[54] J. L. Lee, M. Weber, J. K. Kim, J. W. Lee, Y. J. Park, T. Kim*, et al.*, "Ohmic contact formation mechanism of nonalloyed Pd contacts to p-type GaN observed by positron annihilation spectroscopy," *Applied Physics Letters,* vol. 74, pp. 2289-2291, 1999.

[55] J. O. Song, J. S. Ha, and T. Y. Seong, "Ohmic-contact technology for GaN-based light-emitting diodes: Role of p-type contact," *IEEE Transactions on Electron Devices,* vol. 57, pp. 42-59, 5342486, 2010.

[56] B. A. Hull, S. E. Mohney, H. S. Venugopalan, and J. C. Ramer, "Influence of oxygen on the activation of p-type GaN," *Applied Physics Letters,* vol. 76, pp. 2271-2273, 2000.

[57] J. K. Sheu, Y. K. Su, G. C. Chi, W. C. Chen, C. Y. Chen, C. N. Huang*, et al.*, "The effect of thermal annealing on the Ni/Au contact of *p*-type GaN," *Journal of Applied Physics,* vol. 83, pp. 3172-3175, 1998.

[58] C. S. Lee, Y. J. Lin, and C. T. Lee, "Investigation of oxidation mechanism for ohmic formation in Ni/Au contacts to p-type GaN layers," *Applied Physics Letters,* vol. 79, pp. 3815-3817, 2001.

[59] Y. Koide, T. Maeda, T. Kawakami, S. Fujita, T. Uemura, N. Shibata*, et al.*, "Effects of annealing in an oxygen ambient on electrical properties of ohmic contacts to p-type GaN," vol. 28, pp. 341-346, 1999.

[60] H. Amano, M. Kito, K. Hiramatsu, and I. Akasaki, "P-type conduction in Mg-doped GaN treated with low-energy electron beam irradiation (LEEBI)," *Japanese Journal of Applied Physics,* vol. 28, pp. L2112-L2114, 1989.

[61] S. Nakamura, N. Iwasa, M. Senoh, and T. Mukai, "Hole Compensation Mechanism of P-Type GaN Films," *Japanese Journal of Applied Physics,* vol. 31, pp. 1258-1266, 1992.

[62] M. Suzuki, T. Arai, T. Kawakami, S. Kobayashi, S. Fujita, Y. Koide*, et al.*, "Formation and deterioration mechanisms of low-resistance TaTi ohmic contacts for p-GaN," *Journal of Applied Physics,* vol. 86, pp. 5079-5084, 1999.

[63] M. Suzuki, T. Kawakami, T. Arai, S. Kobayashi, Y. Koide, T. Uemura*, et al.*, "Low-resistance Ta/Ti Ohmic contacts for *p*-type GaN," *Applied Physics Letters,* vol. 74, pp. 275-277, 1999.

[64] J. K. Ho, C. S. Jong, C. C. Chiu, C. N. Huang, C. Y. Chen, and K. K. Shih, "Low-resistance ohmic contacts to *p*-type GaN," *Applied Physics Letters,* vol. 74, pp. 1275-1277, 1999.

[65] J. K. Ho, C. S. Jong, C. C. Chiu, C. N. Huang, K. K. Shih, L. C. Chen*, et al.*, "Low-resistance ohmic contacts to *p*-type GaN achieved by the oxidation of Ni/Au films," *Journal of Applied Physics,* vol. 86, pp. 4491-4497, 1999.

[66] L. Yu and D. Qiao, "Comment on "Low-resistance ohmic contacts to p-type GaN achieved by the oxidation of Ni/Au films" [J. Appl. Phys. 86, 4491 (1999)]," *Journal of Applied Physics,* vol. 96, pp. 4666-4667, 2004.

[67] D. Qiao, L. S. Yu, S. S. Lau, J. Y. Lin, H. X. Jiang, and T. E. Haynes, "A study of the Au/Ni ohmic contact on p-GaN," *Journal of Applied Physics,* vol. 88, pp. 4196-4200, 2000.

[68] G. Greco, P. Prystawko, M. Leszczyski, R. Lo Nigro, V. Raineri, and F. Roccaforte, "Electro-structural evolution and Schottky barrier height in annealed Au/Ni contacts onto p-GaN," *Journal of Applied Physics,* vol. 110, 123703, 2011.

[69] T. Inazu, S. Fukahori, C. Pernot, M. H. Kim, T. Fujita, Y. Nagasawa*, et al.*, "Improvement of light extraction efficiency for AlGaN-based deep ultraviolet light-emitting diodes," *Japanese Journal of Applied Physics,* vol. 50, 122101, 2011.

[70] N. Lobo, H. Rodriguez, A. Knauer, M. Hoppe, S. Einfeldt, P. Vogt*, et al.*, "Enhancement of light extraction in ultraviolet light-emitting diodes using nanopixel contact design with Al reflector," *Applied Physics Letters,* vol. 96, 2010.

[71] N. Maeda and H. Hirayama, "Realization of high-efficiency deep-UV LEDs using transparent p-AlGaN contact layer," *Physica Status Solidi (C) Current Topics in Solid State Physics,* vol. 10, pp. 1521-1524, 2013.

[72] M. Jo, N. Maeda, and H. Hirayama, "Enhanced light extraction in 260 nm light-emitting diode with a highly transparent p-AlGaN layer," *Applied Physics Express,* vol. 9, 012102, 2016.

5 Characterization of UV LEDs

During the research object of this thesis, most of the activities aimed at device characterization were carried out in support of the fabrication work described in Chapter 4, particularly to evaluate the impact of all the different process changes that have been attempted to optimize the UV LEDs. These experimental efforts included activities such as acquisition of EL spectra, measurements of current–voltage (IV) and radiant-power–current (LI) characteristics, near- and far-field analysis, etc.

However, two aspects of the device operation were especially critical to this research, and required much more elaborate and detailed characterization work; they will be the subject of this chapter. These are the evaluation of the optical bandwidth and the enhancement of LEE in μ-LED devices.

The results here discussed were obtained using the best devices available at the time of the analysis, which included an optimized design of the vertical structure—briefly summarized in the next Section 5.1—as well as the improved version of the *p*-contacts discussed in the previous chapter. On the contrary, the optimization of the *n*-type doping and the new version of the *n*-contacts that have been described in Chapters 3 and 4 were developed only at a later stage of the project, and could not be included in this analysis. However, although the devices did not yet include all the improvements that we were able to achieve by the end of the project, and—for this reason—some degradation due to non-perfect contacts was clearly present, still the devices showed enough stability to be reliably tested, and the experiments provided a great deal of useful information that can be used as a basis for any possible future work.

5.1 Structure of the devices

5.1.1 Deep-UV material

The deep-UV devices here considered were grown in our MOVPE reactor on 2-inch sapphire substrates, onto which a low-temperature AlN nucleation layer and a high-temperature AlN buffer layer were deposited to form a template used for the hetero-epitaxial growth, as from our standard approach [1]. On top of the template, a 200-nm-thick composition-graded AlGaN layer (Al content: 100% ⟶ 77%) and a 2-μm-thick *n*-doped $Al_{0.77}Ga_{0.23}N$ layer were grown. The active region consisted of five $Al_{0.63}Ga_{0.37}N$

QWs sandwiched between $Al_{0.75}Ga_{0.25}N$ barriers with thickness of 2.5 and 6.0 nm, respectively. On top of the active region a *p*-$Al_{0.85}Ga_{0.15}N$ EBL and a *p*-$Al_{0.70}Ga_{0.30}N$ cladding layer—both of them 30-nm thick—were grown. Finally, on top of this structure a cap of 50 nm of *p*-GaN was deposited to allow good electrical contact.

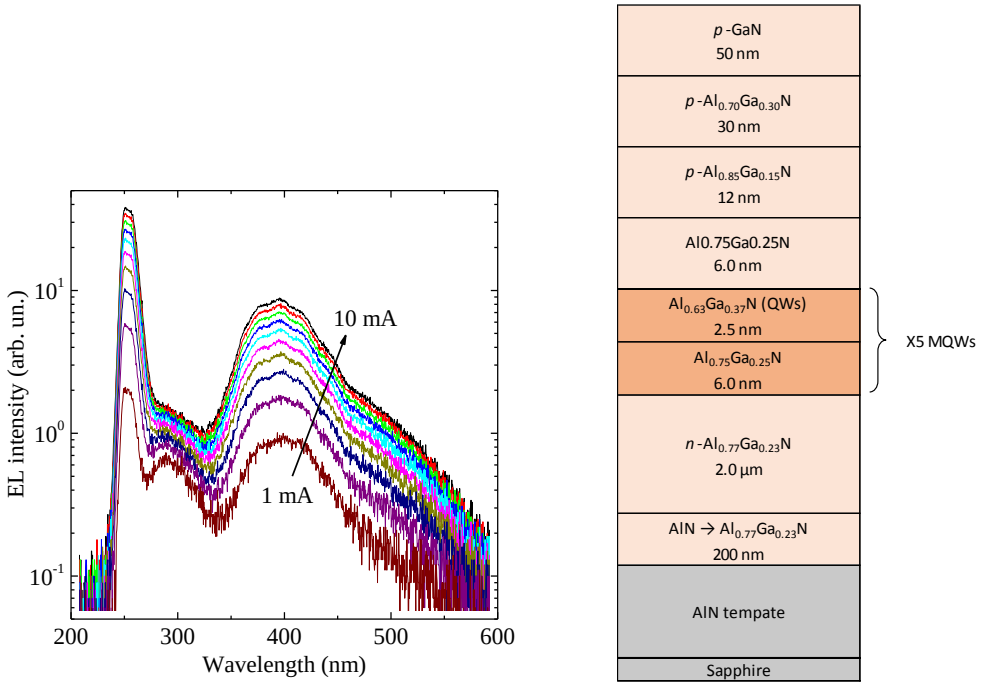

Figure 5.1: EL data of the deep-UV LED

Typical EL spectra collected at different current biases in the range 1–10 mA. The three main peaks described in the text are clearly apparent; however, the one emitted at around 300 nm tends to saturate with the increase of current. A schematic of the heterostructure is also shown.

After growth, the actual µ-LED devices as well as other reference devices were fabricated as described in Section 4.1.1. Typical EL spectra are shown in Figure 5.1 for different currents in the range 1–10 mA, corresponding to a current density range of 100–1000 A/cm^2. In addition to the targeted deep-UV peak at 250 nm due to near-band-edge (NBE) emission from the QWs, two other defect-related peaks were also present at about 300 and 400 nm. Although the latter was generally quite stable in all the tested devices—regardless of the type of fabrication approach used—the former is very sensitive to any increase of temperature and is particularly evident in large-area devices and also in all types of packaged LEDs. Apart from current-density conditions much lower than those reported in Figure 5.1, the NBE emission was always the peak showing the highest intensity; however, because of the large width of the defect peaks, most of the spectral power was actually contained in the defect emission.

An even further optimized material, having a modified active region with only three QWs, was obtained at the very end of the project. While the defect emission of this new material was roughly of the same of intensity, its NBE peak was up to 50 times higher, as can be seen in Figure 5.2. However, due to time constraints, it was not possible to fully characterize the devices obtained with this material.

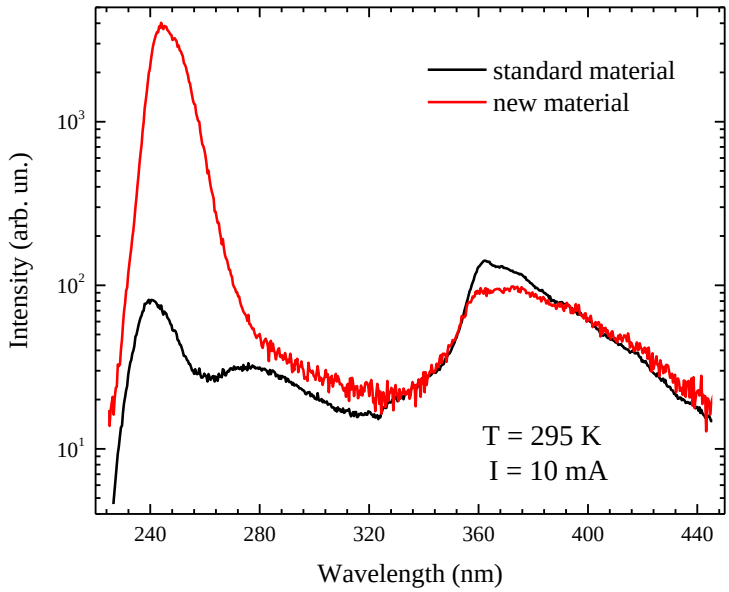

Figure 5.2: Preliminary characterization of the new deep-UV material

Comparison between the EL emission of a deep-UV LED fabricated with a material similar to the one used for the devices described in this chapter, and a preliminary EL measurement performed on a device realized with the higher-efficiency material that has subsequently become available. It should be noticed that in both spectra the NBE peak shifts towards 240 nm, as required by the objectives of the second part of the project.

5.1.2 Near-UV material

The near-UV devices were also grown on 2-inch sapphire substrates prepared with the same AlN templates used for the deep-UV LEDs. The active region—grown on top of a 1.5-µm-thick *n*-$Al_{0.77}Ga_{0.23}N$ cladding layer, consisted of five $In_{0.14}Al_{0.86}N$ QWs sandwiched between $Al_{0.69}Ga_{0.31}N$ barriers with thickness of 1.85 and 6.0 nm, respectively. Because the growth temperature of the InAlN wells is significantly lower than the one commonly used for the AlGaN barriers—in our recipe 770 and 1010 °C, respectively—a low-temperature AlGaN capping layer of about 1 nm was grown immediately after each QW before increasing the temperature to barrier condition. As

already mentioned while discussing the simulation reported in Section 2.5, this capping layer was included to avoid In desorption during the high-temperature growth of the barriers, but, due to its small thickness, it does not significantly affect the carrier transport. On top of the active region a *p*-$Al_{0.80}Ga_{0.20}N$ EBL, plus *p*-$Al_{0.70}Ga_{0.30}N$ and *p*-$Al_{0.55}Ga_{0.45}N$ cladding layers (12, 30, and 20 nm thick, respectively) were grown. Finally, on top of this structure a cap of 50 nm of *p*-GaN was deposited to allow good electrical contact.

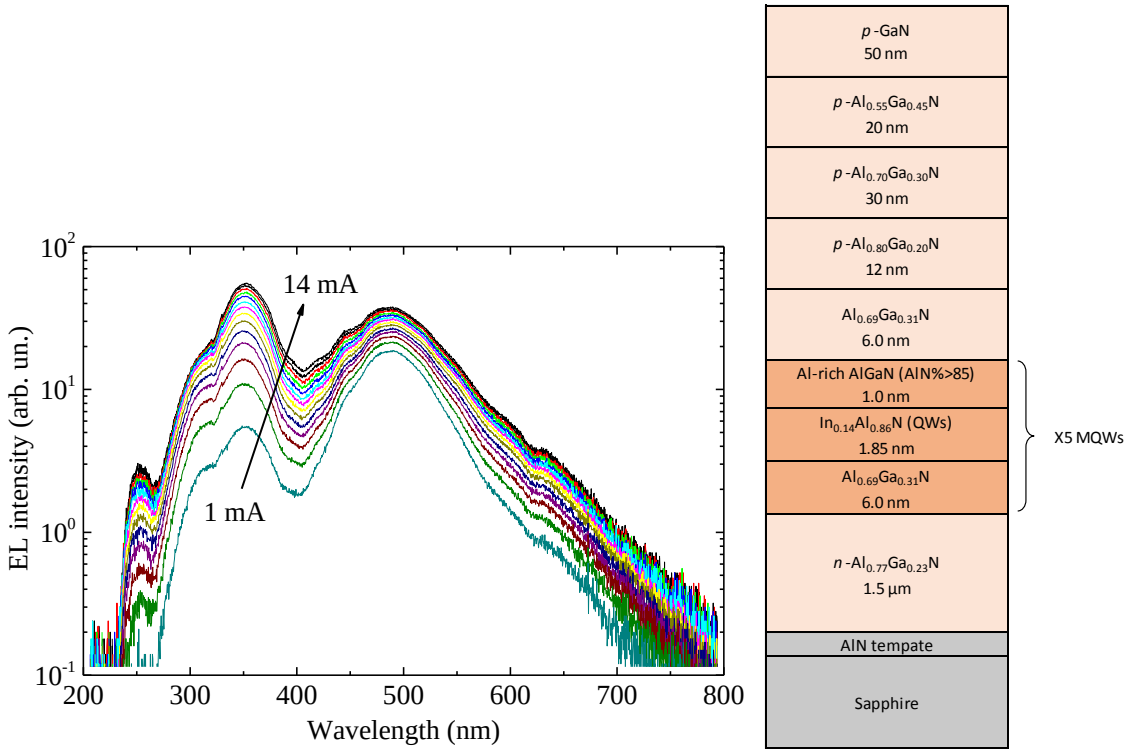

Figure 5.3: EL data of the near-UV InAlN-based LED

Typical EL spectra collected at different current biases in the range 1–14 mA. The three main peaks described in the text are clearly apparent. A schematic of the heterostructure is also shown.

After growth, the devices were fabricated using the same photolithographic mask used for the deep-UV LEDs, and described in Section 4.1.1. Typical EL spectra are shown in Figure 5.3 for different currents in the range 1–14 mA, corresponding to a current density range of 100–1400 A/cm^2. In addition to the targeted near-UV peak at 340–350 nm due to NBE emission from the QWs, a large defect-related peak at about 490 nm and a very faint one at about 250 nm were also present. While the NBE peak initially showed significantly lower intensity than the main defect-related peak, at currents higher than 4 mA it eventually became the dominant one. At even higher currents the devices became unstable due to their very high voltage drop of up to 50 V at 14 mA.

5.2 Measurement of the optical bandwidth of the μ-LEDs

As mentioned in Chapter 1, the project aimed at developing the deep-UV LED was specifically funded by ESA for its possible application in the charge management system of the LISA space mission. This long-term, class-L mission, whose launch is expected to take place in 2034 [2], consists in three drag-free satellites orbiting around the Sun at the same distance as Earth in a triangular formation, spaced 2.5 million km from each other. The satellites will form a high precision interferometer able to detect gravitational waves by monitoring the induced variations of their relative distances [3].

In order to work, this system needs to ensure that the satellites—more precisely their internal proof masses—are moving drag-free, subjected to gravitational forces only. The measurement and cancellation of non-gravitational forces, such as the drag from residual atmosphere, radiation pressure and solar wind, can be achieved if the satellite, while acting as a shield that protects the internal free-falling proof mass, constantly adjusts its position with respect to them using micro-thrusters to contrast all non-gravitational forces [4].

The screening exerted by the outer shell of the satellite, however, can only partially stop the high-energy particles coming from cosmic rays or solar flares, as some of them can reach the proof mass, causing it to become electrically charged. If too much charge builds up, the electrical forces appearing between the mass and its surroundings might become sufficient to interfere with the physics measurements. A simple solution to this problem is to allow the discharge through an ultra-thin metallic wire permanently connected to the proof mass, a solution that has been implemented, for example, in the GOCE mission [5]. However, although this solution has the advantage of not requiring any complicated charge management system, the mechanical disturbances introduced by the wire exceed the limits imposed by the very high precision of the LISA experiment, and make it unsuitable for this mission.

A more complex alternative involves shining UV radiation, either to the proof mass or to its housing, to remove electrons by photoelectric effect when an excess of charge is detected. The use of the 254-nm line of a mercury lamp has already been implemented in the proof-of-concept mission called LISA-pathfinder, which was launched on December 2015. However, the fact that the photons of this radiation have their energy only slightly above the work function of gold—which is used to coat both proof mass and housing—

might render the quantum efficiency of the extraction process highly dependent on the presence of contaminants on the surface. In particular, because some of the UV light shone against one surface is inevitably reflected back onto the other, even small differences between the two materials can cause the charge transfer to happen in the wrong direction. A solution to this issue, which is currently being evaluated for its possible implementation in the final mission, is the use of an AC discharge system in which the UV light is shone onto both surfaces in presence of an alternated electric field with a frequency high enough not to interfere with the physics measurements. The direction of the discharge can then be set by selecting with which of the two half-periods of the alternated field the LED is synchronously switched on.

The use of nitride-based UV LEDs would be advantageous in both types of UV-based discharge systems. In the standard DC approach, the possibility of controlling the emission wavelength by varying the composition of the active region will make it possible to set the photon energy well above the nominal work function of gold, greatly reducing the issue caused by any possible difference between the actual work functions of mass and housing. On the other hand, UV LEDs are the only type of UV sources that could be driven at the frequencies required by the AC system. For this reason the European Space Agency specifically required that we tested the high-frequency capabilities of our device, and set a target optical bandwidth of 10 MHz. This section reports about these measurements, which were my contribution to a paper published by our group [6] regarding the fabrication and testing of the 250-nm LED achieved during the first part of this project.

5.2.1 Typical experimental setup and its limitations

Electrical-to-optical modulation bandwidth measurements are quite common in telecommunications as a way to assess the limitations to the data transmission rate that are due to the light source, being this either an LED or a laser. The typical experimental setup, which is outlined in Figure 5.4, consists in a network analyser that compares the signal sent to the device under test (DUT) with the one coming from a photodetector subject to the modulated radiation. In order to drive the DUT in conditions in which the radiation intensity is—as much as possible—linear with the current, a DC bias is combined through a bias-tee with the actual AC signal, whose frequency can be varied from 0 up to several GHz. The optical bandwidth is usually defined as the frequency of the AC small signal that causes a 50% reduction (i.e. 3dB) of the optical AC power

sensed by the photodetector with respect to the one measured as the frequency approaches zero. Although the actual data transmission rate in communication systems also depends on the type of encoding utilized, the optical bandwidth of the light source is nonetheless a key parameter, as faster data transmissions require faster modulations. This experimental setup has been used, for example, in the bandwidth measurements of the devices fabricated by our group in previous projects [7-10].

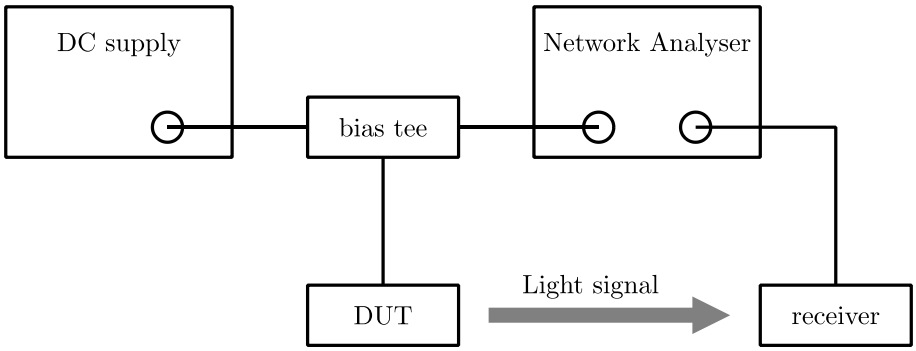

Figure 5.4: Optical bandwidth measurement

Typical experimental setup for the measurement of the optical bandwidth of an LED or laser. Although very common, this approach was not suitable for the measurements described in this section.

In contrast to this approach, the type of modulation required by the ESA application is not meant to carry any type of data transmission, and has completely different requirements. In particular, no DC bias can be superimposed to the modulation, as the UV LED needs to operate at full power when the magnetic field produced by the charge management system is along the desired direction, and completely switched off during the other half-period. In addition to that, experimental issues make it very hard to use an approach similar to the one outlined in Figure 5.4, as the sensitivity of standard silicon photodetectors is very low in the deep-UV spectral range, and also the optical power of the DUT is orders of magnitude lower than the visible or infrared devices used in telecommunications. But even with a detector having enough sensitivity to measure the variations of UV radiation caused by the modulation, it would be very difficult to filter out the component due to the simultaneous modulation of the defect peaks, which might have very different switching times and, as mentioned in Section 5.1.1, carry most of the spectral power emitted by the device.

5.2.2 New experimental approach

In order to overcome the limitations of the standard approach, the following setup was arranged. The device was contacted on-chip by means of a Picoprobe micromanipulator equipped with a coaxial probe tip, and intermittently biased using a high power pulse generator HP8114A. The applied waveform consisted in a square function with a 0 V OFF-state and a fixed-current ON-state, which—in different experiments—was varied in the range 5–60 mA; the duty cycle was kept fixed at 1% to avoid any heating up of the chip, and the repetition period was either 100 or 124 μs.

The light emitted by the device was collected from below the wafer with an UV-transparent optical fibre and brought to the entrance port of a Horiba iHR320 spectrometer. A preliminary spectrum of the emitted light was recorded using a Horiba Synapse CCD detector in the range 200–450 nm and the three main peaks at about 250, 300 and 400 nm were detected, as shown in Figure 5.1. The light was then diverted into a Hamamatsu R943-02 photomultiplier tube (PMT) for the time response measurements. However, to separately explore the switching characteristics of each of the peaks, the orientation of the diffraction grating was modified to direct the light coming from the peak under investigation at the centre of the narrow exit-slits, so that all the other components of the spectral radiation could be stopped before entering the PMT.

In order to convert the small current from the PMT into a voltage, the signal was brought to a 50 Ω impedance channel of a Tektronix TDS3054 Oscilloscope by a BNC cable. With this setup, the PMT operated in low intensity conditions and a large number of waveforms (from 100 to 1000) were to be collected and averaged to obtain a reliable output. To remove the effects of electromagnetic interferences, the signal still present at the PMT when the spectrometer shutter was closed, was collected and subtracted to the actual signal.

The rise and fall times were obtained, during the transients after the commutations, as the time difference between the instants in which the UV intensity was 20% or 80% of the average ON-state. The bandwidth was then estimated approximating the system as a single-pole low-pass filter (i.e. with simple exponential rise and fall times). In this case, the frequency at which the optical power is reduced to half of the low-frequency value (f_{3dB}) can be calculated as:

$$f_{3dB} = \frac{\sqrt{3}\ \ln 4}{2\pi\ t_{mod(20-80)}} \approx \frac{0.38}{t_{mod(20-80)}} \tag{5.1}$$

in which $t_{mod(20-80)}$ is either the rise or the fall time, which in this approximation should be equal to each other. Of course the switching times measured in this way are not only due to the optical bandwidth of the UV LED, but also include the contributions from the pulse generator, the PMT and the oscilloscope, whose rise times are estimated to be 7, 3 and 0.7 ns respectively. Even though the DUT has the longest rise time and hence it dominates the overall time response, the effect due to the pulse generator might not be completely negligible. For this reason, the bandwidth obtained with this setup has to be considered an approximation. The PMT has also a transit time of 23 ns, which causes a delay between the input signal from the pulse generator and the response from the PMT; however this does not affect the switching times.

5.2.3 Discussion and conclusions

Two nominally identical μ-LED samples, named A and B, were tested using the procedure above described; the results of the analysis of the 250-nm peak are summarized in Table 5.1.

Sample	ON current (mA)	ON time (μs)	rise time (ns)	fall time (ns)	bandwidth (MHz)
A	20	1.24	14.8	15.0	25
A	40	1.24	16.4	15.6	23
A	60	1.24	17.8	14.8	21
B	5	1.00	12.4	14.6	26
B	40	1.00	12.0	14.0	27

Table 5.1: Summary of the results

The table shows the measured rise and fall times and the calculated optical bandwidths for two samples (named A and B) at different ON-state time and current conditions. The bandwidth was conservatively calculated using the longer one between rise and fall times.

All the measurements, regardless of the ON-state current level, showed an optical bandwidth higher than 20 MHz, with a maximum of 27 MHz for the sample B, when

biased at 40 mA. Although sample A showed a slight increase of the rise time with increased ON-state current, this behaviour was not present in sample B and it was most likely caused by experimental errors due to the lack of impedance matching between the pulse generator and the DUT. In fact, as can be seen in Figures 5.5–5.7, a clear ringing effect is present in the optical intensity detected by the PMT during the ON-state of all the samples tested. An overshoot after the turn-on is also present, which is particularly evident in sample B when driven at low current (5 mA), as shown in Figure 5.7 (a). These intensity variations make it very difficult to clearly identify the actual ON-state level, whose 20% and 80% values are used in the definition of the switching times. This issue may hence explain the scatter of the optical bandwidth values present in Table 5.1.

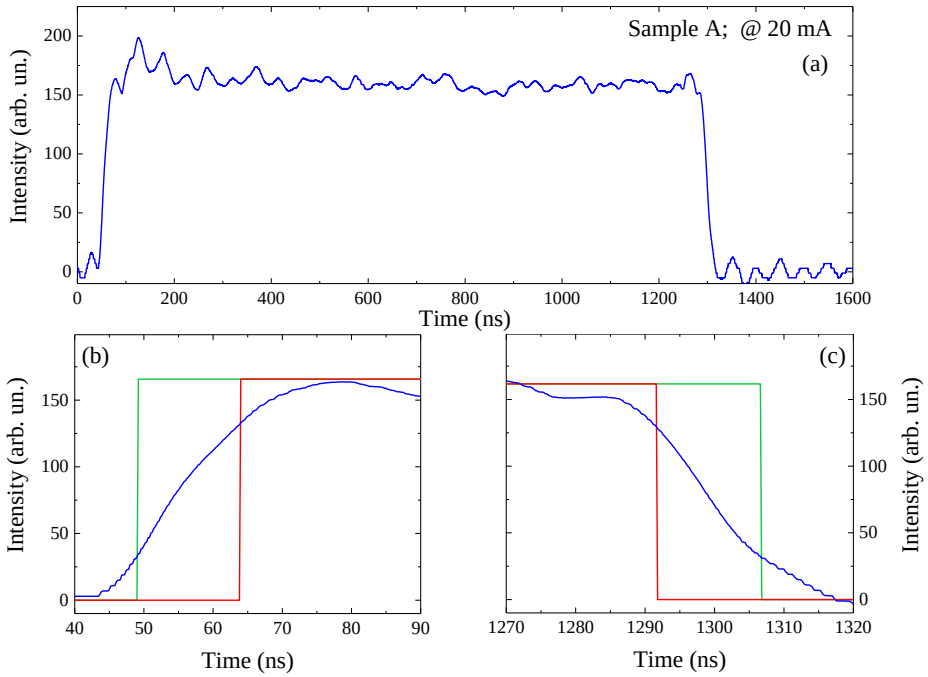

Figure 5.5: Switching transients (1/3)

Transients of the 250-nm peak (a), reconstructed through the averaging of the signal coming from the PMT and the subtraction of electromagnetic interferences. Close-ups of the turn-on (b), and turn-off (c), with the indication of the extremes of the switching times at the 20% and 80% of the ON-state intensity.

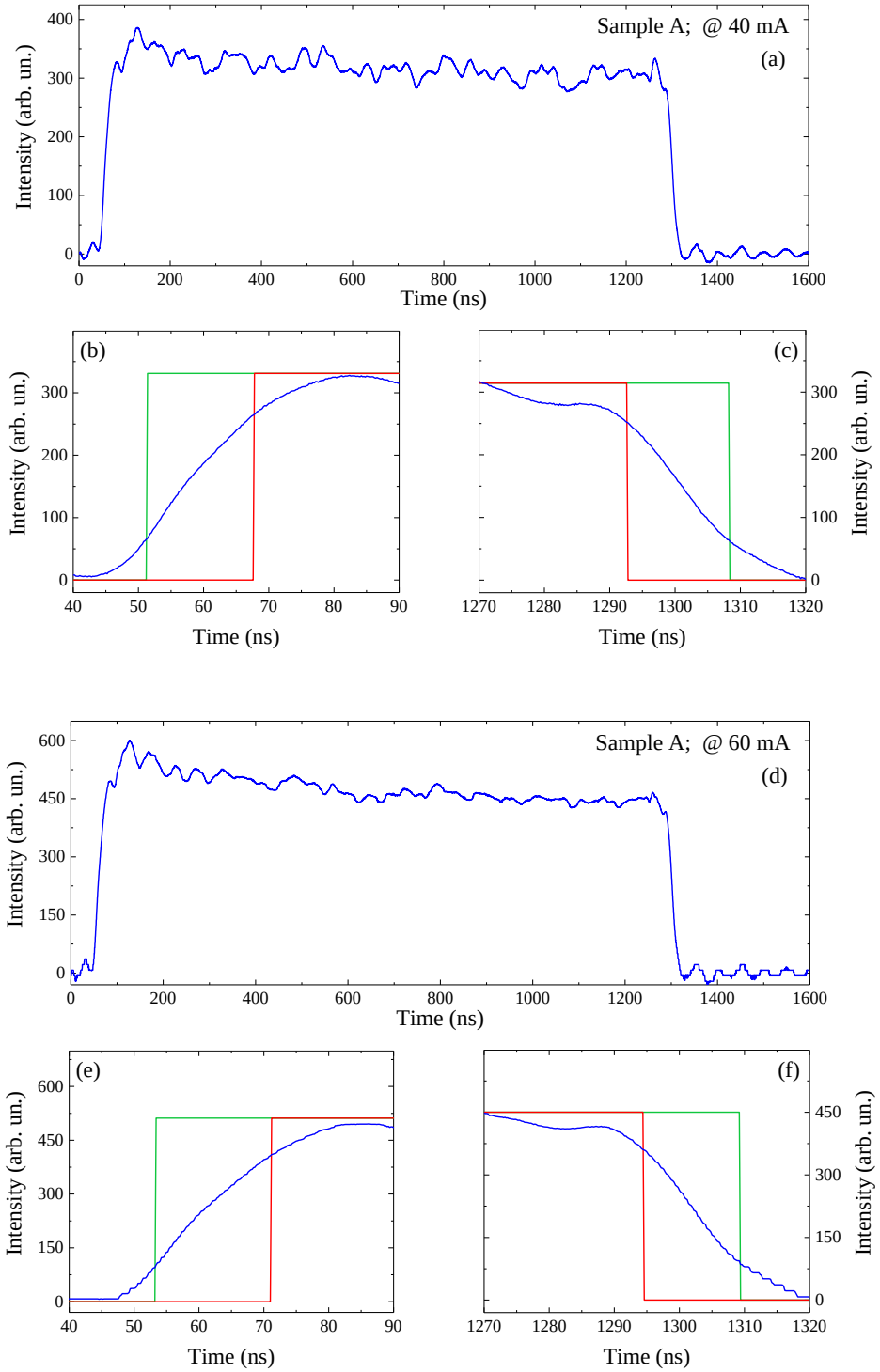

Figure 5.6: Switching transients (2/3)

Transients of the 250-nm peak (a; d), reconstructed through the averaging of the signal coming from the PMT and the subtraction of electromagnetic interferences. Close-ups of the turn-on (b; e), and turn-off (c; f), with the indication of the extremes of the switching times at the 20% and 80% of the ON-state intensity.

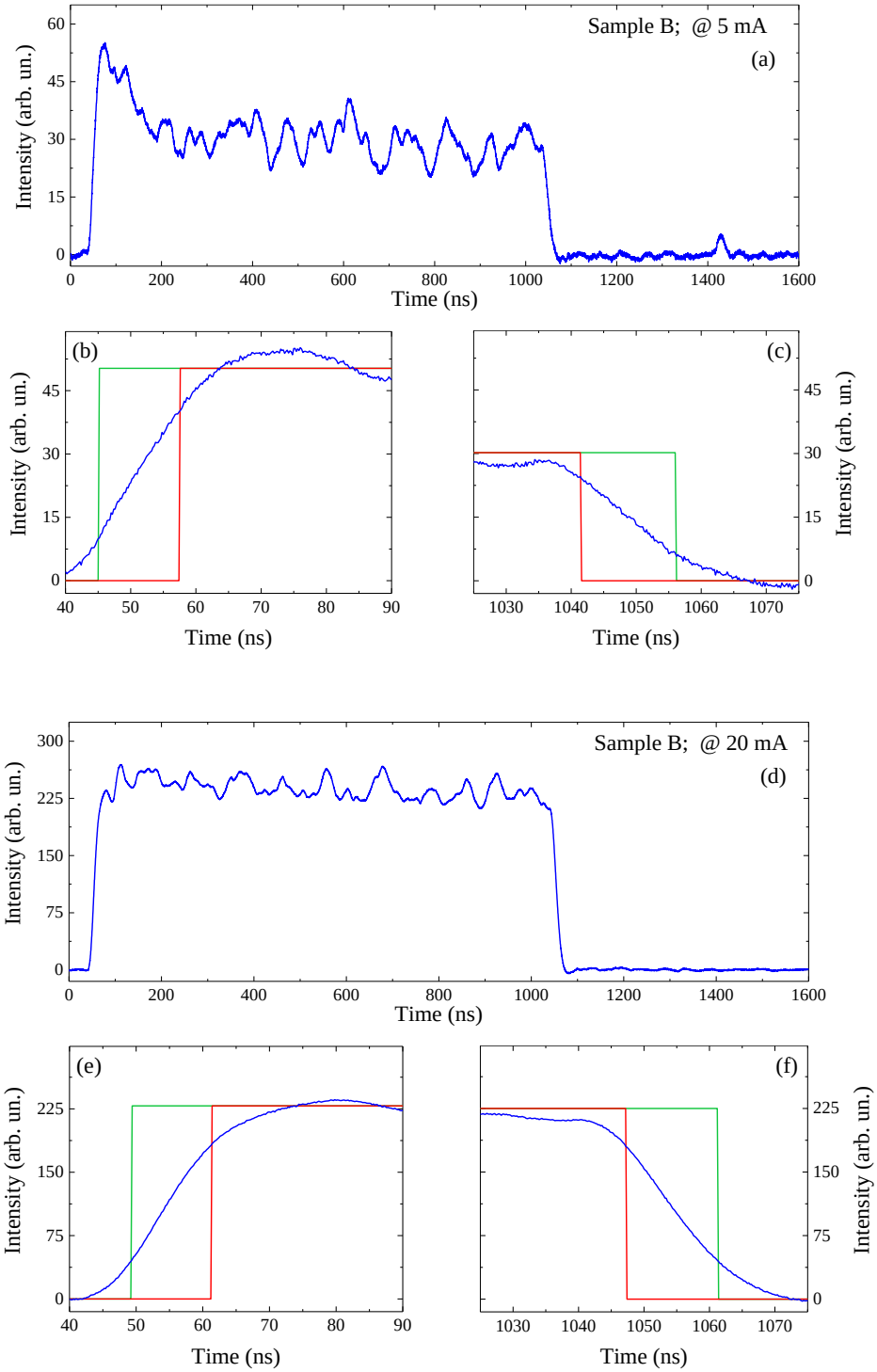

Figure 5.7: Switching transients (3/3)

Transients of the 250-nm peak (a; d), reconstructed through the averaging of the signal coming from the PMT and the subtraction of electromagnetic interferences. Close-ups of the turn-on (b; e), and turn-off (c; f), with the indication of the extremes of the switching times at the 20% and 80% of the ON-state intensity.

However, notwithstanding these experimental limitations, the bandwidth of the UV LEDs proved to be significantly higher than the 10 MHz required by the ESA specifications, making them suitable for the charge control system as envisaged for the LISA mission.

The same type of analysis was also attempted for the light coming from the peaks at 300 and 400 nm but, in both cases, the intensity was too low to allow any reliable estimation of their switching times, particularly for the former of the two. However, the data clearly showed that the fall time of the 400-nm emission is orders of magnitude longer than the one from the peak at 250 nm. In fact, as can be seen in Figure 5.8, photons with wavelength of 400 nm are still detected several tens of µs after the commutation to the OFF-state. Although the origin of this behaviour is unclear, the demonstration of its presence clearly shows that the transients due to the modulation of this defect peak would, if not adequately removed, significantly alter the measurement of the concurrent transient of the deep-UV emission, and confirms the validity of the experimental approach discussed in this section.

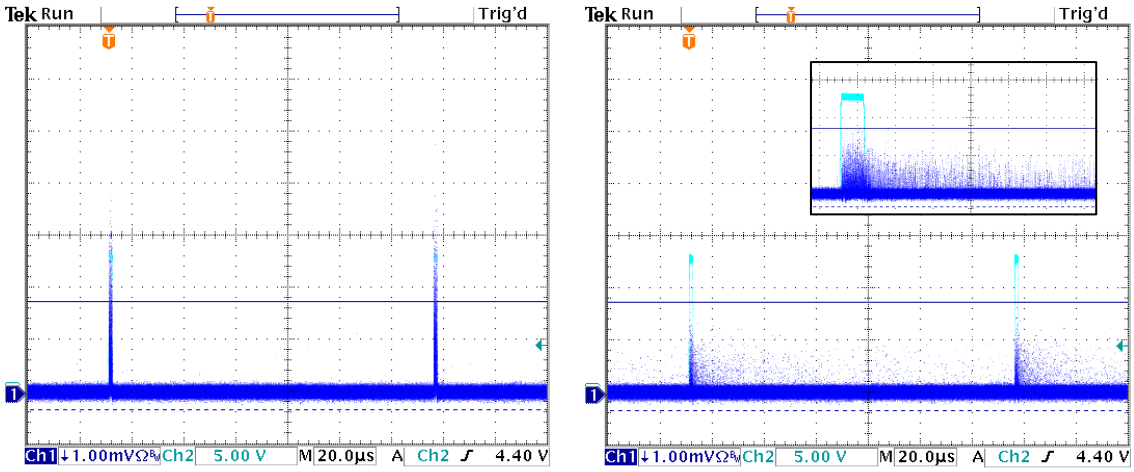

Figure 5.8: Oscilloscope screenshots

Visualization of the signal coming from the PMT (dark blue) and the electrical bias applied to the DUT (light blue) as collected by the oscilloscope before any data treatment. The time responses of the 250-nm peak (a), and the 400-nm peak (b) are compared at the same timescale; the inset shows a magnification of the transient of the 400-nm peak (timescale at 2 µs/div).

5.2.4 Characterization of the InAlN-based near-UV LED

Although there was no specific requirement regarding the switching characteristics of the device developed within the other project, the same setup and approach were also used to study the InAlN-based LED emitting in the near-UV.

Two nominally identical μ-LED samples, named C and D, were initially tested to assess the quality of the signal from the three main emission-peaks discussed in Section 5.1.2. While the emission at about 250 nm was too weak to be analysed, the other two peaks (i.e. the NBE emission at about 340 nm, and the other defect-related emission at about 490 nm) were of sufficient intensity to be acquired and averaged over reasonable lengths of time. However, their intensities were significantly lower compared with the NBE emission of the deep-UV device, which made the measurements particularly difficult. In addition to that, the ringing caused by the already mentioned issue of impedance mismatch produced, in this case, oscillations whose intensity was comparable to the actual signal, especially for the peak at 490 nm. An example of the typical transients obtained for these LEDs is shown in Figure 5.9, in which the data relative to both emission peaks were collected from the same device and with the same optical-fibre coupling. As can be seen in Figure 5.9 (a), the emission at 340 nm also shows an initial intensity maximum whose value is more than two times of the asymptotic level reached about 200 ns after the turn-on, which further complicates the choice of an unambiguous definition of the intensity level relative to the ON-state. Nothwithstanding these experimental challenges, an approximate analysis of the NBE peak was attempted, and the results are summarized in Table 5.2.

Both devices showed a significantly faster modulation speed than the deep-UV ones, with an optical bandwidth of up to 42 MHz for the NBE emission. Considering that both deep- and near-UV devices were fabricated with the same process—and hence share the same geometry—any capacitance effect can be ruled out. While a reduced series resistance of the near-UV LED could in part explain this different behaviour, another important reason can be attributed to a reduced carrier lifetime in the InAlN-based QWs, resulting from an increased recombination rate in either the radiative or the non-radiative channel, or, possibly, by a combination of the two effects. The radiative recombination rate is indeed expected to be higher because of the nearly-polarization-matched InAlN/AlGaN active region that is present in these devices, as discussed in Section 2.5. The non-radiative recombination rate can also be higher, as an increased incorporation of point defects in

the InAlN QWs cannot be definitely ruled out at this moment; on the contrary, the concentration of the dislocations should not be significantly different because this is mostly determined by the quality of the AlN template—which is the same for all the devices here considered—and is consequently not affected by the different conditions set during the growth of the active region. In addition to these considerations, the fact that the QWs in the near-UV devices are thinner than those in the deep-UV ones (namely 1.85 instead of 2.5 nm), is expected to increase the carrier concentration in the wells and, consequently, both the radiative and the non-radiative recombination. Although all these effects can potentially decrease the carrier lifetime and hence induce faster optical modulations, by the results of this experiment it is unfortunately not possible to estimate their relative contribution. In particular, the contribution from the reduced QCSE due to the polarization matching, which has been theoretically demonstrated by the simulations described in Section 2.5, cannot yet be experimentally confirmed. A future experiment, in which the AlGaN/AlGaN or InAlN/AlGaN devices that are compared have exactly the same active-region geometry, would be highly advisable in order to investigate this important matter further.

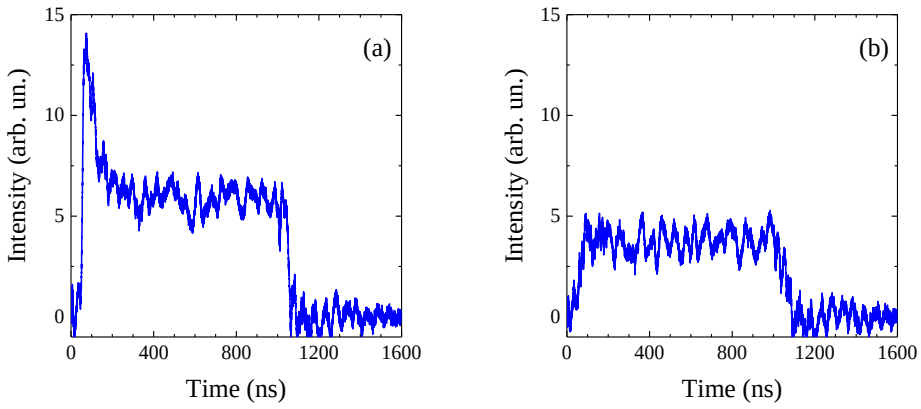

Figure 5.9: Switching transients of the near-UV LED

Transients from sample D relative to the 340-nm peak (a) and the 490-nm peak (b), reconstructed through the averaging of the signal coming from the PMT and the subtraction of electromagnetic interferences. An overshoot in (a) and ringing oscillations (b) greatly complicate the analysis of the data; transients from sample C—not reported here—show similar behaviour.

Although the transient relative to the modulation of the peak at 490 nm could also be collected, the amplitude of the oscillations caused by the ringing effect are so large compared with the low-intensity signal to which they are superimposed, that they are not only visible during the ON and OFF states, as in all the transients here analysed, but are in this case also clearly detectable during the rise and the fall of the signal. As can be seen in Figure 5.9 (b), this completely distorts the shape of the transient during the turn-on and turn-off commutations and makes it impossible to quantitatively estimate both rise and fall times. Despite this, it is evident that the transients of this defect-related emission, although slower than those of the NBE emission, are definitely much faster than the ones due to the defect peak of the deep-UV device, which were orders of magnitude slower than the transients of the NBE emission of the same device, as shown in Figure 5.8. The reason for that is, however, still not clear.

In conclusion, it is worth noticing that, despite the fact that the much lower intensity of this device did not allow the same level of accuracy that was possible for the deep-UV LED, the high modulation bandwidth of the main emission peak is in good agreement with our assignation of it to NBE recombination.

Sample	ON current (mA)	ON time (µs)	rise time (ns)	fall time (ns)	Bandwidth (MHz)
C	10	1.00	10.4	11.2	34
D	10	1.00	7.0	9.0	42

Table 5.2: Summary of the results

The table shows the measured rise and fall times and the calculated optical bandwidths for two samples (named C and D) at different ON-state time and current conditions. The bandwidth was conservatively calculated using the longer one between rise and fall times.

5.3 Characterization of LEE enhancement in deep-UV µ-LEDs

The other area of investigation object of the experimental efforts discussed in this chapter regards the study of the LEE and its possible increase with the use of µ-LED emitters.

As previously detailed in Chapter 4, the use of this type of device was originally proposed as a way to increase the efficiency—especially the LEE—of GaN-based visible devices

[11, 12]. With the particular implementation that was later developed at Tyndall National Institute, in addition to a better light extraction, it was also possible to control the far-field emission pattern [8], a feature that can be used to achieve high optical-coupling efficiency in applications that require the light to be confined within small areas and small acceptance angles. This aspect is particularly important, for example, when coupling to an optical fibre is necessary, such as in the already discussed charge management system of the LISA space mission [3]. However, there is another aspect that makes this approach particularly suitable for deep-UV LEDs.

One of the most serious problems that affect the LEE of Al-rich AlGaN-based devices is the particular structure of the valence band present in this material, in which its three sub-bands change their position with respect to the conduction band as the Al content of the alloy varies. This determines the optical polarization and consequently the direction of the light produced by carrier recombination in the material, which greatly influences the amount of radiation that can be extracted from the device.

This phenomenon is due to the lack of symmetry between the directions along and perpendicular to the *c*-axis of wurtzite III-nitride materials, which forces the valence sub-band with a predominant atomic p_z-like character (i.e. the split-off band) to separate[12] from the p_x- and p_y-like sub-bands (i.e. the heavy- and light-hole bands). However, while in GaN the split-off band lies below the other two and the polarization is still mostly TE (i.e. electric field perpendicular to the *c*-axis), in AlN the split-off band becomes the topmost one [13] and hence dominates the recombination and forces the polarization to be mostly TM (i.e. electric field parallel to the *c*-axis). Because the radiation propagation can only be perpendicular to both the electric and magnetic fields, the type of polarization can suppress emission along certain directions. In AlGaN alloys, which have an intermediate behaviour between GaN and AlN, there is then a critical AlN concentration above which the UV radiation switches from being emitted predominantly along the *c*-axis as in GaN, to being predominantly emitted in-plane as in AlN [14].

Because of the relatively high refractive index of the semiconductor material, only the photons emitted within a small escape cone along the *c*-axis can be extracted. Assuming a

[12] In addition to the crystal-field effect, the position of the split-off band is further influenced by the spin–orbit interaction, which is also responsible for the small separation between heavy- and light-hole bands.

smooth and flat surface, the critical half-angle θ of this cone can be calculated using the Snell's law:

$$\theta = arcsin\frac{n_{ext}}{n_{semi}}, \tag{5.2}$$

in which n_{ext} and n_{semi} are the refractive indexes of the external medium in which the device operates (usually air), and the one of the active semiconductor, respectively. The angle θ is not affected by the presence of cladding layers, sapphire substrate, nor by any other materials apart from the active semiconductor and the external medium; photons emitted at larger angles inevitably experience total internal reflection at some interface and are trapped or waveguided to the edges of the device. On the contrary, if Fresnel reflections due to refractive index discontinuities are neglected, all the light inside the escape cone is extracted and refracted outside the device at all angles. For devices in which the UV radiation is still mostly TE-polarized, the intensity within the escape cone stays roughly constant and, as a consequence, the far-field pattern of the LED does not depart too much from the typical lambertian emission of the visible LEDs. However, as the TM-polarized component of the UV radiation increases, the far-field pattern becomes more and more laterally elongated and, eventually, the typical two-lobed shape appears. This behaviour is summarized in Figure 5.10, where the far-field patterns due the emissions with increasing TM-polarized components are simulated; the normalization coefficients reported in the figure also demonstrate the expected significant decrease in intensity of the extracted light.

Although this polarization switch-over mostly depends on the alloy composition, other factors may also greatly influence the optical behaviour of AlGaN, and shift its transition to a different AlN concentration. This fact can be used to engineer the active regions of the deep-UV LEDs in order to enhance as much as possible the TE-component from their emission, even in presence of high-Al-content AlGaN QWs.

In particular, as shown by Northrup *et al.* [15], compressive strain can almost completely suppress TM polarization even in LEDs emitting at wavelengths as short as 253 nm. The fact that—in absence of relaxation—the strain of the quantum wells depends on the particular substrate used, explains why the enhanced TE-emission was present in the devices grown on bulk AlN substrates, but not on those grown at the same conditions on standard sapphire. In addition to compressive strain, quantum confinement due to narrow

wells, and internal electric fields due to polarization discontinuities within the active region are also known to push the polarization switch-over to higher AlN concentrations [16]. Other factors such as the carrier density may also have an influence. Further analysis about the optical behaviour of AlGaN can also be found in the book chapter by Rass and Lobo-Ploch [17] and in the references therein.

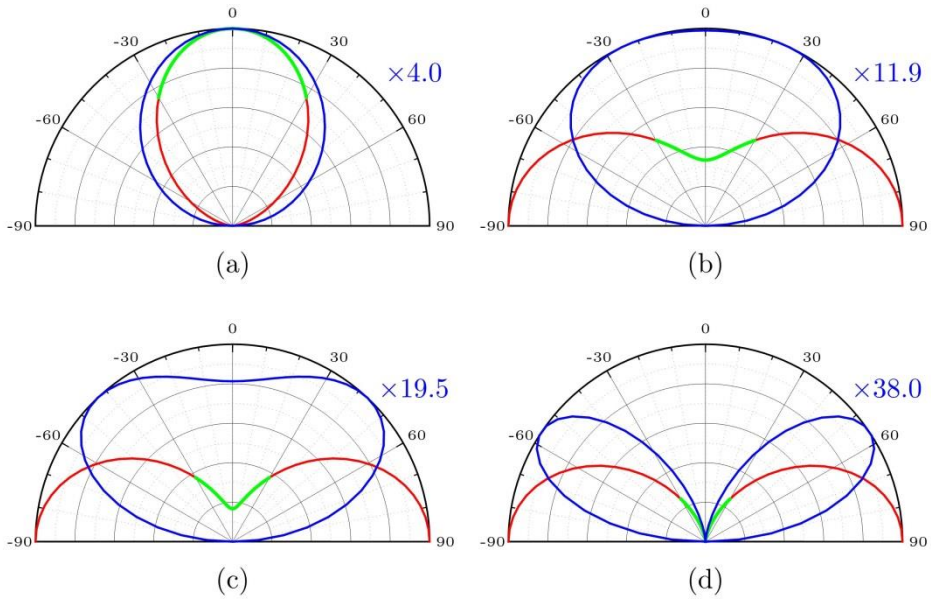

Figure 5.10: Far-field pattern

Simulation of the far-field pattern (blue line) as a function of the angular emission (green line for the fraction of light that can be extracted; red line for the fraction trapped by total internal reflection). The four graphs refer to a fully TE-polarized emission (a), a slightly TM-polarized emission (b), a highly TM-polarized emission (c), and fully TM-polarized emission (d). An arbitrary semiconductor refractive index of 2.0 was assumed (i.e. 30° escape cone) for the purpose of this calculation. The far-field patterns are normalized and the normalization coefficients are reported in figure close to each graph.

Apart from the engineering of the active region during growth, the LEE of deep-UV LEDs can also be greatly enhanced at device fabrication level. Because the light emitted in-plane, if not redirected towards the substrate at shorter angles, is eventually absorbed and lost, a possible strategy is to incorporate scattering elements within the device. For example, in the work of Wierer *et al.* [18] devices emitting at around 270 nm have their whole area of 300 × 300 μm^2 covered with a series of very close trenches obtained by dry etch. These structures, which have sidewall angles of about 70–80° and an average distance from each other that varies from 9 to 15 μm according to the different geometries

investigated, act as scattering elements that intercept the UV radiation emitted in-plane and redirect it at all different angles. Using this approach, an increase of LEE up to four times for the most TM-polarized emission was estimated.

Another solution, which is often used also in visible LEDs, is the inclusion of scattering elements on the external surface of the substrate. In fact, the presence of textured patterns at an interface where light can be trapped because of total internal reflection, causes the angle at which the radiation approaches the surface to randomly vary at any point, increasing the chances of being transmitted, even for angles larger than θ of Equation (5.2). Simulations using finite-difference time-domain approach showed that this approach can be particularly effective in devices having a high degree of TM polarization [19].

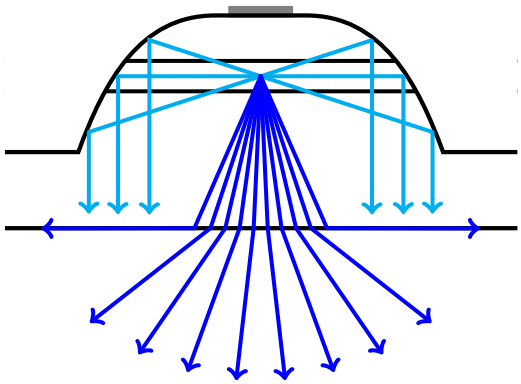

Figure 5.11: Light extraction mechanism in μ-LED

Schematics of the working principle of our version of a μ-LED. The dark-blue rays represent the light emitted within the extraction cone and are hence extracted and refracted at all angles; the light-blue rays represent the in-plane-emitted light that is reflected by the smooth μ-LED sidewalls and ideally extracted at almost perpendicular angles.

Although the use of scattering elements has indeed proven to be effective, the fact that the light is reflected or transmitted by these structures at all possible angles, limits the LEE improvements and also makes it very difficult to optimize the coupling of the device with other components such as optical fibres. Instead, as anticipated earlier, this issue can be largely overcome by our implementation of the μ-LED concept, in which the presence of precisely oriented and smooth mesa sidewalls allows the intercepted light to be reflected towards the sapphire substrate at almost perpendicular angles. As a result of that, as

schematically outlined in Figure 5.11, in addition to the lambertian emission coming from the light propagating within the escape cone, a large amount of the dominant TM radiation emitted in-plane can also be extracted and more easily coupled into other elements of the optical system.

In order to investigate the effectiveness of this approach, a series of experiments was carried out, which will be detailed and discussed in the following sections.

5.3.1 On-chip testing

As described in Section 4.1.1, three different types of devices were developed for this research: the target one consisting of a cluster or μ-LED emitters, a reference device whose emitters do not have any sidewall shaping nor any mesa definition, and a standard large-area LED; they are referred to as devices of type A, B, and C, respectively. In this first experiment, after having completed the processing, one sample for each of the three types was contacted directly on-chip with a Picoprobe micromanipulator, and biased at different currents in the range 1–10 mA. During the measurement, the chip was held by a copper support that also served as a heatsink while the light was collected from its back side by means of a UV-transparent optical fibre through a small aperture in the support. The fibre was a step index, multimode one with a core diameter of 910 μm and a numerical aperture of 0.22, and was held perpendicular to the chip and put in contact with the sapphire substrate just below the device under test, whose dimensions are 520 × 520 μm^2 for all of the three types. The light was then directed into a miniature Ocean Optics 2000+UV–VIS spectrometer, and the relative spectral intensity of the different samples was recorded at current steps of 1 mA.

The integrated intensity, both across the whole emission range (200–600 nm) and around the deep-UV peak (240–270 nm), are reported in Figure 5.12 for the μ-LED devices with and without mesa etch (i.e. type A and B, respectively); the intensity ratio of the two samples, which can be used as an estimation of the LEE enhancement, is also reported for the two spectral ranges.

In all the measurements performed on type-A and type-B devices, the integrated intensity was quite linear with the injected current and no sign of droop was present. While the LEE enhancement relative to the whole emission range was about 1.8 times at all the tested currents, the component only due to deep-UV emission was significantly larger, with an increase of up to 2.8 times, for currents of 3 mA or higher. Although this

preliminary experiment shows that the slanted reflective sidewalls of the μ-LED emitters are indeed able—particularly for the deep-UV emission—to significantly increase the LEE, to thoroughly evaluate the effectiveness of the μ-LED approach, the large-area device (i.e. type C) also needs to be tested and contrasted. However, considering the large difference in the active areas of this type of device and the μ-LED clusters, the results are better displayed as a function of the current density. Unfortunately, the current range initially explored for all the devices (1–10 mA) corresponds to current-density ranges for the μ-LED clusters and the large-area devices that do not overlap (100–1000 A/cm^2 and 5–50 A/cm^2, respectively).

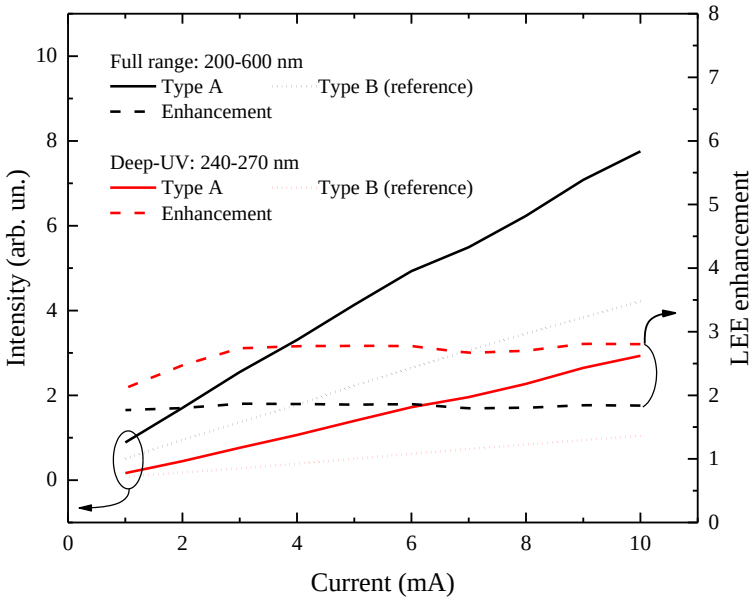

Figure 5.12: LEE enhancement

Comparison of the LI characteristics of a μ-LED device with (solid lines) and without (dotted lines) mesa etch; the values shown are the result of an integration along the deep-UV range (red lines) and the whole emission spectrum (black lines). The ratio of the intensity emitted by devices with and without mesa etch is also reported (dashed lines).

To extend the analysis on the device of type C, currents higher than 10 mA were also attempted, but in these conditions the sample started to show a very unstable behaviour and eventually failed; the results have hence not been recorded. A second type-C device was subsequently tested, this time in the current range 10–60 mA, which corresponds to a current density range of 50–300 A/cm^2. Although some minor instabilities were still present, it was possible to obtain reliable data up to 200 A/cm^2; at higher current densities

the device showed clear signs of degradation—with permanent changes in the IV characteristics and no increase in the emission intensity—before failure at 300 A/cm^2.

As shown in Figure 5.13 (a), due to the much larger active area of the type-C device, the total integrated intensity in the range 200–600 nm was considerably higher than those of both types of μ-LED clusters, with a power emission more than six times greater than that of the type-A device when measured at 200 A/cm^2. However, while the large-area device showed a clear sub-linear behaviour, with degradation and eventually failure when tested at the highest currents explored in this experiment, the μ-LED clusters showed linear increase of intensity with the current density, and no sign of degradation up to 1000 A/cm^2. As a result of this behaviour, for current densities in excess of 455 A/cm^2, the type-A device was eventually able to produce a deep-UV emission of higher intensity than the maximum value obtained with the large-disc device before failure.

These results show that—even without further optimization of the geometry—the better current injection, thermal resistance and LEE that are possible with the devices of type A, are already sufficient to produce a more intense deep-UV emission than what is possible with those of type C.

However, as discussed in Chapter 4, the absolute radiant power that can be achieved with the μ-LED approach strictly depends on the efficient use of the chip area, which in case of devices of type A and type B was clearly not pushed to the extreme limits, with only 3% of the available area used for current injection and hence active UV emission. While this choice was justified by the particular application for which the device was designed—in which a high UV power emission was not required—there is nonetheless room for a significant increase of the maximum achievable power, with the use of denser μ-LED clusters. To remove the effects due to different geometries, and to estimate the potential for this further design evolution, the intensity data previously discussed were also divided by the effective area of the corresponding device to obtain the relative radiant exitance[13] as a function of the current density. As apparent in Figure 5.13 (b) where the devices are compared this way, the large-area device appears to be by far the least performant of the three types, both with respect to the whole emission range and the deep-UV component. In particular, at 200 A/cm^2 the type-A device showed a maximum exitance that was up to

[13] Also referred to as radiant emittance.

2.9 and 7.1 times higher than that of the type-C device in the 200–600 nm and 240–270 nm ranges, respectively.

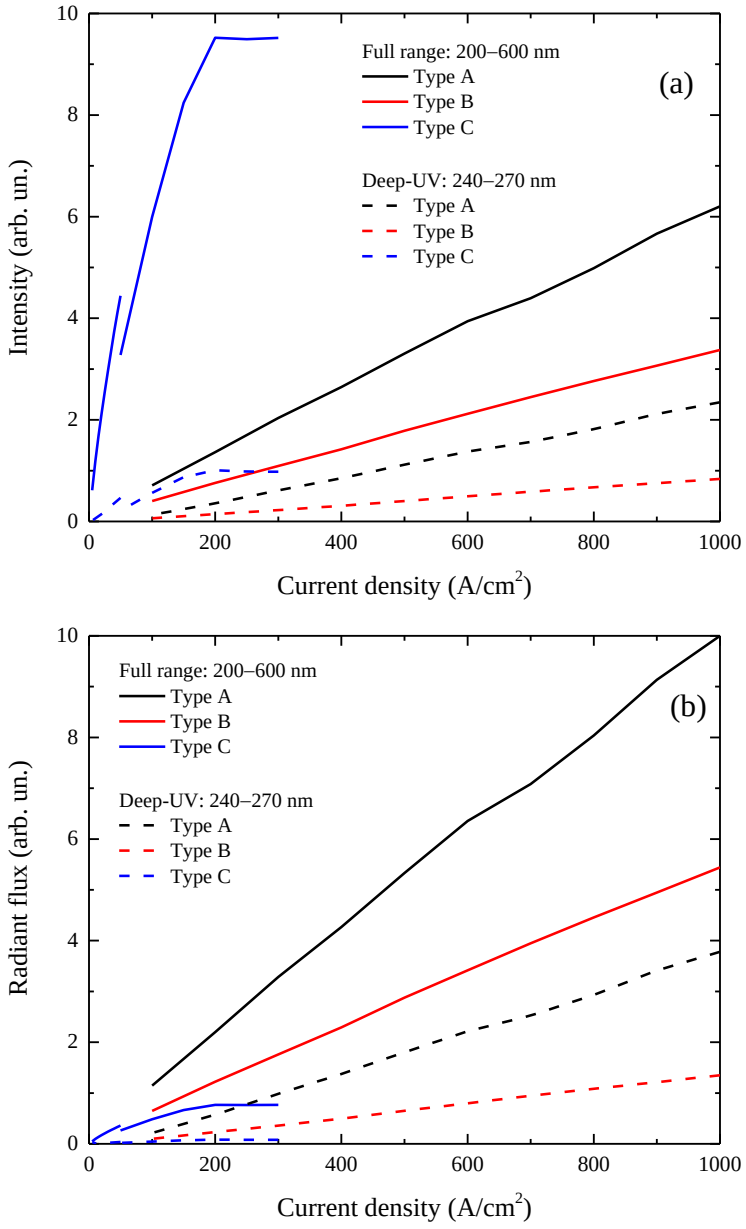

Figure 5.13: Comparison of μ-LEDs with standard large-area devices

Comparison of the radiant flux (a) and radiant emittance (b) of the devices of type A (black lines), type B (red lines), and type (blue lines); the values shown are the result of an integration along the deep-UV range (dashed lines) and the whole emission spectrum (solid lines).

Considering that all the devices compared in this analysis share the same vertical structure and hence—in a first approximation—have the same voltage–current-density characteristics, the graph in Figure 5.13 (b) can then be interpreted as an estimation of the relative WPE of the three devices. Although the use of denser clusters cannot be extended indefinitely, and more research would be necessary to determine whether the upper limit is due to geometrical constraints or to the onset of reliability issues caused by the inevitable increase of temperature, still these results show that the μ-LED emitters are inherently more performant than the standard large-area devices, with an improvement of the maximum allowable radiant flux in excess of an order of magnitude.

LEE variations due to the backside finishing of the chip

All the measurements previously discussed were performed directly after fabrication, before any treatment of the chip backside, which still had the unpolished finishing typical of the standard sapphire substrates. However, before dicing and packaging of the individual devices, our process flow requires that the sapphire substrate be thinned and polished. Although thinning is commonly performed as a way to reduce the thermal resistance of the device [20], in our case—where a flip-chip mounting is used—this procedure is introduced only to facilitate the subsequent dicing step, for which a thickness of 120–130 μm is required by our equipment for optimal results. Polishing, on the other hand, is an optional step that might have an impact on the LEE of the final device; impact that was found to be beneficial in the case of visible μ-LEDs.

To evaluate any possible effect of this treatment on the deep-UV devices object of this study, the integrated intensity of three type-A and four type-B devices was measured, on-chip, after thinning and polishing, but before dicing. As shown on Figure 5.14, where the results relative to the deep-UV spectral range are compared, while no significant difference was detected on the devices of type B, an increase up to 31% was present in the devices of type A.

Although it is well known that the presence of a roughened backside surface can significantly favour the total light extraction from the chip [19], the fact that the results here reported include the coupling with an optical fibre having a numerical aperture of 0.22 (i.e. an acceptance angle of only ±13°) can explain these seemingly contradictory results. In fact, the effect of the unpolished finishing on the light extraction is two-fold: from the one hand, part of the radiation that would be emitted at small angles is instead

diffused at larger angles causing a reduction of the coupling into the fibre; from the other hand, part of the radiation that would be emitted at excessively large angles or even trapped by total internal reflection can instead be coupled into the fibre. In the case of devices of type B, these two mechanisms somewhat compensate with each other and no net effect is present. On the contrary, in the case of devices of type A, the extra amount of radiation that is intercepted by the slanted sidewalls and reflected back towards the substrate is already emitted at the very small angles necessary to ensure extraction and coupling into the optical fibre, and the presence of an unpolished and diffusing surface can only have a negative effect.

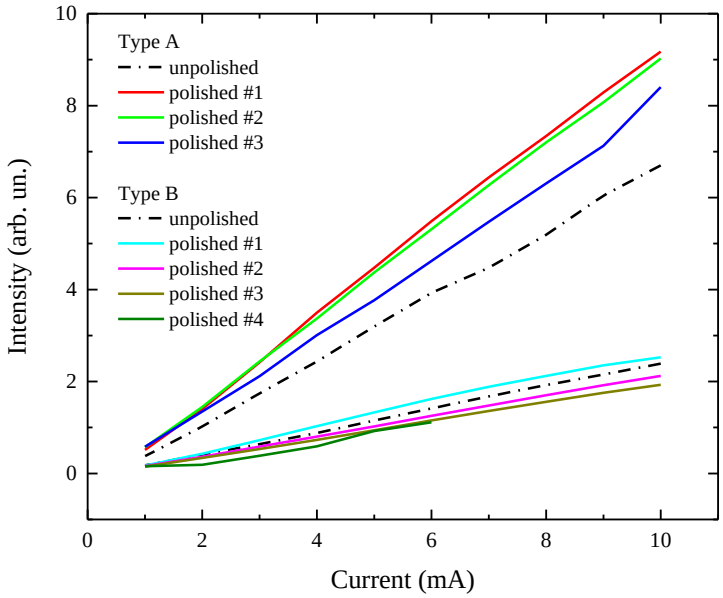

Figure 5.14: Effect of the polishing of the substrate

Comparison of the LI characteristics of a μ-LED device with (solid lines) and without (dot-dashed lines) polishing of the substrate; the values shown are the result of an integration along the deep-UV range only. The results refer to the devices of both type A and B.

This is further demonstrated in Figure 5.15, in which the average integrated intensity of the same polished devices is reported for the whole emission range (200–600 nm) and the deep-UV component (240–270 nm), together with the intensity ratio of the two types of device.

Similarly as for the unpolished devices, apart from a small deviation at the lowest current, the LI characteristics were linear and the LEE enhancement fairly stable, with an increase of about 2.3 and 4.0 times in the whole and deep-UV emission ranges, respectively.

Compared with the results shown in Figure 5.12, the presence of a polished surface accounts for a further 21% increase in the LEE over the whole emission range, and a further 31% in the deep-UV range. This latter result then justifies the choice to include a polishing step for our deep-UV device.

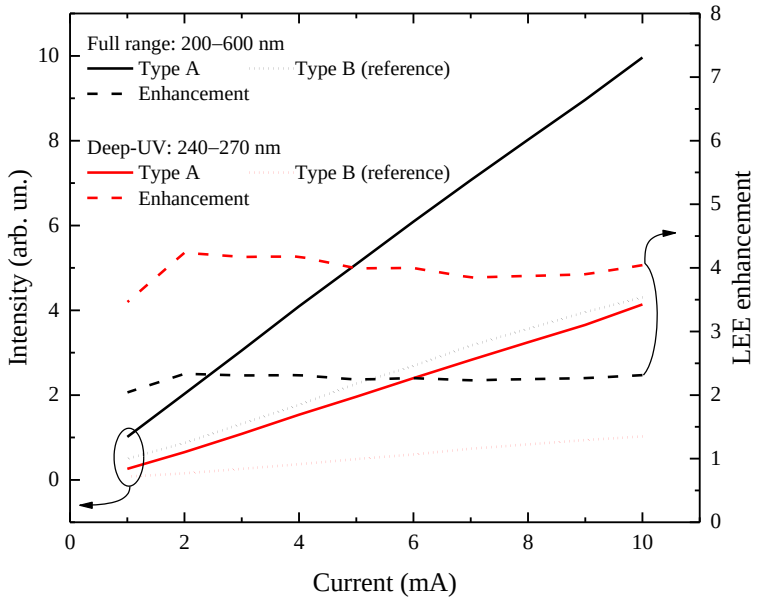

Figure 5.15: LEE enhancement with a polished substrate

Comparison of the LI characteristics of a μ-LED device with (solid lines) and without (dotted lines) mesa etch; the values shown are the result of an integration along the deep-UV range (red lines) and the whole emission spectrum (black lines). The ratio of the intensity emitted by devices with and without mesa etch is also reported (dashed lines).

5.3.2 Far-field analysis

Despite the significance of the measurements previously described, they are not able to provide sufficient information on the optimization of the mesa shaping, particularly on the effectiveness of its depth and sidewalls angles. In fact, because all the light emitted within the acceptance angle of the optical fibre is mixed together and detected while all the rest is lost, this method cannot be used to assess whether the radiation reflected from the sidewalls is actually emitted perpendicularly to the substrate or not.

To investigate this point, an analysis of the far-field emission pattern was undertaken. This type of measurement requires that the radiation emitted by the device is selectively collected as a function of the emission angle, and, for this reason, the DUT needs to be fitted in some form of goniometer. This is usually done on packaged devices that are

much more easily handled than the on-chip LEDs that were subjected to the previous experiments.

To prepare the samples, the chip substrate was thinned and individual devices were separated and flip-chip mounted on a solder-coated polycrystalline AlN submount. Isolation cuts were made through the solder layer into to the insulating AlN substrate with a diamond saw; in this way, separate metal pads were made for the *p*- and *n*-contacts of the LEDs. The contact pads on the devices were studded with gold bumps, and fine placed onto the solder substrate. The solder was then molten to make vertical interconnects between the LED chip and the AlN submount. The whole assembly was then mounted on a TO-46 header and wire bonded to the package pins, as shown in Figure 5.16.

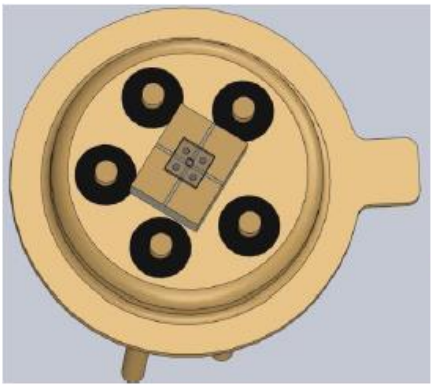

Figure 5.16: Schematic of the final packaged device

The square LED chip is attached to a submount, in turn attached to the TO-46 header. Each corner of the submount is electrically connected—by means of gold bumps—to the corresponding corner of the chip: two of them with the large common *n*-contact, the other two with an independent *p*-contact each. The submount corners are then wire bonded to three of the insulated pins available on the header.

The packaged devices were initially tested with a commercial gonio-photometer Labsphere LED–1100, but the light intensity was not high enough to produce any reliable far-field measurements, even at current biases as high as 15 mA. In addition to that, the heat transfer from the chip to the submount and from the submount to the TO-46 header was poorer than expected, which caused the device to severely heat up and, in some cases, even fail after a few minutes of operation.

For this reason a custom made gonio-photometer was assembled using an Ocean Optics 2000+UV–VIS spectrometer as a detector. In addition to being much more sensitive into the UV range than the silicon photodetector used in the Labsphere gonio-photometer, this solution also allows measuring the spectral content of the emitted radiation, which can be used to acquire far-field patterns for each of the three main emission peaks.

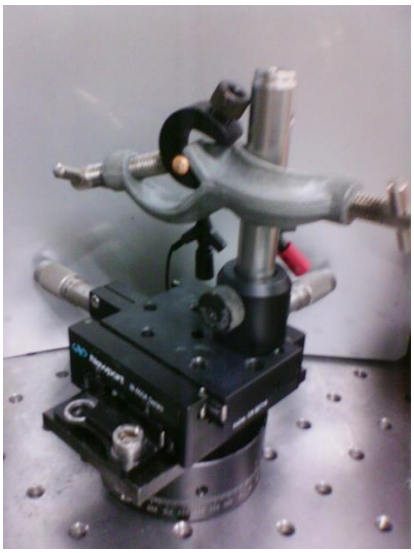

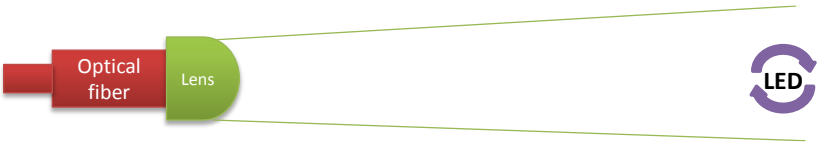

Figure 5.17: Far-field measurement setup

Photograph of the special setup that was used to measure the far-field emission patterns of packaged devices. The TO-46 header containing the DUT is held by a clamp on a XY translation stage, which can in turn rotate with respect to a fixed detector. As shown by the bottom diagram, the detector is the extremity of an UV-transparent optical fibre coupled with a lens; in addition to increasing the detection area of the sensor, the lens can be used to adjust its acceptance angle.

The experimental setup—a picture of which is shown in Figure 5.17—consists of a rotating circular stage onto which the DUT is secured; a XY translation stage integral with the rotating part is used to adjust the position of the DUT so that this can be made to coincide with the axis of rotation. The spectrometer is connected to a UV-transparent optical fibre, whose other extremity is held on the azimuthal plane by a support, and directed towards the rotating DUT at a fixed distance from it. A UV-transparent lens is fitted to the optical-fibre extremity so that a much larger area can collect UV radiation,

which makes it possible to increase the distance from the DUT and minimize the errors induced by the non-prefect adjustment of the DUT position with respect to the rotation axis of the stage. Considering a distance of about 22 cm and a lens diameter of 5 mm, an angular resolution of:

$$\Delta\theta = \frac{0.5\ cm}{22\ cm} = 0.023\ rad \approx 1.3° \tag{5.3}$$

can be estimated, which is more than adequate for the purpose of this experiment. To minimize the collection of any residual ambient light, the position of the lens with respect to the optical-fibre extremity was adjusted in order to limit the acceptance angle as shown in the bottom diagram of Figure 5.17.

A few samples for each of the three types of device were then prepared for this experiment. They were biased with a fixed DC current in the range 1–10 mA, and the emission spectra collected at steps of 5 degrees from 0° to 90° and from -90° to 0°; the acquisition was performed in dark-room conditions and with integration times of 1 min. After the collection of the spectra, the origin of the angular scale (i.e. the 0° direction) was then adjusted to make it coincide with the direction normal to the chip surface.

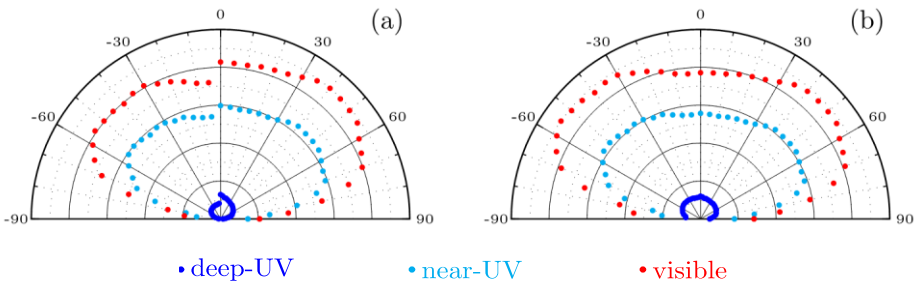

Figure 5.18: Far-field pattern of large-area devices (type C)
Comparison of the emission intensity at different angles for the large-area device. The data relative to the three emission ranges are displayed without (a), and with (b) correction of the intensity degradation due to the aging effects.

The far-field patterns of the large-area devices (i.e. type C) are shown in Figure 5.18, where the emission intensity integrated across the deep-UV (240–270 nm), near-UV (270–350 nm), and visible ranges (350–650 nm) are reported. Although the high sensitivity of the spectrometer made it possible to acquire some data, the large increase in

temperature due to the already mentioned poor thermal management of the packaged devices caused an obvious degradation of the emission intensity. This can be seen in Figure 5.18 (a) in the form of a discontinuity at 0°, where the first and the last measurements meet; discontinuity which is particularly evident for the deep-UV emission.

Because this degradation of the intensity was roughly linear with the total operation time, an approximate compensation of this effect can be put in place. If ΔI_{TOT} is the total degradation after n steps, calculated as the ratio between the last and the first measurement, the incremental degradation taking place at each single step is simply:

$$\Delta I = \sqrt[n]{\Delta I_{TOT}}\,. \tag{5.4}$$

The degradation-corrected far-field patterns shown in Figure 5.18 (b) were hence obtained with this approach. It is worth noticing that their laterally-elongated shapes are a clear signature of the existence of a significant TM-polarized component in the emission from these devices. As discussed in the introductory part of this section—Cf. in particular Figure 5.10—this means that the composition and strain of the active region of these deep-UV LEDs are able to induce a substantial in-plane emission, and justifies the use of μ-LED emitters to increase the LEE.

In case of the μ-LED devices (i.e. type A and B) the issue with the temperature was instead less severe because of their significantly lower thermal resistance. As a consequence of that, the intensity degradation during the acquisition of the data was relatively moderate and no correction was necessary, when the analysis was limited to the range between 0° and +90° only. However, despite the better thermal behaviour of these device compared with those of type C, still the increase of temperature was large enough to change the shape of the spectra by significantly increasing the defect peak at 300 nm, as can be seen clearly seen in Figure 5.19.

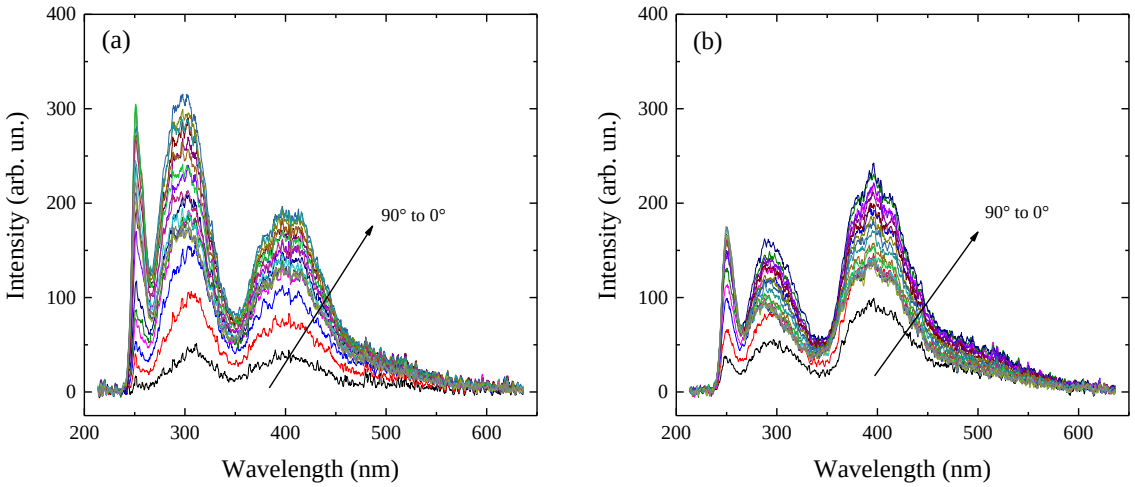

Figure 5.19: Emission spectra of the packaged devices

Example of EL spectra of the type-A (a), and type-B (b) devices, when measured on packaged samples. Compared with the devices measured on-chip, the defect peak at 300 nm is, in both cases, significantly increased, most likely due to an increased working temperature.

In order to estimate the effectiveness of the reflective sidewalls, the far-field patterns of one device of type A and one of type B are compared with each other in Figure 5.20, for each of the three main emission peaks.

In both the near- and deep-UV case, the optical power extracted from the μ-LEDs with sidewalls was indeed higher than that obtained from the reference device without mesa etch; in particular, the increase of intensity varied from 2 times in the front direction up to more than 3 times at an angle of about 30°. However, the fact that the maximum intensity emitted by a μ-LED device not only does not correspond to the direction at 0°, but it is emitted at directions even larger than the acceptance angle of a typical optical fibre, clearly proves that the mesa etch is not yet optimal. This means that a significant part of the radiation that is intercepted and reflected by the sidewalls of the μ-LEDs, although it does get extracted from the device, is emitted at angles so large that make it impossible any coupling into the fibre. Therefore, the results that were shown in Figures 5.12 and 5.15 have the potential to be improved even further; unfortunately, due to the constraints discussed in Chapter 4, this would require a substantial modification of the fabrication process that is outside the scope of this thesis and might be the subject of a possible follow-up project.

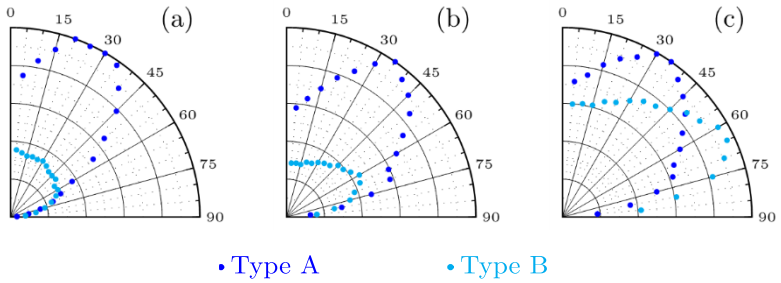

Figure 5.20: Far-field pattern of μ-LEDs (type A and B)

Comparison of the emission intensity at different angles for the devices with and without mesa etch. The three graphs refer to the deep-UV range (a), near-UV range (b), and visible emission range (c).

Another interesting feature can be seen in Figure 5.20 (c), in which the far-field patterns of the visible emission range are compared and, quite unexpectedly, the intensity of the reference device without mesa etch appears to become even higher than that of the fully-processed μ-LED device, for the emission angles larger than 50°. Because the sidewalls angles are definitely larger than the critical angle of total internal reflection, all the light emitted within the extraction cone cannot be stopped or redirected in any way by the presence of the mesa sidewalls, so that no shadowing effect is possible. Instead, this behaviour is most likely due to some form of wave-guiding effect whereby part of the light trapped inside the semiconductor reaches, after multiple reflections, to the edges of the chip, where it can eventually emerge and be collected by the detector. On the contrary, the presence—on top of the chip—of a highly UV-absorbing *p*-GaN layer explains why this effect cannot be seen neither in the near-UV emission, nor in the deep-UV one.

As mentioned earlier, the far-field patterns shown both in Figure 5.18 and 5.20 were measured along the azimuthal plane; however, because of the substantially circular symmetry of both the large-area and the μ-LED emitters, it can be assumed that they also represent the far-field patterns along any other plane that contains the normal to the surface of the chip. For this reason, it is possible to calculate the total radiant flux $\Phi(\theta)$ emitted within the cone of angle θ, by doing a double integration in polar coordinates of the 'overall' far-field pattern that is obtained by a 2π rotation of the azimuthal pattern $I(\theta)$:

$$\Phi(\theta) = 2\pi \int_0^{\theta} I(\theta) \sin\theta \, d\theta \, . \tag{5.5}$$

By applying this formula to the deep-UV data from Figure 5.20 (a), one obtains the curves shown in Figure 5.21 (a), where the total deep-UV optical power that a sensor can detect is displayed as a function of its acceptance angle. As the angle approaches the maximum value of 90°—which corresponds to the ideal case of a complete optical coupling between DUT and sensor—the radiant fluxes of the two devices asymptotically reach their maximum values. For completeness of analysis, the ratio between these two curves, together with the ratios of the near-UV and visible fluxes, are shown in Figure 5.21 (b). As pointed out before, the comparison between devices of type A and B gives an estimation of the LEE enhancement made possible by the use of μ-LED emitters. As expected from the results discussed in Section 0, the extraction efficiency on the visible range was indeed significantly lower than in case of the UV radiation; however, in contrast with that, the calculated values of LEE enhancements were in all cases much lower than what expected. In fact, for the deep-UV radiation, the enhancement was only of 2 times at 0°; it then gradually increased towards a maximum of 2.85 at around 40°, before eventually decreasing back to 2 at 90°. For an acceptance angle of 13°, as in the case of the optical fibre used in the experiments of Section 0, these calculations would give an LEE enhancement of less than 2.5, whereas the actual measurements gave a value of 2.8 for the non-polished sample and a value of 4 for the polished one.

The reasons for this discrepancy are not yet fully understood and need to be further investigated. However, it appears reasonable to assume that the active regions of the packaged devices might radiate light along slightly different emission patterns that those of the devices tested on-chip. As already discussed for the modification of emission spectra shown in Figure 5.19, the increase of temperature might be the cause of this behaviour. This seems to suggest that, although a modification of the mesa etch is indeed necessary, the amount of radiation emitted in-plane—and hence the effectiveness of the μ-LED approach—might be affected by the thermal management of the device.

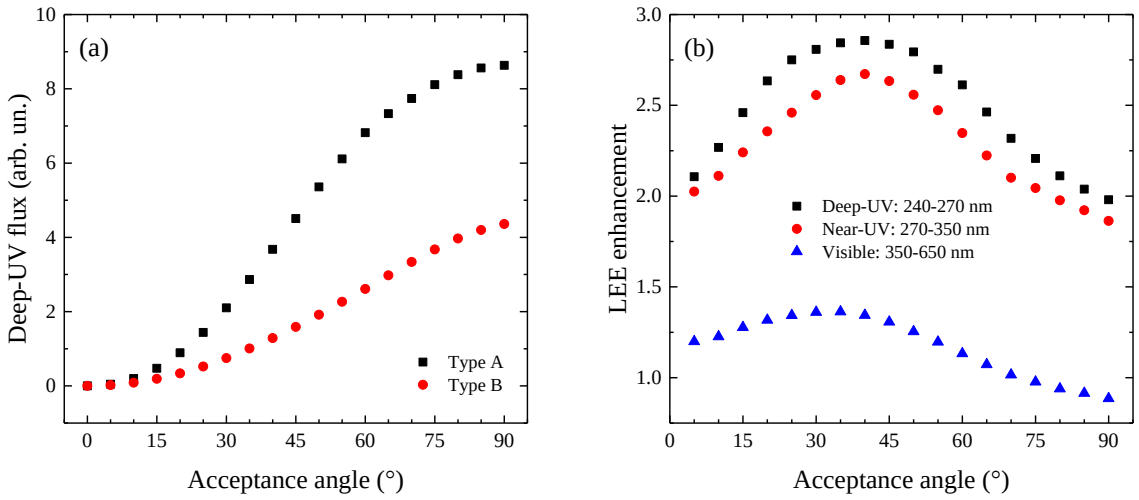

Figure 5.21: Variation of the coupling with acceptance angle

Calculation based on Eq. (5.5) of the deep-UV radiant flux (a), and LEE enhancement for the three emission ranges (b); in both cases the data are shown as a function of the detector acceptance-angle.

5.4 Conclusions

Both the experiments described in this chapter clearly prove that the implementation of the μ-LED emitters, as defined by the procedures described in Chapter 4, are indeed able to confer high performances to the UV LEDs, both in terms of high optical-modulation bandwidth and increased LEE.

More specifically, the measurement of the switching characteristics of the deep-UV LED has shown that this device is able to meet and exceed the 10 MHz of optical bandwidth required by the ESA. In addition to that, the special technique that has been developed to conduct this type of analysis proved to be a valuable tool that can be used to investigate other aspects of the UV LEDs. In particular, preliminary results show that, if adequate reference devices were prepared, it would be possible to use this technique to study how the variation of the internal polarization fields can affect the intensity of the QCSE. This would be especially useful to characterize the devices with InAlN/AlGaN active regions, in which the polarization discontinuities can ideally be completely removed.

With regard to the LEE, it was proven that devices based on clusters of μ-LEDs show a significant enhancement of light extraction, and that this improvement is especially high for the deep-UV emission. Comparison of the radiant exitance of large-area devices and μ-LED ones showed that, when the current bias is increased, the former fail before they can reach the output power demonstrated by the latter. The far-field analysis of the

devices showed that the etching step used to define the μ-LED sidewalls can be further optimized; this is expected to increase the LEE, but fabrication issues would need to be addressed.

The fact that this characterization work was performed on preliminary and inefficient devices, fabricated from non-optimized epitaxial material, is the main reason for the experimental issues that were described in the chapter. The use of devices with higher optical output would have reduced the impact of the ringing effects present on the first experiment, and would have allowed a reduction of the high current bias that was the cause of the device heating on the second experiment. Preliminary tests on the devices based on the final material grown at the end of the project seem to indicate that this would now be possible.

5.5 Bibliography

[1] H. Li, T. C. Sadler, and P. J. Parbrook, "AlN heteroepitaxy on sapphire by metalorganic vapour phase epitaxy using low temperature nucleation layers," *Journal of Crystal Growth,* vol. 383, pp. 72-78, 2013.

[2] *Gravitational wave mission selected, planet-hunting mission moves forward*. Available: http://sci.esa.int/cosmic-vision/59243-gravitational-wave-mission-selected-planet-hunting-mission-moves-forward/ [Accessed September 2017]

[3] *LISA mission, European Space Agency*. Available: https://www.elisascience.org/ [Accessed June 2018]

[4] D. B. Debra and J. W. Conklin, "Measurement of drag and its cancellation," *Classical and Quantum Gravity,* vol. 28, 094015, 2011.

[5] L. Liu, Y. Z. Bai, Z. B. Zhou, H. Yin, D. Y. Tan, and J. Luo, "Measurement of the effect of a thin discharging wire for an electrostatic inertial sensor with a high-quality-factor pendulum," *Classical and Quantum Gravity,* vol. 29, 055010, 2012.

[6] M. Akhter, P. Pampili, V. Z. Zubialevich, C. Eason, Z. H. Quan, P. P. Maaskant*, et al.*, "Over 20 MHz modulation bandwidth on 250 nm emission of AlGaN micro-LEDs," *Electronics Letters,* vol. 51, pp. 354-355, 2015.

[7] M. Akhter, P. Maaskant, B. Roycroft, B. Corbett, P. De Mierry, B. Beaumont*, et al.*, "200 Mbit/s data transmission through 100 m of plastic optical fibre with nitride LEDs," *Electronics Letters,* vol. 38, pp. 1457-1458, 2002.

[8] P. P. Maaskant, H. Shams, M. Akhter, W. Henry, M. J. Kappers, D. Zhu*, et al.*, "High-speed substrate-emitting micro-light-emitting diodes for applications requiring high radiance," *Applied Physics Express,* vol. 6, 022102, 2013.

[9] D. V. Dinh, Z. Quan, B. Roycroft, P. J. Parbrook, and B. Corbett, "GHz bandwidth semipolar (11-22) InGaN/GaN light-emitting diodes," *Optics Letters,* vol. 41, pp. 5752-5755, 2016.

[10] Z. Quan, D. V. Dinh, S. Presa, B. Roycroft, A. Foley, M. Akhter*, et al.*, "High Bandwidth Freestanding Semipolar (11-22) InGaN/GaN Light-Emitting Diodes," *IEEE Photonics Journal,* vol. 8, 2016.

[11] S. X. Jin, J. Li, J. Z. Li, J. Y. Lin, and H. X. Jiang, "GaN microdisk light emitting diodes," *Applied Physics Letters,* vol. 76, pp. 631-633, 2000.

[12] S. X. Jin, J. Li, J. Y. Lin, and H. X. Jiang, "InGaN/GaN quantum well interconnected microdisk light emitting diodes," *Applied Physics Letters,* vol. 77, pp. 3236-3238, 2000.

[13] Y. Taniyasu, M. Kasu, and T. Makimoto, "Radiation and polarization properties of free-exciton emission from AlN (0001) surface," *Applied Physics Letters,* vol. 90, 261911, 2007.

[14] K. B. Nam, J. Li, M. L. Nakarmi, J. Y. Lin, and H. X. Jiang, "Unique optical properties of AlGaN alloys and related ultraviolet emitters," *Applied Physics Letters,* vol. 84, pp. 5264-5266, 2004.

[15] J. E. Northrup, C. L. Chua, Z. Yang, T. Wunderer, M. Kneissl, N. M. Johnson*, et al.*, "Effect of strain and barrier composition on the polarization of light emission from AlGaN/AlN quantum wells," *Applied Physics Letters,* vol. 100, 2012.

[16] R. G. Banal, M. Funato, and Y. Kawakami, "Optical anisotropy in [0001]-oriented $Al_xGa_{1-x}N$/AlN quantum wells (x>0.69)," *Physical Review B - Condensed Matter and Materials Physics,* vol. 79, 2009.

[17] J. Rass and N. Lobo-Ploch, "Optical polarization and light extraction from UV LEDs," in *III-Nitride Ultraviolet Emitters*, vol. 227, M. Kneissl and J. Rass, Eds. Cham (Switzerland): Springer Verlag, 2016, pp. 137-170.

[18] J. J. Wierer, A. A. Allerman, I. Montaño, and M. W. Moseley, "Influence of optical polarization on the improvement of light extraction efficiency from reflective scattering structures in AlGaN ultraviolet light-emitting diodes," *Applied Physics Letters,* vol. 105, 061106, 2014.

[19] H. Y. Ryu, I. G. Choi, H. S. Choi, and J. I. Shim, "Investigation of light extraction efficiency in AlGaN deep-ultraviolet light-emitting diodes," *Applied Physics Express,* vol. 6, 062101, 2013.

[20] H. K. Lee, J. S. Yu, and Y. T. Lee, "Thermal analysis and characterization of the effect of substrate thinning on the peformances of GaN-based light emitting diodes," *Physica Status Solidi (A) Applications and Materials Science,* vol. 207, pp. 1497-1504, 2010.

6 Conclusions and future work

In the previous five chapters of this thesis, the main aspects of the UV LED technology have been critically analysed and discussed. Despite the staggering amount of progress that has been made over the past decade in the design, growth and fabrication of UV LEDs, these devices still suffer from a considerably lower efficiency than their visible counterparts. This ultimately leads to the high selling costs that are believed to be the fundamental issue that still prevents a full replacement of the traditional UV sources with the emerging UV LEDs. Not dissimilarly from the investigations currently ongoing on other institutions, the research efforts undertaken during the study discussed in this thesis were aimed at tackling this efficiency issue from different angles.

In fact, although UV and blue LEDs are both based on the same semiconductor system, the peculiarities of the Al-rich AlGaN materials typical of the former are responsible for a number of very specific technological challenges that, together, explain the striking difference in their efficiencies. These issues and their possible solutions or mitigation strategies were detailed in Chapter 1. In particular, thanks to the introduction of the concept of an "efficiency chain", all the mechanisms that shape the overall efficiency of a light-emitting device were separately reviewed, and the challenges related to the characteristics of the AlGaN alloys were critically discussed. This not only introduces the language that was used in the rest of the thesis, but also explains the rationale behind the engineering solutions investigated in the following chapters.

Within this framework, two main research projects were in particular carried out, whose most significant results are hereafter briefly summarized. As outlined in the relevant chapters, the first project primarily focused on investigating the opportunity to use InAlN—in place of the more standard AlGaN—as an active material in near-UV LEDs, in the hope that the localization effects due to the presence of In would be able to improve the IQE of these devices. At the end of the project, an InAlN-based LED emitting at around 340 nm was indeed demonstrated, as discussed in Chapter 5. In addition to that, the results of the EL analysis performed at pulsed conditions, which is also discussed in Chapter 5, are in good agreement with our assignation of the main emission peak of this device to NBE emission. However, despite temperature-dependent PL measurements performed on InAlN/AlGaN QWs giving very encouraging results—

with apparent IQEs of about 65%, compared with less than 1% in the reference AlGaN/AlGaN devices—the fully-fabricated and electrically injected LEDs showed efficiencies significantly lower, with an optical output power that was always at least one order of magnitude lower than in the reference LEDs. A significant part of the project was hence devoted to understanding the reason for this unexpected underperformance.

A simulation study discussed in Section 2.4 seems to suggest that the decreased crystal quality of the InAlN QWs might play an important role. In fact, although the performed simulations indeed predict a significant increase of the IQE when the localization effects of the In-containing alloys are taken into account, this improvement can be completely thwarted by an increase of the dislocation concentration as low as three times, which, considering how much more difficult is to grow high quality InAlN than AlGaN, does not seem an unreasonable condition.

In addition to that, the incredibly high operating voltages shown by all the InAlN-based LEDs fabricated and tested within this project—in which forward voltage drops of up to 50 V at 14 mA were measured—are a clear signature of very poor electrical efficiency, and justify the thorough analysis of the doping of the cladding layers, which was undertaken in Chapter 3. In fact, these investigations confirmed that both the *n*- and *p*-type doping of the Al-rich AlGaN materials used in these devices were very far from being optimal. In addition to that—although limited to the *n*-type AlGaN only —the optimal growth conditions that lead to the formation of the epilayers with the highest conductivity were also determined for materials with different AlN concentrations.

Finally, it is worth noticing that, in addition to the localization effects previously discussed, the simultaneous use of InAlN and AlGaN materials, respectively as QWs and QBs, makes it possible to engineer the active region so that, while a reasonable quantum confinement of the free-carriers is still possible, almost no discontinuity of the internal polarization field is present, a configuration that should lead to a significant reduction of the QCSE and, consequently, to a further increase of the IQE. This aspect of the InAlN-based devices was analysed in the study reported in Section 2.5.

In contrast with this approach, the focus of the second project (for 240 nm LEDs) was much less on the improvement of the IQE but rather on reliability and fabrication issues. In fact, because of the very specific requirements of the space application for which the

deep-UV LED object of this research was designed, the absolute optical power of the device was not as critical as the LEE or the quality of the coupling of the device with optical fibres. For these reasons, as discussed in detail in Chapter 4, an important part of this project was devoted to the optimization of the μ-LED technology and, in particular, to its adaptation to the specificities of the deep-UV LEDs. This last point was especially important with regard to the investigations of new metallization schemes able to guarantee reasonable electrical performance even on the contacts deposited on Al-rich AlGaN materials, which are typical of these devices. This part of the research was also discussed in Chapter 4.

Although the study of the *n*-type doping of the AlGaN materials was initially motivated by the research carried out within the other project, the type of analysis discussed in Chapter 3 is of fundamental importance also for the optimization of the deep-UV device, and for this reason the investigations about the optimal growth conditions were successfully extended to materials with AlN concentrations up to 85%.

As detailed in Chapter 5, a well-optimized device was eventually realized, which was able to meet all the main specifications set by the funding agency. In particular, NBE emission below 250 nm was demonstrated, as well as an optical-modulation bandwidth in excess of 20 MHz, which were both necessary conditions to make it advantageous the replacement with UV LEDs of the mercury-based UV sources in the charge-management system of the LISA mission. In addition to that, a thorough analysis of the LEE enhancement that can be achieved in the deep-UV LEDs thanks to the implementation of the μ-LED concept was also undertaken and, as reported in Section 5.3, an increased extraction of up to 4 times was demonstrated for the deep-UV range.

In addition to the main results here above summarized, the research activities conducted during this doctoral study allowed obtaining some other interesting, although preliminary, results that it was not possible to fully develop due to time and budget constraints, but that would be worthwhile pursuing in any possible follow-up projects.

For example, the interesting results of the simulation studies described in Chapter 2, and particularly the possible negative interaction of the EBL with the last QB described in Section 2.3.2, might indicate that the InAlN-based LEDs, whose heterostructure does in fact include a thick QB grown immediately before the EBL, might suffer from poor injection efficiency, which might be a contributing reason for the different results

between EL and PL measurements. However, further experimental work would be needed to confirm or disprove this hypothesis.

Another primary area of research that would need to be addressed in any continuation project is the optimization of the *p*-type doping. Although, as discussed in Section 3.4.2, there are already strong indications of over-doping in the *p*-AlGaN films grown according to our standard recipe, to be able to conduct a rigorous analysis similar to the one successfully completed for the *n*-type doping, a great deal of preparatory work would be required. In fact, because the preparation of *p*-doped samples suitable for Hall-effect measurements necessarily requires a dry-etch step that might severely alter both level and type of doping, the development of a special recipe with significantly reduced formation of plasma-induced defects is hence necessary. Even though this would undoubtedly be a quite difficult task to achieve, considering the positive impact on the device performance already obtained with the optimization of the *n*-type doping, the preliminary indications that a similar optimization might also be needed for the *p*-type doping should be thoroughly investigated.

Also related to the important issue of poor hole injection, the experience gained during this research suggests that the quality of the *p*-contact needs to be significantly increased, not only for its impact on the device electrical efficiency, but also for its effects on reliability, as indicated by the lifetime experiments briefly mentioned in Chapter 4. Considering that the use of metallization schemes based on as-deposited Pd—which is the standard approach used by our group in visible µ-LED devices—consistently led to less than satisfactory results, the use of annealed Ni/Au alloys should be considered as an alternative. In fact, as discussed in the relevant literature review present in Chapter 4, there is growing consensus among researchers that the annealing step necessary to achieve ohmic behaviour in Ni/Au-based metallization schemes is especially effective in removing native oxides from the metal–semiconductor interface, a fact that might explain why Pd-based contacts seem to work best in GaN or low-Al-content AlGaN materials, which are less prone to oxidation. In addition to that, although the use of highly reflective Pd layers might indeed be advantageous in achieving good alignment in the critical photolithographic steps of the µ-LED fabrication process, the use of semi-transparent Ni/Au layers did not actually cause any major inconvenience in the few preliminary attempts made to investigate this alternative.

Finally, considering that some of the important results of this research were actually achieved only at the end of the two projects' lifespans, a significant amount of characterization work would still be needed in order to assess the full potential of our UV LEDs. In particular, if a follow-up project were to start, it would be very important to transfer all the fabrication optimizations that were developed for the deep-UV device—most especially the metallization schemes—to the InAlN-based near-UV LED. Similarly, the new higher-efficiency deep-UV material that was eventually grown at the very end of the second project is also worth further characterization, especially because all the experimental issues that somewhat limited the scope of the analysis reported in Chapter 5 were a consequence of the low optical power of the previous samples, and might not be so severe with the new ones.

In addition to the possible future work specifically aimed at further improving the two UV LEDs object of study in this thesis, other new and more general research opportunities have also opened up thanks to the experience gained during this doctoral work. One of them is the characterization technique that was developed to measure the optical bandwidth of the deep-UV LED, which has the potential to be used to study also other types of devices. In fact, by separately analysing the dynamic of the different emission peaks of an LED as a function of the bias conditions, a great deal of information can be extracted to help understanding the competition mechanisms among the different recombination channels. In particular, this technique could be very useful for the design and optimization of fast-switching devices for optical communication.

The other important legacy of this thesis is the discovery of the presence of a significant impurity conduction in Si-doped AlGaN materials, and the development of a method that can be used to separate the contribution of this type of transport from the standard band conduction. Although the *n*-type doping of Al-rich AlGaN materials can now be controlled much better than in the past, still the mechanisms that leads to the well-known shrinkage of the window of optimal doping with the increase of the AlN concentration in the alloy are not fully understood. A systematic study of this issue with the help of the characterization technique described in Chapter 3 would most certainly help to shed some more light into this important mechanism.

In conclusion, at the end of this research programme, and thanks to the experience gained in many different aspects of the UV LED technology, a much deeper

understanding of the physics and operation of these fascinating devices has now been developed through this work. Although in this area of research there is a strong competition from many other groups, the high level of knowledge and expertise so acquired would be the perfect basis for exciting new endeavours in this field.